THE NICE-OHVMS TECHNIQUE:
REALIZING THE FULL POTENTIAL OF PRECISION MOLECULAR ION SPECTROSCOPY

BY

JAMES NEIL HODGES

DISSERTATION

Submitted in partial fulfillment of the requirements
for the degree of Doctor of Philosophy in Chemistry
in the Graduate College of the
University of Illinois at Urbana-Champaign, 2016

Urbana, Illinois

Doctoral Committee:

Professor Benjamin McCall, Chair
Professor Martin Gruebele
Professor Alexander Scheeline
Professor So Hirata

Abstract

Noise Immune Cavity Enhanced Optical Heterodyne Velocity Modulation Spectroscopy (NICE-OHVMS) is one of the most sensitive spectroscopic techniques specific to molecular ions. NICE-OHVMS relies on the combination of three separate techniques, each of which is a powerful tool. Cavity enhancement extends the interaction pathlength of the light through the absorber, frequency modulation (heterodyning) encodes the detected signal at radio frequencies to minimize the $1/f$ noise, and velocity modulation makes the technique specific to ions. The optical cavity also results in a large power enhancement through the absorber which can saturate molecular transitions. The Lamb dips in the spectra, due to saturation, can be fit with high precision, and the use of an optical frequency comb as an accurate frequency reference allows transitions to be recorded with MHz/sub-MHz uncertainty. In many cases, these represent a two order of magnitude improvement on the transition frequency measurement. This thesis is an exploration of the NICE-OHVMS technique. It begins with a description of the low uncertainty measurements that have been made, and then transitions into a discussion on the lineshapes that result from velocity modulation and NICE-OHVMS. The goal of studying these lineshapes is to develop NICE-OHVMS into a quantitative technique that can determine information about the absorber, such as ion mobility, drift velocity, translational temperature, and axial electric field. Understanding the lineshapes can give accurate transition intensities, which are useful in Boltzmann analyses and saturation spectroscopy. The thesis concludes with a proposed series of measurements that can be used to study saturation on a single transition. This information can be used to understand relaxation rates of the transition and the transition dipole moment. NICE-OHVMS is a remarkable experiment with outstanding prospects for future experiments. From frequency metrology applications to saturation studies, NICE-OHVMS is rich with opportunity.

To Mom and Dad. "Why?" is such a tough question.

Acknowledgments

Reflecting on my time at the University of Illinois to write this section has truly been an eye opening experience. There have been so many people who have helped me along the way that I do not think it is possible to individually name them all, but I will endeavor to acknowledge the people who have had the greatest impact on me while I have been here at the U of I.

First and foremost, my advisor, Ben McCall, has always been supportive of my scientific creativity. He has been an immeasurable force in my life responsible for honing my abilities and skills. He has always been kind when I was low and stern when I was being frivolous. Ben saw my potential as an undergrad and provided me a great opportunity to pursue my dreams, and I will never be able to fully express my gratitude. I will remember the lessons he taught and the guidance he gave for all my professional life.

Second, the entire McCall group, past and present, has played important roles in my development. However, I would be remiss to not acknowledge those who have mentored me and those with whom I have worked side-by-side. Kyle Crabtree and Brian Siller were tremendous influences in teaching me how laboratory science is actually accomplished. They personally dedicated a great deal of their time to teach me as much as they could. They also gave me their friendship and welcomed me into their homes. I will always consider them my friends first and scientific peers second. The people that I have worked with have provided equal contributions to my development as a scientist. Among these people I would like to especially thank Adam Perry and Charlie Markus. We have a very complementary skill set as we have grown professionally. I hope that my future collaborations are similar to the relationships we developed. White Horse and the bags boards were a lot of fun too.

I have been very fortunate to meet a lot of people here at the U of I who I consider to be my friends but none more so than Tom Allen, Brad Gibson, and Marcus Tuttle. Having survived the first year together, we became a tight group of friends and a good support group. The number of times they have picked me up when I was down contributed to my ability to complete the Ph.D.

My family also deserves a portion of the credit for my success. My parents have always anxiously awaited phone calls updating them on the latest trials and tribulations that have affected me. They have always

encouraged me to achieve greater and aim higher. Likewise, I would like to mention my fiancée, Heather. She has been a safe harbor in the storm for me. Whether I was struggling with anxiety, external stress, or self-doubt, Heather has maintained a calm demeanor that always helped me to refocus and contextualize negative emotions.

Most scientists have been influenced by important teachers. I am no different in that regard. The first memorable teacher to whom I owe a great deal is my aunt, she made sure that I had a strong scientific grounding both in the classroom and in real world. Her help with my science fair projects as an elementary schooler were very formative. Mrs. Kathy Harris, my high school chemistry teacher, helped me to fully appreciate the wonder of discovery and gave me the freedom in her class to disengage from the group and learn at my own pace. Whether it was letting me experiment after school or graciously allowing me to "supplement" her lessons in front of the class, she started me down the path that has led me here. Further, I would like Profs. Gary Lickfield, Igor Luzinov, and Julia Brumaghim of Clemson University and Prof. Ken Brown of Georgia Tech for mentoring me during undergrad, and furthering my development as an independent researcher. I also would like to thank my committee for being excellent teachers. I learned a great deal about quantum mechanics from Prof. Gruebele. Prof. Scheeline's lessons taught me a great deal about practical experimental design, and Prof. Hirata contributed his valuable insight to our S5 group meetings.

I also must acknowledge my sources of funding, particularly the NSF for granting me a graduate research fellowship, and the U of I for the Springborn Fellowship.

Table of Contents

List of Tables

List of Figures

Chapter 1

Introduction

Molecular ions play a very important role in astrochemical, atmospheric, and combustion processes and are a vibrant field of research for molecular spectroscopists. Molecular ions are important both in the interstellar medium as well as in non-terrestrial atmospheres.[4, 5] In the interstellar medium, molecular ions can be used as tracers for the cosmic ray ionization rate[6] and can be used to help constrain complex chemical models.[7] Chemical models are also used to better understand planetary atmospheres. Molecular ions play critical roles in those chemical models. For example, cyclopropenyl cations are predicted to exist in Titan's atmosphere,[8] and H_3^+ is regularly used as a tracer of atmospheric conditions in the Jovian ionosphere.[9] Likewise, atmospheric models can be used to understand Earth. In Earth's atmosphere, nitrogen, oxygen, and water play important roles in the types of molecular reactions that are pertinent to atmospheric chemical models.[10] Of special importance is the myriad ways in which water forms clusters with ions.[11] Atmospheric models are not the only type of chemical networks in which molecular ions contribute to the study of complex systems. Molecular ions also provide a window into the chemical pathways for combustion reaction networks. Combustion of fossil fuels form a rich mixture of carbonaceous ions as intermediates and by-products.[12, 13]

A brief survey of the literature provides examples demonstrating many practical instances of research involving molecular ions; however, these are not the only interesting fields of study. Despite years of research into molecular vibrations and rotations, there remain some very important fundamental physical questions that rovibrational spectroscopy has yet to address. There is a class of molecules called fluxional which contain many large amplitude motions. In other words, the ground state wavefunctions have large probability amplitudes across low-lying saddle points in the potential energy surface. Effectively, this can be classically interpreted as the molecule continually undergoing internal motion, defying the concept of reference geometry. Without the use of reference geometry, traditional spectroscopic approaches to transition assignment are useless. Two of the most well studied fluxional species are CH_5^+ and H_5^+. The spectrum of CH_5^+ was first observed with high resolution in 1999.[14] It remains unassigned to this day, but there has been some substantial progress recently.[15] On the other hand, there has been no high resolution work on H_5^+, which makes it an exciting prospect for further study. The low resolution spectrum[16] provides an excellent opportunity to search for a rotationally resolved spectrum with higher precision instruments. Obtaining a high resolution spectrum may also present similar challenges to assignment. Together, better measurement of these two ions will assist theorists in their attempts to understand the observed spectra.

Molecular ion spectroscopy is a challenging field for a variety of reasons, including low number density and the presence of interfering neutral species that congest spectra with unwanted transitions. Throughout the years, spectroscopists have employed a variety of approaches to overcome these intrinsic challenges. The invention of velocity modulation spectroscopy (VMS)[17] is one of many methods that have been utilized to overcome the difficulty of discriminating whether the spectral carrier is an ion or a neutral molecule. The importance of this development cannot be overstated. In the ∼30 years since its development, VMS has been responsible for the detection of ∼50 unique molecular species.[18] It has been this successful in large part due to its ability to discriminate ions from neutrals. VMS is capable of distinguishing between an ion and a neutral by utilizing the effects of an electric field on a charged particle. The source responsible for producing molecular ions in VMS is the positive column of an AC modulated glow discharge. As the polarity of the discharge changes, the transition profile of an ion will be alternatively red-shifted and blue-shifted, whereas the neutral is not. Incorporation of phase sensitive detection allows the detection of only the modulated signals, ignoring the unmodulated ones.

VMS was a very important development but this still did not address the difficulty of measuring very shallow absorptions. Oftentimes, VMS instruments would rely on multipass configurations to improve the signal strength, but ultimately, these could only enhance the signal strength by approximately an order of magnitude. The introduction of external cavity enhanced techniques provided an innovative way to perform spectroscopy, particularly cavity ringdown spectroscopy (CRDS).[19, 20] By coupling light into an optical cavity made of high-reflectivity mirrors and placing an analyte inside the cavity, the effective absorptive pathlength could be enhanced by many orders of magnitude paving the way for detecting incredibly weak transitions. The rate at which light intensity decays from a cavity is related to the per-pass-loss, from which absorption of light by the analyte can be inferred. Actively locking the cavity on resonance allowed the introduction of VMS to cavity enhanced techniques.[21] Incorporation of an external optical cavity with VMS was the first time that signal enhancement and ion discrimination were addressed simultaneously in the same technique, but it will prove a potent combination.

Of course, signal enhancement is not the only way to address weak molecular transitions. Reduction of the noise floor improves signal-to-noise from another point of view. One of the greatest sources of noise in electronic systems is flicker noise or $1/f$ noise. A critical innovation that allowed spectroscopists to reduce the noise floor is frequency modulation.[22] Sinusoidal phase modulation of the light creates a frequency triplet and detection via the beat signals effectively encodes the spectrum at radio frequencies dramatically reducing the effect of flicker on the baseline of the spectrum. Likewise, frequency modulation (also called heterodyne modulation) can be combined with VMS to great effect.[23]

Cavities and heterodyne modulation also have been used in concert with the technique Noise Immune Cavity Enhanced Optical Heterodyne Molecular Spectroscopy (NICE-OHMS).[24] Enjoying the signal enhancement from a cavity and the noise reduction of heterodyne spectroscopy allowed the development of what remains the most sensitive optical spectroscopy. One simple insight was required to realize cavity enhancement and heterodyne modulation in use together. The key is that the light must be modulated at exact multiples of the free spectral range of the cavity. This way the entire frequency triplet is coupled into the cavity. This choice also has the added effect of mitigating intensity fluctuation noise as a result of an imperfect lock.

Due to the success of NICE-OHMS the choice to use that technique for ion spectroscopy was straightforward. In 2011, the combination of NICE-OHMS with VMS was realized in the near-infrared and named Noise Immune Cavity Enhanced Optical Heterodyne Velocity Modulation Spectroscopy (NICE-OHVMS) by the McCall laboratory.[25] Siller *et al.* developed this in the near infrared using a Ti:Sapphire laser. Advancing the technique into the mid-infrared to where many important fundamental rovibrational transitions lie was the next important experimental thrust. It was accomplished shortly thereafter using an optical parametric oscillator as the light source.[2]

NICE-OHVMS in the mid-IR is the focus of this dissertation. After the demonstration of NICE-OHVMS in the mid-IR by Crabtree *et al.*, the experimental opportunities were abundant. Due to the high optical powers contained within an on-resonance optical cavity, Crabtree *et al.* were able to saturate the R(1,0) and R(1,1)^u transitions in the ν_2 fundamental band of H_3^+. The counter-propagating beams in the cavity act in a pump-probe scheme and burn holes at the zero velocity component (and symmetrically around the zero velocity component due to frequency modulation) in the transition profile. The holes manifest in the spectrum as Lamb dips which are significantly narrower than the full transition profile. By fitting these dips, precision linecenters can be determined that are insensitive to any drift velocity.

Chapter 2 presents the first effort to extract precision linecenters using NICE-OHVMS. It is adapted from "High-precision and high-accuracy rovibrational spectroscopy of molecular ions"[26]. The same basic principles employed by Crabtree *et al.*[2] are employed with the addition of using an optical frequency comb (OFC) as an accurate tool for frequency calibration. By offset locking the pump beam to the OFC and relying on the relative stability (timescales ~5 s) of the signal beat note on the comb, the mid-IR frequency can be determined as the difference of the pump and signal frequencies to within 10s of kHz. This level of accuracy combined with the precision allowed the determination of H_3^+ transitions to sub-MHz/MHz uncertainties depending on the signal-to-noise ratio of the Lamb dip. This was done with 10 transitions in total from the R-branch of the ν_2 fundamental band, two transitions from the ν_1 band for HCO^+, and a single unassigned transition for CH_5^+. When compared to the H_3^+ transition measured by J.-T. Shy, there was significant disagreement.[27] Initially, this was disheartening, but a careful error analysis, including checking the effect of signal-to-noise ratio, the effect of asymmetry, pressure shift, and comb calibration was performed. Nothing could be shown to be wrong with the NICE-OHVMS experiment. Moreover, combination differences of the HCO^+ transitions were consistent with the pure rotational values, a much lower uncertainty form of spectroscopy. Ultimately, publication proceeded. Later the transition frequencies were confirmed to be correct by the Stephan Schlemmer group.[28]

After demonstrating that NICE-OHVMS could be utilized for measuring molecular ion transition frequencies with extremely low uncertainty, the next natural course of investigation was to attempt to try to understand the very complex lineshapes that arise from the two individual layers of modulation. In order to approach this challenge, custom software was created, making use of the of the basic premises of the two modulation schemes under the assumption that the fundamental lineshape is practically a pure Gaussian, *i.e.* that Doppler broadening is the only significant source of line broadening for VMS based techniques. Using this software, attempts to fit measured transitions were not successful. This initiated an investigation into the precise description of the fundamental VMS lineshape. Despite the maturity of the technique, it has been predominantly used as a tool for discovery spectroscopy, with only two previous attempts made to treat the lineshapes. The first, by Civiš, relied on integration of the derivative-like lineshape, which is not a particularly accurate approach.[29] The VMS signal is much better mathematically treated as a Fourier component of the detected voltage. The second attempt by Gao was better, but it still relied on fixing a parameter to a crude theoretical estimate.[30]. Gao's fits are more meaningful because they utilize J.W. Farley's explanation of the VMS theory;[31] however, the necessity of the fixing a parameter weakens the significance of the determined parameters. The fixed parameter is strongly coupled to other parameters and therefore raises reasonable questions regarding the accuracy of the fitted parameters.

The results of the investigations into the fundamental VMS lineshapes are presented in Chapter 3, and have been published in the Journal of Chemical Physics.[32] In this chapter, an example fit to the R(1,0) transition of H_3^+ as measured by single-pass VMS is performed. Due to the high signal-to-noise ratio, it is feasible to observe subtle changes in the transition profile which allow the strongly coupled parameters to be properly discerned. The parameters that are extracted allow the high-precision determination of the RMS drift velocity of the ions, the RMS electric field strength, the translational temperature, and the relative intensity. A surprising result is the existence of a large homogeneous contribution to the linewidth which was completely unexpected by the theory. Gao had also observed this linewidth and attributed it to pressure broadening, but traditional values of pressure broadening coefficients are not consistent with the magnitude of the observed linewdith. Before the work presented in Chapter 3, it was conceivable that the value of the homogeneous contribution was in error, but now the value is confirmed. In order to explain the large value, a simple model is presented and the homogeneous linewidth is used to infer the ion mobility.

With a clear understanding of the fundamental VMS lineshape, it was possible to revisit the NICE-OHVMS lineshapes with the intention of extracting as much useful information from transition profiles as possible. These fits and the analysis of the fitted parameters are presented in Chapter 4. Fitting of the NICE-OHVMS lineshapes is performed in two parts. The first fit is performed on the magnitude of the recorded signal, the square root of the sum of the squared in-phase and quadrature channels. This type of fit allows access to information such as the overall intensity, homogeneous linewidths, inhomogeneous linewidths, and concentration modulation depth. With these parameters determined, it is possible to fit the recorded lineshapes to access phase related information such as the overall phase and the angle at which concentration modulation occurs. Fitting the parameters in this fashion allows important insight into the the physical environment of the spectral carrier.

The fitted NICE-OHVMS parameters contain all the useful physical information that can be determined from the spectral transitions. The intensity of the transition is particularly interesting as it can be used to carefully extract the saturation parameter. A measurement of the saturation parameter can be used to infer the ratio of the transition dipole moment to the relaxation rate of the transition. Since NICE-OHVMS is a cavity enhanced technique, we can observe Lamb dips as alluded to earlier in the text. Chapter 5 contains a description of an experiment that can used to determine the saturation parameter, which might be used to help assign spectra of fluxional ions. By varying the power and recording spectra, the saturation parameter can either be determined by the examination of the intensity difference between the the apparent absorption and dispersion signals recorded by the instrument or by examining the depth of the Lamb dip to the full profile intensity for both absorption and dispersion. The expected results are presented.

Together, Chapters 2 through 5 detail the efforts to completely characterize everything that can be learned from NICE-OHVMS lineshapes. From applications in frequency metrology to descriptions of the molecular environment to characterization of the degree of saturation, the full potential of the technique is explored. NICE-OHVMS represents the next generation of VMS based experiments and is a valuable addition to the a spectroscopist's arsenal. The future is optimistic.

The appendices in this work contain a complete account of all the papers to which this author has contributed, including the description the first mid-IR NICE-OHVMS instrument, and several other works in precision ion frequency determination. There is also a discussion regarding frequency error analysis using an OFC with one laser and two lasers, which is useful for understanding the uncertainty budget in the experiments described herein. Also, there is a brief discussion of a fringe that is present in the instrument. Another appendix contains a copy of the fitting suite written for this work and its associated documentation. Finally, there is also a lineshape atlas that contains simulations of many different types of spectroscopies and the expected lineshapes that result by varying different parameters. In studying complicated lineshapes, experience showed that visualization of lineshapes under a variety of conditions was immensely useful for qualitative understanding and fit parameter selection.

Chapter 2

High-precision and High-accuracy Rovibrational Spectroscopy of Molecular Ions

2.1 Introduction

In the 30 years since its invention,[17] velocity modulation spectroscopy (VMS) in a positive column discharge has been a tremendously successful method for performing direct absorption spectroscopy of molecular ions. The positive column offers a remarkably rich chemical environment suitable for the production of a wide variety of ions with a high column density.[18]

Traditional VMS has been limited in its frequency precision by broad Doppler-limited linewidths, coupled with modest signal-to-noise ratios, and the uncertainties in line center determinations are typically 30-90 MHz.[14, 33] The Doppler limit was overcome by our group in 2010 by placing the discharge cell in an external cavity, in an approach called cavity enhanced VMS.[34, 21] The high intracavity power enabled saturation spectroscopy, and the resulting Lamb dips enabled the precision to be improved to ∼3 MHz in the near-infrared. The later incorporation of frequency modulation, or heterodyne, spectroscopy improved the signal-to-noise ratio and further improved the precision.[25] This approach, based on the pioneering NICE-OHMS technique,[24] was dubbed NICE-OHVMS, or Noise Immune Cavity Enhanced Optical Heterodyne Velocity Modulation Spectroscopy. This technique was later extended into the mid-infrared, using an optical parametric oscillator, by Crabtree *et al.*[2]

The accuracy of VMS has also been limited by the method of frequency calibration. Typically, VMS experiments relied on a combination of relative calibration using marker etalons and absolute calibration using Doppler-limited reference gas transitions, which were themselves often only known to ∼30 MHz accuracy. The advent of optical frequency combs has revolutionized the accuracy of molecular spectroscopy, making sub-MHz frequency measurements almost routine. Our near-infrared NICE-OHVMS work on N_2^+ used a frequency comb to achieve an accuracy of ∼300 kHz.[25] In recent work without an external cavity, we

---

Adapted from James N. Hodges, Adam J. Perry, Paul A. Jenkins II, Brian M. Siller, Benjamin J. McCall. "High-precision and High-accuracy Rovibrational Spectroscopy of Molecular Ions". Journal of Chemical Physics, 139 (2013) 164201.

have demonstrated that it is possible to extend comb-calibrated spectroscopy to the mid-infrared, to infer pure-rotational transitions of molecular ions such as HCO^+ using combination differences with sub-MHz accuracy.[35]

In this paper, we present the combination of sub-Doppler spectroscopy using mid-infrared NICE-OHVMS[2] with optical frequency comb calibration[35] to yield a versatile method for molecular ion spectroscopy with both high precision and high accuracy. We demonstrate and characterize the effectiveness of this method through spectroscopy of H_3^+, HCO^+, and CH_5^+.

H_3^+ is a natural first target for our spectrometer. As the simplest polyatomic molecule, it has become an important system for benchmarking the increasing accuracy of quantum calculations. Many of its rovibrational transitions have been predicted to within hundredths of a wavenumber by sophisticated calculations that include adiabatic, relativistic electron, and non-adiabatic corrections to the Born-Oppenheimer potential energy surface.[36] In many cases, this degree of precision is comparable to the experimental uncertainties, so more precise measurements will serve to motivate and benchmark ever more accurate calculations, which will require the inclusion of quantum electrodynamic effects as has already been done with diatomics[37] and H_2O.[38]

In addition to its fundamental interest, H_3^+ is also an important molecule in astrochemistry due to its abundance in both dense[39] and diffuse[6] interstellar clouds, as well as in the atmospheres of large gas giants such as Jupiter.[40] Of particular relevance to the present work, the Doppler shifts of H_3^+ rovibrational transitions have been successfully used to determine the velocity of Jovian auroral winds,[41] but the accuracy of those determinations is limited by the uncertainties in the laboratory transition frequencies.

Our second target, HCO^+, was recently used[35] to demonstrate the feasibility of performing “indirect” pure-rotational spectroscopy by calculating combination differences of high-precision rovibrational frequencies. Due to degradation of our cavity mirrors in that work, we were restricted to performing single-pass heterodyne spectroscopy. Here, we revisit HCO^+ with an improved set of cavity mirrors, and we find that the single-pass measurements suffered a slight (∼4 MHz) but systematic offset due to an asymmetry in the AC plasma. This highlights the advantage of using Lamb dips in a bidirectional cavity for line center determination, as they are located symmetrically around the zero-velocity component of the ions and are not shifted by plasma asymmetries.

Our final target, CH_5^+, is an enigmatic ion whose high-resolution infrared spectrum in the C–H stretching region remains completely unassigned nearly 15 years since it was first reported.[14] It has been suggested[42] that one possible way of assigning the spectrum would be to search for four-line combination differences, which would identify energy level separations. However, the high line density results in many “false positives” at the current precision of the line center measurements. Here we report the first sub-Doppler spectrum of CH_5^+, which improves on the precision of the initial detection[14] by more than two orders of magnitude.

2.2 Experimental Description

A block diagram of the instrument is presented in Figure 2.1. A ytterbium doped fiber laser (Koheras Adjustik Y-10) is coupled into a fiber electro-optic modulator (EOSPACE PM-0K5-00-PFU-PFU-106-S), where Pound Drever Hall (PDH) locking side bands (∼4 MHz) and heterodyne sidebands (∼79 MHz, equal to the free spectral range of our external cavity) are imprinted onto the laser. After modulation, the light is amplified by a 10 W fiber amplifier (IPG Photonics YAR-10 K-1064-LP-SF) and is used to pump a singly resonant optical parametric oscillator (OPO; Aculight Argos 2400 SF). The idler, tunable from 3.2 to 3.9 μm, is coupled into a ∼190 cm external cavity composed of two dielectric mirrors (Rocky Mountain Instruments, custom) on silicon substrates with 1 m radius of curvature. For the H_3^+ measurements, the mirrors used were nominally 99.7% reflective between 3.0 and 3.4 μm but suffered high losses at higher frequencies because of water adsorbed in the hygroscopic coating. The measurements of HCO^+ and CH_5^+ have utilized a new set of mirrors, nominally 99% reflective between 3.0 and 3.4 μm, which were specially coated with a protective layer to prevent the uptake of water. Additionally, the newer mirrors are kept under a flow of dry nitrogen at all times.

The cavity and the idler are locked to maintain resonance by using a detector (Boston Electronics Vigo PVM-10.6-1x1) to monitor the back reflection from the front cavity mirror. The signal from that detector is demodulated with a mixer that is referenced to the PDH locking sideband frequency. The output of that mixer is processed by a lock box, and slow corrections ($<$ 100 Hz) are sent to a piezo on which one of the cavity mirrors is mounted, to keep the cavity locked onto the idler on slow timescales. Faster corrections (0.1–10 kHz) are sent to a piezo that controls the length of the OPO cavity, thus making small corrections to the frequency of the signal and the idler to keep the idler resonant with the cavity on fast timescales. Based on the observed magnitude of this error signal, there is an extra ∼500 kHz of random noise imposed upon the signal frequency (and therefore also upon the idler frequency) due to the locking of the idler frequency to the external cavity.

Within the external cavity is a liquid nitrogen cooled positive column discharge cell (Black Widow), which was used extensively for VMS in the Oka group at the University of Chicago. An arbitrary waveform generator (Agilent 33120A) creates a sine wave, which is amplified (Techron 7780) and sent to a step-up transformer to drive the plasma. The AC voltage configuration of the plasma modulates the velocity of the ions at a frequency of 40 kHz. Optimal signals for H_3^+ have been observed at 200 mTorr of cell pressure and 170 mA of current. For HCO^+, we used a mixture of 17:3 H_2:CO at a total pressure of 200 mTorr, and a plasma current of 115 mA. CH_5^+ was observed using a 24:1 mixture of H_2:CH_4 at 250 mTorr and the lowest possible current the discharge could maintain, typically ∼110 mA.

The idler radiation from the OPO is coupled through the discharge cell by CaF_2 windows that are aligned at Brewster's angle. The transmitted light through the cavity is detected and demodulated first at the heterodyne frequency of ∼79 MHz by a pair of mixers that are 90° out of phase with each other. The outputs from these mixers are further demodulated via lock-in amplifiers referenced to 80 kHz, twice the plasma modulation frequency. The detection scheme results in four data channels: in-phase and quadrature detection for each of the two mixers. Previously, we have estimated the sensitivity of our spectrometer in the lowest noise channel to be $9.8 \times 10^{-10}\text{cm}^{-1}\ \text{Hz}^{-1/2}$.[2]

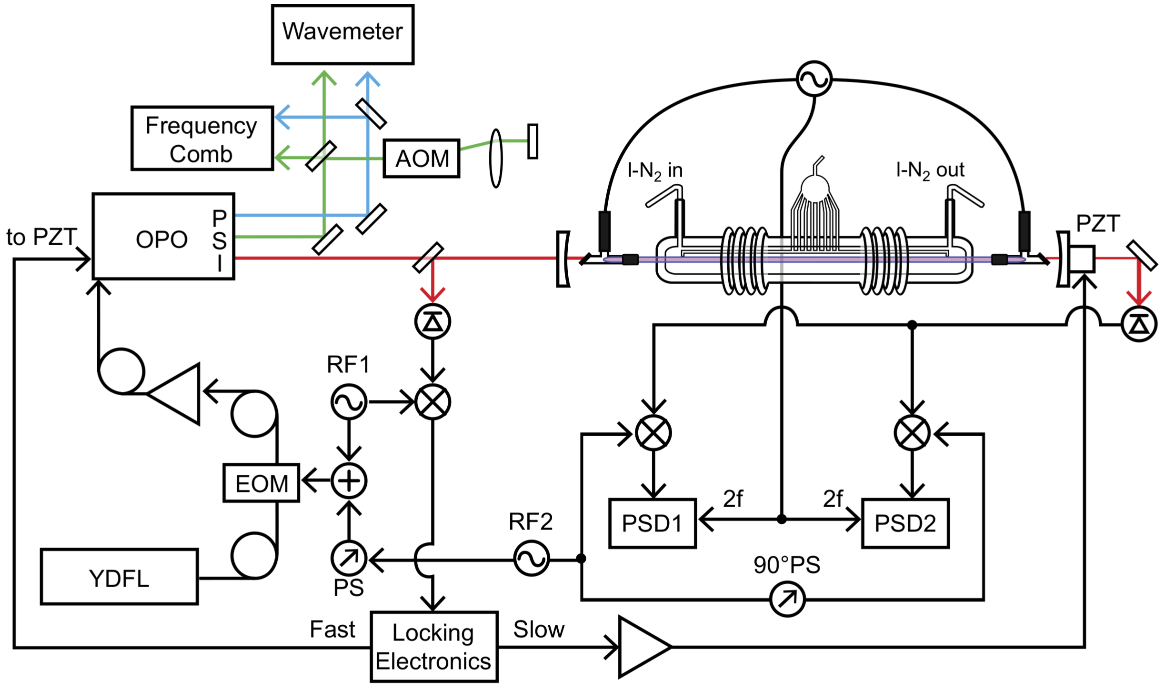

Figure 2.1: Block diagram of the instrument. YDFL: Ytterbium Doped Fiber Laser; EOM: Electro-Optic Modulator; OPO: Optical Parametric Oscillator; P,S,I: Pump(Blue), Signal(Green), Idler(Red); AOM: Acousto-Optic Modulator; PZT: Piezo-electric Transducer; PS: Phase Shifter; RF: Radio-Frequency source; PSD: Phase Sensitive Detector.

Frequency calibration of the idler is accomplished by simultaneously measuring the frequency of the pump and signal beams using an optical frequency comb (Menlo Systems FC-1500, with 100 MHz repetition rate) and determining the difference between them. First, the carrier envelope offset of the comb is tuned to ∼20 MHz to be measured by a frequency counter, although this is not strictly necessary for measuring the idler frequency. The repetition rate of the comb is tuned such that the beat frequency of the signal with the comb is between 25 and 35 MHz, the range of the internal bandpass of the frequency counter used for the signal. Next, the pump is tuned so that its beat with the comb is ∼20 MHz. Then the signs of the beats and carrier envelope offset are determined. The pump is then offset locked to the comb using a frequency to voltage converter to generate an error signal. A wavemeter (Burleigh WA-1500, 0.2 ppm accuracy) then sequentially measures the pump and signal wavelengths to determine the mode numbers of the comb teeth that are closest to these two frequencies.

For spectroscopy, the idler is tuned by changing the repetition rate of the comb. The pump is dragged along with the comb, since it is offset-locked to the comb, but the signal remains relatively constant (aside from slow drift due to thermal variations of the OPO cavity). Without any correction, this would quickly lead to the signal beat with the comb moving out of the bandpass of our frequency counter. Therefore, we double-pass the signal through an acousto-optic modulator (Brimrose IPF-200-80-1600) before sending it to the beat detection unit of the comb. The AOM frequency is adjusted with a feed forward as the comb repetition rate is changed, in order to keep the signal beat within the bandpass. The diffraction efficiency of the AOM allows it to be tuned between 150 and 210 MHz, leading to a shift of the signal frequency by 300 to 420 MHz. When the frequency limit of the AOM is reached, the frequency is increased or decreased by 50 MHz, which corresponds to a 100 MHz change in signal frequency, and the recorded mode number for the signal is incremented or decremented appropriately. The known frequency shift induced by the AOM is subtracted from the signal frequency determined by the comb before the latter is subtracted from the pump frequency to determine the idler frequency.

Data points are acquired with a separation in time of 1.5 seconds, which is ample time for the lock-in amplifiers to integrate (with a time constant of 300 ms) and the frequency counters to update (at a rate of 1 Hz). These steps are taken to minimize any line dragging by delayed detection. Scanning is performed both from low to high frequency and also from high to low frequency in order to remove any systematic errors caused by line dragging.

The use of the repetition rate for tuning limits the width of a single scan window to ∼900 MHz. In practice, this means that entire Doppler profiles of light ions such as H_3^+ cannot be measured in a single scan. In such cases, preliminary scans are taken without the frequency comb (by directly scanning the voltage on the fiber laser) over a wide range, and then the sub-Doppler features are scanned with the comb. For the heavier ions HCO^+ and CH_5^+ it is possible to record the full Doppler profile within a single scan.

2.3 Results and Discussion

2.3.1 Lineshape Fitting and Uncertainty Determination

The symmetry of the overall NICE-OHVMS lineshape is odd in both absorption and dispersion. For high precision line center determination, the most important part of the line is the Lamb dips that are evenly spaced about the transition's center frequency. The Lamb dips are a result of the forward- and counter-propagating beam sampling single velocity components on opposite sides of the Doppler profile. The frequency modulation effectively produces three lasers spaced by the modulation frequency: a carrier and two sidebands, one in phase with the carrier, and the other 180 degrees out of phase. Assuming that both the carrier and sidebands are intense enough to contribute to saturation, and that the modulation index is low enough to avoid contributions of higher-order sidebands, there exist four separate Lamb dips that can be detected in absorption, spaced evenly in half integer multiples of the heterodyne frequency about the linecenter. In dispersion there is also a fifth Lamb dip at the linecenter. In this work, detection was performed at a blended phase that provided the optimal signal-to-noise in all four channels, so the observed Lamb dips are from neither purely absorption nor purely dispersion. However, these individual Lamb dips are not resolved in this experiment because half of the heterodyne frequency is smaller than the full-width at half-maximum of the individual Lamb dips; thus we observe a blend of the five Lamb dips. For purposes of illustration, the full profile from a single detection channel (not comb calibrated) of an H_3^+ transition is shown in Figure 2.2, and an example of the fit to the blended Lamb dips in all four simultaneously acquired detection channels is shown in Figure 2.3.

The derivation of the sub-Doppler lineshape and the fits function have been presented in an earlier paper.[2] However, for clarity, the fitting procedure will be reviewed in brief. The fit is a non-linear least squares fit using an equation that models the Lamb dips and fits the central portion of the Doppler profile with a cubic polynomial. The four individual channels are fit simultaneously with some shared parameters such as the linecenter to make the four fits self-consistent. The equation describing the Lamb dip shape is a sum of absorption and dispersion components, χ_{abs} and χ_{disp} respectively.

$$\chi_{tot}(\nu_d) = \chi_{abs}(\nu_d)\sin\theta_h + \chi_{disp}(\nu_d)\cos\theta_h \tag{2.1}$$

$$\chi_{abs}(\nu_d) = A_1[\chi(\nu_d - \frac{f_h}{2}) - \chi(\nu_d + \frac{f_h}{2})] + A_2[\chi(\nu_d - f_h,) - \chi(\nu_d + f_h)] \tag{2.2}$$

$$\chi_{disp}(\nu_d) = -A_0\chi(\nu_d) + A_1[\chi(\nu_d - \frac{f_h}{2}) + \chi(\nu_d + \frac{f_h}{2})] + A_2[\chi(\nu_d - f_h) + \chi(\nu_d + f_h)] \tag{2.3}$$

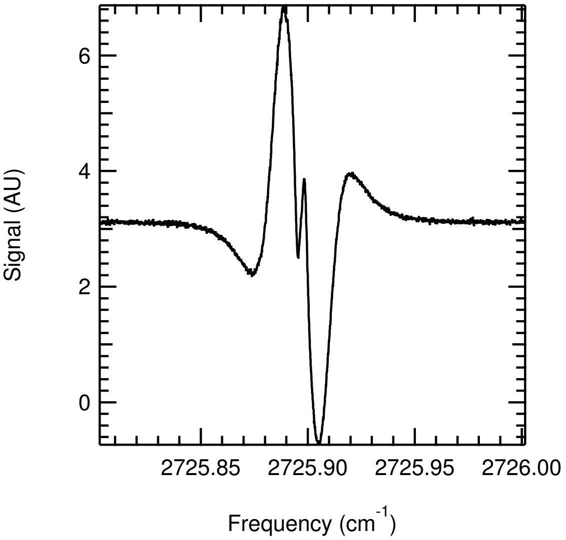

Figure 2.2: A representative scan of the R(1,0) transition of H_3^+, illustrating the odd symmetry of the Doppler broadened lineshape. The sharp central feature is composed of five blended Lamb dips. This spectrum was only calibrated with a wavemeter, limiting its accuracy to 70 MHz.

Here A_n denotes the amplitude of the Lamb dip where n is the order, *i.e.* A_0 is the amplitude of the central Lamb dip, A_1 is the amplitude of the first set of Lamb dips out from the linecenter and so forth. The frequency detuning from the linecenter is given by ν_d, f_h is the heterodyne frequency, and θ_h is the heterodyne detection angle. The χ with no subscript is the lineshape for an individual Lamb dip, which is a function of linewidth though it is not explicitly shown in the above equations. In the case of absorption, it takes the form of a linear combination of a Lorentzian and a Gaussian. In the case of dispersion, the Lamb dips are modeled by the result of the Kramers-Krönig relation applied to the linear combination used in absorption. For more information about the fitting, we refer the reader to Crabtree *et al.*[2] Due to the blended nature of the Lamb dips, we were concerned about the potential for small changes in parameters significantly affecting the determination of the linecenter. The only part of the lineshape function that does not rely on a physical model is the fit to the central portion of the Doppler profile. Changing any of those values might make a detectable difference linecenter frequency. To simulate this, we increased the slope of the linear term in all four channels of a scan of the H_3^+ R(1,0) transition by 3 times the uncertainty in the slope returned by the original fit; this corresponds to ∼3% of the total slope. The cubic term was held at zero to prevent it from compensating for the change in the linear term. This increased slope was held fixed as the data were re-fit. This simulation was repeated, decreasing the slope rather than increasing it. The linear term is the largest contributor to the polynomial part of the fit and adjusting it by 3σ in either direction only produced an error of ∼27 kHz (+28 kHz for $+3\sigma$, −26 kHz for -3σ), which is well below the

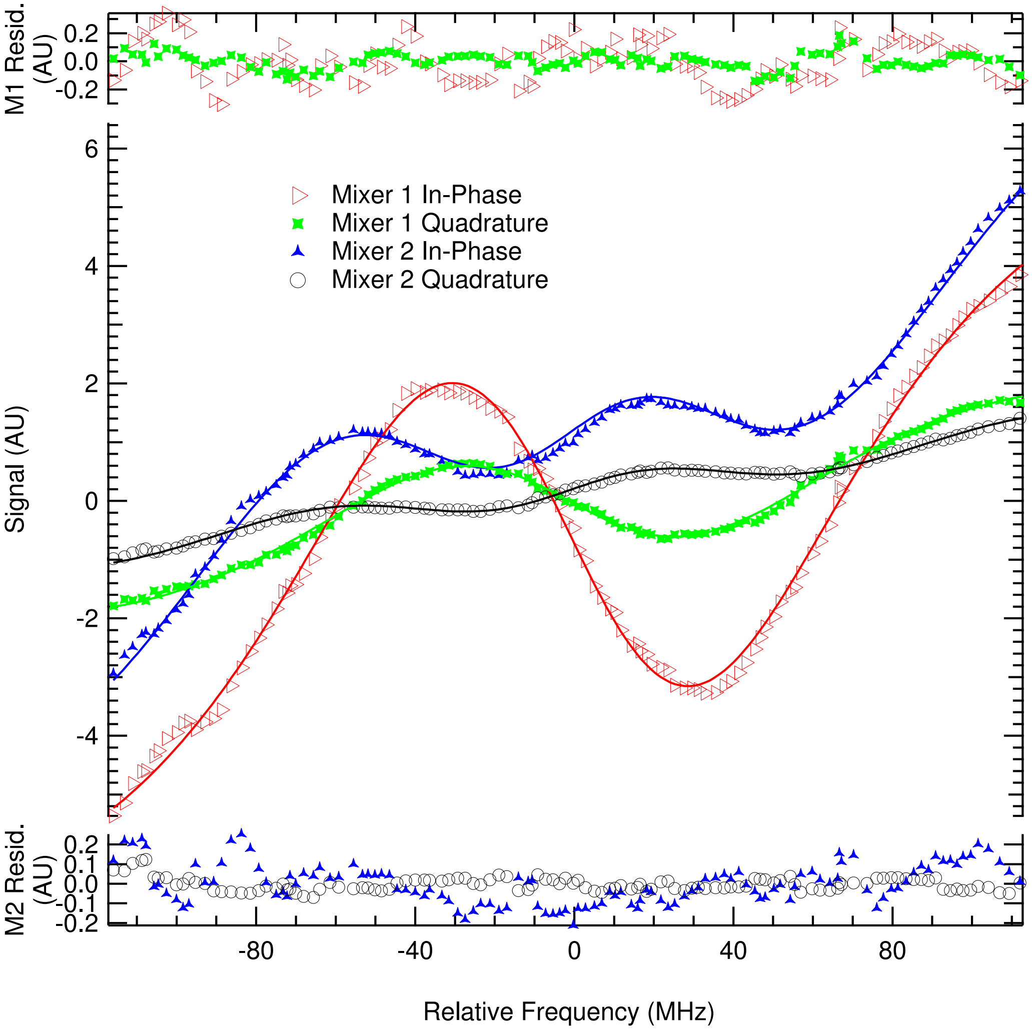

Figure 2.3: Enlarged view of the Lamb dips in the R(2,2)^l transition of H_3^+, along with fits to the functional form presented in an earlier paper.[2] The four channels (two from the phase sensitive detector associated with each mixer) are presented in the center of the panel, with the residuals plotted above and below the fit. The data are shown as markers and the fits as solid lines.

precision of the linecenter derived from the fit (∼80 kHz) or the statistical error resulting from scan-to-scan variability (∼240 kHz).

Each transition was scanned at least five times, and in some cases many more times. The linecenters determined from the fit to each scan were averaged and are reported below as the experimentally determined linecenter. The standard deviation of the individual linecenter measurements was determined and is reported to illustrate the spread of the distribution for linecenters. The standard error, also known as the standard deviation of the mean, which is simply the standard deviation divided by the square root of the number of samples, is also reported as our best estimate of the uncertainty of the average linecenter, under the assumption that the measurements are normally distributed.

2.3.2 H_3^+ Spectroscopy

Our results for ten transitions of the R-branch of the ν_2 band of H_3^+ are reported in Table 2.1. Our results are compared with those from the best available Doppler-limited spectra from the literature. In most cases these are from the Ph.D. thesis of K.-Y. Wu[43] in the group of J.-T. Shy, using frequency comb calibration; two transitions not observed by Wu were measured in the FTIR spectra of McKellar & Watson[1], and the R(4,4)^l transition has not been reported since Oka's work in 1981.[44] In all cases there is good agreement with the previous values, given the uncertainties of the latter, and in all but two cases the standard error of our measurements is sub-MHz.

Table 2.1: Determined line center frequencies, standard deviations, and standard errors of transitions in the ν_2 band of H_3^+. Previous values are given with the source as a footnote. The differences between the measured frequency and the previous best frequency are also reported. All values are in MHz.

Transition	Freq.	St. Dev.	St. Err.	Prev. Value	Diff.
R(1,1)^l	80687424.25	1.65	0.62	80687432(10)^1	-7.75
R(1,0)	81720377.29	0.86	0.23	81720370(10)^1	7.29
R(1,1)^u	81730020.44	0.84	0.38	81730026(20)^1	-5.56
R(2,2)^l	82804769.99	0.70	0.31	82804764(10)^1	5.99
R(2,1)^l	82908940.58	2.79	1.25	82908950(150)^2	-9.42
R(2,2)^u	84635537.25	1.21	0.54	84635542(10)^1	-4.75
R(2,1)^u	84724846.57	0.85	0.38	84724851(10)^1	-4.43
R(3,3)^l	84839013.46	0.88	0.39	84839025(10)^1	-11.54
R(3,2)^l	84907118.76	2.99	1.34	84907160(150)^2	-41.24
R(4,4)^l	86774648.52	1.28	0.39	86774570(300)^3	78.52

With such high precision transition frequency data available, it is interesting to compare the determined transition frequencies to those previously determined to assess the quality of the older work. Especially noteworthy in this comparison is the high degree of accuracy of the FTIR work by McKellar and Watson.[1] As can be seen in Table 2.2, their work is considerably more accurate than their stated uncertainty (150 MHz). Indeed, one of the weakest lines observed in their experiment, R(3,2)^l, is only ∼40 MHz away from our determined linecenter.

There has been one other recently reported sub-Doppler measurement of the linecenter of the R(1,0) transition, from Shy's group.[27] They produce H_3^+ in an extended negative glow discharge at 30-80 mTorr and use an OPO in a strong pump, weak probe double pass configuration. Rather than scanning over the transition, calibrating each point, and fitting to determine the line center (as we have done), they instead lock their laser to the Lamb dip and use a frequency comb to measure the laser's frequency while locked. Their reported linecenter is 5.74 MHz lower than ours, a discrepancy which is far larger than the adopted uncertainties (∼250 kHz in both cases). Subsequent measurements of other transitions in Shy's laboratory[45] also differ from our values, with discrepancies that vary in sign but are all of order 5 MHz.

Table 2.2: A comparison to the FTIR values as determined by McKellar and Watson[1]. The error listed is the difference between our reported value and that determined by McKellar and Watson.

Transition	Error (MHz)
R(1,1)^{l}	-5.75
R(1,0)	11.12
R(1,1)^{u}	19.65
R(2,2)^{l}	-5.03
R(2,1)^{l}	-12.42
R(2,2)^{u}	-10.75
R(2,1)^{u}	-9.43
R(3,3)^{l}	-3.54
R(3,2)^{l}	-41.24

Because of these discrepancies, we have taken great care to characterize potential sources of systematic and random errors in our experiment, as described in the following sections.

Effect of Signal-to-Noise Ratio

The precision of the linecenters derived from the fits to our individual scans is typically a few hundred kHz, but can be as low as 70 kHz. Clearly, the fit precision is not the limiting factor in our measurements. To assess the effect of the signal-to-noise ratio of the Lamb dips on our linecenter measurements, the average signal-to-noise ratio of the blended Lamb dips for each transition is plotted against the standard deviation of its linecenter, as determined from several scans over each transition, in Figure 2.4.

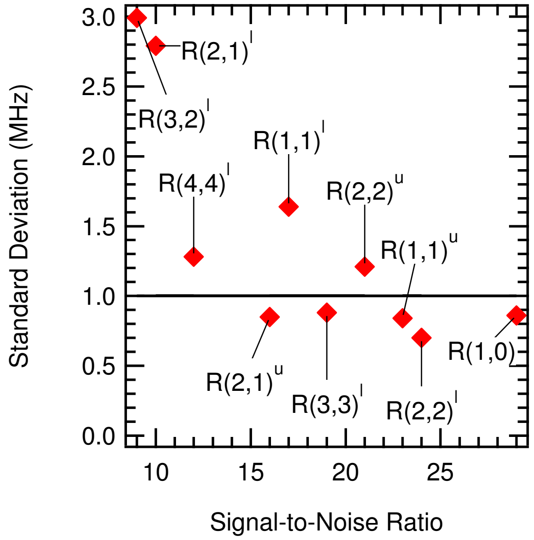

Figure 2.4: The standard deviation of the frequency measurements for each H_3^+ transition plotted against the average signal-to-noise ratio of the blended Lamb dip. The horizontal line at 1 MHz is drawn to indicate that the standard deviation is scattered about it for most transitions.

All except the two weakest transitions are clustered near the horizontal line at 1 MHz; these two transitions have fits that are less well determined, which is the cause of the greater uncertainty in their linecenters. No gradual trend in the standard deviation as a function of signal-to-noise ratio is evident, indicating that there is some other dominant effect limiting the standard deviation for all but the weakest lines.

Effect of Asymmetry

In Crabtree *et al.*[2] the effect of asymmetry on the determined transition frequency was left as an unanswered question due to the fact that the accuracy was limited to ∼70 MHz by the wavemeter calibration. In that work, several simulated asymmetries were used to intentionally affect the ability to fit the lines; though no physical meaning or mechanism was used in the simulations. The largest magnitude effects were found to cause a few MHz shift in transition frequency, and this was interpreted as a firm upper limit on the potential effect of asymmetry.

With the inclusion of a frequency comb, the effect caused by asymmetry can now be better characterized. For this purpose, the R(1,0) transition was scanned many times on many different days to study the asymmetry. In all cases, the fit residuals do not indicate any obvious asymmetry in the Lamb dips, which would have the largest effect in the determination of linecenters. Instead, the Doppler profiles clearly exhibit asymmetric lineshapes, and the amount and sign of this asymmetry changes over time and from scan to scan.

To quantify the amount of asymmetry (deviation from the expected odd symmetry) in each scan, we first trimmed each channel of a scan to an equal number of data points on each side of the line center, and shifted it by the y-offset determined from the fit. A copy of the data was made and then the frequency axis was inverted, mirroring the data across the linecenter. The original scan channels and mirrored scan channels were added together to create a graphical representation of the asymmetry (Figure 2.5), which we refer to as the inversion residuals.

From the inversion residuals, two parameters were determined. The first, the offset asymmetry parameter, was defined as the average value of all four channels. The average value from each individual channel was determined, then these four averages were averaged together. The offset asymmetry parameter was defined in this manner to capture the effect that each individual channel would have on the simultaneous least squares fit of all four channels. In the case of a perfectly symmetric line, the offset parameter would have a value of zero because the odd lineshape would cancel itself out. Negative values of the offset parameter indicate that the lower frequency (negative-going) lobe is stronger than the higher frequency lobe; whereas, positive values indicate stronger lobes on the high frequency side.

The second parameter, which we refer to as the high-low asymmetry parameter, represents the average

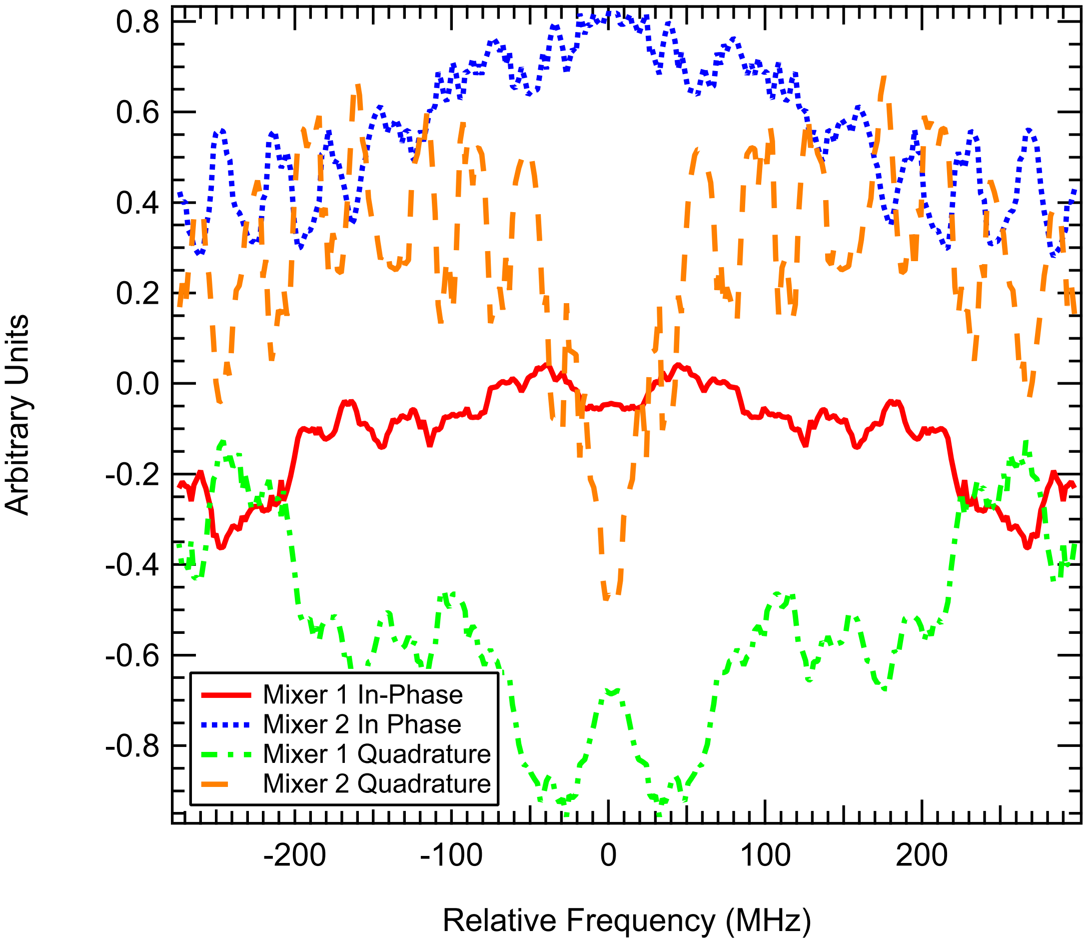

Figure 2.5: A typical graph depicting the inversion residuals. It is evident that they are symmetric about the transition frequency, due to the process of additively imprinting the noise of one half of the line on the other. These data are used to calculate characteristic parameters of the asymmetry.

difference between the maximum and minimum values for each of the four inversion residuals. The high-low parameter is intended to capture an imbalance in the shape of the line. Such an imbalance would manifest itself in the inversion residuals as a sloped or curved line. The magnitude of the slope is parameterized by differencing the maximum and minimum values of the residuals. These differences for each data channel are averaged just like the offset parameter. As above, the sign indicates which lobe was larger.

In Figure 2.6, the deviation of the linecenter of an individual scan from the mean of all R(1,0) scans is plotted against these two asymmetry parameters. The data show no clear trend; not even a consistent change in the sign of the deviation with the sign of the asymmetry parameter. Instead, the data are well scattered. If the scan-to-scan reproducibility in the linecenter of ∼1 MHz is due to the changing asymmetry, it must depend on the asymmetry in a way that is not captured by these particular metrics.

In any case, the fact that the amount and the sign of the asymmetry change from scan to scan strongly

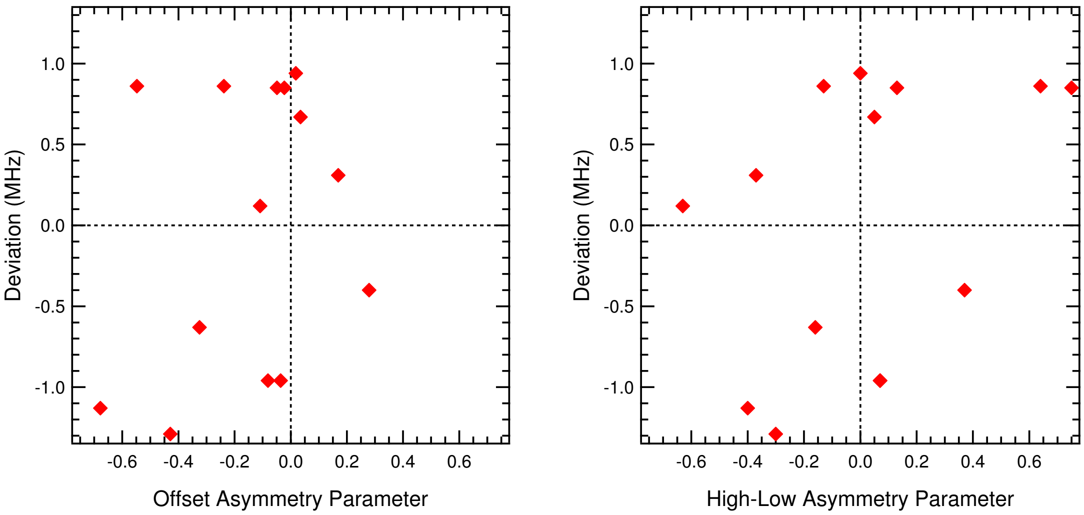

Figure 2.6: The deviation of the linecenter of a given scan from the mean value versus the offset asymmetry parameter (left panel) and the high-low asymmetry parameter (right panel). The dotted lines shows the zero crossings to emphasize the insensitivity of the sign of the difference to the sign of the asymmetry parameter.

suggests that the asymmetry cannot cause a systematic shift in the linecenter in an ensemble of scans. Instead, we conclude that the impact of the asymmetry manifests itself as a random error, reflected in the magnitude of the standard deviation of the linecenter determinations.

Pressure Shift

Given the difference in pressure between our experiment and Shy's, we decided to measure the linecenter of the R(1,0) transition at three different pressures to rule out the possibility of an unexpectedly large pressure shift. The results are displayed in Table 2.3, and show the same linecenter (within uncertainties) from pressures between 200 and 500 mTorr. The largest pressure shift consistent with the data, determined from the lower bound of the 200 mTorr data (81720377.06 MHz) and the upper bound of the 500 mTorr data (81720377.86 MHz), would be 2.7 MHz/Torr at the 1σ level. This would mean our linecenter measured at 200 mTorr could be too high by at most 0.4 MHz from the value at 55 mTorr (the midpoint of Shy's range).

Table 2.3: Measured linecenters of the R(1,0) transition of H_3^+ at different pressures.

Pressure (mTorr)	Frequency (MHz)
200	81720377.29(23)
350	81720377.47(32)
500	81720377.44(42)

Comb Calibration Test

In order to rule out any unexpected problems with the calibration of our optical frequency comb, we wished to measure another transition that had been previously measured with high precision. Since there are no other ion transitions known to this level of accuracy in the mid-infrared, we pursued spectroscopy of neutral methane, which has comb calibrated lines in our spectral region that are known to high accuracy and precision.[3]

Obviously, NICE-OHVMS could not be performed because the instrument cannot modulate the velocity of a neutral molecule. Ordinary NICE-OHMS is challenging to perform with a fiber based EOM due to strong baseline drifts from residual amplitude modulation (RAM),[46, 47] so an additional layer of modulation is necessary. The logical choice was wavelength modulation, but our pump laser must be locked to the comb and our use of an external cavity requires feedback to the OPO cavity length, which fixes the frequency of the signal. Therefore, the cavity was removed and the back reflection detector was used in a double pass configuration for wavelength modulated heterodyne spectroscopy.

Without the need to apply feedback to the OPO cavity length, this control could be used to apply a dither necessary to modulate the wavelength of the signal, and hence also the idler. A 1.4 kHz dither was applied to the cavity, and the lock-in amplifiers were referenced to three times the dither frequency. This allowed the system to be insensitive to the Doppler profile of the methane transition. The chosen target was the $F_1^{(2)}$ component of the P(7) transition in the ν_3 band, which has been reported to kHz precision.[3] A few mTorr of methane was leaked into the discharge cell, and the central Lamb dip, which corresponds only to dispersion, was recorded.

The result of our methane spectroscopy is shown in Figure 2.7. We fit the data to both the third Fourier coefficient for a Lorentzian dispersion lineshape[48] and a simple second derivative of a Lorentzian. While neither fit perfectly reproduces the observed lineshape, the derived linecenters compare very favorably with the previous work of Takahata *et al.* The linecenter as determined by the second derivative fit is 5±22 kHz less than Takahata's, and that from the third Fourier coefficient fit was 10±30 kHz greater than Takahata's. Even by the roughest approximation of simply picking the highest recorded point and calling it the line center, the error is only 222 kHz. Therefore, we conclude that our frequency comb system is working well, and is not the limiting source of error in our ion measurements.

2.3.3 HCO^+ Spectroscopy

While there are no molecular ion transitions in the mid-infrared previously measured with sub-MHz accuracy, there are ions (such as HCO^+) for which pure rotational transitions are known with such accuracy. By

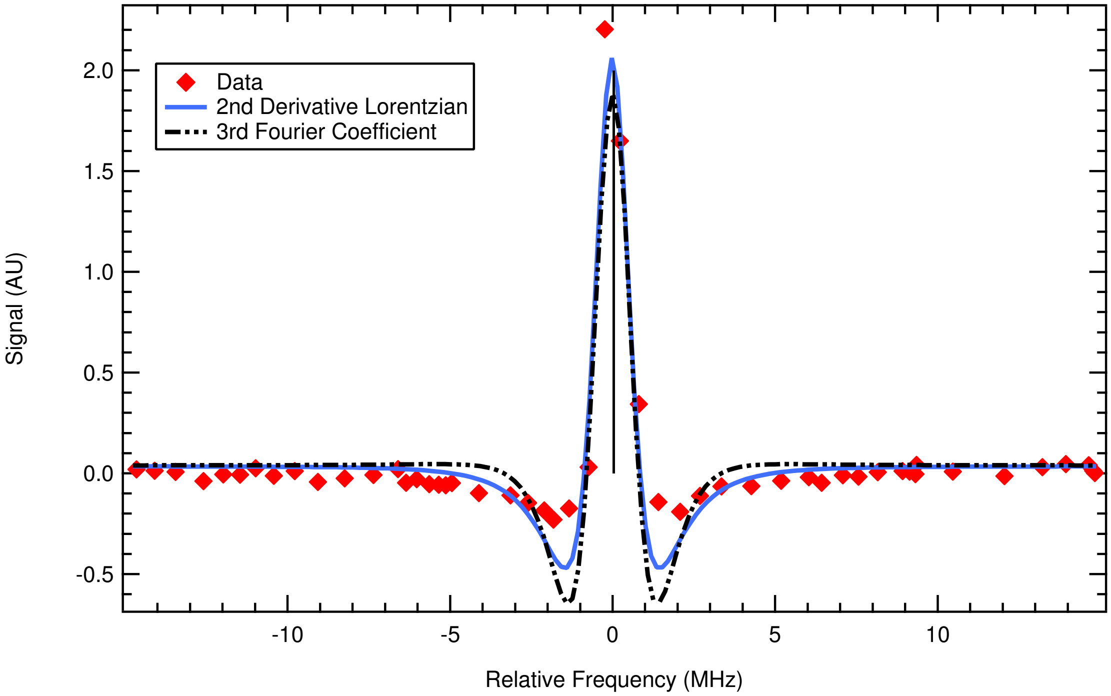

Figure 2.7: The comb calibrated central Lamb dip of the $F_1^{(2)}$ component of the P(7) transition in the ν_3 band of methane. Fits to an analytical expression of the third Fourier coefficient for a wavelength modulated dispersion signal (dashed curve) and to the second derivative of a Lorentzian (solid curve) are shown. The black line is the linecenter determined by Takahata *et al.*[3].

measuring multiple rovibrational transitions and using combination differences, we can compare the results with observed rotational transitions as yet another check on the accuracy of our ion transition measurements.

We have recently performed such "indirect rotational spectroscopy" using Doppler-limited spectra of HCO^+ with comb calibration.[35] Ultimately, we expect this approach to be a useful tool for inferring rotational spectra that have not been directly measured, in order to support astronomical observations with far-infrared/THz instruments such as SOFIA and ALMA. Here, we simply extend our previous work on HCO^+ to demonstrate the accuracy of our sub-Doppler NICE-OHVMS spectra.

The P(5) and R(3) lines from the ν_1 band of HCO^+ were measured (see Figure 2.8) in order to determine the energy level separation between J = 5 and J = 3 in the ground vibrational state. The two transitions were measured multiple times to determine their linecenters, which were 92145080.8(4) MHz for P(5) and 92947717.3(5) MHz for R(3). The difference between these frequencies, 802636.5(7) MHz, agrees within its uncertainty with the sum of the J=3 → 4 and J=4 → 5 pure rotational transitions observed by Cazzoli et al.,[49] 356734.2230(15) + 445902.8721(15) = 802637.0951(21) MHz. The excellent agreement of this combination difference strongly suggests that our experiment does not suffer from any systematic errors that differ from one line to the next, beyond those at the sub-MHz level that result from scan-to-scan variations.

It is interesting to note that the P(5) and R(3) frequencies determined from the Lamb dips are both ~4 MHz lower than those determined from our earlier Doppler-limited, single-pass measurements.[35] This difference is evidently due to an asymmetry in the drift velocity of the ions on the two half-cycles of the AC discharge; such an asymmetry results in a net Doppler shift in the single-pass measurements, but the present measurements are insensitive to this effect due to the bi-directional nature of the cavity and the fact that the Lamb dips are located symmetrically about the zero-velocity component.

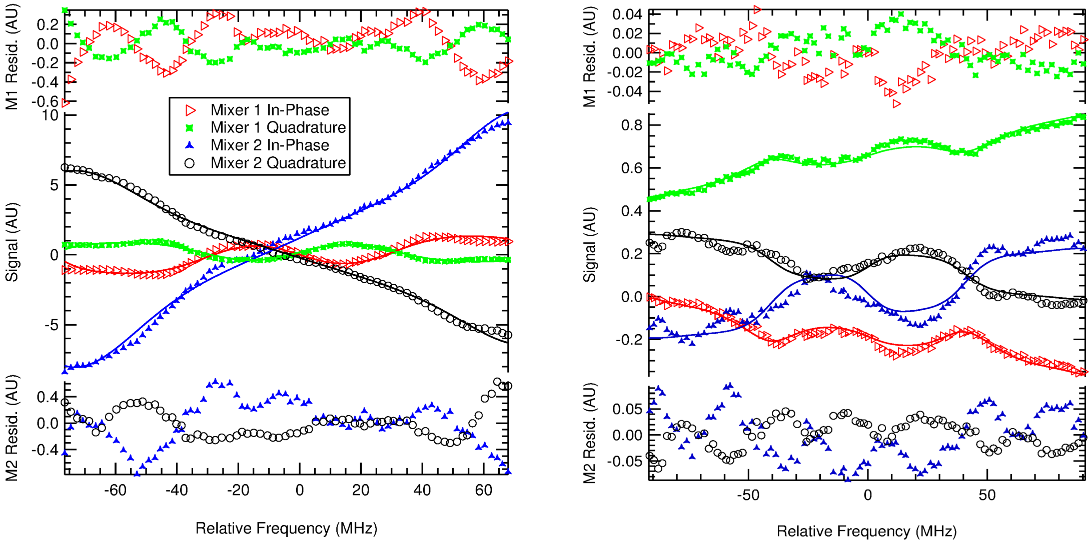

Figure 2.8: Results from fitting the Lamb dips from the P(5) transition (left) and R(3) transition (right) of HCO^+. The four channels are presented with residuals from each mixer plotted above and below the fit. The data are shown as markers and the fits as solid lines.

2.3.4 CH_5^+ Spectroscopy

An important future application of this technique will be high-precision and high-accuracy spectroscopy of highly congested spectra, such as that of CH_5^+. The infrared spectrum of this ion was first reported by the Oka group in 1999,[14] and consisted of about 900 spectral lines between 2770 and 3150 cm^{-1}, with no discernable patterns. The spectrum is complicated by the fact that CH_5^+ does not have a single equilibrium structure, but can sample all 5!=120 equivalent minima of C_s symmetry on its potential energy surface, as well as the C_s and C_{2v} saddle points that interconnect them. Many important theoretical studies (see, e.g., references [50, 51, 52, 53, 54, 55, 56]) have been undertaken since the publication of Oka's spectrum, and low-resolution spectra have been reported covering different frequency ranges[57] and temperatures.[52] Despite nearly 15 years of effort since the Oka group's first report, the community seems to be no closer to an assignment of Oka's spectrum.

One possible way forward is to search for four-line combination differences in the spectrum; that is, to look for two pairs of transitions with the same combination difference. This would represent an experimental measure of the separation between two rotational energy levels. If spectra with reliable intensities could be obtained at different temperatures, it may be possible to begin assembling an energy level diagram. Comparison between such experimentally-determined energy levels and those predicted by sophisticated theoretical techniques might eventually lead to an assignment. However, the frequency uncertainties in the Oka group spectrum range from 90–180 MHz, as their measurements were limited by their Doppler linewidth, relatively low signal-to-noise ratio, and traditional frequency calibration techniques (reference gases). Given the line density, there are almost innumerable pairs of transitions whose combination differences agree within this level of uncertainty, and the vast majority of those are accidental rather than true four-line combination differences.

Progress on this front will necessitate remeasurements of CH_5^+ transitions with considerably higher accuracy and precision. The Schlemmer group recently made the first report of a high-resolution spectrum since Oka's, using a cryogenically cooled ion trap and laser-induced reaction spectroscopy.[58] With their smaller Doppler linewidth (∼70 MHz at 20 K) and frequency comb calibration, they determined the central frequency of a CH_5^+ transition at 2932.998460 cm^{-1} to within ∼200 kHz. An alternative approach, which we are pursuing, is to obtain sub-Doppler spectra in a positive column discharge.

Our experiment uses the same discharge cell that was used for the first report of the CH_5^+ spectrum. We are attempting to reproduce the plasma conditions as closely as possible, but the CH_5^+ signal is exquisitely sensitive to the exact discharge conditions and we are still in the process of optimizing the system. Nevertheless, we have obtained several comb-calibrated scans of the transition Oka's group reported at 2898.008 cm^{-1}, with a signal-to-noise ratio that is somewhat higher than that of the Oka group. Given our ∼10-fold longer effective pathlength (from the cavity enhancement) and the fact that our noise level should be lower than Oka's (because of the frequency modulation), we suspect that further tuning of plasma conditions should lead to significantly stronger signals.

The average of five spectra of this transition is displayed in Figure 2.9, and represents the first sub-Doppler spectrum of CH_5^+. A fit to the averaged spectrum yields a linecenter of 86,880,178.469(126) MHz; the precision of this fit is more than two orders of magnitude lower than the ∼90 MHz uncertainty from the Oka group's measurements. The Schlemmer group has independently measured a CH_5^+ line centered at 86,880,178.22(63) MHz.[59] This transition is only ∼240 kHz different from our measurement, which agrees with our transition frequency within 1σ of their uncertainty and 2σ of our uncertainty. This provides

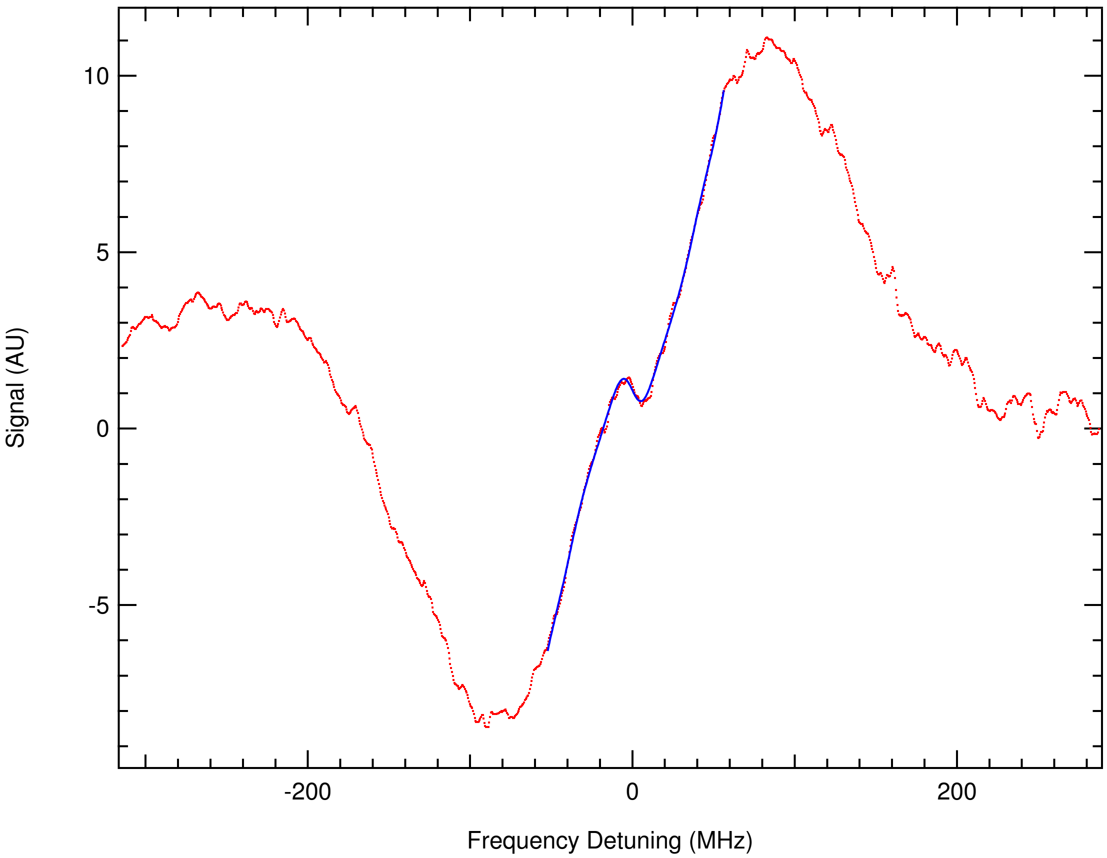

Figure 2.9: Comb-calibrated NICE-OHVMS spectrum of Oka's "2898.008 cm^{-1}" transition of CH_5^+. The data are shown as red dots and the fit to the Lamb dip is shown as a blue line.

independent confirmation of the accuracy of our technique. The weakness of the CH_5^+ Lamb dip, compared to those seen in H_3^+ and HCO^+, is likely the result of the lower transition dipole moment of CH_5^+. Although we are not aware of any predictions for the transition dipole moment, the MULTIMODE calculations of Huang et al.[52] show an integrated band intensity of ~50 km/mol, which is considerably lower than the calculated value of 227 km/mol[60] for HCO^+.

In the future, we hope to increase the Lamb dip depth by increasing the power injected into our cavity and/or by obtaining mirrors with higher reflectivity. Even if this is not effective, we expect to be able to improve the signal-to-noise ratio on the Lamb dip by further optimization of the plasma conditions and by reducing technical noise sources in our spectrometer.

2.4 Conclusions

We have demonstrated the first instrument capable of routine sub-Doppler spectroscopy of a wide variety of molecular ions, offering both high precision from optical saturation and high accuracy from optical frequency comb calibration. Using this instrument, ten lines of the doubly degenerate ν_2 band of H_3^+ have been measured, eight of which have sub-MHz uncertainties. Two lines from the ν_1 band of HCO^+ have also been measured with similar uncertainties, and their combination difference is in excellent agreement with pure rotational spectroscopy. The first sub-Doppler spectrum of CH_5^+ has also been recorded with sub-MHz precision, a substantial improvement over the ∼90 MHz uncertainty of the initial detection in the Oka group.[14]

Because our measurements of H_3^+ transitions disagree with those reported by Shy's group[27, 45] by ∼5 MHz, we have conducted an extensive analysis of potential sources of experimental error in our instrument. The limiting factor in our frequency determinations appears to be scan-to-scan variability that is not yet understood, but results in a standard deviation among individual scans of ∼1 MHz. The standard error of a set of scans can be reduced to ∼250 kHz by performing multiple scans. The scan-to-scan variability may be due to varying asymmetry of the Doppler-broadened lineshape, but our attempts to find correlations between the center frequency deviations and measures of the asymmetry have not been successful. All indications are that our determined standard errors accurately capture the random errors in our measurements. This conclusion is further supported by the excellent combination difference between the HCO^+ transitions we measured. We have also excluded the possibility of systematic errors due to pressure shift, and we have confirmed the accuracy of our frequency comb calibration within tens of kHz using a known transition of methane. Most importantly, the independent measurement of the same CH_5^+ transition by Schlemmer's group[59] is the strongest evidence that our technique does not exhibit errors of order 5 MHz, which provides us with the utmost confidence in the values that we have reported.

The instrument is currently limited in wavelength coverage by the coverage of our OPO module (3.2–3.9 μm), and to some extent by the coatings of our external cavity mirrors (nominally 3.0–3.4 μm, but usable outside this range). However, OPO modules are available that cover 2.3–4.6 μm, and it should be possible to produce moderate reflectivity (∼ 99.0–99.7%) cavity mirrors across that range. Considering the chemical versatility of the positive column discharge and the general applicability of direct absorption/dispersion spectroscopy, our technique will enable the high-precision, high-accuracy spectroscopy of a wide variety of molecular ions. Possible applications include tests of high accuracy ab initio calculations, supporting astronomical observations, and aiding in the assignment of congested spectra.

2.5 Acknowledgments

We would like to acknowledge support from a National Science Foundation Chemistry grant (CHE 12-13811) and a NASA Laboratory Astrophysics grant (NNX13AE62G). JNH is grateful for the support from a Robert & Carolyn Springborn Fellowship and an NSF Graduate Research Fellowship (DGE 11-44245 FLLW). JNH and AJP are grateful to Mr. George S. Kocheril for assisting with the HCO^+ and CH_5^+ data acquisition. We also are especially thankful to Prof. Takeshi Oka for providing the liquid nitrogen cooled discharge cell and associated pumps and electronics.

Chapter 3

Quantitative Velocity Modulation Spectroscopy

3.1 Introduction

The study of molecular ions poses several challenges to traditional direct absorption spectroscopy, such as low number density in glow discharges and large numbers of interfering neutrals. For 35 years, the gold standard for addressing these obstacles has been velocity modulation spectroscopy (VMS), which is a sensitive, ion-selective technique. Since its inception[17], VMS has been used to study ∼50 individual molecules[18], and has been enhanced by combination with heterodyne modulation, cavity enhancement, and direct frequency comb spectroscopy. [21, 25, 26, 61, 62, 63, 64] Despite the fact that VMS was developed in the infrared spectral region, it has seen extensive deployment in the millimeter/submillimeter wavelengths in support of rotational spectroscopy of molecular ions.[65, 66, 67]

The key to understanding ion selectivity in VMS is that the source responsible for generating the ions, the positive column of a glow discharge, is driven by an alternating electric field. As the polarity of the positive column changes, the ions experience a force that is proportional to the magnitude of the electric field and is along the axis of the discharge in the direction of the cathode. This ionic motion results in an oscillatory Doppler shift that can be detected by demodulation of the photo-signal with a phase sensitive detector, such as a lock-in amplifier. Under most conditions, the signals of neutrals are largely not affected by the electric field (the notable exception being processes involving excitation from charge transfer), so neutral signals can be filtered out at the demodulated frequency.[18] The demodulation scheme results in a derivative-like lineshape which makes it difficult to accurately determine linewidths, line strengths, and modulation depths (the ratio of the Doppler shift to the linewidth), as all these parameters are strongly correlated.

The theory of VMS lineshapes has been well established by John Farley in 1991.[31] The drift velocity (v)

Adapted from James N. Hodges, Benjamin J. McCall. "Quantitative Velocity Modulation Spectroscopy". Journal of Chemical Physics, 144 (2016) 184201.

of ions in a positive column is directly proportional to the electric field magnitude (E), the proportionality constant being the ion mobility (K). The drift velocity of an ion in a static electric field is well known[68] and described in Equation 3.1.

$$v = KE. \tag{3.1}$$

The ion mobility depends on the temperature and pressure of the neutral collision partner, and it is often reported as a reduced ion mobility, K_0, adjusted to standard temperature and pressure. Because molecular collisions occur on the nanosecond timescale, whereas the period of the discharge is on the order of tens or hundreds of microseconds, we can assume that ions will rapidly achieve drift velocity,[31] because there are on the order of 10^3 to 10^4 collisions per half cycle of the discharge. For experiments with a sinusoidal variation in electric field, there is, therefore, a sinusoidal variation in velocity such that

$$v(t) = KE\cos(2\pi t). \tag{3.2}$$

In this work we define the time (t) in fractional periods, a dimensionless quantity. This is a convenient choice as it avoids consideration of the driving frequency and any prefactors in the equations as a result of integration. The Doppler shift formula can be used to rewrite Equation 3.2 in frequency space:

$$\nu_{mod}(t) = v(t)\frac{\nu_0}{c} = \nu_{ma}\cos(2\pi t), \tag{3.3}$$

where $\nu_{mod}(t)$ is the time dependent transition frequency modulation in terms of ν_{ma}, the velocity modulation amplitude (VMA). The term, ν_0, is the center frequency of the transition. Over the course of the discharge cycle the line center changes as a function of time so the following transform must be applied to the spectroscopic lineshape (χ, a function of frequency detuning, ν) in order to model the experiment:

$$\chi(\nu) \to \chi(\nu + \nu_{mod}(t)). \tag{3.4}$$

Incidentally, this same transformation is used to model wavelength modulation lineshapes.[69] Velocity modulation and wavelength modulation are mathematically equivalent but differ in experimental realization. The former modulates the transition linecenter and the latter modulates the laser frequency. Wavelength modulation is sensitive to both ions and and neutrals and lacks the ability to discriminate between the two, which is why VMS is preferentially used for molecular ion spectroscopy.

In most VMS experiments, there are two ion-related modulation processes that occur in tandem, and velocity modulation is not the only process that must be considered. Concentration modulation, the creation and destruction of ions during every half cycle of the discharge, occurs at twice the frequency of the discharge. This is a challenging process to model *a priori*, but typically it has been assumed to follow the magnitude of the current sourced to the plasma. Generally, ion concentration increases with increased electron concentration,[31, 30] so we assume a functional form for the ion concentration (ρ)

$$\rho(t) = \rho_0 |\cos(2\pi t)|, \tag{3.5}$$

where ρ_0 is the maximum ion concentration. This form is the same one previously used in other VMS works.[31, 30]

The detected signal, the product of Equation 3.5 and the lineshape $\chi(\nu, t)$ as transformed by Equation 3.4, is demodulated by a lock-in amplifier, which may be considered a Fourier filter that selects only a single frequency component of the incoming signal. This is a multiplication of the signal by a reference signal and integration of the result over a period of the reference signal.

$$\chi_{vms}(\nu) = \int_{-1/2}^{1/2} \rho(t)\chi(\nu, t)\cos(2\pi t + \phi)\ \mathrm{d}t \tag{3.6}$$

Equation 3.6 describes the recorded lineshape, with an arbitrary phase, ϕ, which results in a maximum signal when velocity modulation is in-phase with the reference signal.

A proper fit of the VMS lineshape, though challenging due to the correlation of the width, intensity, and modulation depth, would allow for simultaneous determination of the electric field strength, the ion mobility, and the kinetic temperature of the spectral carrier. In cases where the carrier is unidentified, determination of the linewidth with sufficient precision could determine the mass of the carrier relative to the other species in the discharge, which has seen limited success in practice due to the problematic simultaneous determination of linewidth and VMA. Only large differences in mass were found to be reliable, such as the difference between one and two carbon atoms. As positive columns are rich chemical environments, mass identification by VMS is an untapped resource with many applications.

Presumably due to the difficulty of reliably determining covariant fit parameters, only two attempts to extract information from fits to VMS data have been made. The first was a study on ArH^+ and ArD^+ in 1994, wherein the lineshapes were integrated and fit to two overlapping Voigt profiles.[29] Although the results of that work are interesting, integration is not physically meaningful as VMS lineshapes are not the derivative of the underlying lineshape; rather, they are the time average of a function that oscillates in frequency and amplitude. In the second lineshape study by H. Gao *et al.*,[30] N_2^+ rovibronic transitions were fit with a Voigt profile as the fundamental lineshape, and they attributed the substantial homogeneous

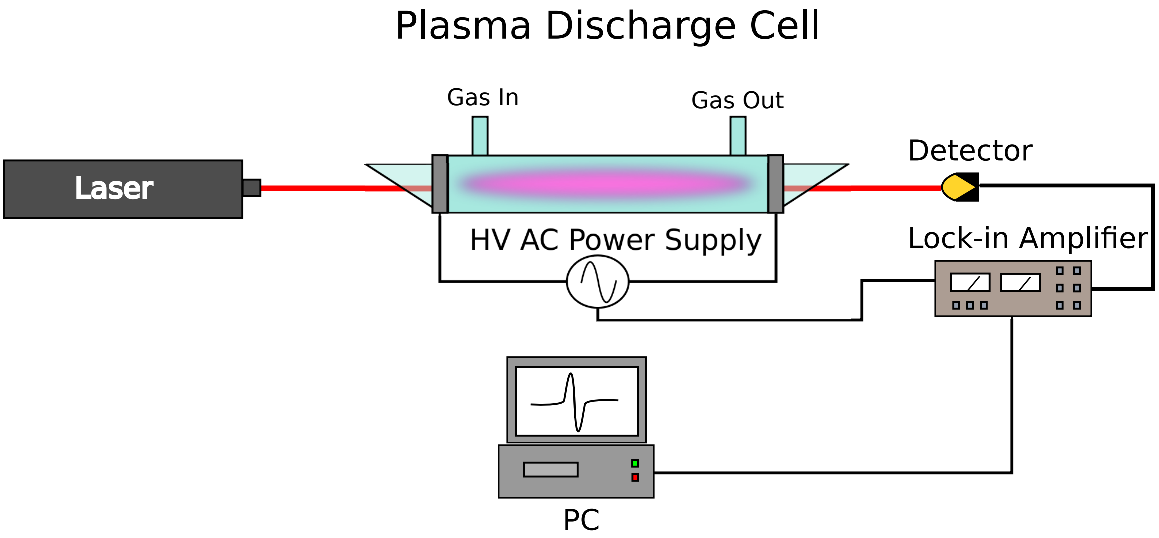

Figure 3.1: A typical layout of a VMS spectrometer. It comprises a laser that spectroscopically probes a velocity modulated plasma. A detector converts the light into a voltage that is read by a lock-in amplifier, which is referenced to the voltage that drives the discharge.

linewidth to pressure broadening. The primary limitation in that work is that the velocity modulation amplitude was held fixed to a theoretical value.

In this work, we present a computationally rapid method of separating the velocity modulation depth and the linewidth. The application of a pseudo-Voigt profile[70] is used as a reasonably accurate (∼1%) and computationally trivial replacement to the full Voigt profile. Translational temperature assuming a known ionic mass, ion mobility, peak electric field strength, and line intensity are determined with low uncertainty. As VMS continues to be utilized in more complex techniques with additional layers of modulation,[25, 26, 61] a quantitative understanding of the fundamental VMS lineshape is crucial to successful fitting and analysis of more complicated data.

3.2 Experiment and Methodology

3.2.1 Experiment

VMS experiments, though varied with specific light sources and detection scheme complexity, all are fundamentally the same type of experiment. Effectively, a laser passes through an AC modulated discharge cell and irradiates a detector. The output of that detector is read by a lock-in amplifier which is referenced to the discharge voltage. The output of the lock-in amplifier is then recorded as the frequency of the laser is tuned. A basic experiment is depicted in Fig. 3.1.

The molecule that is experimentally examined in this work is H_3^+. In this case, a continuous wave laser is single passed through a discharge cell and demodulated with a lock-in amplifier. For this work, a mid-IR optical parametric oscillator is used to scan the R(1,0) transition of the ν_2 fundamental band. Ions are generated in a liquid nitrogen cooled discharge of H_2 at a pressure of 500 mTorr. The cell has a central bore diameter of 18 mm.[71] The discharge is driven at 40 kHz by a ~4 kV peak-to-peak sinusoid. Frequency calibration is accomplished with a wavemeter (Bristol 621 IR-A) with a nominal uncertainty of 0.2 ppm. However, sub-optimal alignment results in less accurate readings. In the present work, the sole purpose of frequency calibration is to ensure a linear frequency axis as precision is more important to the contour of the lineshape than absolute frequency calibration. The light source, detector, and lock-in amplifiers used in the present work are described in detail in Crabtree *et al.*[2]

3.2.2 Method

As alluded to in Section 3.1, the Voigt profile is required to adequately model the lineshape. Due to the fact that a nonlinear least squares routine makes multiple calls, and recognizing that numerical integration is part of the lineshape model, it is advantageous to have a computationally inexpensive form of the Voigt profile with which to work. Hence, the pseudo-Voigt profile described in Thompson *et al.* was chosen.[70]

The pseudo-Voigt profile (χ_{pV}) approximates the Voigt profile as a linear combination of Lorentzian and Gaussian transition profiles, given by Equation 3.7.[70]

$$\chi_{pV}(\nu;\nu_0,\Delta_V,\eta) = \eta L(\nu;\nu_0,\Delta_V) + (1-\eta)G(\nu;\nu_0,\Delta_V) \tag{3.7}$$

where,

$$L(\nu;\nu_0,\Delta_V) = \frac{2\Delta_V}{\pi(4(\nu-\nu_0)^2+\Delta_V^2)} \tag{3.8}$$

and

$$G(\nu;\nu_0,\Delta_V) = \frac{2\sqrt{\ln 2}}{\Delta_V\sqrt{\pi}} e^{\frac{-(\nu-\nu_0)^2 4\ln 2}{\Delta_V^2}}. \tag{3.9}$$

The relevant parameters are the linear combination coefficient (η), the Voigt full-width at half-maximum (Δ_V), and the linecenter (ν_0). The η coefficient can be described in terms of the Lorentzian (Δ_L) and Voigt full-widths (Δ_V), and the Voigt full-width can be written in terms of the individual contributions to the full-width from the underlying Gaussian (Δ_G) and Lorentzian (Δ_L) profiles, which are the spectroscopically relevant parameters.[70]

$$\Delta_V(\Delta_L,\Delta_G) = (\Delta_G^5 + 2.69269\Delta_G^4\Delta_L + 2.42843\Delta_G^3\Delta_L^2 + 4.47163\Delta_G^2\Delta_L^3 + 0.07842\Delta_G\Delta_L^4 + \Delta_L^5)^{\frac{1}{5}} \tag{3.10}$$

$$\eta(\Delta_L, \Delta_V) = 1.36603(\frac{\Delta_L}{\Delta_V}) - 0.47719(\frac{\Delta_L}{\Delta_V})^2 + 0.11116(\frac{\Delta_L}{\Delta_V})^3 \tag{3.11}$$

This approximation has a maximum deviation of 1.2% at the center of the profile[72], which contributes to the minimum relative uncertainty for any contour-based parameters extracted from the fit, *i.e.* terms that affect the actual lineshape such as width and velocity modulation amplitude. With a suitable expression for the fundamental lineshape (Equation 3.7), the transform from Equation 3.4 is applied to cause the linecenter to oscillate in time with an amplitude of ν_{ma}, resulting in

$$\chi_{pV}(\nu, t; \nu_0, \Delta_V, \eta, \nu_{ma}) = \eta L(\nu + \nu_{ma}\cos 2\pi t; \nu_0, \Delta_V) + (1-\eta)G(\nu + \nu_{ma}\cos 2\pi t; \nu_0, \Delta_V). \tag{3.12}$$

In order to arrive at a final functional form for integration, Equation 3.12 is multiplied by $\cos 2\pi t$ (selecting the frequency component equal to the driving frequency), multiplied by a transition intensity (A), and a y-offset (y_0) is added to account for a non-zero baseline. By integrating over a full discharge period, the final lineshape, χ_{vms}, is

$$\chi_{vms}(\nu; A, \nu_0, \Delta_L, \Delta_G, \nu_{ma}, y_0) = A\int_{-\frac{1}{2}}^{\frac{1}{2}} \chi_{pV}(\nu, t; \nu_0, \Delta_V(\Delta_L, \Delta_G), \eta(\Delta_L, \Delta_V), \nu_{ma}) \cos 2\pi t \; \mathrm{d}t + y_0. \tag{3.13}$$

To summarize, the parameters from Equation 3.13 that are to be determined by the fit of Equation 3.13 to the experimental spectrum are the line intensity (A), linecenter (ν_0), homogeneous and inhomogeneous full-widths (Δ_L, Δ_V), velocity modulation amplitude (ν_{ma}), and y-offset (y_0).

In order to fit VMS lineshapes, a custom fitting program was written in `python3`, using the extensive `numpy` and `scipy` modules. The core functionality of the program is derived from the Levenberg-Marquardt nonlinear least squares routine from the `scipy.optimize` module. Integration is performed by the `numpy` module's `trapz` function, which is a trapezoidal rule numerical integration. The first step for integration is to define a two-dimensional array with frequency along one axis and time along the other. The size of the array is determined by a combination of the experimentally measured frequency data and the time step size that gives a sufficiently converged lineshape. Moreover, the number of time points is equal to the period divided by the step size, and the step size is chosen as a compromise between accuracy and integration time. Once the array is populated, the `trapz` function integrates along the time axis, which results in a one-dimensional array equivalent to the observed lineshape.

In order to determine a good step size, the integration was performed repeatedly with incrementally decreasing step size for a variety of different lineshape parameters. The integration time and the peak-to-peak intensity were recorded. Additionally, the standard deviation of the difference between the resultant

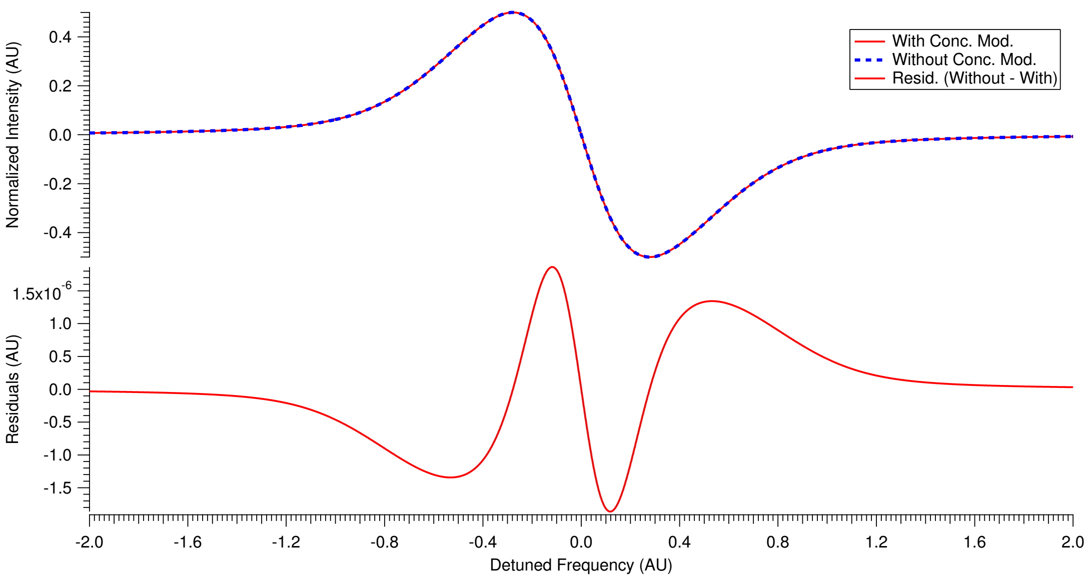

Figure 3.2: Here, the effect of including concentration modulation versus ignoring it is highlighted. The overall peak-to-peak signal with concentration modulation is smaller than without it, so the signal for each was normalized to unity to illustrate errors in the contour. The residuals show some clear structure, though it is insignificant (∼2 ppm) relative to other sources of error (∼2%).

lineshape with a given time step size and the lineshape of the previous step size are determined. In other words, after a new, smaller time step size is used for the integration, the new lineshape is differenced with the lineshape determined by a larger step size, and the standard deviation of the differences is recorded. This metric is useful as a measure of how much the line's contour changes from one time step size to the next smaller one.

As a result of this convergence testing, a step size of 0.004 was chosen due to its reasonably quick integration time. The chosen step size exhibits less than 1% error as compared to the smallest time step (taken as the converged lineshape), 0.00025 fractional periods. The 1% is the discrepancy between the peak-to-peak values of the chosen time step and the converged time step, and it is considered a contributing source of error to the contour of the lineshape.

Farley and Gao *et al.* include in their VMS models a term that accounts for concentration modulation, as described in Equation 3.5.[31, 30] In tests we found that inclusion of Equation 3.5 does affect the absolute intensity; however, the overall effect on the contour is less than 2 ppm. As 2 ppm is far less than the error introduced by the pseudo-Voigt approximation and the numerical integration (∼2% total), we have omitted concentration modulation from fits and simulations. Figure 3.2 illustrates the effect of including concentration modulation. The intensities were normalized to examine contour-based errors.

Fits of experimental data to Equation 3.13 with all parameters floating initially did not converge due

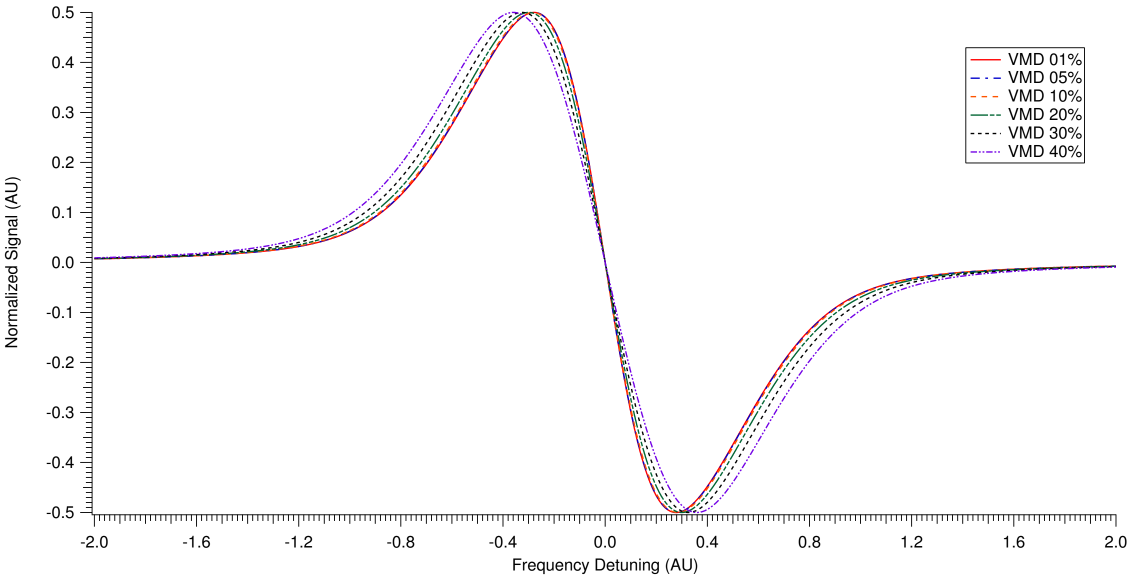

Figure 3.3: The velocity modulation depth (VMD) has a subtle effect on the contour of VMS lineshapes. The peak-to-peak intensities of each lineshape are normalized to unity.

to the large covariance between the velocity modulation amplitude (VMA) and full-width parameters. To circumvent this problem, the fit was performed first by holding the VMA constant at a value that corresponds to a rough estimate informed by the magnitude of the electric field and the ion mobility. The ion mobility can be approximated by the equation for the reduced ion mobility in Mason and McDaniel:[68]

$$K_0 = \frac{13.876}{\sqrt{\alpha\mu}}. \tag{3.14}$$

The only necessary information is the polarizability of the neutral species (α in Å^3) and the reduced mass of the ion and its collision partner (μ in amu). The electric field strength can be approximated by dividing the applied voltage to the electrodes by the distance between the electrodes and reducing the result by an order of magnitude to account for the fact that most of the voltage drop in a glow discharge occurs in the space before the negative glow.[73] After the first fit converges, the residuals are examined for structure that indicates that the velocity modulation depth or VMD (ν_{ma}/Δ_V) is incorrect. The fixed VMA fit is performed several times to refine the VMA estimate, each time examining the residuals. When a good value for the VMA is determined, the fit is performed again floating all the parameters, and convergence is achieved. This approach works because the VMD has subtle effects on the central slope and extrema of the two lobes of VMS-type lines as summarized in Figures 3.3 and 3.4. As the VMD is increased, the interior of the extrema become more curved and the interior slope becomes less steep. The reason for these differences is that as the VMD is increased, the individual Doppler-shifted components become more resolved. For VMD $< 10\%$

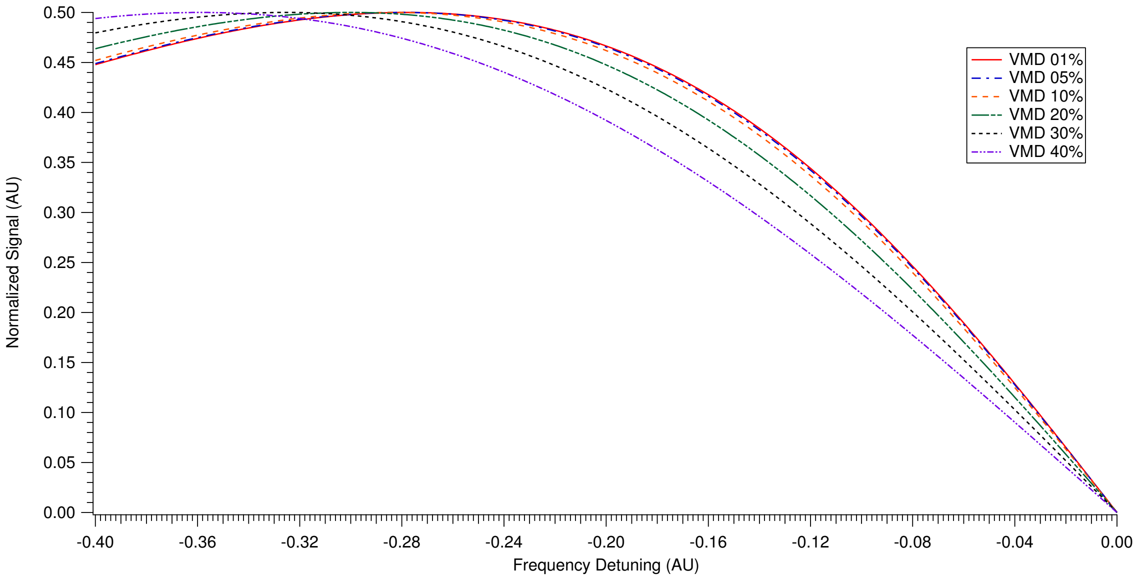

Figure 3.4: Closer inspection of Figure 3.3 makes plain the effect of velocity modulation depth (VMD) on the lineshape.

Table 3.1: Fit parameters from the R(1,0) transition of H_3^+

Parameter	**Symbol**	**Value**	**Error**
Intensity	A	0.0220 V	0.0003 V
Linecenter	ν_0	2725.907331 cm^{-1}	0.000006 cm^{-1} [1]
Homogeneous Linewidth	Δ_L	0.0140 cm^{-1}	0.0001 cm^{-1}
Inhomogeneous Linewidth	Δ_G	0.0163 cm^{-1}	0.0001 cm^{-1}
Modulation Amplitude	ν_{ma}	0.0079 cm^{-1}	0.0002 cm^{-1}
y-offset	y_0	-0.00859 V	0.00003 V

it becomes more difficult to distinguish one value of VMD from another. Fits to data with low VMD are therefore likely prone to substantial error. The VMD determined from the fits to the data presented in this work are ∼30%, which gives confidence in the fitting approach. After the fit was converged, the value of the VMA can be substantially changed and the fit with the floating VMA will converge on the correct result.

3.3 Results and Discussion

A single scan of the R(1,0) transition was recorded as described in Section 3.2.1. Using the method described in Section 3.2.2, a good fit was determined. The data, fit, and residuals can be seen in Figure 3.5, and a summary of the fitted parameters is presented in Table 3.1.

The fitted parameters all exhibit extremely small uncertainties as reported by the least squares regression.

---

[1] This is not to suggest this is the total uncertainty of the transition frequency; rather, it is the uncertainty of the fit. This work is calibrated via a wavemeter, limiting the accuracy. For an accurate linecenter determination, see Hodges *et al.*[26]

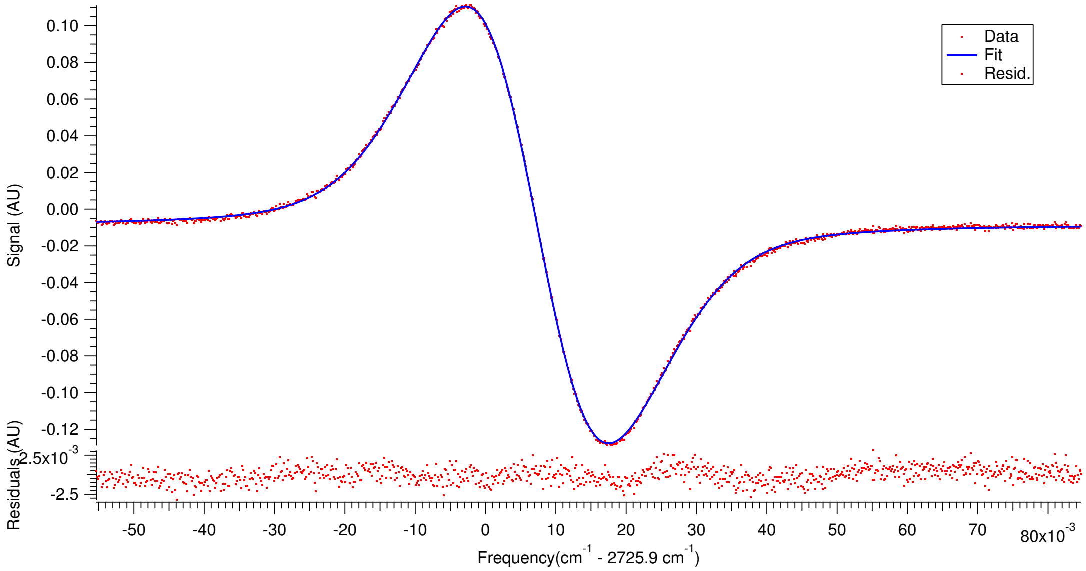

Figure 3.5: Experimental spectrum and fit to the R(1,0) rovibrational transition in the ν_2 fundamental band of H_3^+. The standard deviation of the residuals is less than 1% of the peak-to-peak signal. The signal-to-noise ratio is ~ 240 which is very useful in determining the values accurately. There is some structure remaining in the residuals, but it is attributed to the negative lobe being slightly wider than the positive lobe, possibly as a result of an asymmetric drift velocity during half the discharge cycle.

In the case of the linecenter and y-offset these values can be taken as is, since they are not determined by the contour of the line and are not subject to the convergence error or the pseudo-Voigt approximation, which combined present the need for an additional 2% relative error to be added to the overall uncertainty of the remaining parameters (1% from the pseudo-Voigt approximation and 1% from the convergence error).

The intensity of the transition is sufficiently well determined as to present the opportunity for determining the relative populations of rovibrational levels. The absolute populations cannot be determined because concentration modulation has been excluded from the model. Under the assumption that the same concentration modulation uniformly affects each quantum state, relative determinations of populations are possible. Testing this hypothesis may provide for an interesting avenue of future investigation. Regardless of this limitation, more precise intensity will lead to more accurate rotational/vibrational temperature determination.

Another exciting prospect is that the relative uncertainty of the linecenter is sub-MHz. Though this work was performed with a wavemeter which has an appreciable accuracy error (~ 200 MHz), proper calibration with a frequency comb and careful control of the experimental conditions may allow this approach to rival the uncertainties determined by sub-Doppler techniques[26, 61] without the added experimental difficulty. This would rely on the lines being very symmetric and highly reproducible, which may not always be the case. This problem could be mitigated with balanced detection of counter-propagating beams but would still be susceptible to any average drift velocity caused by asymmetries in the electrodes. This has been confirmed with these discharge electronics in the case of HCO^+, which exhibited between a 13 and 14 m/s average drift velocity.[35]

Both the inhomogeneous and homogeneous components of the linewidth were well determined. The two dominant broadening mechanisms for VMS spectroscopy are Doppler and collisional broadening. Plasmas are used for ion generation and result in large thermal energies. Typical VMS targets are low mass ions[18] which when combined with high temperatures result in mid-IR Doppler widths on the order of ~0.5 to ~1.0 GHz. The importance of collisional broadening is less obvious, considering a typical value for the pressure broadening coefficient is ~1-10 MHz/Torr, and VMS spectroscopy is generally performed at pressures between 0.5 and 10 Torr. Nevertheless, Gao *et al.* showed that treating the lineshapes as completely inhomogeneously broadened is insufficient to describe the lineshape.[30] The magnitude of both these broadening mechanisms requires the use of a Voigt profile.

The Doppler width (Gaussian, Δ_G) is determined by the formula

$$\Delta_G = \sqrt{\frac{8kT\ln 2}{mc^2}} \tag{3.15}$$

and depends on the translational temperature (T) and mass (m) of the ion. The collisionally broadened full-width (Lorentzian, Δ_L) is inversely proportional to the mean time between phase-changing collisions (τ),

$$\Delta_L = \frac{1}{\pi\tau}. \tag{3.16}$$

To characterize the collisional process, we must consider the predominant collision partner for ions in a plasma. A typical fractional ionization is 10^{-4}, indicating that there are 10,000 more neutral molecules than ions or electrons in a plasma. Conventionally, the ion-ion and ion-electron collisions are neglected because the positive column is assumed to have zero net charge.[68] Higher order corrections for the non-uniform distribution of charge are generally neglected.[18] Therefore, the relevant collision partner is the more abundant neutral, and ion-neutral collisions are the principal type assumed in all VMS experiments.[31, 18] Collisions of this type are typically described by Langevin capture theory, a simple model that has been successfully utilized to predict pressure broadening.[74]

The Langevin rate coefficient (k) is expressed in Equation 3.17 in terms of the polarizibility of the neutral (α), the charge of the ion (q), and the reduced mass (μ) of the ion and its collision partner.

$$k = 2\pi q\sqrt{\frac{\alpha}{\mu}} \tag{3.17}$$

The relationship between the Langevin rate coefficient and the pressure broadening coefficient (γ), pressure (P), and mean time between collisions (τ) is given in Equation 3.18,[74]

$$\frac{1}{\tau} = nk = 2\pi\gamma P, \tag{3.18}$$

which can be combined with the ideal gas law and solved for the pressure broadening coefficient.

$$\gamma = \frac{q\sqrt{\frac{\alpha}{\mu}}}{kT} \tag{3.19}$$

This linewidth is a half-width value, so one would expect $\Delta_L = 2\gamma P$, resulting in a Δ_L on the order of tens of MHz, but Gao and coworkers required much larger values[30] as did the fits in the present work, indicating that Equation 3.19 is insufficient. Using the Langevin model, the expected homogeneous linewidth in Gao's experiment (N_2^+ at a pressure of 10 Torr) would be 26 MHz; however, Gao's reported homogeneous linewidth is much larger, on the order of the Gaussian linewidth. The collisional process must not be well described by the Langevin model, and there must be a different source for the homogeneous contribution to the linewidth.

In order to better understand the collisional environment that an ion in a positive column experiences, we must start from basic principles. Let us begin by considering the equation of motion for ions in an electric field, as described by Chen[75] and summarized by Civiš:[29]

$$\mu\frac{\partial v}{\partial t} = qE - \frac{\mu}{\tau_D}v, \tag{3.20}$$

where the reduced mass of the ion and its collision partner is μ, v is the drift velocity, t is time, τ_D is the mean time between momentum transfer or diffusion related collisions, q is charge and E is electric field strength. The first term on the right hand side is the force of the electric field on a charged particle, and the second term is analogous to a drag force linearly proportional to the speed of the charged particle. Solving this equation of motion by assuming a constant electric field gives

$$v(t) = \frac{q\tau_D}{\mu}E(1 - e^{-t/\tau_D}) + v_0 e^{-t/\tau_D} \tag{3.21}$$

where $v_0 e^{-t/\tau_D}$ is a collisional deceleration term indicating that as time increases, the initial velocity is less significant. Likewise, as time increases the velocity approaches $\frac{q\tau_D}{\mu}E$.

Equation 3.21 is a complete description of an ion's speed, but it can be greatly simplified. Recall that the relationship between drift velocity (v), ion mobility (K), and electric field strength (E) is given by

Equation 3.1. As the timescale of the discharge is many orders larger than the timescale of molecular collisions, the relevant time, t, is much greater than τ_D, and Equation 3.21 can be simplified to

$$v(t) \cong \frac{q\tau_D}{\mu}E. \tag{3.22}$$

Comparison of Equation 3.22 to Equation 3.1 reveals that the ion mobility is

$$K \cong \frac{q\tau_D}{\mu}, \tag{3.23}$$

which indicates that an estimate of the ion mobility can be made provided information about the mean time between momentum transfer collisions can be determined.

However, τ from Equation 3.16 and τ_D from Equation 3.22 are not equivalent. The value τ is related to an ion's collisional cross section ($\sigma(\bar{v})$) at a mean speed ($\bar{v}$) by $\tau = (n\bar{v}\sigma(\bar{v}))^{-1}$; whereas, τ_D is related to the momentum transfer/diffusional cross section (Q_D) by $\tau_D = (n\bar{v}Q_D)^{-1}$. Here n is the number density and $\bar{v}$ is the mean velocity. Both values of τ can be related through n and $\bar{v}$:

$$\tau_D = \frac{\sigma}{Q_D}\tau. \tag{3.24}$$

The definition of Q_D, as described by Mason and McDaniel,[68] is

$$Q_D \equiv 2\pi \int_0^\pi (1-\cos\theta)\sigma(\theta,\bar{v})\sin\theta \; \mathrm{d}\theta \tag{3.25}$$

where $\sigma(\theta,\bar{v})$ is the collisional cross section as a function of scattering angle, θ and mean relative speed of the ion, $\bar{v}$. Without detailed knowledge of the potential energy surface of a scattering event for a particular ion-neutral pair, it is impossible to determine $\sigma(\theta,\bar{v})$. For simplicity, we make the assumption that the cross section is only weakly dependent on the scattering angle such that $\sigma(\bar{v}) \approx \sigma(\theta,\bar{v})$. Using this assumption, Equation 3.25 becomes

$$Q_D \approx 2\pi\sigma \int_0^\pi (1-\cos\theta)\sin\theta \; \mathrm{d}\theta = 4\pi\sigma. \tag{3.26}$$

Combining Equation 3.24 and Equation 3.26, an approximate relation for τ and τ_D can be formulated:

$$\tau_D \cong \frac{\tau}{4\pi}. \tag{3.27}$$

This simple equation relates the spectroscopically observed linewidth from τ and Equation 3.16 to the ion mobility through τ_D and Equation 3.23. Simultaneously it provides an explanation of the large values of the homogeneous linewidth with a simple model derived from the equation of motion presented in Equation 3.20. The source of the homogeneous linewidth is the collisional enhancement due to the macroscopic motion of the ions in the plasma. As the electric field drives the ions, collisions with neutrals create a drag force balancing the electromagnetic force resulting in a fixed single velocity. The rate of these collisions is determined by the diffusional cross section, which ultimately determines an ion's mobility. This relationship allows us to express the homogeneous full-width in terms of the ion mobility by

$$\Delta_L = \frac{q}{4\pi^2 \ \mu \ K(T,p)}. \tag{3.28}$$

With a clear understanding of the homogeneous and inhomogeneous linewidths, the fitted values can be used to infer information about the physical conditions and molecule being spectroscopically interrogated. Application of Equation 3.15 results in a translational temperature of 209 ± 10 K. This is a reasonable temperature and is in accord with previous estimates (200-400 K) of the temperature of liquid nitrogen cooled discharges of molecular hydrogen.[76, 71] As the inhomogeneous linewidth is also mass dependent, an analysis of many spectral lines could, in principle, be used to properly distinguish the relative masses of carriers, assuming a Maxwellian velocity distribution. In this case, the mass resolution is 0.03 amu, which is determined by propagating the linewidth error in Equation 3.15 using a fixed value for temperature. With such a small mass resolution, VMS could be a very powerful tool for distinguishing spectral carriers in chemically rich positive columns, which would be invaluable for assigning unknown spectra.

Using the homogeneous linewidth we can determine the ion mobility. The Langevin model linewidth is estimated using the temperature and the polarizability of molecular hydrogen (0.787 $\text{Å}^3 \pm 5\%$).[77] This results in a Langevin pressure broadened component equal to 14 ± 2 MHz. Just as in Gao's measurements of N_2^+, this is a dramatic underestimate. With Equation 3.16, τ is determined to be $7.8 \pm 0.3 \times 10^{-10}$ s. With Equation 3.27, the value of τ_D is calculated to be $6.0 \pm 0.2 \times 10^{-11}$ s. This can be used with Equation 3.23 to infer the ion mobility. The determination of reduced ion mobility assumes that the reading of the pressure capacitance monometer is accurate to 5%, and it is calculated to be 12.5 ± 1.5 cm^2 V^{-1} s^{-1} which agrees with the most recent literature value of 11.1 cm^2 V^{-1} s^{-1} within 13% error.[78]

In this case it is fortunate that there is a large signal-to-noise ratio and the VMD (∼30%) is in a range that allows for reasonable determination of the VMA (refer to Figure 3.4). This may not be the case in all VMS experiments. Since the VMD is the ratio of the VMA to the linewidth there are only a limited number of experimental parameters that can be adjusted to ensure a large VMD. The temperature can be reduced and the pressure decreased to minimize the linewidth, and the applied voltage to the electrodes can be increased in order to increase the VMA. Nevertheless, the VMD may still prove too small for some systems. Moving forward, caution is required to properly determine the fitted parameters. Determination of fit parameters below a VMD of ∼20% becomes more challenging, and ultimately becomes an exercise in futility. This is a direct consequence of how insensitive the contour of the lineshape becomes to changes in VMD (refer to Figure 3.4).

The RMS value of the drift velocity (determined as 614 ± 16 m/s from Equation 3.4 and the VMA from the fit) can be used to determine the RMS field strength using Equation 3.1, provided the ion mobility is accurately known. Using the literature value, the RMS field strength is determined to be 4.8 ± 0.6 V/cm. If one were to take the applied voltage and divide it by the distance between the electrodes, the resultant RMS field strength would be 24 V/cm. Typically, the values in the positive column are an order of magnitude lower,[73] and our inferred field strength of 4.8 V/cm is in accord with that rough estimate. The calculated value of the ion mobility can be used in cases where the reduced ion mobility is not known. With this method, the RMS field strength is determined to be 4.2 ± 0.2 V/cm, which is in reasonable agreement with the other measurement.

3.4 Conclusions

In this work, we present a method for quantitatively fitting VMS lineshapes. This method relies on a detailed examination of the slope of the center portion of the profile and the curvature near the edges of the lobes. Additionally, we confirm that there is a large homogeneous component to the linewidth of VMS greater than what can be explained by Langevin capture theory. This is attributed to the macroscopic movement of ions at the drift speed and the resulting collisional enhancement. From the fit, the translational temperature, transition intensity, ion mobility, and electric field strength are handily determined to reasonable uncertainty.

Together, these values are critical for the quantitative understanding of both the plasma environment and the species being interrogated spectroscopically. This may help lead to better quantification of relative ion populations, rotational and vibrational temperatures, mass identification of spectral carriers, and a better understanding of the lineshapes of more complicated VMS experiments with additional layers of modulation. As a final note, although this method is completely general to any VMS experiment, it does require high data quality and that the VMD be appreciably sized. As the VMD value becomes smaller the task becomes more challenging and requires higher signal-to-noise data.

So long as there is highly reproducible data with high signal-to-noise, it is expected that statistical errors, determined by scanning the same transition multiple times, will be on the same order as the estimated error of fitted parameters. This might be an interesting endeavor for future experiments in addition to performing the same analysis on different molecules to confirm the generality of this approach.

3.5 Acknowledgments

We would like to acknowledge support from the National Science Foundation (CHE 12-13811) and the NASA Laboratory Astrophysics program (NNX13AE62G). J.N.H. is appreciative for the support from a Robert & Carolyn Springborn Fellowship and an NSF Graduate Research Fellowship (DGE 11-44245 FLLW). J.N.H. is grateful to Adam J. Perry for his assistance in collecting data for the paper. J.N.H. is also appreciative to Thomas C. Allen for useful discussions regarding approaches to fast and accurate numerical integration, Charles R. Markus for useful discussions regarding the homogeneous broadening model, and Daniel N. Gresh for sharing his experimental data that was useful in demonstrating the necessity of high signal-to-noise ratios for the success of this approach. J.N.H. is also especially appreciative of Yahsin Chen for her hard work in translation of H. Gao's paper.

Chapter 4

NICE-OHVMS Lineshapes

4.1 Introduction

The recent emergence of Noise Immune Cavity Enhanced Optical Heterodyne Velocity Modulation Spectroscopy (NICE-OHVMS) has opened up the field of sensitive, high precision spectroscopy of molecular ions.[2, 25] It simultaneously addresses the weak signals, high noise, and congested spectra that create many of the difficulties associated with molecular ion spectroscopy. NICE-OHVMS is the combination of Noise Immune Cavity Enhanced Optical Heterodyne Molecular Spectroscopy (NICE-OHMS)[24] and Velocity Modulation Spectroscopy (VMS)[17]. It combines the advantages of pathlength enhancement and sensitivity from NICE-OHMS[24] with the ability to discriminate between ion and neutral signals resulting in the most general, sensitive, ion specific approach to date.

This technique is simultaneously accurate and precise. It has been referenced to a frequency comb resulting in kHz-level frequency accuracy, and the use of a high intensity light source results in optical saturation, which produces Lamb dips in the spectra. These Lamb dips can been fit to measure the rest frequencies of transitions with sub-MHz/MHz precision, resulting in typical relative uncertainties of $\sim 10^{-8}-10^{-9}$. NICE-OHVMS has been successfully employed to measure transition frequencies in H_3^+, HCO^+, CH_5^+, HeH^+, and OH^+.[26, 61, 63] The introduction of NICE-OHVMS as a frequency metrology tool shares a similar origin to that of NICE-OHMS, originally developed for creating frequency standards.[24]. Later, other investigators carefully modeled NICE-OHMS lineshapes[79, 80] in order to advance NICE-OHMS into a robust analytical technique for trace gas detection.[46, 81] Likewise, characterization of the NICE-OHVMS lineshapes will provide opportunities for further development of the technique.

One of the principal motivations for developing this spectroscopic approach is that ions pose additional challenges to traditional spectroscopy as they often are produced in low abundance and highly interfering chemical environments. Additionally, plasma sources used to generate ions often have a great deal of electronic noise. VMS has largely overcome these challenges. The ubiquitous use of the technique in the 1980s and 1990s spurred the need to fully understand the modulated lineshape. The theory of VMS lineshapes was described by John Farley,[31] and attempts using that theoretical foundation to fit the VMS spectra have been carried out by Gao *et al.*[30] Improved fit methods using Farley's foundation are presented in Chapter 3. The future of velocity modulation as a part of NICE-OHVMS requires a rigorous investigation of the lineshapes in order to obtain more detailed information about the spectral carrier. With a proper understanding of the modulated lineshape, it may be possible to not only quantitatively detect ions at minute concentrations, but also to gain information about the relaxation rates, improve the precision of a spectral carrier's mass, and infer the degree of optical saturation in a transition based on the relationship between the dispersive and absorptive components of a transition.

The most simple, complete theory of lineshapes describes homogeneously and inhomogeneously broadened spectral features as Lorentzian, Gaussian, or Voigt profiles. The choice of profile is completely dependent on underlying dynamics within the analyte's environment and the timescales of processes in the experiment. Inherent to a spectral feature's profile is the experimental methodology by which the feature is measured. NICE-OHVMS is a technique that relies on two layers of modulation, which requires both complicated methods for signal processing and a sophisticated understanding of the effects that the signal processing produces on fundamental lineshapes.

NICE-OHVMS has been employed in an AC modulated positive column discharge at pressures that have been traditionally believed to be dominantly Doppler broadened.[18, 31] The only two attempts at fitting VMS type experiments used Voigt profiles, and attributed the anomalously large homogeneous linewidth to pressure broadening.[29, 30] Chapter 3 demonstrated that there is a collisional enhancement in VMS experiments and presented a simple model that can be used to relate the linewidth to the ion mobility. Because both homogeneous and inhomogeneous broadening are pertinent processes, the pseudo-Voigt approximation is used to model the fundamental lineshape (for more details refer to Chapter 3). For ease of reading, the pseudo-Voigt is reprinted as Equation 4.1.

$$\chi_{abs}(\nu_d) = \eta(L_{abs}(\nu_d;\Delta\nu)) + (1-\eta)G_{abs}(\nu_d;\Delta\nu) \tag{4.1}$$

Equation 4.1 is written in terms of a detuning axis, *i.e.* $\nu_d = \nu - \nu_0$, where ν is the frequency and ν_0 is the transition frequency. The pseudo-Voigt is a linear combination of a Gaussian lineshape and a Lorentzian lineshape given by Equations 4.2 and 4.3.

$$L_{abs}(\nu_d;\Delta\nu) = \frac{2\Delta\nu}{\pi(4\nu_d^2 + \Delta\nu^2)} \tag{4.2}$$

$$G_{abs}(\nu_d; \Delta\nu) = \frac{2\sqrt{2\ln 2}}{\Delta\nu\sqrt{\pi}} e^{-(\frac{2\sqrt{\ln 2}\,\nu_d}{\Delta\nu})^2} \tag{4.3}$$

The full-width at half-maximum, $\Delta\nu$, is same in both the Lorentzian and Gaussian components of the pseudo-Voigt, and it is related to the homogenous linewidth, and inhomogeneous linewidth by the coefficient, η, in Equation 4.1.

NICE-OHVMS is not only sensitive to absorption of light but also to dispersion which can be described mathematically through the Kramers-Kronig relations.[82] Dispersion is detected at a phase angle that is 90° separated from the absorptive signal. The transform of the Voigt profile is not trivial so the use of the pseudo-Voigt is particularly useful for dispersion. The individual transforms of the Gaussian and Lorentzian cases are substituted for the absorption counterparts. In the case of a Gaussian absorption profile, the dispersion relation can be written as[83]

$$G_{disp}(\nu_d; \Delta\nu) = -\frac{4\sqrt{2\ln 2}\, S}{\Delta\nu\, \pi} e^{-(\frac{2\sqrt{2\ln 2}\,\nu_d}{\Delta\nu})^2} \int_0^{\frac{2\sqrt{2\ln 2}\,\nu_d}{\Delta\nu}} e^{u^2}\, \mathrm{d}u, \tag{4.4}$$

which can also be simplified in terms of a prefactor and the Dawson function, D_+, as

$$G_{disp}(\nu_d; \Delta\nu) = -\frac{4\sqrt{2\ln 2}}{\Delta\nu\, \pi}\, D_+(\frac{2\sqrt{2\ln 2}\,\nu_d}{\Delta\nu}). \tag{4.5}$$

The Dawson function is calculated numerically and is typically available as a tabulated function in a variety of mathematical software suites.

Fortunately, the Lorentzian case has an analytical solution and is given by

$$L_{disp}(\nu_d; \Delta\nu) = \frac{2\Delta\nu\, \nu_d}{\pi(4\nu_d^2 + \Delta_\nu^2)}. \tag{4.6}$$

Ultimately, this means that the dispersion lineshape can be written as

$$\chi_{disp}(\nu_d; \Delta\nu) = \eta(L_{disp}(\nu_d; \Delta\nu)) + (1-\eta)(G_{disp}(\nu_d; \Delta\nu)). \tag{4.7}$$

Together, Equation 4.1 and Equation 4.7 describe the fundamental lineshape that is present in the discharge.

After understanding the fundamental lineshape, we must consider the effect of the two layers of modulation on the recorded transition profile. Frequency modulation in the small modulation limit results in a laser spectrum triplet, *i.e.* a carrier frequency and two sidebands spaced at the modulation frequency (ν_H). These sidebands are 180° out-of-phase with each other. The absorption signal depends on the difference between the beat amplitudes of the sidebands against the carrier. The dispersion signal is described as the dispersive contribution of each individual component of the triplet, but with the component of the carrier contributing twice as much signal of the opposite phase. Mathematically, these can be written as

$$\chi_{H-abs}(\nu_d) = J_0(\beta)J_1(\beta)\frac{2F}{\pi}\{\chi_{abs}(\nu_d+\nu_H) - \chi_{abs}(\nu_d-\nu_H)\} \tag{4.8}$$

and

$$\chi_{H-disp}(\nu_d) = J_0(\beta)J_1(\beta)\frac{2F}{\pi}\{\chi_{disp}(\nu_d-\nu_H) - 2\chi_{disp}(\nu_d) - \chi_{disp}(\nu_d+\nu_H)\}. \tag{4.9}$$

The product of the zeroth order and first order Bessel functions of the first kind, $J_0(\beta)J_1(\beta)$, accounts for the determination of the intensity of the beat notes from the unmodulated intensity. The argument β is the modulation index. The factor $\frac{2F}{\pi}$ accounts for the pathlength enhancement as a result of using an external optical cavity.[24, 79]

Velocity modulation of the ion is the second type of modulation in the NICE-OHVMS technique. When a discharge is ignited for the purpose of spectroscopically probing the AC positive column, it is typically driven by a sinusoidal power supply.[31] A reasonable approximation of this behavior is that the transition profile oscillates about the zero velocity frequency in a sinusoidal fashion. This is typically modeled by the addition of a sinusoid to the rest transition frequency, *i.e.* by the transform

$$\nu_d \rightarrow \nu_d(t) = \nu_d + \nu_{vm}\cos 2\pi t \tag{4.10}$$

where ν_{vm} is the velocity modulation amplitude, the maximum Doppler shift in a half cycle of the plasma. The convention here is that t is the period normalized time to avoid miscellaneous factors of the plasma driving frequency in the model. The range of t is -0.5 to $+0.5$. Equation 4.10 has been successfully used as a part of the fit model in Chapter 3 and is expected to be applicable here as well.

This transform can be performed on any lineshape and is simple enough to consider in the case of single pass spectroscopy, uni-directional cavities, and uni-directional multi-pass cells. However, it is not a sufficient descriptor for bi-directional cavities, such as the symmetric two mirror cavity used in NICE-OHVMS. The transform becomes more complex because forward- and counter-propagating beams alternatively measure red and blue shifted transition profiles. When the the forward-propagating beam measures an ion that is red-shifted, the counter-propagating beam measures an ion that is blue-shifted. To account for this phenomenon, the transform must be rewritten as

$$\chi(\nu_d) \rightarrow \chi(\nu_d(t)) = \chi(\nu_d + \nu_{vm}\cos(2\pi t)) + \chi(\nu_d - \nu_{vm}\cos(2\pi t)) \tag{4.11}$$

where χ is any generic transition profile.

Using phase sensitive detection, such as a lock-in amplifier, the Fourier coefficient of interest can extracted from the time dependent signal. In the case of the uni-directional cavity or multipass configuration, the odd and even components of the first Fourier coefficient represent the in-phase and quadrature detection channels. For a bi-directional cavity, the second Fourier coefficient encodes the relevant velocity information.[21] The formulae used to calculate the n^{th} even and odd Fourier coefficients of interest from a lock-in amplifier are

$$F_{n,even}(\chi) = \int_{-0.5}^{+0.5} \chi(\nu_d(t)) \cos(2n\pi t)\, \mathrm{d}t \tag{4.12}$$

$$F_{n,odd}(\chi) = \int_{-0.5}^{+0.5} \chi(\nu_d(t)) \sin(2n\pi t)\, \mathrm{d}t \tag{4.13}$$

Again, χ is any lineshape after either of the transforms in Equations 4.10 or 4.11 have been applied. In the case of NICE-OHVMS in a bi-directional cavity, it is Equations 4.8 (absorption) and 4.9 (dispersion) that have the transform in Equation 4.11 applied, which have their second Fourier coefficient measured as the observed lineshape.

Ultimately, it is Equations 4.12 and 4.13 which represent the final detected waveform, but that is not a complete view. There is also concentration modulation to be considered. During a cycle through the plasma, as the voltage increases and decreases, so too can the total population of the ions. To attempt to account for this, a concentration modulation depth, α, is defined as the fractional quantity of the ion population that recombines with electrons during a half cycle of the plasma. This leads to a time dependent line intensity factor, $A(t)$, which must have a functional form that is twice the period of the voltage source driving the plasma, and the functional form must exist in the range of 0 to 1 inclusive. A simple functional form that is used in this work is

$$A(t) = (1-\alpha) + \alpha \cos^2(2\pi t + \phi). \tag{4.14}$$

It is been previously demonstrated that there is a phase delay between concentration modulation and the velocity modulation within the plasma, and the term, ϕ, accounts for this delay.[21]. This functional form was chosen because it fulfills the requirements and is a simple, reasonable approximation for the time dependent production and destruction of ions.

4.2 Experiment and Methodology

4.2.1 Experiment

The NICE-OHVMS spectrometer used in this work has been described before by Crabtree *et al.* and Siller *et al.*[2, 35] It will not be described in great detail; rather, a general overview will be given to explain the basic equipment and layout of the instrument. The light source is an optical parametric oscillator (OPO, Aculight Argos 2400 SF, C Module), which is pumped by a fiber amplified (IPG Photonics YAR-10 K-1064-LP-SF) ytterbium doped fiber laser (Koheras Adjustik Y-10). Before the fiber amplifier, the fiber laser is phase modulated by an electro-optic modulator (EOSPACE PM-0K5-00-PFU-PFU-106-S) to produce sidebands which are imprinted onto the mid-IR idler in the OPO. The frequencies of the pump and signal beams from the OPO head are used to infer the mid-infrared frequency, and are measured either with a wavemeter (Burleigh WA-1500) or a frequency comb (Menlo Systems FC-1500, 100 MHz repetition rate) for higher accuracy work.

The idler beam is shaped by a telescope and coupled into a symmetric external optical cavity comprised of two mirrors(99% reflective, silicon substrate 1m radius of curvature, Rocky Mountain Instruments) and resonance is maintained with PDH locking. Within the optical cavity, a liquid nitrogen cooled positive column discharge cell is placed. An arbitrary waveform generator sends a sine wave to an audio amplifier (Techron 7780) to produce a high current, low voltage signal, which is stepped up with a transformer. The the secondary line of the transformer is attached to the electrodes on the discharge cell. Light that is exiting the optical cavity is detected with a fast photodiode (Boston Electronics Vigo PVM-10.6-1x1). Two mixers, 90 degrees out of phase with each other, demodulate the heterodyne signal and then two lock-in amplifiers are used to extract the velocity modulation information from the signal. The R(1,0) fundamental transition of H_3^+ is recorded a single time at a pressure of 140 mTorr of H_2 using the wavemeter as a frequency reference.

4.2.2 Methodology

One of the challenges of working with two layers of modulation is understanding and accounting for the different phase angles that complicate the recorded signal. There is the heterodyne detection angle that determines whether the signal from a mixer is pure absorption, pure dispersion, or a blend. Also, there is a velocity modulation angle that determines whether the signal is in-phase with the velocity modulation signal, or whether it is recording a projection of the concentration modulation signal. The concentration modulation also has a phase angle that is relative to the velocity modulation signal. These three angles thwarted many early attempts at proper fitting, but there are ways to mitigate the problems associated with bad angle selection.

The heterodyne angle can be set prior to a scan by maximizing the amplitude of some residual amplitude modulation (RAM). After the data are collected, close examination of the Lamb dips and the concentration modulation portion of the signal can be performed to confirm the isolation of absorption and dispersion. The Lamb dips must be fit as described previously and the heterodyne angle is a parameter of that fit.[2, 26] Examination of the wings of the transition should be used to additionally confirm the absorption/dispersion isolation. The dispersion wings in ordinary NICE-OHMS contain an additional lobe. The concentration modulated signal from NICE-OHVMS is the same lineshape. Figures 4.1 and 4.2 illustrate the differences.

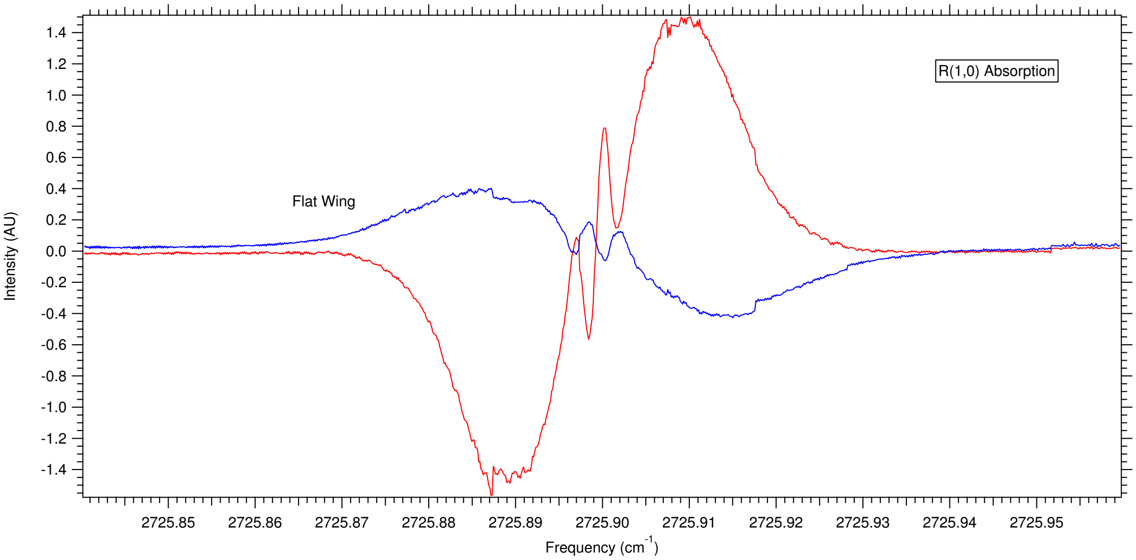

Figure 4.1: Absorption measurement of the R(1,0) transition of H_3^+. The red trace is the X channel of the lock-in amplifier and the blue trace is the Y channel, which is separated by 90°. The flat wing is indicative of absorption. The sharp discontinuities are artifacts of cavity re-locking events.

The velocity modulation angle is more challenging to properly isolate. Attempts have been made to measure the phase difference between the primary and secondary transformer lines to determine the phase shift of the voltage step-up process; however, these efforts did not result in adequate identification of the velocity phase. As the concentration modulation phase is set relative to the velocity modulation phase, this further complicates fitting efforts. To sidestep these velocity modulation phase related issues, the magnitudes of the absorption and dispersion signals are considered instead. Using the magnitude of the X and Y channels of a lock-in amplifier means that the model developed in Section 4.1, assuming the detection is at twice the

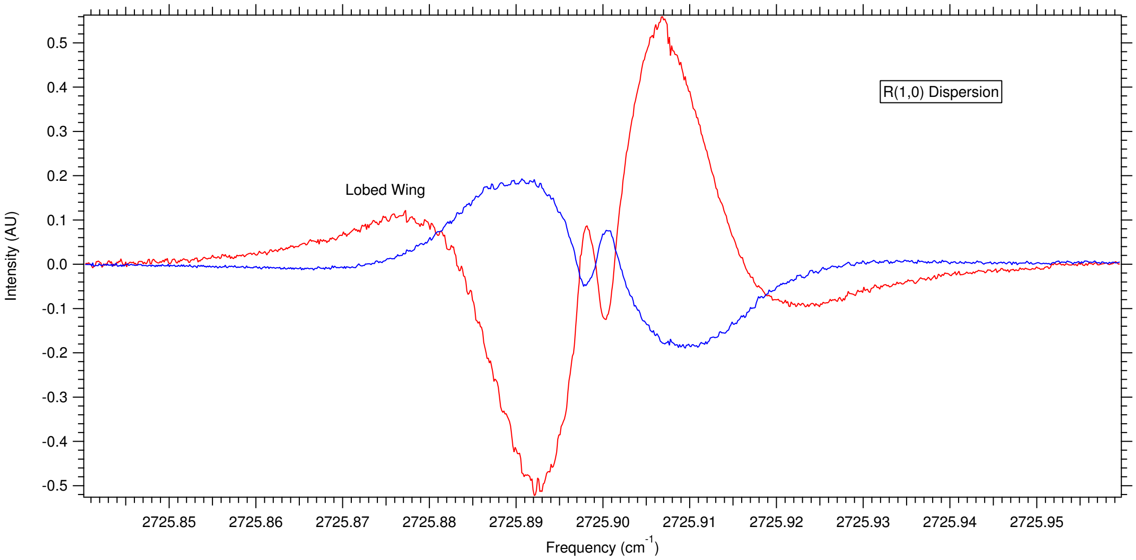

Figure 4.2: Dispersion measurement of the R(1,0) transition of H_3^+. The red trace is the X channel of the lock-in amplifier and the blue trace is the Y channel, which is separated by 90°. The lobed wing is indicative of absorption. The sharp discontinuities are artifacts of cavity re-locking events.

driving plasma frequency, must take the form:

$$\chi_{NO-mag}(\nu_d; S, \alpha, \Delta_L, \Delta_G, \nu_{vm}, y_0) = \sqrt{\left(S\int_{-0.5}^{+0.5} A(t)\chi_H(\nu_d, t)\cos(4\pi t)\,\mathrm{d}t\right)^2 + \left(S\int_{-0.5}^{+0.5} A(t)\chi_H(\nu_d, t)\sin(4\pi t)\,\mathrm{d}t\right)^2} + y_0. \quad (4.15)$$

The fitting parameters are the concentration modulation depth (α, from Equation 4.14), the line strength (S), the homogeneous linewidth (Δ_L, see Chapter 3), the inhomogeneous linewidth (Δ_G, see Chapter 3), the velocity modulation amplitude (ν_{vm}, from Equation 4.11), and the y-offset (y_0). The lineshape χ_H can be either χ_{H-abs} or χ_{H-disp} depending on whichever type of data are being fit.

One additional complication is that the Lamb dips are very large for all observed NICE-OHVMS scans,[2, 26, 61, 62, 63] and they must be simulated on top of the lineshape to properly fit the transition profile. The Lamb dip fitting approach presented by Crabtree *et al.*[2] and Hodges *et al.*[26] must be performed on any recorded Lamb dips in data to be fit, and the parameters returned from that fit are used to simulate the Lamb dips via addition to the functions that are used in the fitting routine.

The fitting routine is custom software written in `python3`, which makes extensive use of the `numpy` and `scipy` modules for numerical integration and useful functions. The integrals in Equation 4.15 are solved numerically by the trapezoidal rule with the `trapz` function from `numpy`. The non-linear least-squares algorithm is the Levenburg-Marquardt method from the `scipy.optimize` module. A pair of two-dimensional arrays are populated by determining the value of the integrands in Equation 4.15 as a function of frequency along one axis and a function of period-normalized time on the other axis. Integration is performed over the time axis resulting in a one dimensional array containing the lineshape. The time-step of 0.04 fractional periods was chosen as a compromise between the time required to complete the integration and achieve reasonable accuracy in the lineshape. The pseudo-Voigt and numerical integration result in about 2% increase in uncertainty, 1% from the pseudo-Voigt and an additional 1% as numerical error.

4.3 Results and Analysis

A single scan of the R(1,0) transition was recorded with the absorption separated from the dispersion by the method described in Section 4.2.2. The Lamb dips were fit according to the methods presented in previous work.[2, 26] Figure 4.3 shows the X and Y channels from the lock-in amplifier which corresponds to absorption. The quality of the Lamb dip fit is not ideal, as the residuals represent ~14% of the Lamb dip signal. Nevertheless, the rough characteristics of the Lamb dips are captured. The parameters that were determined by the fit can be used to simulate the Lamb dips in the fitting routine. It should also be noted that there appears to be a strong cubic component to the background in Figure 4.3, which means that the background free simulation may perform poorly on the edges of the Lamb dip. The lower quality of this fit will likely cause the Doppler fit to suffer in the accuracy of its determined parameters.

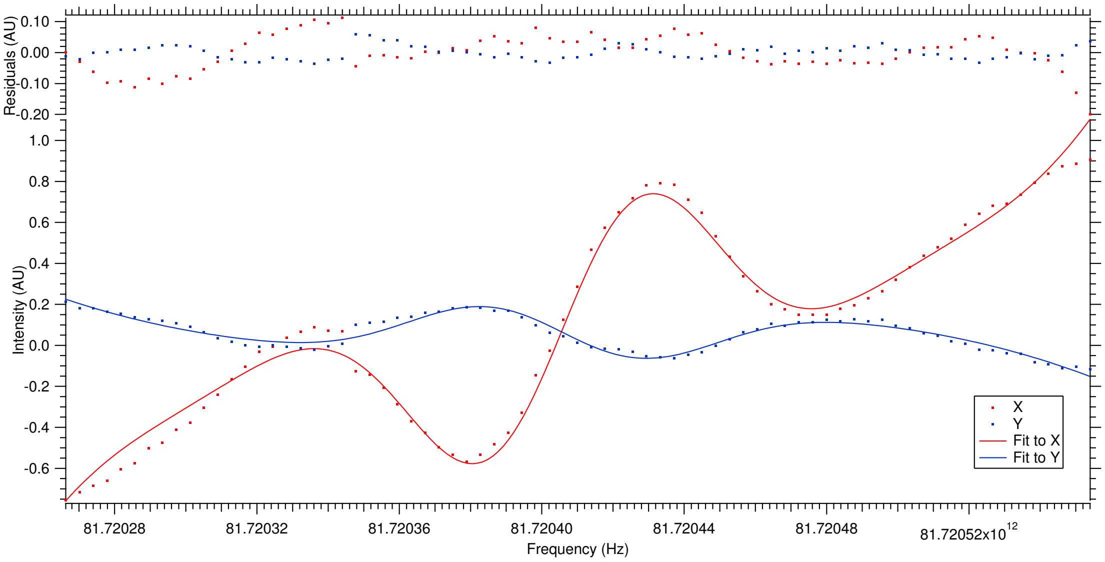

Figure 4.3: Fit of the absorption Lamb dips.

After the Lamb dip fit is recorded, the magnitude of the X and Y channels are determined by the standard formula: $R = \sqrt{X^2 + Y^2}$. The only parameter held constant for the fit is the y-offset. Initial attempts to float the baseline resulted in negative values for the baseline, which should be impossible. The magnitude cannot be negative. Because the magnitude of the lineshape is even, there must be adequate baseline to properly determine the y-offset, and it is possible there is insufficient baseline to fit the baseline. By holding the baseline constant at the fixed value the shorter baseline is less likely to cause convergence problems.

The initial guesses for most of the parameters are not particularly sensitive to the exact value though it is likely important to estimate the velocity modulation amplitude in the same way as presented in Chapter 3. This estimation is made by approximating the ion mobility and electric field of the of the discharge. The product of those two parameters give the ion drift velocity, which can be converted to a Doppler shift and used as an initial guess for the velocity modulation amplitude. The results of the fit to absorption data are presented in Figure 4.4. It is clear that the fit is not perfect. There are many possible reasons for an imperfect fit in this case. The most significant contributor to the imperfections in the fit is probably the low quality Lamb dip fit. Improving that will certainly improve the linewidth determination, and probably the velocity modulation amplitude as well. These parameters should be improved because they are particularly sensitive to the interior slopes of the two lobes. Another concern is the presence of large discontinuities that occur during re-locking events. As the piezoelectric transducer sweeps the cavity back to the starting length, there is probably a mismatch in the heterodyne to the free spectral range, which results in residual amplitude modulation (RAM). RAM decreases the quality of the absorption measurement. DeVoe-Brewer locking, which would lock the free spectral range to the cavity length, would minimize the RAM that results from changing the length of the cavity. There may also be some incomplete isolation of dispersion from

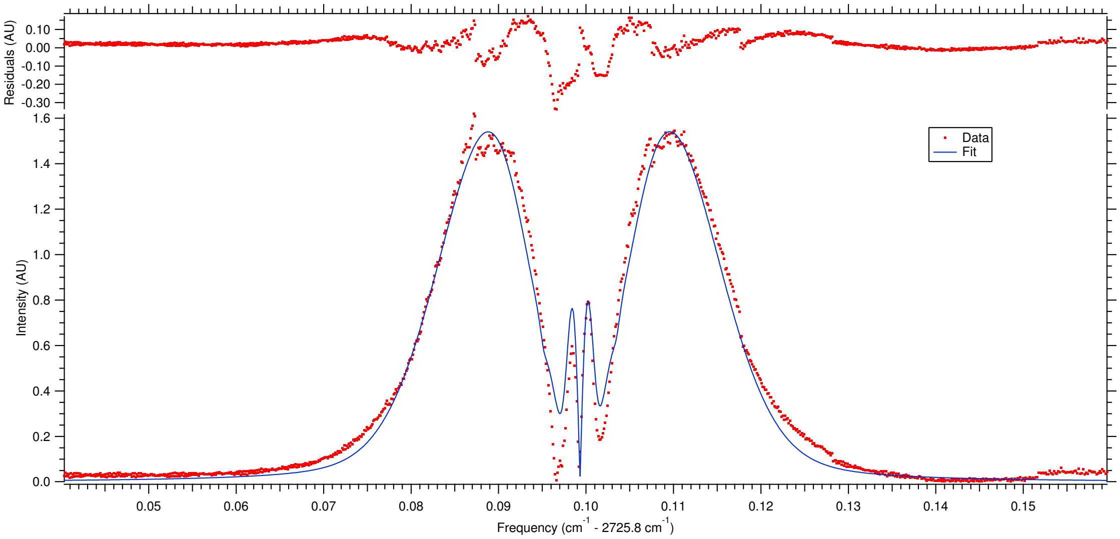

Figure 4.4: Fit of the complete Doppler profile using the parameters from the Lamb dip depth to simulate the large Lamb dip features in the middle of the spectrum.

absorption, which means that the underlying lineshape model is not an exact descriptor; however, that has been addressed as well as can be done within the current experimental limitations. One final source of error that can be introduced is bad parameters as a result of fixing the y-offset. By holding the y-offset at a fixed value some error may be introduced in the linewidth determination. For instance, if the y-offset was too large, it would underestimate the linewidth. If the y-offset were too small the opposite would be true. Despite these difficulties, the fit still provides useful data. The parameters returned from the fit are reported in Table 4.1. All of the parameters except the linecenter are subject to an additional 2% uncertainty for convergence errors and pseudo-Voigt errors so the final values of those parameters are reported in Table 4.2.

The concentration modulation is found to be effectively 1, which is consistent with the notion that the molecular ions that are formed are completely destroyed when the driving voltage crosses zero. The absolute intensity is determined with a total error of approximately 5%, which is very good and may present an opportunity to determine ion population in that state, assuming that the concentration modulation model is an adequate functional description of the process. Furthermore, this can be used to determine the saturation parameter which is discussed in Chapter 5.

Table 4.1: Fit parameters and fit uncertainties from the R(1,0) transition of H_3^+ fit by NICE-OHVMS.

Parameter	**Symbol**	**Value**	**Error**
Conc. Mod. Depth	α	1	1×10^{-57}
Intensity	S	0.405 V	0.007 V
Linecenter	ν_0	2725.89919 cm^{-1}	0.00002 cm^{-1}[1]
Homogeneous Linewidth	Δ_L	0.0054 cm^{-1}	0.0004 cm^{-1}
Inhomogeneous Linewidth	Δ_G	0.0121 cm^{-1}	0.0002 cm^{-1}
Modulation Amplitude	ν_{ma}	0.00635 cm^{-1}	0.00002 cm^{-1}

Table 4.2: Fit parameters and with total uncertainties from the R(1,0) transition of H_3^+ fit by NICE-OHVMS. This includes the 2% error from the approximation methods.

Parameter	**Symbol**	**Value**	**Error**
Conc. Mod. Depth	α	1	0.02
Intensity	S	0.41 V	0.02 V
Homogeneous Linewidth	Δ_L	0.0054 cm^{-1}	0.0005 cm^{-1}
Inhomogeneous Linewidth	Δ_G	0.0121 cm^{-1}	0.0004 cm^{-1}
Modulation Amplitude	ν_{ma}	0.00635 cm^{-1}	0.0001 cm^{-1}

The linecenter is well determined (though not accurate due to the limitations of wavemeter calibration) and comparison of the Doppler fitted line center to that of the Lamb dips provides an interesting opportunity to determine the asymmetry in drift velocity. This method works because the Lamb dips are symmetrically spaced about the transition center, and the Doppler profile is shifted if the average velocity is not zero. The

---

[1] This is not the total uncertainty of the transition frequency. This is merely the uncertainty associated with the fit. For an accurate value for the linecenter, see Hodges *et al.*[26]

difference in values between the lineshapes is about 4 MHz, which is consistent with a 15 m/s asymmetry. This measurement is in accord with the previous estimates.[35]

The inhomogeneous linewidth is well determined and can be used calculate the translational temperature, which is 115 ± 8 K. This is a reasonable value as the discharge cell is cooled with liquid nitrogen, and the gas is at low pressure. The homogeneous linewidth is also well determined. Using the methods developed in Chapter 3, the reduced ion mobility can be estimated to be 16 ± 3 cm^2 V^{-1} s^{-1}. This is not consistent with the literature value of 11.1 cm^2 V^{-1} s^{-1}.[78] However, inspection of the fit in Figure 4.4 suggests that the homogenous linewidth is underestimated, which would overestimate the ion mobility. The velocity modulation amplitude can be used to determine the RMS drift velocity, 490 ± 16 m/s, and the value of the RMS axial electric field using the literature value of the ion mobility, 1.9 ± 0.3 V/cm.

4.4 Conclusions and Future Work

We have successfully demonstrated the first fit to a NICE-OHVMS absorption Doppler profile. Despite it not being perfect, it represents a tangible step forward in describing the complex lineshapes and expanding the abilities of the NICE-OHVMS technique outside the realm of precision frequency measurement. The NICE-OHVMS data have been used to adequately describe the physical environment of the discharge.

There are two areas that need to be addressed to further advance this method. First a dispersion lineshape must be fit. The relative intensities of the absorption to the dispersion measurement of a transition can be used to infer the saturation parameter and provide wide new avenues of investigation. Second, there are some obvious problems with the Lamb dip fitting routine, and they must be addressed. The Lamb dips are very complicated. They are off-center on the Doppler profile, which may lead to asymmetric depths on either side of the transition center. They are very wide and not resolved, and they are concentration modulated. There is much more to learn from the Lamb dips. With further investigation better approaches to fitting Lamb dips will improve the ability to fit Doppler profiles.

Chapter 5

Saturation Spectroscopy

5.1 Introduction

Saturation of optical transitions is a non-linear response of an absorbing medium to the intensity of the light, *i.e.* the number of absorbers in a material is not linear with intensity. For most traditional types of spectroscopy, saturation presents an undesirable complexity. For analytical purposes, it can lead to an underestimate of the quantity of the analyte present in the sample. Any measurements that rely on this linearity will also be made more difficult; for example, any estimate of temperature by a Boltzmann analysis should ideally be performed in non-saturated media.

However, saturation spectroscopy has seen wide-spread success in the field of frequency standards and high precision spectroscopy.[24, 26, 34, 84, 85] Small spectral features in counter-propagating pump-probe experiments can be fit provided the frequency calibration is adequate. Nevertheless, the utility of saturation spectroscopy is not limited to frequency measurements. Saturation spectroscopy provides access to information about the transition dipole moment and the relaxation rate of the dipole, which may be used to gain insight into the relaxation rates and relaxation mechanisms for an absorber in a particular physical environment. For example, CH_5^+ is a highly fluxional molecule, which has evaded spectral assignment. The first spectrum was recorded in 1999,[14] and it remains unassigned today. There has been substantial theoretical work to understand the molecule, but *ab initio* calculations are difficult.[50, 51, 52, 53, 54, 56, 57] Likely the best calculation is by Wang and Carrington which is limited to only the vibrational energy levels.[55] Recently, the Schlemmer group has made high precision frequency measurements of the CH_5^+ infrared spectrum at 4 K and 10 K.[15] In this experiment, they create a combination difference spectrum by subtracting all possible pairs of transitions and binning them together. As coincidences rose out of the noise, they were attributed to rotational energy level spacings by noting whether a combination was observed at the lower temperature or the higher temperature. This approach is purely statistical and would be dramatically improved if saturation spectroscopy was used instead. Saturation spectroscopy would provide access to invaluable information about the transition dipole, which would be useful in the efforts to assign the

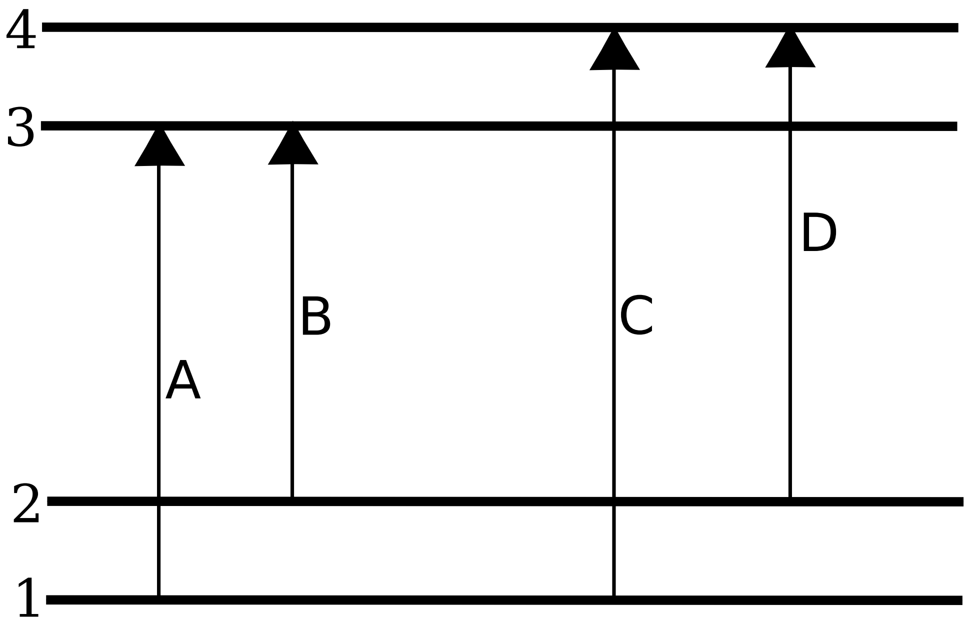

Figure 5.1: A diagram of a four-line combination difference. The image depicts a set of four transitions (labeled A through D) between energy levels 1 through 4. The difference in energy between A and B results in the energy level spacing between 1 and 2. This is also true for C and D. When the transitions are not assigned, pairs of these transitions that return the same energy difference likely result in a real energy level spacing.

transitions.

In contrast to the coincidence spectrum approach, another method is to use four-line combination differences. Figure 5.1 demonstrates how four independent transitions can be used to gain information about energy level spacings. Four line combination differences rely on a pair of transitions that share an energy level. For example, the transitions labeled A and B share level 3. The difference in energy between A and B is the energy level spacing between 1 and 2. Because C and D also share an upstairs level (number 4), and they share the same original levels as A and B, they can also be used to calculate the energy level spacing between 1 and 2. The energy spacing between 3 and 4 can be calculated by the difference of the pairs A-C and B-D. Without *a priori* knowledge of the transition assignment, a single combination difference cannot be trusted to determine a single energy level. Any two transitions can be subtracted from each other. With a pair of combination differences there is greater confidence that the energy level spacing is real. The limitation of this approach is that it requires incredibly small uncertainties to avoid false positives, which may be challenging due to the unusually high density of states within CH_5^+.

With a four-line combination difference analysis, information about the transition dipole can be used to rule out false positives. If we can normalize the intensities of the observed transitions by a measured dipole, then we determine the product of the of the energy level's degeneracy and the Boltzmann factor of that state, assuming thermal equilibrium. The product of the degeneracy and the Boltzmann factor is a unique identifier for any given energy level. Assuming that the uncertainties are sufficiently small on these determined parameters, they can be used in concert with combination differences to rule out false positives. However, before we can determine any information about the transition dipole, we must understand how the degree of saturation affects the lineshape.

When light, resonant with an allowed transition, interacts with an ensemble of molecules, there are two processes that can occur. A photon can be absorbed and the molecule can be promoted to a higher energy quantum state, or a photon can stimulate emission of a second photon resulting in a demotion to a lower energy quantum level. The probability of absorption versus emission is proportional to the number of molecules in each state. As the number of photons that interact with the ensemble increase, more molecules are promoted to the higher energy level, which means that stimulated emission becomes more probable. This means that as the intensity of the light is increased, the ensemble becomes transparent to the light, *i.e.* it is equally likely that a photon is absorbed or stimulates an emission.

In order to quantitatively understand saturation (non-linear absorption), master equations describing a two-level system are constructed which account for the absorption, emission, and relaxation.[86, 87] The results from steady-state solutions are incredibly useful for determining the effect of saturation on linewidth and absorption coefficient. Ultimately, the relevant parameter defined by solutions to master equations is S, called the saturation parameter.[86] It is defined in Equation 5.1.

$$S(\omega) = \frac{2\sigma(\omega)I(\omega)}{\hbar\omega\Gamma} \tag{5.1}$$

The parameters in Equation 5.1 are intensity (I), transition cross section (σ), angular frequency (ω), and relaxation rate (Γ). The processes that contribute to Γ are completely dependent on the particular system of interest and the experimental configuration. For homogeneously broadened lines, the absorption coefficient ($\alpha(\omega)$) of the line, and therefore the lineshape, is governed by Equation 5.2 which is derived by Demtröder.[86]

$$\alpha(\omega) = \frac{\alpha_0(\omega)}{1 + S(\omega)} \tag{5.2}$$

The unsaturated absorption coefficient, α_0, is effectively scaled by the saturation parameter. This equation succinctly captures the transparency behavior of a saturated transition. As the saturation parameter approaches infinity, the absorption coefficient approaches zero. Scaling the absorption depth however is not the only pertinent effect of saturation on homogeneously broadened transitions. It also broadens them. This is referred to as power broadening. This arises as a result of driving oscillations of the population between the two levels and shortening their lifetimes. Functionally this takes the form

$$\gamma_s = \gamma\sqrt{1 + S_0} \tag{5.3}$$

where $S_0 = S(\omega_0)$ is the saturation parameter at the resonance frequency of the transition, γ_s is the saturation linewidth, and γ is the unsaturated linewidth.

The case for an inhomogeneously broadened line is also derived by Demtröder.[87]. The absorption coefficient is given by Equation 5.4 as

$$\alpha(\omega) = \frac{\alpha_0(\omega)}{\sqrt{1 + S_0}}. \tag{5.4}$$

Similar to the homogeneously broadened case, the absorption coefficient is reduced to zero as the saturation parameter goes to infinity. As a result of there being no additional broadening mechanisms in the inhomogeneous case, the transition profile shape is only attenuated by a fixed amount that is determined by the value of the saturation parameter on resonance (S_0). There is no change in the linewidth as a result of saturation for inhomogeneous broadening. A simple way to conceptualize why there is no additional broadening is to consider Doppler broadening. When a molecule absorbs a photon there is only a very small change in momentum. Given the speeds that these species are traveling, absorption only minimally affects the overall momentum distribution. Therefore, there is no large change in the inhomogenous linewidth of the molecules. This is especially true when considering that the molecules are in thermal contact with some other part of the experimental apparatus.

These equations represent the simplest, textbook scenarios for saturation, but with techniques such as NICE-OHMS and NICE-OHVMS which rely on frequency modulation, extra care must be given to properly describe the recorded signal and how it depends on the saturation parameter. A complete description of the NICE-OHMS lineshapes was published in 2007 and describes both the absorption and the dispersion signals that are detected by this technique.[79] NICE-OHMS is a frequency modulation technique, so the detected signal is generated by recording the difference in beat note amplitude for absorption, and the relative phase shift of each component of the fm-triplet for dispersion. The unsaturated signal from absorption is

$$S_{abs} = \eta\frac{2F}{\pi}J_0(\beta)J_1(\beta)P_0\alpha L[\chi_{abs}(\nu_d - \nu_H) - \chi_{abs}(\nu_d + \nu_H)]. \tag{5.5}$$

The absorption coefficient (α), initial power (P_0), interaction length (L), finesse (F), and instrument gain (η) are used to calibrate the intensity of the absorption. The product of Bessel functions ($J_0(\beta)J_1(\beta)$) converts the carrier power into a beat note power. The transition profile (χ_{abs}) is a Voigt profile with a frequency detuning axis (ν_d). The recorded signal is a superposition of two out-of-phase transition profiles offset by plus and minus the heterodyne modulation frequency (ν_H). Similarly, the detected dispersion signal is given by

$$S_{disp} = \eta \frac{2F}{\pi} J_0(\beta) J_1(\beta) P_0 \alpha L [\chi_{disp}(\nu_d - \nu_H) - 2\chi_{disp}(\nu_d) + \chi_{disp}(\nu_d + \nu_H)]. \tag{5.6}$$

There are two major differences between absorption and dispersion. The first is the sensitivity of dispersion to the carrier portion of the triplet, which is represented by the term: $-2\chi_{disp}(\nu_d)$. The second is that χ_{disp} is the Kramers-Kronig transform of χ_{abs}.

The effect of saturation on the transition profile was presented for the NICE-OHMS case by Ma *et al.*[80] The carrier and two sidebands have three individual intensities and are responsible for recording different parts of the transition profile, they must be considered individually. As such, the saturation parameter for the jth component of the triplet (G_j) is written as

$$G_j = \frac{2\mu^2 I}{3c\epsilon_0 \hbar^2 \Gamma^2} J_j^2(\beta) \tag{5.7}$$

where μ is the transition dipole moment, c is the speed of light, and ϵ_0 is the permittivity of free space. This is effectively equivalent to Equation 5.1 multiplied by the appropriate Bessel function to account for the intensity of the sideband. Together, this means that Equations 5.5 and 5.6 must now be written as

$$S_{abs} = \eta \frac{2F}{\pi} J_0(\beta) J_1(\beta) P_0 \alpha L [\chi_{abs}^{sat}(\nu_d - \nu_H, G_{-1}) - \chi_{abs}^{sat}(\nu_d + \nu_H, G_1)] \tag{5.8}$$

and

$$S_{disp} = \eta \frac{2F}{\pi} J_0(\beta) J_1(\beta) P_0 \alpha L [\chi_{disp}^{sat}(\nu_d - \nu_H, G_{-1}) - 2\chi_{disp}^{sat}(\nu_d, G_0) + \chi_{disp}^{sat}(\nu_d + \nu_H, G_1)] \tag{5.9}$$

respectively, where

$$\chi_{abs}^{sat} = \frac{1}{\sqrt{1 + G_j}} \chi_{abs} \tag{5.10}$$

and

$$\chi_{disp}^{sat} = \chi_{disp}. \tag{5.11}$$

The important result by Ma *et al.* is that only the intensity of absorption is reduced by saturation but that is not the case in dispersion.[80] This can be deceptive though because power broadening is still a factor in the lineshape. The two components in absorption are governed by the same value of saturation parameter, $G_{\pm 1}$ but in dispersion, the homogenous linewidth of the central component must be wider than the two sideband components because $G_0 > G_{\pm 1}$.

Equations 5.8 and 5.9 are a complete description of the NICE-OHMS Doppler broadened lineshape, but they do not form a complete summary of all the processes that occur in a saturation experiment. By using a cavity enhanced technique, the counter-propagating beams will act as a pump-probe experiment when they probe molecules within the same velocity component of the Doppler profile. The effect of this experimental configuration is an increase in the effective intensity. This will increase the saturation parameter for a given velocity component. This burns a hole in the population of the lower level and is recorded as a Lamb dip in the Doppler profile. The peak-to-peak signal of that Lamb dip can be used as a probe of the saturation parameter. In the case of absorption the peak-to-peak signal is described by

$$\delta_{pp} = \alpha_0 \left(\frac{1}{\sqrt{1+S}} - \frac{1}{\sqrt{1+2S}} \right). \tag{5.12}$$

In the case of weakly saturated transitions, the Lamb dips resulting from dispersion also follow this expression divided by two.[88, 89] However, the Kramers-Kronig relations do not hold true under optically saturated conditions so Axner *et al.* derived an expression specifically for dispersion:[89]

$$\phi_{pp} = \frac{\alpha_0}{2} \left(\frac{0.45S}{1+S} \right). \tag{5.13}$$

These Lamb dip depths are derived using three important assumptions.[89] The first is that coherences between the two excitations can be neglected. This means that the effect of the counter-propagating beams are considered to be a superposition of two separate optical events, one contribution from each wave. The second assumption is that the molecules interact with the average intracavity field. In other words, the varying intensity along the z-axis of the cavity as a result of optical resonances are not important. This is a good assumption due to the speed of the molecules being sufficiently large as to make the time it takes to travel half a wavelength is shorter than the excitation/deexcitation rate. Finally, the system is assumed to be in steady state which is justified because of the number of collisions molecules experience during traversal of the laser beam.[89]

Together Equations 5.8, 5.9, 5.3, 5.7, 5.12, and 5.13 describe NICE-OHMS saturation. The case for NICE-OHVMS is no different. NICE-OHVMS is identical to NICE-OHMS except that it incorporates an additional layer of modulation. Essentially, these equations are still applicable. One complication is that the recorded Lamb dips in NICE-OHVMS are concentration modulated. However, the contour of the lineshape is not expected to change but the intensity may change as a result of concentration modulation. So long as it is not dependent on the optical power, which seems unlikely, the only limitation will be that exact values of the absorption coefficient cannot readily be determined.

5.2 Proposed Experiment

The goal of this experiment is straightforward; the validity of the saturation models for NICE-OHMS need to be confirmed for NICE-OHVMS. Then with confirmation, several transitions with known transition dipole moments should be measured at different power levels. There are several parameters that need to be carefully measured and controlled throughout the experiment. The instrument gain must be correctly determined in order to properly calibrate the intensity axis. The finesse and coupling efficiency are also to be determined in order to determine the intracavity power. Because the intracavity power must be known, it is necessary to measure the power incident on the cavity. Also, the modulation index, β, needs to be measured before the work can proceed.

The choice of target is clear, H_3^+. It is the simplest molecule that can be generated in a AC modulated positive column. It only requires hydrogen in the discharge. Due to the simple set of chemical reactions that generate H_3^+, it is created in large abundances. From the standpoint of fundamental physics, a great deal is known about it, including the transition dipole moment for each transition in the fundamental band.[39, 90]

For a given transition with known transition dipole moment, a scan should be performed at many different laser intensities. This can be accomplished by either reducing the power incident on the cavity, by spoiling the finesse, or by spoiling the coupling efficiency. Given the available equipment,[2, 26] a combination of the three approaches may need to be performed to adequately sample different saturation parameters. It is necessary to calibrate the frequency axis due to the large hysteresis in the piezoelectric transducer that stretches the fiber to scan the seed laser, in order to ensure a linear axis.

This process is repeated for several transitions. Strong transitions with high signal-to-noise ratios for Lamb dips are R(1,0), R(1,1)^u, and R(3,0), therefore they will make the best targets.

5.3 Expected Results

After recording all of the required spectra, each must be fit to the Doppler profile model described in Chapter 4. The Lamb dips must be fit as has been previously demonstrated.[2, 26] After the fitted parameters are obtained, they may be used to determine the saturation power. The saturation power is defined by its relation to the saturation parameter,

$$S = \frac{P}{P_{sat}}. \tag{5.14}$$

Acquiring spectra at different intracavity powers allows us to calculate the saturation power, which is proportional to the squared ratio of the transition dipole moment to the relaxation rate. Accessing that ratio is the primary goal of this proposed work, and it is convenient to combine all the parameters that define the saturation parameter but power into a single term, P_sat. This encodes all the relevant molecular information including the transition dipole moment.

I propose three different approaches to try to determine the saturation power. The first uses the transition intensities of the absorption and dispersion signals; the ratio of the absorption intensity to the dispersion intensity can be used to determine the saturation parameter. The second method that can be used is to measure the Lamb dip peak-to-peak values. The absorption and dispersion intensities of the Lamb dips follow unique trends as a function of saturation parameter. Together, they can be used to adequately determine saturation power. The final approach is to examine the ratio of the power broadened homogeneous linewidth measured by the central component of the dispersion Doppler profile to the power broadened homogeneous linewidth of one of the components measured by the sidebands.

Regardless of the method used, the known values of the transition dipole moment should be used to determine how strong the state specific contribution to the relaxation rate is. In an environment with many collisions, such as velocity modulation spectroscopy (VMS), it may be that there is a relatively flat relaxation rate determined by the collisional environment.

5.3.1 Determination of Saturation Parameter by Doppler Height

By extracting the fitted intensity from the absorption signal and comparing it to the intensity of one of the sideband components from the dispersion signal, the saturation parameter for a given power can be determined. After plotting the ratio of the intensity against the intracavity power, a fit can be performed with the function

$$y = \frac{1}{\sqrt{1 + kP}}. \tag{5.15}$$

Only one parameter is floated, k, which is the inverse of the saturation power (P_{sat}^{-1}). P is the intracavity power. Examples of the expected trend are displayed in Figure 5.2. As k is increased, the curve becomes deeper, and the transition becomes transparent more rapidly. This relationship relies on the dispersion transition intensity not changing as a function of optical power. To extract the ratio of the transition dipole from the inverse saturation power, k, we must use this relation:

$$k = \frac{3c\epsilon_0\hbar^2(\pi r_0^2)}{2J_j(\beta)^2}\frac{\Gamma^2}{\mu^2} \tag{5.16}$$

To derive this equation, two additional assumptions are made. The first is that the beam cross section is circular, and the second is that the column of light in the cavity is described by a cylinder of radius equal

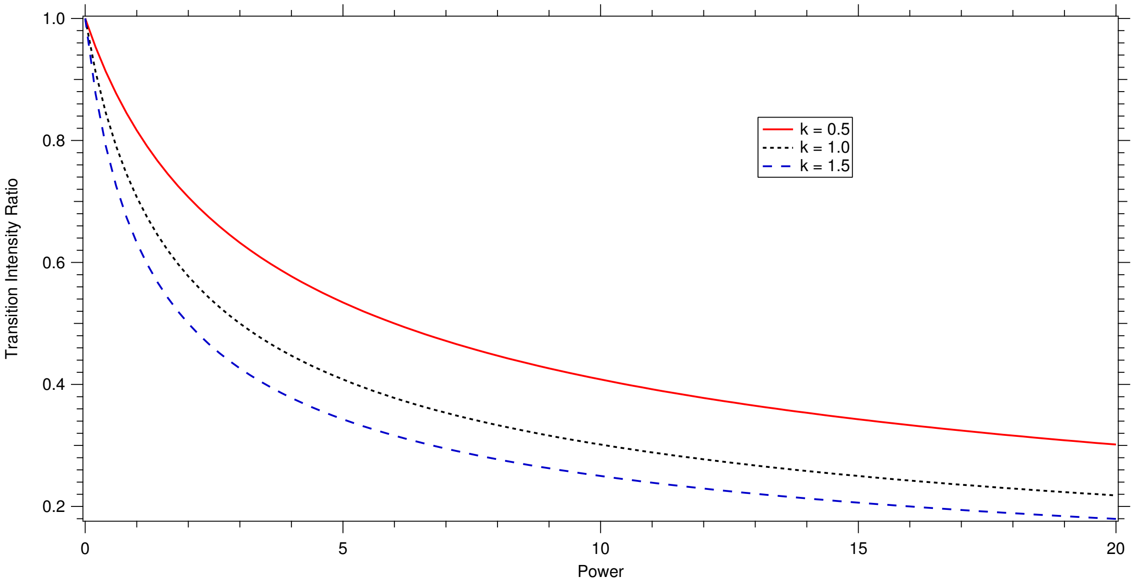

Figure 5.2: The ratio of the absorption transition intensity to the dispersion transition intensity plotted as a function of power (in arbitrary units). Different saturation powers are displayed. At no optical power, there is no saturation, and as the power is increased infinitely, the transition becomes transparent. As the value of k is increased the ratio approaches zero.

to the beam waist (r_0). Equation 5.16 is derived by combining Equation 5.14 with Equation 5.7 and solving for k. The main challenges of this approach are ensuring the quality of the fits is adequate. It should be relatively insensitive to systematic errors in estimates of any other fit parameters so long as both the absorption and the dispersion fits return the same values. The precision of the fits should be the limiting uncertainty in the determination of saturation power.

5.3.2 Determination of Saturation Parameter by Lamb Dip Depth

The determination of the saturation power by estimating the Lamb dip depth is the second approach. The approach is similar. The scans must be fit, and the Lamb dip peak-to-peak must be plotted as a function of the power. In this case, absorption and dispersion are treated separately. The fitting expression for absorption is

$$y = A\left(\frac{1}{\sqrt{1+kP}} - \frac{1}{\sqrt{1+2kP}}\right). \tag{5.17}$$

Though this fit is a two parameter fit, it should be well determined, provided there are sufficient data. The expected trends are displayed in Figure 5.3. As the inverse of the saturation power (k) is increased, the peak depth that can be achieved is shifted to lower intracavity powers. The same assessment should then

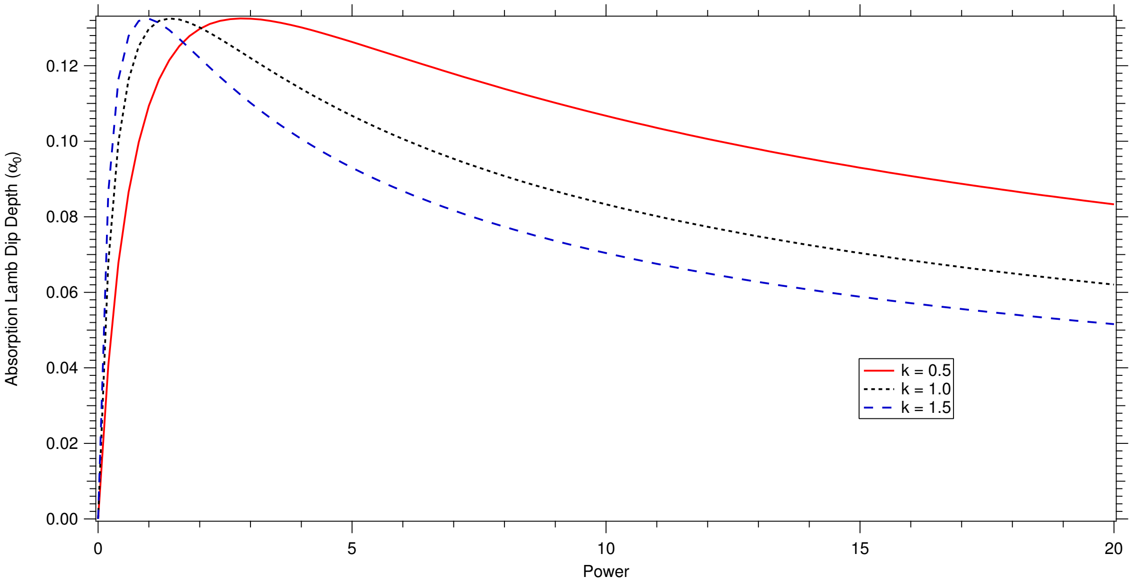

Figure 5.3: Absorption Lamb dip depth as a function of power (in arbitrary units). The maximum depth a Lamb dip can achieve is $\sim 0.1325\alpha_0$. The power required to achieve maximum depth depends on the saturation power. Smaller saturation powers (greater values of k) cause the trend to peak at lower intracavity powers.

be performed with the dispersion data. In that case, the fit equation is

$$y = A\left(\frac{0.45kP}{1+kP}\right). \tag{5.18}$$

The expected trends for the dispersion data are displayed in Figure 5.4. In the case of dispersion, decreasing the saturation power causes the peak-to-peak signal of the Lamb dip to approach the asymptote more rapidly. For either case, the ratio of the dipole to the relaxation rate is determined by the fitted value of k. One advantage to this approach is that the two trends can be simultaneously fit with shared A and k values. Simultaneous fitting would provide additional precision on the determined values. A possible drawback is that the fitted Lamb dips, as demonstrated up to this point by experiment, are not resolved, which may provide some uncertainty in the fitted parameter. As in the Doppler broadened case, if those errors are predominantly systematic in the same way, only the magnitude of A should be affected as the curvature of the fit would not be affected. The curvature is what determines k.

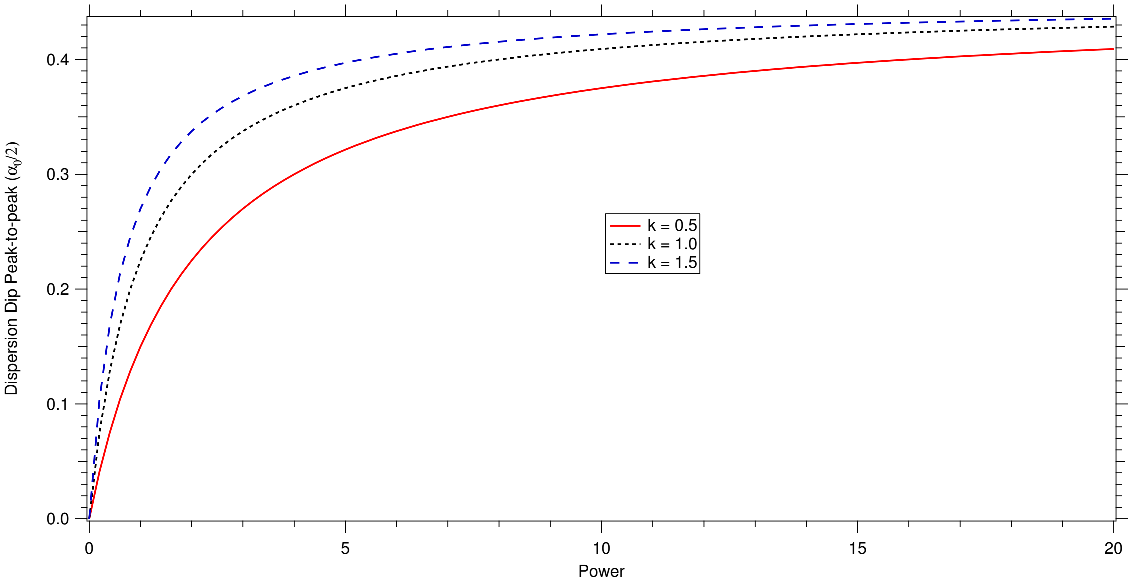

Figure 5.4: Dispersion Lamb dip peak-to-peak as a function of power (in arbitrary units). The dispersion never achieves a maximum and instead asymptotically approaches $0.45\alpha_0/2$. Decreasing the saturation power (increasing the value of k) causes the peak-to-peak signal to approach it's maximum value more rapidly.

5.3.3 Determination of Saturation Parameter by Dispersion Linewidth Broadening

The final proposed method for determining the saturation parameter is accomplished by only examining dispersion data. Equation 5.9 shows that there are three Doppler components whose individual degrees of saturation derive from which component of the triplet is sampling the lineshape. The sidebands have a saturation parameter G_1; whereas, the central component has a saturation parameter G_0. Equation 5.3 shows that the amount of homogeneous line broadening increases with increasing saturation parameter. We can write an equation for the ratio of of linewidths that depends on the saturation parameters,

$$\frac{\gamma_{s0}}{\gamma_{s1}} = \frac{\gamma\sqrt{1+G_0}}{\gamma\sqrt{1+G_1}}. \tag{5.19}$$

The only difference between G_0 and G_1 is that the first is S multiplied by $J_0(\beta)^2$ and the second is S multiplied by $J_1(\beta)^2$. This means that we can rewrite the Equation 5.19 as

$$\frac{\gamma_{s0}}{\gamma_{s1}} = \frac{\sqrt{1+SJ_0(\beta)^2}}{\sqrt{1+SJ_1(\beta)^2}}. \tag{5.20}$$

Solving for S and defining the ratio of power broadened lines as $\rho = \frac{\gamma_{s0}}{\gamma_{s1}}$ gives

$$S = \frac{\rho^2 - 1}{J_0(\beta)^2 - \rho^2 J_1(\beta)^2} = kP. \tag{5.21}$$

By determining the difference in homogenous linewidth between the two components, the saturation power can be determined and the transition dipole moment can be calculated. This approach is the most interesting, but it is also the most difficult. It relies on having a large homogeneous contribution to the linewidth, which VMS spectra tend to have. However, it may prove difficult to exactly determine the individual linewidths for the central dispersion component given it is overlapped with other components from the heterodyne modulation. Furthermore, the VMS modulation would likely complicate the lineshape by smearing out the centeral part of the line in the low modulation limit. Additionally, the systematic errors cannot be canceled out because it is a ratio approach. Nevertheless, if only dispersion data were available, this method would provide an estimate of the dipole.

5.4 Conclusion

Three different methods for determining the ratio of the transition dipole moment to the relaxation rate were described. If the relaxation rate is relatively independent of the quantum state, then it is feasible to apply this approach to CH_5^+ to rule out false positives in a data set comprised of combination differences. In most treatments of relaxation rates, the experimental configuration is what predominantly determines relaxation rates. In saturation studies it is more typical to be concerned with pressure broadening and transit time broadening.[80] In the case of pressure broadening predicted by the Langevin model there is no quantum dependence.[74] More importantly, the homogeneous linewidth model developed for VMS and presented in Chapter 3 is the dominant relaxation process in NICE-OHVMS, and it has no state dependence. Ultimately, extracting information about the transition dipole moments from the saturation power would represent a significant advancement in the field and greatly assist the assignment of CH_5^+.

Appendix A

Sub-Doppler Mid-infrared Spectroscopy of Molecular Ions

This appendix is a complete reprint with permission from Kyle N. Crabtree, James N. Hodges, Brian M. Siller, Adam J. Perry, Joseph E. Kelly, Paul A. Jenkins II, Benjamin J. McCall. Chemical Physics Letters, 551 (2012) 1-6, Copyright Elsevier 2012.

Chemical Physics Letters 551 (2012) 1–6

Contents lists available at SciVerse ScienceDirect

Chemical Physics Letters

journal homepage: www.elsevier.com/locate/cplett

FRONTIERS ARTICLE

Sub-Doppler mid-infrared spectroscopy of molecular ions

Kyle N. Crabtree [a,1], James N. Hodges [a], Brian M. Siller [a], Adam J. Perry [a], Joseph E. Kelly [a], Paul A. Jenkins II [a], Benjamin J. McCall [a,b,*]

[a] *Department of Chemistry, University of Illinois, Urbana, IL 61801, USA*
[b] *Departments of Astronomy and Physics, University of Illinois, Urbana, IL 61801, USA*

ARTICLE INFO

Article history:
Available online 15 September 2012

ABSTRACT

The technique of velocity modulation spectroscopy has recently been combined with cavity enhancement and frequency modulation methods into a technique called noise-immune cavity-enhanced optical heterodyne velocity modulation spectroscopy (NICE-OHVMS). We have implemented NICE-OHVMS with a cw-optical parametric oscillator (OPO) tunable from 3.2 to 3.9 μm, and used it to record spectra of the $R(1,0)$ and $R(1,1)^u$ transitions of the ν_2 fundamental band of H_3^+. The high optical power and cavity enhancement enable saturation of rovibrational transitions, which allows for line center frequencies to be measured with a precision of 70 kHz.

1. Introduction

Molecular ions play a key role as intermediates in chemical reactions, and a detailed understanding of their structure and intramolecular dynamics in the gas phase, generally obtained by spectroscopy, is a critical first step toward understanding their behavior in more complicated systems. The primary technique used for ion spectroscopy over the past 30 years has been velocity modulation spectroscopy (VMS) [1,2]. In VMS, ions are produced in an AC positive column plasma whose polarity is alternated at frequency f_{vm}. The average drift velocity of the ions in the plasma is shifted toward the cathode from the applied electric field, while neutral molecules are generally unaffected. As the polarity is reversed, the average ion drift velocity also reverses, resulting in a periodic oscillation in the ion velocity distribution at f_{vm}. By interrogating the ions with a laser beam passing in one direction through the plasma, the absorption profiles are alternately red- and blue-shifted with respect to their rest frequencies, and phase-sensitive detection at f_{vm} allows for selective retrieval of ionic signals. VMS therefore addresses one of the main challenges of ion spectroscopy, i.e., detection of ionic species that are only $\sim 10^{-5}$–10^{-6} as abundant as neutral molecules. Well over 40 unique molecular ions (not including isotopologues) have been detected with VMS; these have been extensively reviewed by Stephenson and Saykally [3].

Recently, the use of a Fabry–Perot optical cavity to enhance the optical path length was demonstrated by Siller et al. (cavity-enhanced velocity modulation spectroscopy, CEVMS), who locked a Ti:Sapphire laser to an optical cavity surrounding a velocity modulated positive column cell and detected the transmitted light [4]. Because the light in the cavity is bidirectional, red and blue Doppler shifts are simultaneously superimposed, encoding the velocity modulation (VM) signal at $2f_{vm}$. Initially, this was believed to be problematic because any neutral molecules produced or excited by the discharge are concentration modulated (CM) at $2f_{vm}$; that is, the population of the excited species varies with the magnitude of the applied voltage, but not the sign of the voltage. By also encoding the ion signal at $2f_{vm}$, it was thought the concentration modulation signal of neutral molecules would overwhelm the ion velocity modulation signal. Siller et al. showed that the ion and neutral signals occurred at different phases with respect to the plasma voltage, thereby preserving ion-neutral discrimination through phase-sensitive detection. Additionally, the power enhancement from the optical cavity enables saturation spectroscopy and precise line-center determination [5]. A related technique has also been employed using an optical frequency comb as the light source and a unidirectional ring cavity surrounding a plasma cell, effectively converting VMS to a broadband technique while preserving the high resolution of laser spectroscopy [6].

Cavity enhanced absorption spectroscopy suffers from the fact that frequency noise in the laser is directly converted into intensity noise as a result of reduced cavity transmission. This limitation was overcome by Ye et al. with noise-immune cavity-enhanced

---

* Corresponding author at: Department of Chemistry, University of Illinois, Urbana, IL 61801, USA.

E-mail addresses: kcrabtr2@illinois.edu (K.N. Crabtree), jnhodge@illinois.edu (J.N. Hodges), bsiller2@illinois.edu (B.M. Siller), aperry10@illinois.edu (A.J. Perry), bjmccall@illinois.edu (B.J. McCall).

URL: http://bjm.scs.illinois.edu (B.J. McCall).

[1] Present address: Harvard-Smithsonian Center for Astrophysics, Cambridge, MA 02138, USA.

0009-2614/$ - see front matter © 2012 Elsevier B.V. All rights reserved.
http://dx.doi.org/10.1016/j.cplett.2012.09.015

optical heterodyne molecular spectroscopy (NICE-OHMS) [7]. In this technique, the laser is phase modulated at f_h (typically ~100s of MHz), effectively generating an FM triplet consisting of a carrier (at the optical frequency f_o) and a pair of sidebands with opposite phase at $f_o \pm f_h$. The triplet is coupled into the optical cavity by setting f_h equal to an integer multiple of the cavity free spectral range (FSR). In the absence of any intracavity absorption or dispersion, the beat notes between each sideband beating with the carrier are balanced in both amplitude and phase, so there is no net signal at f_h. However, in the presence of an intracavity absorber or disperser, the beat notes are unbalanced in amplitude and/or phase, yielding a net signal. By encoding absorption/dispersion information at a high frequency, $1/f$ technical noise is reduced. Another advantage is that any laser frequency noise affects the cavity coupling efficiency of the carrier and both sidebands equally, which keeps the beat notes of each sideband with the carrier balanced, and eliminates direct conversion of laser frequency noise to noise in the final spectrum. The disadvantages are the complexity of the technique, particularly the demands of maintaining the laser-cavity lock, and the requirement of a detector whose bandwidth is at least f_h. An extensive review of the NICE-OHMS technique has been published by Foltynowicz et al. [8].

CEVMS and NICE-OHMS have been combined into a technique called noise-immune cavity enhanced optical heterodyne velocity modulation spectroscopy (NICE-OHVMS) in the near-infrared with a Ti:Sapphire laser [9]. Because f_h and f_{vm} are at significantly different frequencies (typically ~100 MHz and ~10 kHz, respectively), the detector signal is first demodulated at f_h, and then sent on to further phase-sensitive detection at $2f_{vm}$. NICE-OHVMS preserves the ion-neutral discrimination afforded by VMS, and takes advantage of the ultra-high sensitivity, saturation, and noise immunity of NICE-OHMS.

However, the technical demands of the NICE-OHMS technique have largely precluded its use in the mid-infrared spectral region in which VMS has been successfully exploited. The high bandwidth detectors and phase modulators required for NICE-OHMS are not as readily available in the mid-IR compared with the visible/near-IR. The only published mid-IR NICE-OHMS work was done with a quantum cascade laser near 8.5 μm, and was limited by the detector bandwidth and the phase modulation characteristics of the device [10]. Work is currently underway in our laboratory to extend NICE-OHMS into the mid-IR using a difference frequency generation (DFG) source in the 3–5 μm region [11], which is particularly attractive for a general-purpose ion spectrometer because the vast majority of molecules have at least one fundamental vibrational band in that portion of the spectrum.

Here we report the first mid-IR NICE-OHVMS spectrometer, which uses a commercially available cw-optical parametric oscillator (OPO) tunable from 3.2 to 3.9 μm. The high optical power of the OPO (~1 W) allows for use of high bandwidth mid-IR detectors that are not sensitive enough to be used with many other lower-power cw lasers in this region. This technique enables all of the advantages of the NICE-OHVMS technique to be brought to bear on fundamental vibrational transitions of molecular ions, including high precision sub-Doppler spectroscopy.

Our initial demonstration of this instrument focuses on the study of H_3^+, which is the simplest polyatomic molecular ion and serves as the primary initiator of ion–molecule chemistry in interstellar clouds [12,13]. Its infrared spectrum was first observed by Oka in 1980 [14], and since then it has been extensively studied spectroscopically (see, for instance, the review in Ref. [15]). More recent research on H_3^+ focuses on spectroscopy above the so-called "barrier to linearity," at which point the molecule adopts a linear geometry that induces a singularity in the Hamiltonian, complicating its theoretical treatment [16]. Nevertheless, for the lowest-lying energy levels, the agreement between experiment and ab initio theory is good to spectroscopic accuracy [17]. Measuring the energy level spacings experimentally with higher precision and accuracy would present a greater challenge for ab initio theory, possibly spurring new developments. The NICE-OHVMS technique opens the possibility of measuring such energy level spacings in H_3^+.

As a demonstration of the capabilities of this instrument, we present in this Letter spectra of the ν_2 fundamental band of H_3^+ at 3.67 μm. In Section 2 we describe the instrumental details, and in Section 3 we discuss NICE-OHVMS lineshapes and present spectra acquired with the instrument. Finally, in Section 4, the performance of the instrument is assessed, and future directions are discussed.

2. Experimental details

Our NICE-OHVMS instrument is outlined in Figure 1. A Ytterbium-doped fiber laser (YDFL, Koheras Adjustik Y-10) is sent through a fiber EOM (EOSPACE PM-0K5–00-PFU-PFU-106-S), amplified (IPG Photonics YAR-10 K-1064-LP-SF), and used to pump a singly-resonant OPO (Aculight Argos 2400 SF). The pump (1.064 μm) and signal (1.5–1.6 μm) beams are sent to a wavemeter (Burleigh WA-1500) for frequency calibration. The idler (3.2–3.9 μm) is locked with the Pound-Drever-Hall (PDH) technique to a 1.9-m-long optical cavity consisting of two 1 m radius of curvature concave Si mirrors dielectric coated for 99.7% reflectivity over 3.1–3.4 μm surrounding a plasma cell. Cavity reflection and transmission are monitored by photodiodes (Boston Electronics Vigo PVM-10.6-1x1) with an effective bandwidth of ~125 MHz.

Heterodyne and PDH sidebands are generated by applying voltages at their respective frequencies to the fiber EOM on the seed laser simultaneously. The resultant frequency spectrum of the pump laser is imprinted on the idler beam. A PDH error signal used for cavity locking is generated by demodulating the cavity reflection signal at the frequency RF1 (typically 2–20 MHz). The error signal is sent to feedback electronics which stabilize the length of the cavity on slow timescales via a piezoelectric transducer (PZT) attached to one of the cavity mirrors, and apply fast corrections to the idler frequency by a PZT mounted to one of the signal cavity mirrors inside the OPO head. The cavity transmission detector signal is sent to a pair of mixers ~90° out of phase with one another, and each is demodulated at frequency RF2 (equal to the cavity FSR of 79.12 MHz). The overall phase of the heterodyne detection is adjusted by phase shifting the RF signal driving the EOM using cables of appropriate lengths. The demodulated signal from each mixer is then sent to a lock-in amplifier referenced to twice the frequency used to drive the plasma, and the in-phase and quadrature outputs of each amplifier are digitized and stored on a computer.

Ions are produced in a liquid-nitrogen-cooled multi-inlet multi-outlet positive column discharge cell, which is placed between the two free-standing mirrors of the optical cavity [18]. Intracavity radiation is admitted into the cell by means of CaF_2 windows aligned at Brewster's angle. The plasma is driven by a 40 kHz sine wave voltage produced by amplifying the output of an arbitrary waveform generator with an audio amplifier (Techron 7780) and a step-up transformer. H_3^+ was produced at a pressure of 200 mTorr and a discharge current of 170 mA. The outputs of the two mixers were each demodulated at 80 kHz with a lock-in amplifier set to a 10 ms time constant (16 Hz detection bandwidth).

Typical operation begins by filling the cooling jacket of the cell with liquid nitrogen and igniting the plasma. The cavity length is adjusted to bring it into resonance with the laser, and the laser-cavity lock is established. The idler frequency is tuned by applying a voltage to an internal PZT on the YDFL, and the cavity length is

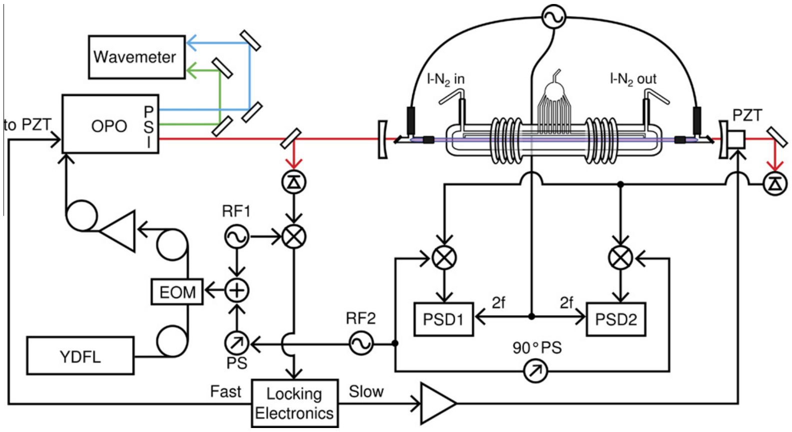

Figure 1. Block diagram of NICE-OHVMS instrument. Details of its operation are given in the main text. YDFL: Ytterbium-doped fiber laser; EOM: electro-optic modulator; OPO: optical parametric oscillator with pump (P, blue), signal (S, green) and idler (I, red) beams; PZT: piezoelectric transducer, PS: phase shifter; PSD: phase sensitive detector; •: signal splitter.

controlled with the locking electronics to maintain the resonance condition. When the cavity PZT reaches the end of its travel, the laser-cavity lock is electronically interrupted, the cavity length is reset to the other end of its travel, a new resonance is found, and the lock is reestablished. In this manner, the spectrometer can scan without manual intervention over the entire range of the YDFL PZT (around 100 GHz), although in practice a scan is generally much shorter. It is in principle possible to extend the automated tuning range further by electronic control of the intracavity etalon of the OPO and the nonlinear crystal position/temperature, but the practical utility of such efforts would likely be minimal.

3. Results and analysis

3.1. Lineshapes

The overall Doppler lineshape for NICE-OHVMS in both absorption and dispersion has odd symmetry, and qualitatively appears similar to the third derivative of a Gaussian absorption profile. A detailed analysis of the lineshape is beyond the scope of this Letter and will be the subject of a future work, but a qualitative description follows. Consider a general NICE-OHMS lineshape such as that shown in panels a and b of Figure 2 in Ref. [8]. If the signal belongs to an ion, then the AC voltage of the plasma causes velocity modulation (VM), Doppler shifting the lineshape at the plasma frequency. As a result of the bidirectional nature of light in our optical cavity, the lineshape is simultaneously Doppler shifted to the red and to the blue by the same amount at each point in time along the plasma voltage cycle. Consequently, the time-dependent signal repeats itself every plasma half-cycle, or at twice the AC plasma frequency ($2f_{vm}$). In addition to VM, an ion also experiences concentration modulation (CM) at $2f_{vm}$, and CM may be phase shifted with respect to VM. Thus, in addition to a periodic Doppler shift at $2f_{vm}$ from VM, the lineshape amplitude varies at $2f_{vm}$ from CM. The net signal observed comes in 4 channels corresponding to the even and odd second order Fourier coefficients of the absorption and dispersion profiles affected by VM and CM.

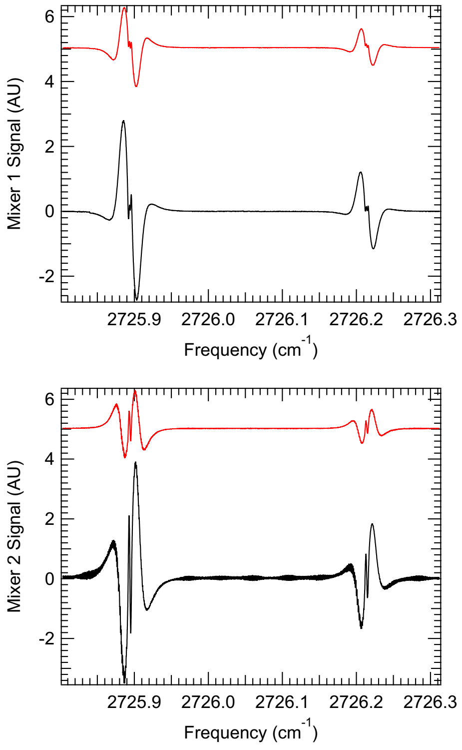

Figure 2. NICE-OHVMS spectrum of the $R(1,0)$ and $R(1,1)^u$ transitions of the ν_2 fundamental band of H_3^+. Each panel shows the in-phase (black, bottom) and quadrature (red, top) outputs of a lock-in amplifier demodulating the indicated mixer's signal.

The sub-Doppler lineshape is more straightforward. As has been discussed in regard to previous NICE-OHMS setups [19,20,9], the carrier and sidebands can each act as pumps and probes for saturation spectroscopy. The Lamb dips arising from the Bennet holes burned in the population appear at half-integer multiples of the carrier-sideband spacing f_h, i.e., at all frequencies at which forward- and reverse-propagating beams sample the same velocity component of the Doppler distribution. At the line center ν_0, when the zero-velocity distribution is both pumped and probed by the carrier, a signal only appears in dispersion as the heterodyne detection scheme employed by NICE-OHMS is insensitive to absorption of the carrier. In the current work, the heterodyne modulation index (β) is small enough (~0.63) that only the carrier has sufficient power to saturate transitions, while the sidebands can only act as probes. The dispersion signal therefore contains Lamb dips at ν_0 and $\nu_0 \pm f_h/2$, while the absorption signal contains them at $\nu_0 \pm f_h/2$.

While VM and CM have a strong influence on the lineshape of the Doppler profile, they do not affect the sub-Doppler features in the same way. Because Bennet holes are only burned in the population at or spaced evenly around the zero-velocity component of the ion distribution, VM effectively changes the abundance of ions with the appropriate velocity. In that way, VM effectively behaves like CM, and the net effect is to influence the amplitude of the Lamb dip lineshape and the relationship between the amplitudes of the even and odd Fourier coefficients within absorption or dispersion. Neglecting any change of the ions' collision rate with changing velocity, VM and CM do not affect the sub-Doppler profile beyond its amplitude. The sub-Doppler lineshape function [9] is

$$\chi(\nu_d) = \left(A_1\left[\chi_a\left(\nu_d - \frac{f_h}{2}\right) - \chi_a\left(\nu_d + \frac{f_h}{2}\right)\right]\right)\sin\theta_h + \left(-2A_0\chi_d(\nu_d) + A_1\left[\chi_d\left(\nu_d - \frac{f_h}{2}\right) + \chi_d\left(\nu_d + \frac{f_h}{2}\right)\right]\right)\cos\theta_h, \quad (1)$$

where ν_d is the frequency detuning from the transition center frequency, θ_h is the heterodyne detection phase, A_0 is the effective amplitude of the central (carrier-carrier) dispersion Lamb dip, and A_1 is the effective amplitude of the carrier-sideband Lamb dips for absorption and dispersion. $\chi_a(\omega)$ is a Lorentzian lineshape function for absorption, and $\chi_d(\omega)$ is a lineshape function for dispersion related to $\chi_a(\omega)$ by the Kramers–Kronig relations. These are defined as

$$\chi_a(\omega) = \frac{1}{1+\gamma^2(\omega-\omega_0)^2} \quad \text{and} \quad \chi_d(\omega) = \frac{-(\omega-\omega_0)\gamma}{1+\gamma^2(\omega-\omega_0)^2},$$

where ω_0 is the center and γ is the inverse of the half-width at half-maximum. When using this fit function, f_h is held at the cavity FSR (79.12 MHz), the amplitudes are constrained such that $A_0 > A_1$, and the Doppler profile near the line center is approximated by a third-order polynomial with the quadratic term set to 0.

3.2. H_3^+ Spectra

A sample spectrum of the $R(1,0)$ and $R(1,1)^u$ transitions of the ν_2 fundamental band of H_3^+ is shown in Figure 2. The signals in the top and bottom panels are the demodulated in-phase (black) and quadrature (red, offset) components of the two mixers, which in our setup we measure to be 96° out of phase with one another. The in-phase components of the $R(1,0)$ transition are shown in greater detail in Figure 3. The overall lineshape is slightly asymmetric; the blue side of the transition is stronger than the red side, particularly in mixer 2. The origin of this asymmetry is unknown, and its impact on the spectroscopic accuracy will be discussed below.

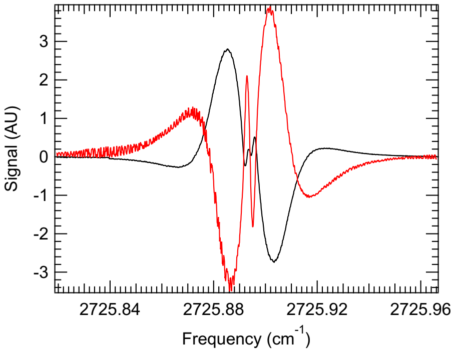

Figure 3. NICE-OHVMS spectrum of the $R(1,0)$ transition of the ν_2 fundamental band of H_3^+. The black trace is the in-phase output of mixer 1, and the red is the in-phase output of mixer 2.

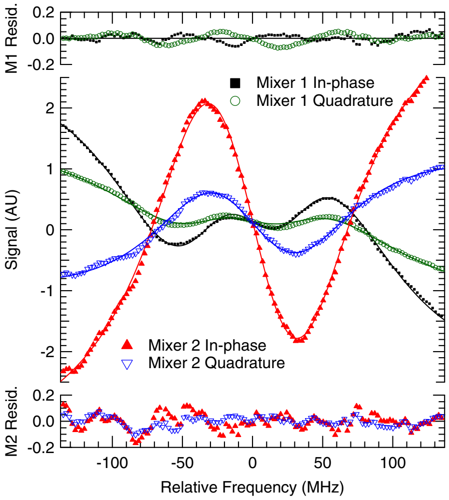

Figure 4. A simultaneous fit of the central sub-Doppler region of the H_3^+ $R(1,0)$ transition from all four data channels to Eq. (1). The symbols in the central portion of the graph are the data, and the solid lines are the fit results. The residuals of the fits are shown in the upper panel for mixer 1 and in the lower panel for mixer 2; in each case the symbols correspond to those in the central panel.

A simultaneous fit of the $R(1,0)$ sub-Doppler features in all four detection channels to Eq. (1) is shown in Figure 4. A number of constraints were employed to ensure that the fit parameters were all internally consistent. The line center frequency and Lamb dip width were forced to be equal for all four data channels. Mixers 1 and 2 were held at 96° apart, and the sideband spacing was held equal to the cavity FSR of 79.12 MHz. Because the in-phase and quadrature components of each mixer sample different blends of CM and VM, the Lamb dip amplitudes were allowed to be different for the in-phase channels and the quadrature channels. However, the two in-phase channels were forced to have equal Lamb-dip amplitudes, and likewise for the two quadrature channels. After all of these constraints, there are a total of 19 fit parameters for the entire data set: the line center frequency ν_0, the Lamb dip full width at half maximum ($2/\gamma$), the overall detection phase θ_h, Lamb dip amplitudes A_0 and A_1 for the in-phase channels and the quadrature channels, and baseline terms of the form $c_0 + c_1x + c_3x^3$ to approximate the central portion of the Doppler profile in each channel.

The overall quality of the fit is quite good; the residuals are composed primarily of fringing evident on top of the spectrum (especially mixer 2) with the notable exception of the quadrature channel of mixer 1, which has some small systematic deviations on the Lamb dips. The line center ν_0 derived from the fit is $2725.89401954 \pm 0.0000023$ cm^{-1}, but the absolute accuracy is limited by the $> 2 \times 10^{-3}$ cm^{-1} accuracy of the wavemeter, so the exact frequency should not be trusted. More important is the uncertainty of the line center determination, which is ~70 kHz; this represents the maximum potential accuracy of the technique provided suitable frequency calibration is made (but see the discussion below about the effects of the asymmetry). The overall detection phase θ_h was found to be 132°, indicating a blend of absorption and dispersion in each mixer. Because the Lamb dip widths (full width at half maximum of $\sim$110 MHz as indicated by our fit) are much broader than the Lamb dip spacing of 39.56 MHz ($f_h/2$), the individual Lamb dips for absorption and dispersion cannot be resolved at any RF detection phase. Rather than tuning the phase to separate absorption from dispersion in the two mixers, a phase of 132° was chosen because it was found to isolate the fringing as much as possible in a single detection channel (mixer 2 in-phase), thus minimizing the fringing in the other 3 channels.

4. Discussion

The most interesting aspect of the NICE-OHVMS technique is the presence of Lamb dips which enables high precision measurements of line center frequencies. Prior to the development of NICE-OHVMS, the only methods capable of routine sub-Doppler molecular ion spectroscopy utilized fast ion beams which, due to kinematic compression, give linewidths on the order of 10 to 120 MHz [21–23]. The linewidths from ion beams are comparable to the Lamb dips presented here, though the current work with a positive column has the advantage of much higher ion density than that within an ion beam.

With the H_3^+ Lamb dip linewidths of $\sim$110 MHz demonstrated here, the precision of the line center determination is on the order of 70 kHz. In its present implementation, the technique's accuracy is limited by the wavemeter, and also by slow drifts in the frequency of the signal and idler beams caused by thermal fluctuations of the OPO cavity. Use of an optical frequency comb to stabilize and measure the frequencies of the pump and signal beams would reduce the accuracy uncertainty to < 100 kHz. Ultimately, the total uncertainty of the technique will be determined by the reproducibility of line center determinations once appropriately calibrated.

The asymmetry observed in the overall NICE-OHVMS lineshape can adversely affect the overall accuracy. As mentioned above, the origin of this asymmetry is unknown, although it varies with heterodyne detection phase; similar effects were not observed in the near-IR implementation of NICE-OHVMS [9]. Nevertheless, we have performed simulations of the effects of the asymmetry by synthesizing skewed profiles and comparing the results of our fit function to the actual location of the Lamb dips. Based on the fitting of our simulations, we estimate the magnitude of this line center shifting to be less than a few MHz, even for Doppler profiles that are much more asymmetric than those shown in this Letter. Further study of this phenomenon will be possible with an optical frequency comb, and such work is envisioned in the near future.

The width of the Lamb dips ($\sim$110 MHz FWHM from the fitting) is fairly broad. We have varied the intracavity laser power and the cell pressure, but any differences in the linewidth were not observable. However, the ranges of the power and pressure measurements were limited: the intracavity power could only be changed by a factor of 2 before the laser-cavity lock was adversely affected, and the plasma could only give stable operation over 200–600 mTorr. Such wide Lamb dips were also observed in the NICE-OHVMS experiment performed on N_2^+ in the near-IR [9]; in that study, the authors were able to observe a change in linewidth with pressure, but extrapolating to zero pressure still gave a linewidth of $\sim$30 MHz. Assuming that the linewidth is related to the time an ion spends at zero velocity, it is perhaps unsurprising that a less massive ion like H_3^+ has a broader linewidth than N_2^+, as its velocity may be more easily altered by weak long-range interactions.

The fringing apparent in the figures above limits the sensitivity of the present measurements in 2 of the 4 detection channels. The origin of the fringing is not fully understood; however, it appears to have a definite phase with respect to both the heterodyne detection and the plasma modulation. When the plasma is turned off, the fringing does not appear in a scan, and if the cavity transmission detector is blocked while a signal originating from a single fringe is present on a lock-in channel, the signal vanishes. Thus, it appears that the fringing is the result of the plasma interacting with the laser light rather than a purely electronic effect. One possibility is that residual amplitude modulation (RAM) in the heterodyne sidebands is being modulated by the plasma. RAM is an imbalance in the amplitude and/or phase of the sidebands with respect to one another. When demodulated, RAM appears as a DC offset in the heterodyne signal; because of our detection scheme using velocity modulation and $2f$ detection, the NICE-OHVMS would ordinarily be insensitive to such an offset. However, if the refractive index of the plasma varies at $2f$, the DC signal from RAM will be modulated at $2f$ as well, resulting in a net NICE-OHVMS signal. Because RAM is also affected by the presence of etalons in the optical system and the optical frequency, a fringing pattern could possibly result as a function of laser frequency. Testing whether this is truly the origin of the fringing is difficult; however, it is probable that the fringing would be reduced by employing a RAM compensation scheme via temperature and voltage control of the fiber EOM [24].

The sensitivity of the technique at the experimental detection bandwidth of 16 Hz, as determined from the noise-equivalent absorption in the baseline of the in-phase component of mixer 1 (which has the least fringing of the four detection channels), is 3.4×10^{-9} cm^{-1}. which is about two orders of magnitude above the shot noise limit of 3.9×10^{-11} cm^{-1} calculated from

$$\alpha_{\min} = \frac{\pi}{2F}\sqrt{\frac{eB}{\eta P_0}}\frac{1}{J_0(\beta)J_1(\beta)L}, \tag{2}$$

where F is the cavity finesse (120), e the fundamental electric charge, B the detection bandwidth (16 Hz), η the detector responsivity, P_0 the power incident on the detector, $J_n(\beta)$ the nth order Bessel function for modulation index β (0.63), and L the cavity length (190 cm). While NICE-OHMS has been able to achieve a noise level within a factor of 2 of the shot noise limit in one implementation [7], the performance achieved by NICE-OHVMS relative to the shot noise limit is already comparable to a number of other NICE-OHMS setups (see the extensive discussion in Section 4 of [8]).

Ultimately, the absolute sensitivity can be improved by identifying and eliminating noise sources and by increasing the cavity finesse. An increase in cavity finesse leads to additional technical challenge in maintaining the laser-cavity lock, and may make the system even more susceptible to the fringing effects that have already been observed. Such challenges can likely be overcome by improving the bandwidth of the laser frequency corrections (currently limited to the 10 kHz bandwidth of the signal cavity PZT), and correcting for RAM as discussed above.

5. Conclusions

In this Letter, we have demonstrated sub-Doppler spectroscopy of molecular ions in the mid-infrared spectral region using the NICE-OHVMS technique with a cw-OPO. By phase modulating the seed laser with a fiber EOM prior to amplification and optical parametric oscillation, the mid-infrared idler is also phase modulated without requiring a mid-IR EOM. The high optical power of the idler beam allows use of high-bandwidth detectors, which in turn make ultra-sensitive spectroscopy via NICE-OHMS possible. Velocity modulation spectroscopy is then combined with NICE-OHMS to afford ion-neutral discrimination, and the intracavity laser power is sufficient for saturating fundamental rovibrational transitions as demonstrated by spectroscopy of H_3^+. By fitting the sub-Doppler spectral features, the center frequencies of individual rovibrational lines can be measured with a precision of 70 kHz, and the maximum achieved sensitivity is within a factor of ∼90 of the shot noise limit. Improvements to the technique, such as addition of an optical frequency comb for accurate wavelength calibration, technical modifications to improve its sensitivity, and expanding the frequency coverage of the OPO from 3.2–3.9 μm to 2.8–4.8 μm, are envisioned.

The authors thank Takeshi Oka for providing us with the liquid nitrogen cooled plasma cell and its associated pumps and plasma electronics. KNC and BMS acknowledge support from a NASA Earth and Space Science Fellowship. JNH acknowledges support from a Springborn Fellowship and a National Science Foundation Graduate Research Fellowship (DGE 11-44245 FLLW). This work has been supported by the National Science Foundation (PHY 08-55633), the NASA Laboratory Astrophysics program (NNX08AN82G), and a David and Lucile Packard Fellowship.

References

[1] C.S. Gudeman, M.H. Begemann, J. Pfaff, R.J. Saykally, Phys. Rev. Lett. 50 (1983) 727.
[2] C.S. Gudeman, M.H. Begemann, J. Pfaff, R.J. Saykally, J. Chem. Phys. 78 (1983) 5837.
[3] S.K. Stephenson, R.J. Saykally, Chem. Rev. 105 (2005) 3220.
[4] B.M. Siller, A.A. Mills, B.J. McCall, Opt. Lett. 35 (2010) 1266.
[5] A.A. Mills, B.M. Siller, B.J. McCall, Chem. Phys. Lett. 501 (2010) 1.
[6] L.C. Sinclair, K.C. Cossel, T. Coffey, J. Ye, E.A. Cornell, Phys. Rev. Lett. 107 (2011) 093002.
[7] J. Ye, L.-S. Ma, J.L. Hall, J. Opt. Soc. Am. B 15 (1998) 6.
[8] A. Foltynowicz, F. Schmidt, W. Ma, O. Axner, Appl. Phys. B 92 (2008) 313.
[9] B.M. Siller, M.W. Porambo, A.A. Mills, B.J. McCall, Opt. Exp. 19 (2011) 24822.
[10] M.S. Taubman, T.L. Myers, B.D. Cannon, R.M. Williams, Spectrochim. Acta 60 (2004) 3457.
[11] M.W. Porambo, B.M. Siller, J.M. Pearson, B.J. McCall, Opt. Lett., in press.
[12] W.D. Watson, Astrophys. J. 183 (1973) L17.
[13] E. Herbst, W. Klemperer, Astrophys. J. 185 (1973) 505.
[14] T. Oka, Phys. Rev. Lett. 45 (1980) 531.
[15] C.M. Lindsay, B.J. McCall, J. Mol. Spectrosc. 210 (2001) 60.
[16] C.P. Morong, J.L. Gottfried, T. Oka, J. Mol. Spectrosc. 255 (2009) 13.
[17] L. Velilla, B. Lepetit, A. Aguado, J.A. Beswick, M. Paniagua, J. Chem. Phys. 129 (2008) 084307.
[18] C. Lindsay, E.T. White, T. Oka, Chem. Phys. Lett. 328 (2000) 129.
[19] A. Foltynowicz, W. Ma, O. Axner, Opt. Exp. 16 (2008) 14689.
[20] O. Axner, W. Ma, A. Foltynowicz, J. Opt. Soc. Am. B 25 (2008) 1166.
[21] C.S. Gudeman, R.J. Saykally, Ann. Rev. Phys. Chem. 35 (1984) 387.
[22] J.V. Coe, J.C. Owrutsky, E.R. Keim, N.V. Agman, D.C. Hovde, R.J. Saykally, J. Chem. Phys. 90 (1989) 3893.
[23] A.A. Mills, B.M. Siller, M.W. Porambo, M. Perera, H. Kreckel, B.J. McCall, J. Chem. Phys. 135 (2011) 224201.
[24] I. Silander, P. Ehlers, J. Wang, O. Axner, J. Opt. Soc. Am. B 29 (2012) 916

Kyle Crabtree graduated with a B.S. in Chemistry from Ball State University in 2006, and received his Ph.D. in Chemistry from the University of Illinois in 2012. He is currently a CfA Postdoctoral Fellow at the Harvard-Smithsonian Center for Astrophysics.

James Hodges received a B.S. in Chemistry and a B.S. in Polymer & Fiber Chemistry in 2010 from Clemson University. He currently attends the University of Illinois pursuing a PhD in Chemistry as a Springborn Fellow and an NSF Graduate Research Fellow.

Brian Siller graduated with a B.A. in Chemistry, Computer Science, and Mathematics from Ohio Wesleyan University in 2007, and is currently pursuing a Ph.D. in Physical Chemistry at the University of Illinois.

Adam Perry graduated with a B.S. in Chemistry from Oregon State University in 2011, and is currently a graduate student in Physical Chemistry at the University of Illinois.

Joe Kelly graduated with a B.S. in Chemistry from the University of Illinois in 2012.

Paul Jenkins II is currently pursuing his B.S. in Chemical Engineering at the University of Illinois, and plans to graduate in 2015.

Ben McCall received his Ph.D. from the University of Chicago in Chemistry and Astronomy & Astrophysics. Following a Miller Research Fellowship at the University of California at Berkeley, he joined the faculty of the University of Illinois, where he is currently an Associate Professor of Chemistry and Astronomy.

Appendix B

Indirect Rotational Spectroscopy of HCO^+

This appendix is a complete reprint with permission from Brian M. Siller, James N. Hodges, Adam J. Perry, Benjamin J. McCall. Journal of Physical Chemistry A, 117 (2013) 10034-10040, Copyright American Chemical Society 2013.

THE JOURNAL OF
PHYSICAL CHEMISTRY A

Article

pubs.acs.org/JPCA

Indirect Rotational Spectroscopy of HCO^+

Brian M. Siller,[†] James N. Hodges,[†] Adam J. Perry,[†] and Benjamin J. McCall*[,†,‡]

[†]Department of Chemistry and [‡]Departments of Physics and Astronomy, University of Illinois at Urbana−Champaign, Urbana, Illinois 61801, United States

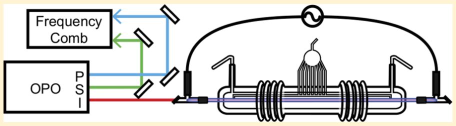

ABSTRACT: Spectroscopy of the ν_1 band of the astrophysically relevant ion HCO^+ is performed with an optical parametric oscillator calibrated with an optical frequency comb. The sub-MHz accuracy of this technique was confirmed by performing a combination differences analysis with the acquired rovibrational data and comparing the results to known ground-state rotational transitions. A similar combination differences analysis was performed from the same data set to calculate the previously unobserved rotational spectrum of the ν_1 vibrationally excited state with precision sufficient for astronomical detection. Initial results of cavity-enhanced sub-Doppler spectroscopy are also presented and hold promise for further improving the accuracy and precision in the near future.

■ INTRODUCTION

Molecular ions are a particularly challenging group of species to study with optical spectroscopy. Even in laboratory plasmas that are designed to observe only a specific ion, neutral molecules are still orders of magnitude more abundant than their charged counterparts. This is why the most productive techniques for ion spectroscopy tend to have some method for discriminating ionic absorption signals from neutral ones. Since the late 1980s, the predominant tool for this has been velocity modulation spectroscopy (VMS). The groundwork of VMS was laid by Wing et al. in a velocity modulated ion beam,[1] and the first application of VMS as it is known today was by Gudeman et al. in a velocity modulated positive column discharge cell.[2] Since the initial work, the technique has become a mainstay in ion spectroscopy and has been extensively reviewed.[3,4]

Protonated carbon monoxide, HCO^+, was the first ion whose spectrum was acquired using VMS. The R-branch of the ν_1 C−H stretch band was first measured by Gudeman et al. in a positive column discharge cell out to R(18).[2] Shortly after, the P-branch was also observed out to P(10) in a modulated DC glow.[6] After these lines were published, it was another 24 years before any work revisited the ν_1 band, when Verbraak et al. used a continuous wave optical parametric oscillator (cw-OPO) operating in the mid-infrared and a supersonic expansion discharge source to rotationally cool the ions.[7]

The first observation of an HCO^+ rotational transition was via telescope rather than in a laboratory in 1970 by Buhl and Snyder.[8] Because the line that they observed was unidentified at the time, it was referred to as "X-ogen". Later that year, Klemperer suggested that the X-ogen line was due to the $J = 1 \leftarrow 0$ transition of HCO^+.[9] Five years later, Woods et al. confirmed its identity by microwave spectroscopy.[10] Since that time, HCO^+ has been found in a variety of astronomical environments including protoplanetary nebulae,[11] star forming regions,[12] the interstellar medium,[13] and even the comet Hale−Bopp.[14] The abundance of HCO^+ makes it an important participant in the rich chemistry that exists in the interstellar medium. Because of the large rotational constant of HCO^+, its higher rotational transitions exist in the submillimeter/terahertz region. Newer telescopes such as the Atacama Large Millimeter and submillimeter Array (ALMA) and the Stratospheric Observatory For Infrared Astronomy (SOFIA) have submillimeter/terahertz capability. These new astronomical capabilities lend necessity to a relatively simple way to gain laboratory information in that spectral region, a challenging region for laboratory spectroscopy, due in part to the relative scarcity of quality sources and detectors compared to the microwave and infrared spectral regions. In this work, we present a demonstration of how precision rovibrational spectroscopy can be used to infer rotational transitions to precision sufficient to facilitate astronomical searches.

In the case of HCO^+, most of the ground state transitions have been observed up to $J = 17 \leftarrow 16$, with the exception of a few gaps in coverage.[15] Additionally, only a few pure rotational lines have been observed in vibrationally excited states. One such transition is the $J = 3 \leftarrow 2$ rotational transition in the ν_1 first vibrationally excited state.[16] With this single transition combined with our high-precision IR spectrum, the entire rotational spectrum of the ν_1 state can be calculated, limited only by the number of rovibrational lines that have been observed. The technique demonstrated here is also useful for determining high precision rotational constants in excited states.

In this work, we present spectra of the ν_1 fundamental band of HCO^+ acquired using optical heterodyne spectroscopy coupled with VMS (OH-VMS). This technique combines the advantages of the low noise of heterodyne spectroscopy with

Special Issue: Oka Festschrift: Celebrating 45 Years of Astrochemistry

Received: January 17, 2013
Revised: June 11, 2013
Published: June 12, 2013

dx.doi.org/10.1021/jp400570m | J. Phys. Chem. A 2013, 117, 10034−10040

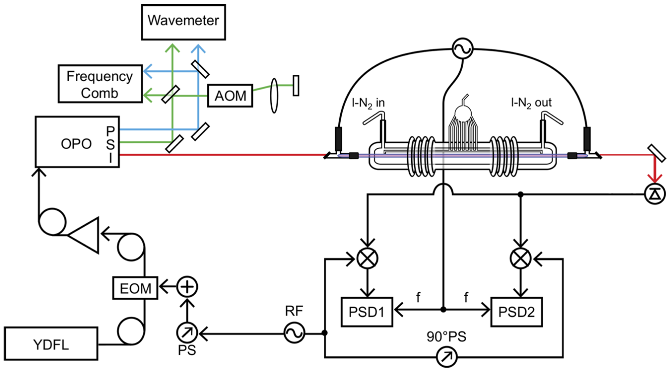

Figure 1. Experimental layout. YDFL, ytterbium-doped fiber laser; EOM, electro-optic modulator; PS, phase shifter; RF, radio frequency generator; OPO, optical parametric oscillator; P,S,I, pump, signal, idler; AOM, acousto-optic modulator; PSD, phase-sensitive detector.

the ion-neutral discrimination of VMS. Our instrument utilizes a cw-OPO tunable from 3.2 to 3.9 μm, and produces ions within a liquid nitrogen cooled positive column discharge cell. Optical frequency comb calibrated scans were acquired and fit with sub-MHz precision, and the resulting fits were used to calculate rotational transitions for the ground state and the first vibrationally excited C−H stretch state. These calculations result in the first experimental observation, albeit indirectly, of the $J = 3 \leftarrow 2$ transition in the ground state and the complete determination of the rotational spectrum up to $J = 10 \leftarrow 9$ in the ν_1 first excited state.

EXPERIMENTAL SECTION

The experimental setup, shown in Figure 1, has been described previously[17] with the exception of the frequency comb integration, so it will be discussed only briefly here. A Ytterbium-doped fiber laser is frequency modulated with a fiber-coupled electro optic modulator (EOM) using two RF generators: one at ~80 MHz for heterodyne detection, and the other at ~2 MHz for locking to the optical cavity around the discharge cell. After the modulation is applied, this seed laser is amplified to 10 W total power using a fiber amplifier, and this amplified beam acts as the pump for the optical parametric oscillator (OPO).

Three beams exit the OPO head: the pump (~1064 nm), the signal (tunable from 1.5 to 1.6 μm), and the idler (tunable from 3.2 to 3.9 μm). The idler is used for spectroscopy of HCO^+, while the other beams are used for frequency measurements using a near-infrared wavemeter and frequency comb. For the comb-calibrated scans, the wavemeter is only used prior to a scan to determine which comb modes the pump and signal are each closest to, while the comb is used throughout the scan to take frequency readings at each acquired data point.

Comb Integration. The optical frequency comb used in this work (Menlo FC1500) has been described previously in operation with a different laser system.[18] In this work, the comb is used for both stabilizing and measuring the pump frequency. It is also used for measuring the frequency of the signal after it is shifted by a double-pass AOM. The shifted-signal frequency and the AOM frequency are then used to calculate the unshifted signal frequency, which when combined with the pump frequency measurement, are used to determine the frequency of the idler. A detailed explanation of the comb operation follows.

Scanning the OPO with the comb is accomplished by first tuning the carrier-envelope offset of the comb to approximately 20 MHz and determining its sign. Then the comb repetition rate is tuned to make the signal offset beat lie within the range of 25−35 MHz from the nearest comb mode, limited by the RF bandpass filter built into the frequency counter used to record that beat. Then the frequency of the pump is tuned to approximately 20 MHz from its nearest comb mode, and the signs of the offset beats for both the pump and the signal are determined and recorded. Finally, the pump is offset-locked to the comb using a frequency-to-voltage converter circuit that generates an appropriate error signal for offset locking.

The nearest comb mode numbers are determined for the pump and the signal before each scan using the wavemeter, then are recorded (and incremented/decremented for the signal when necessary) as the scan progresses. At each frequency step, the data acquisition program pauses for 1.5 s, then the comb repetition rate and offset beats are recorded by frequency counters with 1 Hz refresh rates, and the lock-in amplifier outputs are recorded. With the lock-in amplifier time constant set to 300 ms, the lock-in amplifiers have 5 time constants to respond before the reading is polled for each point, so any scanning direction dependent line center pulling is smaller than the random scan-to-scan variability in line center determination.

After each point, the repetition rate is tuned by an amount sufficient to slew the pump frequency by ~5 MHz (~1.8 Hz change in repetition rate). The pump remains offset locked to the same comb mode throughout the course of each scan. The total continuous scanning range of the pump (and therefore for the idler) for comb-calibrated scans is limited to ~800 MHz by the comb scanning electronics; the comb repetition rate can only be changed by a relatively small amount while still retaining its lock onto the direct digital synthesizer (DDS) that stabilizes the repetition rate.

To keep the signal offset within the frequency counter bandpass filter at each point, a feed-forward system is used to tune the signal frequency using a double-pass acousto-optic modulator (AOM) setup. In a double-pass configuration, the frequency shift induced by the AOM is doubled, while making the pointing of the beam independent of the frequency applied to the AOM.[19] Stable pointing is crucial to the operation of the system, as good spatial overlap between the comb light and each of the cw beams is important for generating offset beat signals on the high speed detectors.

After the counters are read for a data point and the repetition rate is slewed to the next point, the amount the signal frequency needs to be shifted by is calculated using the change in the repetition rate, the signal comb mode number, and the amount the signal was away from the 30 MHz target offset frequency for the previous point; this frequency shift is then applied to the frequency of the RF generator that drives the AOM. The AOM diffraction efficiency is high enough to provide reliable signal/comb offset beat measurements in the driving frequency range of 150−210 MHz, which corresponds to a frequency shift of 300−420 MHz when taking into account the double-pass configuration. When the calculated desired AOM frequency lies outside this range, the drive frequency is shifted by 50 MHz (corresponding to a 100 MHz change in the shifted signal frequency, matching the comb repetition rate), and the signal mode number is incremented or decremented by one, depending on whether the 100 MHz shift was positive or negative.

This signal-shifting scheme allows the shifted signal frequency to be determined using the frequency comb at each point, despite the fact that the signal frequency is fixed (with the exception of some slow drift) while the comb repetition rate is slewing. The unshifted signal frequency can then be determined simply by subtracting the AOM frequency shift, which is precisely known from the digital setting of the RF generator at each point, and this unshifted signal frequency is subtracted from the directly measured pump frequency to determine the idler frequency.

Spectroscopic Configuration. The plasma cell used in this work, Black Widow, shown in Figure 2, was the same cell used by Takeshi Oka in many of his velocity modulation experiments. It allows for liquid nitrogen cooling of the plasma to reach an estimated rotational temperature of ∼166 K for HCO^+, as shown in the Boltzmann plot in Figure 3, using plasma conditions of 30 mTorr CO in 500 mTorr H_2 with a 35 kHz, 140 mA discharge. The idler beam is coupled through Brewster windows on either end of the cell into the central bore of the discharge cell. For this work, three different optical configurations were used: single-pass, double-pass, and cavity-enhanced, all of which relied on heterodyne modulation and detection at ∼80 MHz.

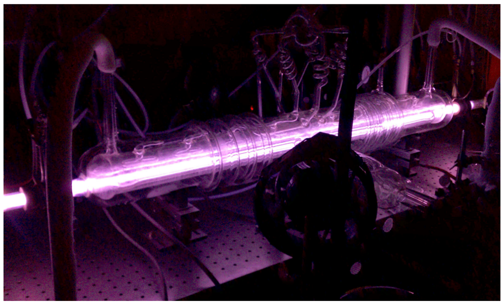

Figure 2. Black Widow, the liquid nitrogen cooled positive column discharge cell acquired from Takeshi Oka and used for the work in this article. The central bore, where the plasma discharge occurs, is surrounded by a sheath of flowing liquid nitrogen, which is in turn surrounded by a vacuum jacket to prevent ice from forming on the cell.

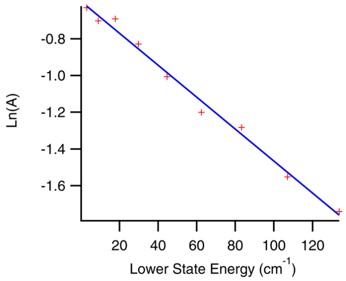

Figure 3. Boltzmann plot for R(1) through R(9), with the slope indicating a rotational temperature of ∼166 K. The vertical axis is the natural log of the line strength normalized peak-to-peak amplitude of a double-pass scan for each transition.

The comb calibrated scans presented in this article used a simple single-pass configuration, as shown in Figure 1. This allowed for the acquisition of Doppler-broadened scans with signal-to-noise ratios of ∼300 for the strongest lines and ∼100 for the weakest ones but, because of the lack of a bidirectional beam and sufficient laser power, did not allow for the observation of Lamb dips. A typical comb-calibrated scan is shown in Figure 4.

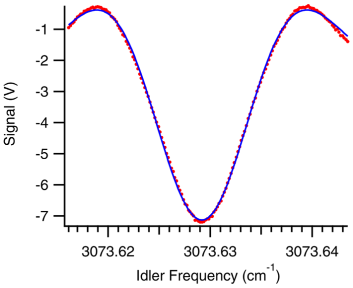

Figure 4. Typical comb-calibrated scan (red dots) of the P(5) transition of HCO^+, along with a fit to the data (blue line). Error bars for the points are not shown, as they would be smaller than the point size for both intensity and frequency.

A series of double-pass wavemeter-calibrated scans were collected for the previously unobserved P(11) through P(17) transitions. In the double-pass configuration, a single mirror was placed on the far side of the cell to back-reflect the idler for a second pass through the cell. Approximately 30% of the reflected beam was then picked off with a silicon window and directed to a high-speed detector, the signal from which was demodulated first at the heterodyne frequency, then at twice the plasma frequency ($2f$), as opposed to the $1f$ demodulation that was used for the single-pass work.

A few uncalibrated scans were collected with the laser frequency locked to an optical cavity positioned around the discharge cell, in a noise immune cavity enhanced optical heterodyne velocity modulation spectroscopy (NICE−

OHVMS)[20] configuration, as was done by Crabtree et al.[17] One such scan, showing strong central Lamb dip features on top of the Doppler profile, is shown in Figure 5. In this experiment, cavity enhancement is combined with 2*f* demodulation, making detection sensitive to not only velocity modulation but also concentration modulation of the ions of interest. This detection scheme allows for the observation of Lamb dips as the zero-velocity population of ions is modulated throughout the course of a discharge cycle.

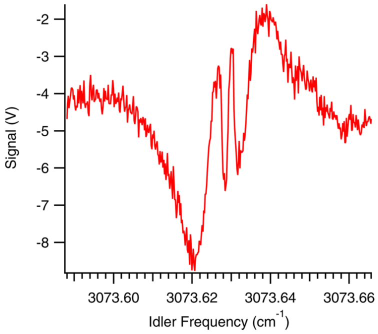

Figure 5. Roughly calibrated scan of the P(5) transition of HCO^+, showing the Lamb dips that are obtainable with cavity enhancement combined with lower cell pressure. The frequency calibration of this scan was based on the line center determined from the comb calibrated scans combined with the approximate scan voltage to frequency transfer function of the seed laser.

Unfortunately, the dielectric coatings on the mirrors were found to be hygroscopic, which led to poor laser coupling efficiency through the cavity in this wavelength range and degraded performance over time. To obtain optimal Lamb dip depth, the total cell pressure had to be decreased to ∼200 mTorr, and the discharge current had to be turned down as low as possible while still maintaining a stable plasma, to ∼100 mA. Both the lower pressure and the lower discharge current produce lower overall density of HCO^+ within the cell. This decreased density combined with the poor laser transmission through the cavity cause the signal-to-noise in the NICE−OHVMS scans to be significantly compromised compared to the single- and double-pass scans, despite the factor of ∼400 greater path length that NICE−OHVMS provides through the plasma.

■ RESULTS AND DISCUSSION

Each comb calibrated scan was fit to a second derivative of a Gaussian function, which approximates the convolution of heterodyne modulation with velocity modulation observed in the experiment. As can be seen in Figure 4, the fit is not perfect, especially near the outer lobes of the line shape. Lineshapes in velocity modulation experiments are often significantly more complex than simple derivatives of ordinary unmodulated lineshapes,[5] but for the purposes of determining line centers, the chosen function is sufficient. Between 4 and 7 scans were acquired of each transition, and the data acquired from those fits were used to compute the average line centers and standard errors shown in Table 1. The errors varied somewhat from one transition to the next, but the average uncertainty was found to be ∼600 kHz.

Table 1. List of the Comb-Calibrated HCO^+ Transition Center Frequencies (With Associated Uncertainties) Observed in the Current Work, Compared with Previous Measurements

transition	line center (cm^{-1})	previous work[6] (cm^{-1})	previous − current (MHz)
R(0)	3091.690432(16)	3091.6919(10)	44
R(1)	3094.618099(27)	3094.6181(10)	0
R(2)	3097.522054(07)	3097.5223(10)	7
R(3)	3100.402249(25)	3100.4034(10)	35
R(4)	3103.258604(21)	3103.2586(10)	0
R(5)	3106.090956(19)	3106.0909(10)	−2
R(6)	3108.899376(20)	3108.9002(10)	25
R(7)	3111.683680(04)	3111.6841(10)	13
R(8)	3114.443835(05)	3114.4445(10)	20
R(9)	3117.179881(41)	3117.1800(10)	4
P(1)	3085.763903(23)	3085.7646(10)	21
P(2)	3082.765487(53)	3082.7662(10)	21
P(3)	3079.743422(15)	3079.7437(10)	8
P(4)	3076.698005(05)	3076.6977(10)	−9
P(5)	3073.629188(16)	3073.6291(10)	−3
P(6)	3070.537136(19)	3070.5377(10)	17
P(7)	3067.421924(37)	3067.4224(10)	14
P(8)	3064.283464(10)	3064.2834(10)	−2
P(9)	3061.122045(18)	3061.1226(10)	17
P(10)	3057.937606(08)	3057.9380(10)	12

As can be seen by the fit in Figure 4, this fit function is not perfect, likely due to imperfect setting of the detection phases. For this work, both the RF and plasma demodulation phases were set to maximize the signal-to-noise of a single detection channel out of the four channels that were acquired with each scan. It is likely that there is some dispersive component to the line shape function, rather than it being purely absorptive. It is also likely that the velocity modulation of the ions is not purely sinusoidal and that the lock-in demodulation is not exactly in phase with the velocity modulation, and both of these factors can also affect the overall line shape.

There is also a slight asymmetry in the observed line shapes for several of the scans that is not fully understood at this time. By adding a slightly sloped baseline to the data, we can make it significantly more symmetric and also make the fit slightly better. Symmetrizing the data in this way causes the determined line center to shift by less than 1 MHz for even the most asymmetric scans. Given that we do not know the physical cause of this phenomenon, we have taken the approach of manipulating the data as little as possible, so this symmetrizing was only done to estimate the potential error induced by the asymmetry.

When asymmetry is present, it tends to manifest with the low-frequency lobe of the line shape having a greater maximum than the high-frequency one, although by tuning detection phases and plasma conditions, we are able to reverse the asymmetry, making the high-frequency lobe larger. Fitting the same line with opposite asymmetry slopes provides line centers that are shifted by less than 1 MHz relative to one another, providing further evidence that any asymmetry-induced errors in line center determination must be fairly small, on the order of 1 MHz or smaller.

All of the comb-calibrated data presented in this work was performed with the identical phase settings and plasma conditions, leading to line shapes that were similarly asymmetric. Such a systematic error would be mitigated by subtraction of observed line centers, as is done in the combination differences analysis described in the following several paragraphs. On the basis of the errors in the calculation of rotational transitions, it appears that random scan-to-scan variability is the limiting factor in line center determination and not the effects of this asymmetry.

For approximately half of the comb-calibrated scans, the determined line centers disagreed with the previously measured HCO^+ transition frequencies[6] by greater than the specified accuracy of 30 MHz. It was found that the source of the errors was incorrect comb mode number determination for either the signal or the pump beams due to inaccuracy of the wavemeter. These incorrectly calibrated scans were easily corrected by adding or subtracting a multiple of the comb repetition rate to or from the calculated idler frequency. After correcting the idler frequency calibration, it was found that all but two of the observed transitions agreed with Amano's previous work to within 30 MHz. The two exceptions to the 30 MHz agreement were the R(0) and R(3) transitions, but those were both further verified by comparing the combination difference analysis with directly measured rotation transitions, as shown in Table 2. Any remaining error in the determination of comb mode numbers would appear as an error of ∼100 MHz, which is not observed.

Table 2. Indirectly Calculated Rotational Transition Frequencies Derived from the Data in Table 1 Compared to the Directly Measured Rotational Transitions Compiled by Cazzoli et al.[15]

J'	J''	calc freq (MHz)	obs freq[15] (MHz)	calc − obs (MHz)
0	1	n/a	89188.5247	n/a
1	2	178374.6(17)	178375.0563	−0.5
2	3	267557.0(19)	n/a	n/a
3	4	356732.3(19)	356734.2230	−2.0
4	5	445903.9(21)	445902.8721	1.0
5	6	535061.0(23)	535061.5810	−0.5
6	7	624207.4(26)	624208.3606	−1.0
7	8	713344.0(27)	713341.2278	2.8
8	9	802455.7(27)	802458.1995	−2.5
9	10	891558.4(27)	891557.2903	1.1

A combination differences analysis was performed to demonstrate the accuracy of our comb-calibrated rovibrational compared to known rotational transitions. First, frequencies of transitions sharing the same upper state energy level, e.g., R(0) and P(2), were subtracted from one another to generate ground state energy level spacings for pairs of energy levels separated by two rotational energy levels. For example, the $J = 2 \leftarrow 0$ spacing was calculated from $f_{R(0)} - f_{P(2)}$, the $J = 3 \leftarrow 1$ spacing was calculated from $f_{R(1)} - f_{P(3)}$, and so forth for all observed transitions up to the $J = 10 \leftarrow 8$ spacing.

Then the directly measured $J = 1 \leftarrow 0$ transition was subtracted from the $J = 2 \leftarrow 0$ energy level spacing to indirectly compute the $J = 2 \leftarrow 1$ rotational transition frequency. This computed frequency was then subtracted from the $J = 3 \leftarrow 1$ spacing to compute the $J = 3 \leftarrow 2$ transition frequency, and the process was repeated for higher rotational energy levels up to $J = 10 \leftarrow 9$. At each step, the calculated rotational transition from the previous step was used with a new energy level difference to compute a new rotational transition. The indirectly calculated rotational transitions in the current work are compared to the previously observed rotational transition frequencies in Table 2.

Such an analysis was also carried out for the ν_1 (C−H stretch mode) first vibrationally excited state. To our knowledge, the only directly observed rotational transition was $J = 3 \leftarrow 2$.[16] This single transition, combined with our rovibrational data, is sufficient to compute the expected rotational transitions from $J = 1 \leftarrow 0$ up to $J = 10 \leftarrow 9$, as shown in Table 5.

The rovibrational comb-calibrated data were also fit to a simple Hamiltonian to determine the constants shown in Table 3, where the quartic distortion terms for the lower and upper vibrational states were constrained to be equal to one another. The full results of the fit, showing the deviations of the data from the fit result, is shown in Table 4. The experimental data agree with the fit within 2σ for all but three of the observed transitions, and all of the data agree with the fit to within 4σ. This provides further evidence for the internal consistency of this rovibrational data set, and validation that the random errors that contribute to the statistical uncertainties are the limiting factor of the accuracy and precision (as oppposed to other effects that vary from one line to the next, such as the observed asymmetry in the lineshapes).

Table 3. Molecular Constants (And Associated Uncertainties) Obtained from a Least Squares Fit of the Full Comb-Calibrated Rovibrational Data Set; Full Fit Results, Including the Associated Residuals, Are Given in Table 4

constant	value (MHz)
ν_0	92598065.20(19)
B''	44594.166(25)
B'	44240.297(27)
D''	−0.07784(49)
D'	−0.07760(49)
$H' = H''$	$-0.0269(28) \times 10^{-3}$

Table 4. Full Results of the Least Squares Fit of the Full Comb-Calibrated Rovibrational Data Set

J'	J''	obs freq (cm^{-1})	calc freq (cm^{-1})	obs − calc (cm^{-1})
0	1	3091.690432(16)	3091.690368	0.000064
1	2	3094.618099(27)	3094.618083	0.000016
2	3	3097.522054(07)	3097.522065	−0.000011
3	4	3100.402249(25)	3100.402251	−0.000002
4	5	3103.258604(21)	3103.258575	0.000030
5	6	3106.090956(19)	3106.090968	−0.000012
6	7	3108.899376(20)	3108.899361	0.000015
7	8	3111.683680(04)	3111.683678	0.000002
8	9	3114.443835(05)	3114.443840	−0.000005
9	10	3117.179881(41)	3117.179764	0.000117
1	0	3085.763903(23)	3085.763992	−0.000089
2	1	3082.765487(53)	3082.765454	0.000033
3	2	3079.743422(15)	3079.743436	−0.000014
4	3	3076.698005(05)	3076.698000	0.000005
5	4	3073.629188(16)	3073.629214	−0.000026
6	5	3070.537136(19)	3070.537148	−0.000012
7	6	3067.421924(37)	3067.421874	0.000050
8	7	3064.283464(10)	3064.283471	−0.000007
9	8	3061.122045(18)	3061.122020	0.000025
10	9	3057.937606(08)	3057.937608	−0.000002

In addition to the comb-calibrated scans that were collected for the combination differences analysis, several previously unobserved P-branch transitions were recorded with only wavemeter calibration. All but one of the linecenters determined from these scans fall within the expected 70 MHz uncertainty from the wavemeter calibration. The one exception, P(17), is thought to be off by more than the uncertainty due to an inaccurate signal wavelength reading caused by poor optical alignment of the wavemeter. These transitions, whose frequencies are given in Table 6, could not be used for combination differences calculations because their corresponding R-branch transitions lie outside the tuning range of our current OPO module, though additional tuning could be obtained with other modules.

Table 5. Pure Rotational Transitions for the Vibrationally Excited ν_1 State of HCO$^+$, Calculated from the Rovibrational Data in Table 1 and the Directly Observed[21] $J = 3 \leftarrow 2$ Rotational Transition

J'	J''	calc freq (MHz)	uncertainty (MHz)
0	1	88486.7	1.9
1	2	176955.4	1.6
2	3	n/a	n/a
3	4	353900.7	0.9
4	5	442366.0	1.1
5	6	530813.3	1.3
6	7	619257.7	1.6
7	8	707676.3	1.9
8	9	796093.7	1.9
9	10	884477.9	2.4

Table 6. Previously Unobserved Wavemeter-Calibrated Scans of the P(11) through P(17) Transitions[a]

transition	obs (cm^{-1})	calc (cm^{-1})	obs − calc (MHz)
P(11)	3054.730	3054.73019(4)	−6
P(12)	3051.502	3051.49993(5)	62
P(13)	3048.245	3048.24688(6)	−57
P(14)	3044.969	3044.97111(7)	−63
P(15)	3041.672	3041.67269(8)	−21
P(16)	3038.354	3038.35169(9)	69
P(17)	3035.013	3035.00817(10)	145

[a] Uncertainties are ~70 MHz, limited by the wavemeter uncertainties for the pump and signal frequencies added in quadrature. Calculations are based on ground state constants from Cazzoli et al.,[15] and excited state constants are determined from our comb-calibrated scans.

■ CONCLUSIONS

The current work demonstrates the ability of Doppler-broadened comb-calibrated velocity modulation spectroscopy to determine line centers with sub-MHz accuracy and precision. This accuracy has been verified by performing a combination differences analysis of the rovibrational data and comparing the results to the previously observed rotational spectrum of vibrational ground state HCO$^+$. The potential of extending the technique to sub-Doppler work has also been demonstrated. With a proper set of cavity mirrors, it should be possible to further improve the precision of this technique. From the current series of fits, the Doppler-limited line width is ~450 MHz, and the uncertainty of a single fit is ~350 kHz. From the Lamb dip scan of HCO$^+$ shown in Figure 5, the peak-to-peak line width of the central sub-Doppler feature is only ~50 MHz, so it is reasonable to assume that the precision of a fit to sub-Doppler features would be approximately an order of magnitude more precise than one to a Doppler-broadened scan, assuming the S/N problem can be solved by a non-hygroscopic set of cavity mirrors. The investigation into whether the accuracy is also improved by the same factor will be the subject of future work.

One of the greatest advantages of this indirect approach over direct rotational spectroscopy is the generality of it. The chemistry within positive column discharge cells tends to be very rich, so it is possible to make a wide variety of molecular ions. The cell used in the current work was cooled with liquid nitrogen, but it could easily be cooled by water or air, or even heated to attain greater population in higher rotational levels and compute the rotational spectrum up to very high J values. The infrared source and detectors are also very versatile in terms of spectral coverage; entire rovibrational bands for a wide variety of ions lie within its tuning range and can be observed without any changes to the optoelectronic system.

This work also has implications for astronomical searches for the astrophysically relevant ion HCO$^+$. While the ground vibrational state has been thoroughly studied, little work has previously been done in this vibrationally excited state. Rotational transitions in the vibrationally excited state could be of astrophysical interest, particularly in hot, dense environments such as hot cores and circumstellar envelopes.[22]

■ AUTHOR INFORMATION

Corresponding Author

*(B.J.M.) E-mail: bjmccall@illinois.edu.

Notes

The authors declare no competing financial interest.

■ ACKNOWLEDGMENTS

We would like to acknowledge an NSF grant (CHE 12-13811) and a NASA Laboratory Astrophysics grant (NNX13AE62G) for funding. B.J.M. wishes to acknowledge support from a David & Lucile Packard Fellowship and a Camille Dreyfus Teacher-Scholar award. B.M.S. would like to thank a NASA Earth and Space Science Fellowship (NESSF NNX11AO06H), and J.N.H. is grateful for support by a Robert & Carolyn Springborn fellowship and an NSF Graduate Research Fellowship (DGE 11-44245 FLLW). We would also like to thank Takeshi Oka for supplying the discharge cell and associated electronics and pumps used for this work.

■ REFERENCES

(1) Wing, W.; Ruff, G.; Lamb, W.; Spezeski, J. Observation of the Infrared Spectrum of the Hydrogen Molecular Ion HD$^+$. *Phys. Rev. Lett.* **1976**, *36*, 1488−1491.

(2) Gudeman, C. S.; Begemann, M. H.; Pfaff, J.; Saykally, R. J. Velocity-Modulated Infrared Laser Spectroscopy of Molecular Ions: The ν_1 Band of HCO$^+$. *Phys. Rev. Lett.* **1983**, *50*, 727−731.

(3) Stephenson, S. K.; Saykally, R. J. Terahertz Laser Velocity Modulation Spectroscopy of Ions. *J. Mol. Spectrosc.* **2005**, *231*, 145−153.

(4) Gudeman, C. S.; Saykally, R. J. Velocity Modulation Infrared Laser Spectroscopy of Molecular Ions. *Annu. Rev. Phys. Chem.* **1984**, *35*, 387−418.

(5) Farley, J. Theory of the Resonance Line-Shape in Velocity-Modulation Spectroscopy. *J. Chem. Phys.* **1991**, *95*, 5590−5602.

(6) Amano, T. The ν_1 Fundamental Band of HCO$^+$ by Difference Frequency Laser Spectroscopy. *J. Chem. Phys.* **1983**, *79*, 3595.

(7) Verbraak, H.; Ngai, A. K. Y.; Persijn, S. T.; Harren, F. J. M.; Linnartz, H. Mid-Infrared Continuous Wave Cavity Ring Down

Spectroscopy of Molecular Ions Using an Optical Parametric Oscillator. *Chem. Phys. Lett.* **2007**, *442*, 145−149.

(8) Buhl, D.; Snyder, L. E. Unidentified Interstellar Microwave Line. *Nature* **1970**, *228*, 267−269.

(9) Klemperer, W. Carrier of the Interstellar 89.190 GHz Line. *Nature* **1970**, *227*, 1230−1230.

(10) Woods, R.; Dixon, T.; Saykally, R.; Szanto, P. Laboratory Microwave Spectrum of HCO^+. *Phys. Rev. Lett.* **1975**, *35*, 1269−1272.

(11) Sanchez Contreras, C.; Sahai, R. Physical Structure of the Protoplanetary Nebula CRL 618. II. Interferometric Mapping of Millimeter-Wavelength HCN $J = 1-0$, HCO^+ $J = 1-0$, and Continuum Emission. *Astrophys. J.* **2004**, *602*, 960−977.

(12) Purcell, C. R.; Balasubramanyam, R.; Burton, M. G.; Walsh, A. J.; Minier, V.; Hunt-Cunningham, M. R.; Kedziora-Chudczer, L. L.; Longmore, S. N.; Hill, T.; Bains, I.; et al. A CH_3CN and HCO^+ Survey Towards Southern Methanol Masers Associated with Star Formation. *Mon. Not. R. Astron. Soc.* **2006**, *367*, 553−576.

(13) Liszt, H.; Lucas, R. mm-wave HCO^+, HCN and CO Absorption Toward NGC-1052. *Astron. Astrophys.* **2004**, *428*, 445−450.

(14) Milam, S. N.; Savage, C.; Ziurys, L. M.; Wyckoff, S. HCO^+ Observations Toward Comet Hale-Bopp (C/1995 O1): Ion−Molecule Chemistry and Evidence for a Volatile Secondary Source. *Astrophys. J.* **2004**, *615*, 1054−1062.

(15) Cazzoli, G.; Cludi, L.; Buffa, G.; Puzzarini, C. Precise THz Measurements of HCO^+, N_2H^+, and CF^+ for Astronomical Observations. *Astrophys. J., Suppl. Ser.* **2012**, *203*, 11.

(16) Lattanzi, V.; Walters, A.; Drouin, B. J.; Pearson, J. C. Rotational Spectrum of the Formyl Cation, HCO^+, to 1.2 THz. *Astrophys. J.* **2007**, *662*, 771−778.

(17) Crabtree, K. N.; Hodges, J. N.; Siller, B. M.; Perry, A. J.; Kelly, J. E.; Jenkins, P. A., II; McCall, B. J. Sub-Doppler Mid-Infrared Spectroscopy of Molecular Ions. *Chem. Phys. Lett.* **2012**, *551*, 1−6.

(18) Mills, A. A.; Siller, B. M.; McCall, B. J. Precision Cavity Enhanced Velocity Modulation Spectroscopy. *Chem. Phys. Lett.* **2010**, *501*, 1−5.

(19) Donley, E. A.; Heavner, T. P.; Levi, F.; Tataw, M. O.; Jefferts, S. R. Double-Pass Acousto-Optic Modulator System. *Rev. Sci. Instrum.* **2005**, *76*, 063112.

(20) Siller, B. M.; Porambo, M. W.; Mills, A. A.; McCall, B. J. Noise Immune Cavity Enhanced Optical Heterodyne Velocity Modulation Spectroscopy. *Opt. Express* **2011**, *19*, 24822−24827.

(21) Hirota, E.; Endo, Y. Microwave Spectroscopy of HCO^+ and DCO^+ in Excited Vibrational States. *J. Mol. Spectrosc.* **1988**, *127*, 527−534.

(22) Blake, G. A.; Laughlin, K. B.; Cohen, R. C.; Busarow, K. L.; Saykally, R. J. Laboratory Measurement of the Pure Rotational Spectrum of Vibrationally Excited HCO^+ ($\nu_2 = 1$) by Far-Infrared Laser Sideband Spectroscopy. *Astrophys. J.* **1987**, *316*, L45−L48.

■ NOTE ADDED AFTER ASAP PUBLICATION

This article was published ASAP on July 3, 2013. After this paper was finalized, comb-calibrated sub-Doppler spectra were obtained for the P(5) and R(3) transitions, and the line centers were 4.1(6) and 3.7(8) MHz, respectively, lower than the values in Table 1 from our single-pass measurements. This evidently systematic offset is likely due to an asymmetry in the ion drift velocity in our AC plasma, and does not affect the indirect rotational transitions reported here as the offset is removed by subtraction. Since the observed Lamb dips probe only the zero-velocity ion population, we expect their frequencies to be independent of any plasma asymmetry. The corrected version was published ASAP on July 10, 2013.

THE JOURNAL OF
PHYSICAL CHEMISTRY A

Addition/Correction

pubs.acs.org/JPCA

Addition to “Indirect Rotational Spectroscopy of HCO^+”

Brian M. Siller, James N. Hodges, Adam J. Perry, and Benjamin J. McCall*

J. Phys. Chem. A **2013**, *117* (39), 10034−10040. DOI: 10.1021/jp400570m

After publication, we learned that pure rotational transitions in the $1\nu_1$ vibrationally excited state of HCO^+ had been measured by Warner in his Ph.D. thesis[1] and by Hirao et al.,[2] so our combination differences and fit results should be compared to the results from this work.

Additionally, a 1 MHz error was found in the calculation of all of the vibrationally excited combination differences as a result of a single transcription error in the $J = 3 \leftarrow 2$ excited state transition[3] used in determining the combination differences. The corrected values are reported in Table 1.

Table 1. Summary of the Corrected Rotational Transitions in the $1\nu_1$ Vibrationally Excited State and a Comparison of Those to Previously Determined Values[a]

$J'-J''$	frequency	previous	calc − prev
1−0	88485.7(19)	88480.748(100)[b]	5.0
2−1	176956.4(16)	176959.485[c]	−3.1
4−3	353901.7(9)	353903.215(30)[d]	−1.5
5−4	442365.0(11)	442364.230(30)[d]	0.8
6−5	530814.3(13)	530815.436[c]	−1.1
7−6	619256.7(16)	619254.813(30)[d]	1.9
8−7	707677.4(19)	707680.392(30)[d]	−3.0
9−8	796092.7(19)	796090.220(20)[d]	2.5
10−9	884478.9(24)	884482.326[c]	−3.4

[a] The comparison column is the difference between our calculated combination difference and the previously calculated or observed value. All the values are in MHz. [b] Warner.[1] [c] Hirao et al. calculated.[2] [d] Hirao et al. observed.[2]

Excluding the $J = 1 \leftarrow 0$ transition, all previous values are within 2σ of our determined frequencies.

The differences between the B and D constants in this paper and those in Hirao et al. arise from the inclusion of a sextic distortion constant. When the sextic distortion constant is not included, the B and D constants ($B = 44240.511(41)$ MHz and $D = 82.13(30)$ kHz) are in good agreement with those of Hirao et al. ($B = 44240.52774(118)$ MHz and $D = 82.0571(87)$ kHz).

■ ACKNOWLEDGMENTS

We thank Prof. Takayoshi Amano for kindly bringing his paper to our attention, which allowed us to compare our work to the submillimeter work.

■ REFERENCES

(1) Warner, H. The Microwave Spectroscopy of Ions and Other Transient Species in DC Glow and Extended Negative Glow Discharges. Ph.D. thesis, University of Wisconsin−Madison, 1988.

(2) Hirao, T.; Yu, S.; Amano, T. Sub-millimeter Spectroscopy of HCO^+ in the Excited Vibrational States. *J. Mol. Spectrosc.* **2008**, *248*, 26−40.

(3) Hirota, E.; Endo, Y. Microwave Spectroscopy of HCO^+ and DCO^+ in the Excited Vibrational States. *J. Mol. Spectrosc.* **1988**, *127*, 527−534.

Published: October 28, 2013

Appendix C

High-precision and High-accuracy Rovibrational Spectroscopy of Molecular Ions

This appendix is a complete reprint with permission from James N. Hodges, Adam J. Perry, Paul A. Jenkins II, Brian M. Siller, Benjamin J. McCall. Journal of Chemical Physics, 139 (2013) 164201, Copyright American Physical Society 2013.

THE JOURNAL OF CHEMICAL PHYSICS **139**, 164201 (2013)

High-precision and high-accuracy rovibrational spectroscopy of molecular ions

James N. Hodges,[1] Adam J. Perry,[1] Paul A. Jenkins II,[1] Brian M. Siller,[1,a)]
and Benjamin J. McCall[1,2,b)]
[1]*Department of Chemistry, University of Illinois, Urbana, Illinois 61801, USA*
[2]*Departments of Astronomy and Physics, University of Illinois, Urbana, Illinois 61801, USA*

(Received 22 July 2013; accepted 2 October 2013; published online 29 October 2013)

We present a versatile new instrument capable of measuring rovibrational transition frequencies of molecular ions with sub-MHz accuracy and precision. A liquid-nitrogen cooled positive column discharge cell, which can produce large column densities of a wide variety of molecular ions, is probed with sub-Doppler spectroscopy enabled by a high-power optical parametric oscillator locked to a moderate finesse external cavity. Frequency modulation (heterodyne) spectroscopy is employed to reduce intensity fluctuations due to the cavity lock, and velocity modulation spectroscopy permits ion-neutral discrimination. The relatively narrow Lamb dips are precisely and accurately calibrated using an optical frequency comb. This method is completely general as it relies on the direct measurement of absorption or dispersion of rovibrational transitions. We expect that this new approach will open up many new possibilities: from providing new benchmarks for state-of-the-art *ab initio* calculations to supporting astronomical observations to helping assign congested spectra by combination differences. Herein, we describe the instrument in detail and demonstrate its performance by measuring ten R-branch transitions in the ν_2 band of H_3^+, two transitions in the ν_1 band of HCO^+, and the first sub-Doppler transition of CH_5^+. © *2013 AIP Publishing LLC*. [http://dx.doi.org/10.1063/1.4825251]

I. INTRODUCTION

In the 30 years since its discovery,[1] velocity modulation spectroscopy (VMS) in a positive column discharge has been a tremendously successful method for performing direct absorption spectroscopy of molecular ions. The positive column offers a remarkably rich chemical environment suitable for the production of a wide variety of ions with a high column density.[2]

Traditional VMS has been limited in its frequency precision by broad Doppler-limited linewidths, coupled with modest signal-to-noise ratios, and the uncertainties in line center determinations are typically 30-90 MHz.[3,4] The Doppler limit was overcome by our group in 2010 by placing the discharge cell in an external cavity, in an approach called cavity enhanced VMS.[5,6] The high intracavity power enabled saturation spectroscopy, and the resulting Lamb dips enabled the precision to be improved to ~3 MHz in the near-infrared. The later incorporation of frequency modulation, or heterodyne, spectroscopy improved the signal-to-noise ratio and further improved the precision.[7] This approach, based on the pioneering NICE-OHMS technique,[8] was dubbed NICE-OHVMS, or Noise Immune Cavity Enhanced Optical Heterodyne Velocity Modulation Spectroscopy. This technique was later extended into the mid-infrared, using an optical parametric oscillator, by Crabtree *et al.*[9]

The accuracy of VMS has also been limited by the method of frequency calibration. Typically, VMS experiments relied on a combination of relative calibration using marker etalons and absolute calibration using Doppler-limited reference gas transitions, which were themselves often only known to ~30 MHz accuracy. The advent of optical frequency combs has revolutionized the accuracy of molecular spectroscopy, making sub-MHz frequency measurements almost routine. Our near-infrared NICE-OHVMS work on N_2^+ used a frequency comb to achieve an accuracy of ~300 kHz.[7] In recent work without an external cavity, we have demonstrated that it is possible to extend comb-calibrated spectroscopy to the mid-infrared, to infer pure-rotational transitions of molecular ions such as HCO^+ using combination differences with sub-MHz accuracy.[10]

In this paper, we present the combination of sub-Doppler spectroscopy using mid-infrared NICE-OHVMS[9] with optical frequency comb calibration[10] to yield a versatile method for molecular ion spectroscopy with both high precision and high accuracy. We demonstrate and characterize the effectiveness of this method through spectroscopy of H_3^+, HCO^+, and CH_5^+.

H_3^+ is a natural first target for our spectrometer. As the simplest polyatomic molecule, it has become an important system for benchmarking the increasing accuracy of quantum calculations. Many of its rovibrational transitions have been predicted to within hundredths of a wavenumber by sophisticated calculations that include adiabatic, relativistic electron, and non-adiabatic corrections to the Born-Oppenheimer potential energy surface.[11] In many cases, this degree of precision is comparable to the experimental uncertainties, so more precise measurements will serve to motivate and benchmark ever more accurate calculations, which will require the

---

[a)] Present address: Tiger Optics, Warrington, Pennsylvania 18976, USA.
[b)] Electronic mail: bjmccall@illinois.edu. URL: http://bjm.scs.illinois.edu.

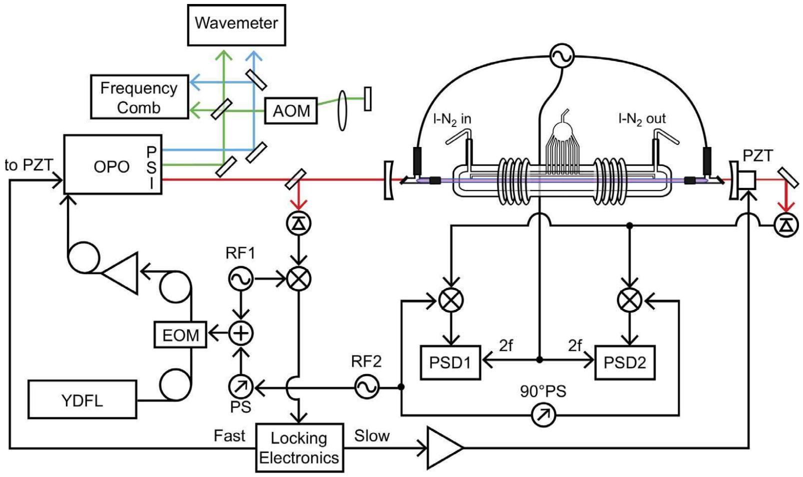

FIG. 1. Block diagram of the instrument. YDFL: Ytterbium Doped Fiber Laser; EOM: Electro-Optic Modulator; OPO: Optical Parametric Oscillator; P,S,I: Pump(Blue), Signal(Green), Idler(Red); AOM: Acousto-Optic Modulator; PZT: Piezo-electric Transducer; PS: Phase Shifter; RF: Radio-Frequency source; and PSD: Phase Sensitive Detector.

inclusion of quantum electrodynamic effects as has already been done with diatomics[12] and H_2O.[13]

In addition to its fundamental interest, H_3^+ is also an important molecule in astrochemistry due to its abundance in both dense[14] and diffuse[15] interstellar clouds, as well as in the atmospheres of large gas giants such as Jupiter.[16] Of particular relevance to the present work, the Doppler shifts of H_3^+ rovibrational transitions have been successfully used to determine the velocity of Jovian auroral winds,[17] but the accuracy of those determinations is limited by the uncertainties in the laboratory transition frequencies.

Our second target, HCO^+, was recently used[10] to demonstrate the feasibility of performing "indirect" pure-rotational spectroscopy by calculating combination differences of high-precision rovibrational frequencies. Due to degradation of our cavity mirrors in that work, we were restricted to performing single-pass heterodyne spectroscopy. Here, we revisit HCO^+ with an improved set of cavity mirrors, and we find that the single-pass measurements suffered a slight (∼4 MHz) but systematic offset due to an asymmetry in the AC plasma. This highlights the advantage of using Lamb dips in a bidirectional cavity for line center determination, as they are located symmetrically around the zero-velocity component of the ions and are not shifted by plasma asymmetries.

Our final target, CH_5^+, is an enigmatic ion whose high-resolution infrared spectrum in the C–H stretching region remains completely unassigned nearly 15 years since it was first reported.[3] It has been suggested[18] that one possible way of assigning the spectrum would be to search for four-line combination differences, which would identify energy level separations. However, the high line density results in many "false positives" at the current precision of the line center measurements. Here we report the first sub-Doppler spectrum of CH_5^+, which improves on the precision of the initial detection[3] by more than two orders of magnitude.

II. EXPERIMENTAL DESCRIPTION

A block diagram of the instrument is presented in Figure 1. A ytterbium doped fiber laser (Koheras Adjustik Y-10) is coupled into a fiber electro-optic modulator (EOSPACE PM-0K5-00-PFU-PFU-106-S), where Pound Drever Hall (PDH) locking side bands (∼4 MHz) and heterodyne sidebands (∼79 MHz, equal to the free spectral range of our external cavity) are imprinted onto the laser. After modulation, the light is amplified by a 10 W fiber amplifier (IPG Photonics YAR-10 K-1064-LP-SF) and is used to pump a singly resonant optical parametric oscillator (OPO; Aculight Argos 2400 SF). The idler, tunable from 3.2 to 3.9 μm, is coupled into a ∼190 cm external cavity composed of two dielectric mirrors (Rocky Mountain Instruments, custom) on silicon substrates with 1 m radius of curvature. For the H_3^+ measurements, the mirrors used were nominally 99.7% reflective between 3.0 and 3.4 μm but suffered high losses at higher frequencies because of water adsorbed in the hygroscopic coating. The measurements of HCO^+ and CH_5^+ have utilized a new set of mirrors, nominally 99% reflective between 3.0 and 3.4 μm, which were specially coated with a protective layer to prevent the uptake of water. Additionally, the newer mirrors are kept under a flow of dry nitrogen at all times.

The cavity and the idler are locked to maintain resonance by using a detector (Boston Electronics Vigo PVM-10.6-1x1) to monitor the back reflection from the front cavity mirror. The signal from that detector is demodulated with a mixer that is referenced to the PDH locking sideband frequency. The output of that mixer is processed by a lock box, and slow corrections ($<$100 Hz) are sent to a piezo on which one of the cavity mirrors is mounted, to keep the cavity locked onto the idler on slow timescales. Faster corrections (0.1–10 kHz) are sent to a piezo that controls the length of the OPO cavity, thus making small corrections to the frequency of the signal and the idler to keep the idler resonant with the cavity on fast timescales. Based on the observed magnitude of this error signal, there is an extra ∼500 kHz of random noise imposed upon the signal frequency (and therefore also upon the idler frequency) due to the locking of the idler frequency to the external cavity.

Within the external cavity is a liquid nitrogen cooled positive column discharge cell (Black Widow), which was used extensively for VMS in the Oka group at the University of Chicago. An arbitrary waveform generator (Agilent 33120A) creates a sine wave, which is amplified (Techron 7780) and sent to a step-up transformer to drive the plasma. The AC voltage configuration of the plasma modulates the velocity of the ions at a frequency of 40 kHz. Optimal signals for H_3^+ have been observed at 200 mTorr of cell pressure and 170 mA of current. For HCO^+, we used a mixture of 17:3 H_2:CO at a total pressure of 200 mTorr, and a plasma current of 115 mA. CH_5^+ was observed using a 24:1 mixture of H_2:CH_4 at 250 mTorr and the lowest possible current the discharge could maintain, typically ∼110 mA.

The idler radiation from the OPO is coupled through the discharge cell by CaF_2 windows that are aligned at Brewster's angle. The transmitted light through the cavity is detected and demodulated first at the heterodyne frequency of ∼79 MHz by a pair of mixers that are 90° out of phase with each other. The outputs from these mixers are further demodulated via lock-in amplifiers referenced to 80 kHz, twice the plasma modulation frequency. The detection scheme results in four data channels: in-phase and quadrature detection for each of the two mixers. Previously, we have estimated the sensitivity of our spectrometer in the lowest noise channel to be 9.8×10^{-10} cm^{-1} Hz$^{-1/2}$.[9]

Frequency calibration of the idler is accomplished by simultaneously measuring the frequency of the pump and signal beams using an optical frequency comb (Menlo Systems FC-1500, with 100 MHz repetition rate) and determining the difference between them. First, the carrier envelope offset of the comb is tuned to ∼20 MHz to be measured by a frequency counter, although this is not strictly necessary for measuring the idler frequency. The repetition rate of the comb is tuned such that the beat frequency of the signal with the comb is between 25 and 35 MHz, the range of the internal bandpass of the frequency counter used for the signal. Next, the pump is tuned so that its beat with the comb is ∼20 MHz. Then the signs of the beats and carrier envelope offset are determined. The pump is then offset locked to the comb using a frequency to voltage converter to generate an error signal. A wavemeter (Burleigh WA-1500, 0.2 ppm accuracy) then sequentially measures the pump and signal wavelengths to determine the mode numbers of the comb teeth that are closest to these two frequencies.

For spectroscopy, the idler is tuned by changing the repetition rate of the comb. The pump is dragged along with the comb, since it is offset-locked to the comb, but the signal remains relatively constant (aside from slow drift due to thermal variations of the OPO cavity). Without any correction, this would quickly lead to the signal beat with the comb moving out of the bandpass of our frequency counter. Therefore, we double-pass the signal through an acousto-optic modulator (Brimrose IPF-200-80-1600) before sending it to the beat detection unit of the comb. The AOM frequency is adjusted with a feed forward as the comb repetition rate is changed, in order to keep the signal beat within the bandpass. The diffraction efficiency of the AOM allows it to be tuned between 150 and 210 MHz, leading to a shift of the signal frequency by 300 to 420 MHz. When the frequency limit of the AOM is reached, the frequency is increased or decreased by 50 MHz, which corresponds to a 100 MHz change in signal frequency, and the recorded mode number for the signal is incremented or decremented appropriately. The known frequency shift induced by the AOM is subtracted from the signal frequency determined by the comb before the latter is subtracted from the pump frequency to determine the idler frequency.

Data points are acquired with a separation in time of 1.5 s, which is ample time for the lock-in amplifiers to integrate (with a time constant of 300 ms) and the frequency counters to update (at a rate of 1 Hz). These steps are taken to minimize any line dragging by delayed detection. Scanning is performed both from low to high frequency and also from high to low frequency in order to remove any systematic errors caused by line dragging.

The use of the repetition rate for tuning limits the width of a single scan window to ∼900 MHz. In practice, this means that entire Doppler profiles of light ions such as H_3^+ cannot be measured in a single scan. In such cases, preliminary scans are taken without the frequency comb (by directly scanning the voltage on the fiber laser) over a wide range, and then the sub-Doppler features are scanned with the comb. For the heavier ions HCO^+ and CH_5^+, it is possible to record the full Doppler profile within a single scan.

III. RESULTS AND DISCUSSION

A. Lineshape fitting and uncertainty determination

The symmetry of the overall NICE-OHVMS lineshape is odd in both absorption and dispersion. For high precision line center determination, the most important part of the line is the Lamb dips that are evenly spaced about the transition's center frequency. The Lamb dips are a result of the forward- and counter-propagating beam sampling single velocity components on opposite sides of the Doppler profile. The frequency modulation effectively produces three lasers spaced by the modulation frequency: a carrier and two sidebands, one in phase with the carrier, and the other 180° out of phase. Assuming that both the carrier and sidebands are intense enough to contribute to saturation, and that the modulation index is low enough to avoid contributions of higher-order sidebands, there exist four separate Lamb dips that can be detected in absorption, spaced evenly in half integer multiples of the heterodyne frequency about the linecenter. In dispersion, there is also a fifth Lamb dip at the linecenter. In this work, detection was performed at a blended phase that provided the optimal signal-to-noise in all four channels, so the observed Lamb dips are from neither purely absorption nor purely dispersion. However, these individual Lamb dips are not resolved in this experiment because half of the heterodyne frequency is smaller than the full-width at half-maximum of the individual Lamb dips; thus we observe a blend of the five Lamb dips. For

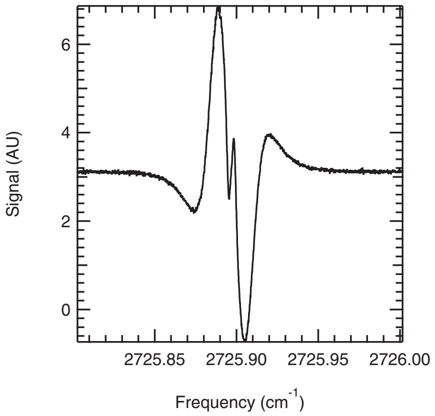

FIG. 2. A representative scan of the R(1,0) transition of H_3^+, illustrating the odd symmetry of the Doppler broadened lineshape. The sharp central feature is composed of five blended Lamb dips. This spectrum was only calibrated with a wavemeter, limiting its accuracy to 70 MHz.

purposes of illustration, the full profile from a single detection channel (not comb calibrated) of an H_3^+ transition is shown in Figure 2, and an example of the fit to the blended Lamb dips in all four simultaneously acquired detection channels is shown in Figure 3.

The derivation of the sub-Doppler lineshape and the fits function have been presented in an earlier paper.[9] However, for clarity, the fitting procedure will be reviewed in brief. The fit is a nonlinear least squares fit using an equation that models the Lamb dips and fits the central portion of the Doppler profile with a cubic polynomial. The four individual channels are fit simultaneously with some shared parameters such as the linecenter to make the four fits self-consistent. The equation describing the Lamb dip shape is a sum of absorption and dispersion components, χ_{abs} and χ_{disp}, respectively,

$$\chi_{tot}(\nu_d) = \chi_{abs}(\nu_d)\sin\theta_h + \chi_{disp}(\nu_d)\cos\theta_h, \tag{1}$$

$$\begin{aligned}\chi_{abs}(\nu_d) = A_1\left[\chi\left(\nu_d - \frac{f_h}{2}\right) - \chi\left(\nu_d + \frac{f_h}{2}\right)\right]\\ + A_2[\chi(\nu_d - f_h) - \chi(\nu_d + f_h)],\end{aligned} \tag{2}$$

$$\begin{aligned}\chi_{disp}(\nu_d) = -A_0\chi(\nu_d) + A_1\left[\chi\left(\nu_d - \frac{f_h}{2}\right) + \chi\left(\nu_d + \frac{f_h}{2}\right)\right]\\ + A_2[\chi(\nu_d - f_h) + \chi(\nu_d + f_h)].\end{aligned} \tag{3}$$

Here A_n denotes the amplitude of the Lamb dip where n is the order, i.e., A_0 is the amplitude of the central Lamb dip, A_1 is the amplitude of the first set of Lamb dips out from the linecenter and so forth. The frequency detuning from the linecenter is given by ν_d, f_h is the heterodyne frequency, and

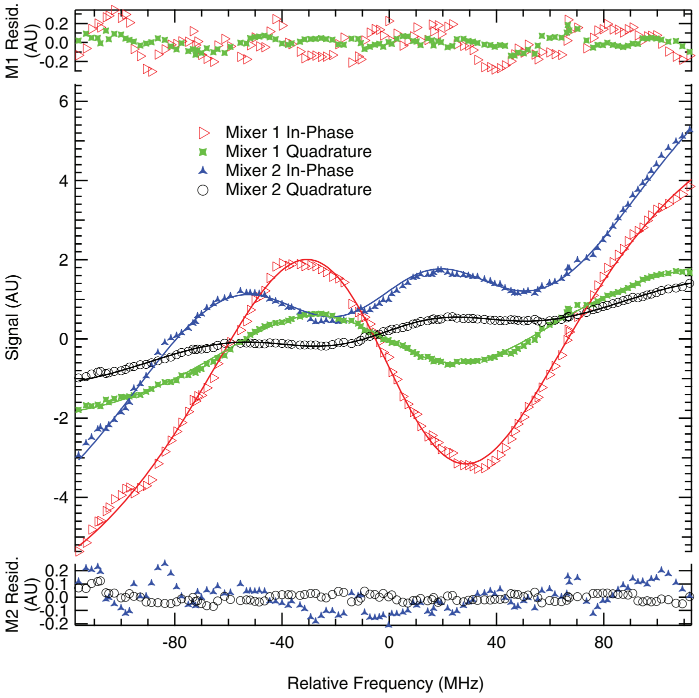

FIG. 3. Enlarged view of the Lamb dips in the R(2,2)^l transition of H_3^+, along with fits to the functional form presented in an earlier paper.[9] The four channels (two from the phase sensitive detector associated with each mixer) are presented in the center of the panel, with the residuals plotted above and below the fit. The data are shown as markers and the fits as solid lines.

θ_h is the heterodyne detection angle. The χ with no subscript is the lineshape for an individual Lamb dip, which depends on the linewdith though it is not explicitly shown in the above equations. In the case of absorption, it takes the form of a linear combination of a Lorentzian and a Gaussian. In the case of dispersion, the Lamb dips are modeled by the result of the Kramers-Krönig relation applied to the linear combination used in absorption. For more information about the fitting, we refer the reader to Crabtree *et al.*[9] Due to the blended nature of the Lamb dips, we were concerned about the potential for small changes in parameters significantly affecting the determination of the linecenter. The only part of the lineshape function that does not rely on a physical model is the fit to the central portion of the Doppler profile. Changing any of those values might make a detectable difference linecenter frequency. To simulate this, we increased the slope of the linear term in all four channels of a scan of the H_3^+ R(1,0) transition by 3 times the uncertainty in the slope returned by the original fit; this corresponds to ∼3% of the total slope. The cubic term was held at zero to prevent it from compensating for the change in the linear term. This increased slope was held fixed as the data were re-fit. This simulation was repeated, decreasing the slope rather than increasing it. The linear term is the largest contributor to the polynomial part of the fit and adjusting it by 3σ in either direction only produced an error of ∼27 kHz (+28 kHz for $+3\sigma$, −26 kHz for -3σ), which is well below the precision of the linecenter derived from the fit (∼80 kHz) or the statistical error resulting from scan-to-scan variability (∼240 kHz).

Each transition was scanned at least five times, and in some cases many more times. The linecenters determined from the fit to each scan were averaged and are reported below as the experimentally determined linecenter. The standard deviation of the individual linecenter measurements was determined and is reported to illustrate the spread of the distribution for linecenters. The standard error, also known as the standard deviation of the mean, which is simply the standard deviation divided by the square root of the number of samples, is also reported as our best estimate of the uncertainty of the average linecenter, under the assumption that the measurements are normally distributed.

TABLE I. Determined line center frequencies, standard deviations, and standard errors of transitions in the ν_2 band of H_3^+. Previous values are given with the source as a footnote. The differences between the measured frequency and the previous best frequency are also reported. All values are in MHz.

Transition	Freq.	St. Dev.	St. Err.	Prev. Value	Diff.
$R(1,1)^l$	80687424.25	1.65	0.62	80687432(10)[a]	− 7.75
R(1,0)	81720377.29	0.86	0.23	81720370(10)[a]	7.29
$R(1,1)^u$	81730020.44	0.84	0.38	81730026(20)[a]	− 5.56
$R(2,2)^l$	82804769.99	0.70	0.31	82804764(10)[a]	5.99
$R(2,1)^l$	82908940.58	2.79	1.25	82908950(150)[b]	− 9.42
$R(2,2)^u$	84635537.25	1.21	0.54	84635542(10)[a]	− 4.75
$R(2,1)^u$	84724846.57	0.85	0.38	84724851(10)[a]	− 4.43
$R(3,3)^l$	84839013.46	0.88	0.39	84839025(10)[a]	− 11.54
$R(3,2)^l$	84907118.76	2.99	1.34	84907160(150)[b]	− 41.24
$R(4,4)^l$	86774648.52	1.28	0.39	86774570(300)[c]	78.52

[a] Reference 19.
[b] Reference 20.
[c] Reference 21.

B. H_3^+ spectroscopy

Our results for ten transitions of the R-branch of the ν_2 band of H_3^+ are reported in Table I. Our results are compared with those from the best available Doppler-limited spectra from the literature. In most cases, these are from the Ph.D. thesis of Wu[19] in the group of Shy, using frequency comb calibration; two transitions not observed by Wu were measured in the FTIR spectra of McKellar and Watson,[20] and the $R(4,4)^l$ transition has not been reported since Oka's work in 1981.[21] In all cases, there is good agreement with the previous values, given the uncertainties of the latter, and in all but two cases the standard error of our measurements is sub-MHz.

With such high precision transition frequency data available, it is interesting to compare the determined transition frequencies to those previously determined to assess the quality of the older work. Especially noteworthy in this comparison is the high degree of accuracy of the FTIR work by McKellar and Watson.[20] As can be seen in Table II, their work is considerably more accurate than their stated uncertainty (150 MHz). Indeed, one of the weakest lines observed in their experiment, $R(3,2)^l$, is only ∼40 MHz away from our determined linecenter.

There has been one other recently reported sub-Doppler measurement of the linecenter of the R(1,0) transition, from Shy's group.[22] They produce H_3^+ in an extended negative glow discharge at 30-80 mTorr and use an OPO in a strong pump, weak probe double pass configuration. Rather than scanning over the transition, calibrating each point, and fitting to determine the line center (as we have done), they instead lock their laser to the Lamb dip and use a frequency comb to measure the laser's frequency while locked. Their reported linecenter is 5.74 MHz lower than ours, a discrepancy which is far larger than the adopted uncertainties (∼250 kHz in both cases). Subsequent measurements of other transitions in Shy's laboratory[23] also differ from our values, with discrepancies that vary in sign but are all of order 5 MHz.

TABLE II. A comparison to the FTIR values as determined by McKellar and Watson.[20] The error listed is the difference between our reported value and that determined by McKellar and Watson.

Transition	Error (MHz)
$R(1,1)^l$	− 5.75
R(1,0)	11.12
$R(1,1)^u$	19.65
$R(2,2)^l$	− 5.03
$R(2,1)^l$	− 12.42
$R(2,2)^u$	− 10.75
$R(2,1)^u$	− 9.43
$R(3,3)^l$	− 3.54
$R(3,2)^l$	− 41.24

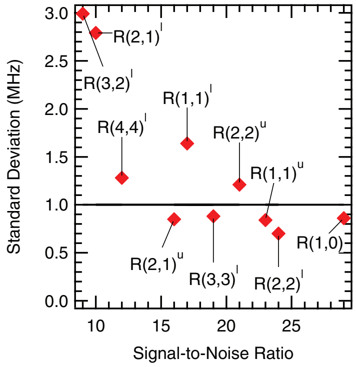

FIG. 4. The standard deviation of the frequency measurements for each H_3^+ transition plotted against the average signal-to-noise ratio of the blended Lamb dip. The horizontal line at 1 MHz is drawn to indicate that the standard deviation is scattered about it for most transitions.

Because of these discrepancies, we have taken great care to characterize potential sources of systematic and random errors in our experiment, as described in Secs. III B 1–III B 4.

1. Effect of signal-to-noise ratio

The precision of the linecenters derived from the fits to our individual scans is typically a few hundred kHz, but can be as low as 70 kHz. Clearly, the fit precision is not the limiting factor in our measurements. To assess the effect of the signal-to-noise ratio of the Lamb dips on our linecenter measurements, the average signal-to-noise ratio of the blended Lamb dips for each transition is plotted against the standard deviation of its linecenter, as determined from several scans over each transition, in Figure 4.

All except the two weakest transitions are clustered near the horizontal line at 1 MHz; these two transitions have fits that are less well determined, which is the cause of the greater uncertainty in their linecenters. No gradual trend in the standard deviation as a function of signal-to-noise ratio is evident, indicating that there is some other dominant effect limiting the standard deviation for all but the weakest lines.

2. Effect of asymmetry

In Crabtree *et al.*,[9] the effect of asymmetry on the determined transition frequency was left as an unanswered question due to the fact that the accuracy was limited to ∼70 MHz by the wavemeter calibration. In that work, several simulated asymmetries were used to intentionally affect the ability to fit the lines, though no physical meaning or mechanism was used in the simulations. The largest magnitude effects were found to cause a few MHz shift in transition frequency, and this was interpreted as a firm upper limit on the potential effect of asymmetry.

With the inclusion of a frequency comb, the effect caused by asymmetry can now be better characterized. For this purpose, the R(1,0) transition was scanned many times on many different days to study the asymmetry. In all cases, the fit residuals do not indicate any obvious asymmetry in the Lamb dips, which would have the largest effect in the determination of linecenters. Instead, the Doppler profiles clearly exhibit asymmetric lineshapes, and the amount and sign of this asymmetry changes over time and from scan to scan.

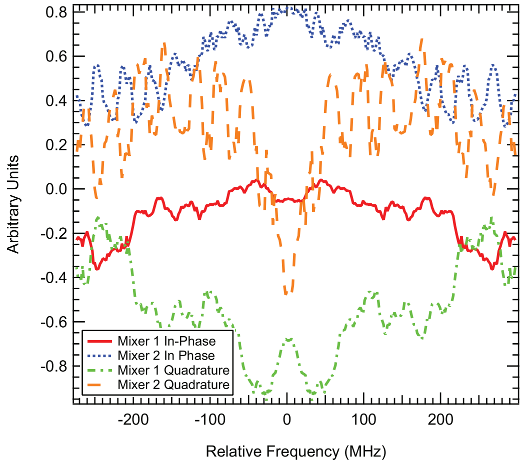

FIG. 5. A typical graph depicting the inversion residuals. It is evident that they are symmetric about the transition frequency, due to the process of additively imprinting the noise of one half of the line on the other. These data are used to calculate characteristic parameters of the asymmetry.

To quantify the amount of asymmetry (deviation from the expected odd symmetry) in each scan, we first trimmed each channel of a scan to an equal number of data points on each side of the line center, and shifted it by the y-offset determined from the fit. A copy of the data was made and then the frequency axis was inverted, mirroring the data across the linecenter. The original scan channels and mirrored scan channels were added together to create a graphical representation of the asymmetry (Figure 5), which we refer to as the inversion residuals.

From the inversion residuals, two parameters were determined. The first, the offset asymmetry parameter, was defined as the average value of all four channels. The average value from each individual channel was determined, then these four averages were averaged together. The offset asymmetry parameter was defined in this manner to capture the effect that each individual channel would have on the simultaneous least squares fit of all four channels. In the case of a perfectly symmetric line, the offset parameter would have a value of zero because the odd lineshape would cancel itself out. Negative values of the offset parameter indicate that the lower frequency (negative-going) lobe is stronger than the higher frequency lobe; whereas, positive values indicate stronger lobes on the high frequency side.

The second parameter, which we refer to as the high-low asymmetry parameter, represents the average difference between the maximum and minimum values for each of the four inversion residuals. The high-low parameter is intended to capture an imbalance in the shape of the line. Such an imbalance would manifest itself in the inversion residuals as a

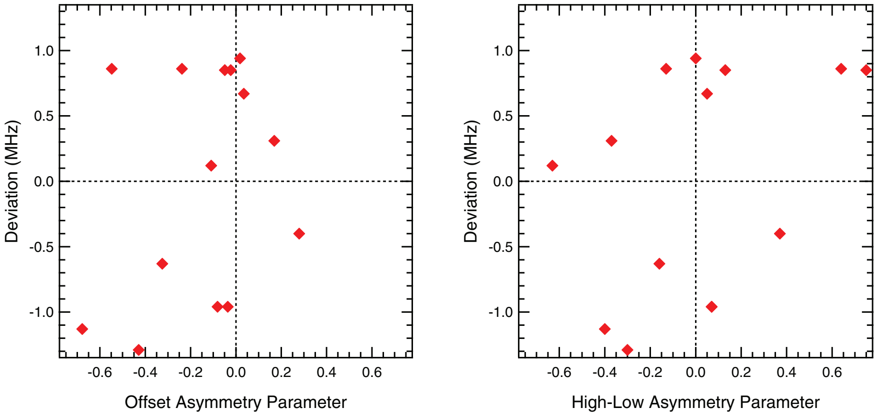

FIG. 6. The deviation of the linecenter of a given scan from the mean value versus the offset asymmetry parameter (left panel) and the high-low asymmetry parameter (right panel). The dotted lines shows the zero crossings to emphasize the insensitivity of the sign of the difference to the sign of the asymmetry parameter.

sloped or curved line. The magnitude of the slope is parameterized by differencing the maximum and minimum values of the residuals. These differences for each data channel are averaged just like the offset parameter. As above, the sign indicates which lobe was larger.

In Figure 6, the deviation of the linecenter of an individual scan from the mean of all R(1,0) scans is plotted against these two asymmetry parameters. The data show no clear trend, not even a consistent change in the sign of the deviation with the sign of the asymmetry parameter. Instead, the data are well scattered. If the scan-to-scan reproducibility in the linecenter of $\sim$1 MHz is due to the changing asymmetry, it must depend on the asymmetry in a way that is not captured by these particular metrics.

In any case, the fact that the amount and the sign of the asymmetry change from scan to scan strongly suggests that the asymmetry cannot cause a systematic shift in the linecenter in an ensemble of scans. Instead, we conclude that the impact of the asymmetry manifests itself as a random error, reflected in the magnitude of the standard deviation of the linecenter determinations.

3. Pressure shift

Given the difference in pressure between our experiment and Shy's, we decided to measure the linecenter of the R(1,0) transition at three different pressures to rule out the possibility of an unexpectedly large pressure shift. The results are displayed in Table III, and show the same linecenter (within uncertainties) from pressures between 200 and 500 mTorr. The largest pressure shift consistent with the data, determined from the lower bound of the 200 mTorr data (81 720 377.06 MHz) and the upper bound of the 500 mTorr data (81 720 377.86 MHz), would be 2.7 MHz/Torr at the 1σ level. This would mean our linecenter measured at 200 mTorr could be too high by at most 0.4 MHz from the value at 55 mTorr (the midpoint of Shy's range).

4. Comb calibration test

In order to rule out any unexpected problems with the calibration of our optical frequency comb, we wished to measure another transition that had been previously measured with high precision. Since there are no other ion transitions known to this level of accuracy in the mid-infrared, we pursued spectroscopy of neutral methane, which has comb calibrated lines in our spectral region that are known to high accuracy and precision.[24]

Obviously, NICE-OHVMS could not be performed because the instrument cannot modulate the velocity of a neutral molecule. Ordinary NICE-OHMS is challenging to perform with a fiber based EOM due to strong baseline drifts from residual amplitude modulation (RAM),[25,26] so an additional layer of modulation is necessary. The logical choice was wavelength modulation, but our pump laser must be locked to the comb and our use of an external cavity requires feedback to the OPO cavity length, which fixes the frequency of the signal. Therefore, the cavity was removed and the back reflection detector was used in a double pass configuration for wavelength modulated heterodyne spectroscopy.

Without the need to apply feedback to the OPO cavity length, this control could be used to apply a dither necessary to modulate the wavelength of the signal, and hence also the idler. A 1.4 kHz dither was applied to the cavity, and the lock-in amplifiers were referenced to three times the dither frequency. This allowed the system to be insensitive to the Doppler profile of the methane transition. The chosen target

TABLE III. Measured linecenters of the R(1,0) transition of H_3^+ at different pressures.

Pressure (mTorr)	Frequency (MHz)
200	81720377.29(23)
350	81720377.47(32)
500	81720377.44(42)

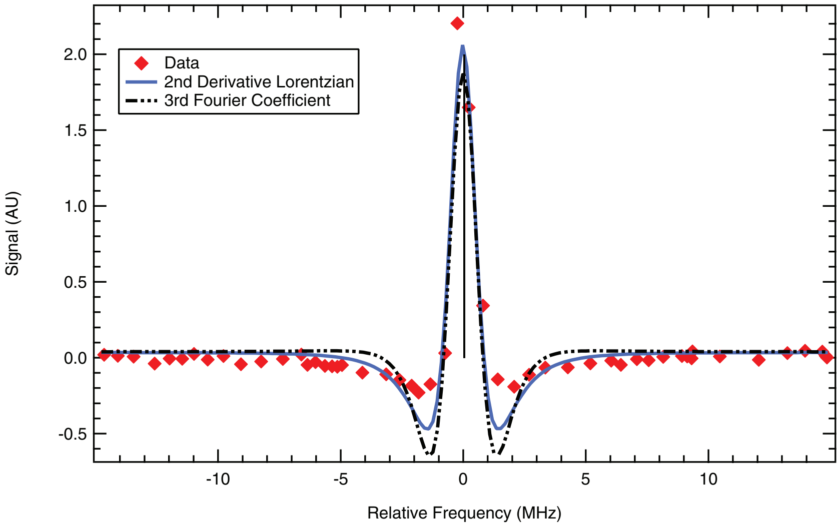

FIG. 7. The comb calibrated central Lamb dip of the $F_1^{(2)}$ component of the P(7) transition in the ν_3 band of methane. Fits to an analytical expression of the third Fourier coefficient for a wavelength modulated dispersion signal (dashed curve) and to the second derivative of a Lorentzian (solid curve) are shown. The black line is the linecenter determined by Takahata *et al.*[24]

was the $F_1^{(2)}$ component of the P(7) transition in the ν_3 band, which has been reported to kHz precision.[24] A few mTorr of methane was leaked into the discharge cell, and the central Lamb dip, which corresponds only to dispersion, was recorded.

The result of our methane spectroscopy is shown in Figure 7. We fit the data to both the third Fourier coefficient for a Lorentzian dispersion lineshape[27] and a simple second derivative of a Lorentzian. While neither fit perfectly reproduces the observed lineshape, the derived linecenters compare very favorably with the previous work of Takahata *et al.*[24] The linecenter as determined by the second derivative fit is 5 ± 22 kHz less than Takahata's, and that from the third Fourier coefficient fit was 10 ± 30 kHz greater than Takahata's. Even by the roughest approximation of simply picking the highest recorded point and calling it the line center, the error is only 222 kHz. Therefore, we conclude that our frequency comb system is working well, and is not the limiting source of error in our ion measurements.

C. HCO^+ spectroscopy

While there are no molecular ion transitions in the mid-infrared previously measured with sub-MHz accuracy, there are ions (such as HCO^+) for which pure rotational transitions are known with such accuracy. By measuring multiple rovibrational transitions and using combination differences, we can compare the results with observed rotational transitions as yet another check on the accuracy of our ion transition measurements.

We have recently performed such "indirect rotational spectroscopy" using Doppler-limited spectra of HCO^+ with comb calibration.[10] Ultimately, we expect this approach to be a useful tool for inferring rotational spectra that have not been directly measured, in order to support astronomical observations with far-infrared/THz instruments such as SOFIA and ALMA. Here, we simply extend our previous work on HCO^+ to demonstrate the accuracy of our sub-Doppler NICE-OHVMS spectra.

The P(5) and R(3) lines from the ν_1 band of HCO^+ were measured (see Figure 8) in order to determine the energy level separation between J = 5 and J = 3 in the ground vibrational state. The two transitions were measured multiple times to determine their linecenters, which were 92 145 080.8(4) MHz for P(5) and 92 947 717.3(5) MHz for R(3). The difference between these frequencies, 802 636.5(7) MHz, agrees within its uncertainty with the sum of the J = 3 → 4 and J = 4 → 5 pure rotational transitions observed by Cazzoli *et al.*,[28] 356 734.2230(15) + 445 902.8721(15) = 802 637.0951(21) MHz. The excellent agreement of this combination difference strongly suggests that our experiment does not suffer from any systematic errors that differ from one line to the next, beyond those at the sub-MHz level that result from scan-to-scan variations.

It is interesting to note that the P(5) and R(3) frequencies determined from the Lamb dips are both ~4 MHz lower than those determined from our earlier Doppler-limited, single-pass measurements.[10] This difference is evidently due to an asymmetry in the drift velocity of the ions on the two half-cycles of the AC discharge; such an asymmetry results in a net Doppler shift in the single-pass measurements, but the present measurements are insensitive to this effect due to the bi-directional nature of the cavity and the fact that the Lamb dips are located symmetrically about the zero-velocity component.

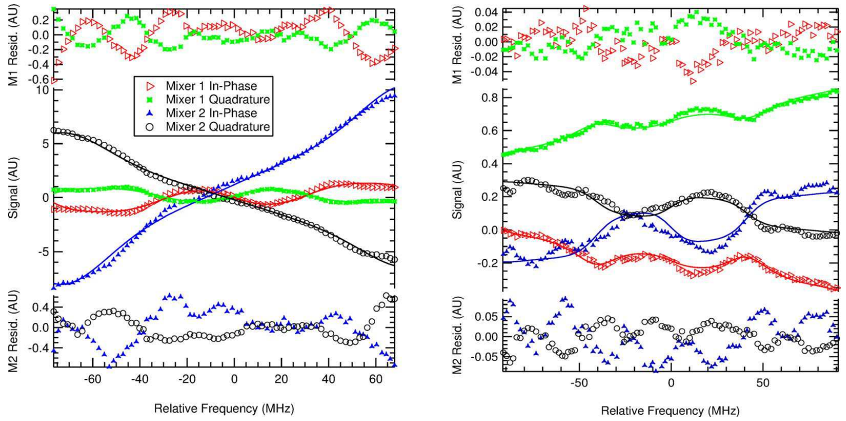

FIG. 8. Results from fitting the Lamb dips from the P(5) transition (left) and R(3) transition (right) of HCO^+. The four channels are presented with residuals from each mixer plotted above and below the fit. The data are shown as markers and the fits as solid lines.

D. CH_5^+ spectroscopy

An important future application of this technique will be high-precision and high-accuracy spectroscopy of highly congested spectra, such as that of CH_5^+. The infrared spectrum of this ion was first reported by the Oka group in 1999,[3] and consisted of about 900 spectral lines between 2770 and 3150 cm^{-1}, with no discernable patterns. The spectrum is complicated by the fact that CH_5^+ does not have a single equilibrium structure, but can sample all $5! = 120$ equivalent minima of C_s symmetry on its potential energy surface, as well as the C_s and C_{2v} saddle points that interconnect them. Many important theoretical studies (see, e.g., Refs. 29–35) have been undertaken since the publication of Oka's spectrum, and low-resolution spectra have been reported covering different frequency ranges[36] and temperatures.[31] Despite nearly 15 years of effort since the Oka group's first report, the community seems to be no closer to an assignment of Oka's spectrum.

One possible way forward is to search for four-line combination differences in the spectrum, that is, to look for two pairs of transitions with the same combination difference. This would represent an experimental measure of the separation between two rotational energy levels. If spectra with reliable intensities could be obtained at different temperatures, it may be possible to begin assembling an energy level diagram. Comparison between such experimentally determined energy levels and those predicted by sophisticated theoretical techniques might eventually lead to an assignment. However, the frequency uncertainties in the Oka group spectrum range from 90 to 180 MHz, as their measurements were limited by their Doppler linewidth, relatively low signal-to-noise ratio, and traditional frequency calibration techniques (reference gases). Given the line density, there are almost innumerable pairs of transitions whose combination differences agree within this level of uncertainty, and the vast majority of those are accidental rather than true four-line combination differences.

Progress on this front will necessitate remeasurements of CH_5^+ transitions with considerably higher accuracy and precision. The Schlemmer group recently made the first report of a high-resolution spectrum since Oka's, using a cryogenically cooled ion trap and laser-induced reaction spectroscopy.[37] With their smaller Doppler linewidth (~70 MHz at 20 K) and frequency comb calibration, they determined the central frequency of a CH_5^+ transition at 2932.998460 cm^{-1} to within ~200 kHz. An alternative approach, which we are pursuing, is to obtain sub-Doppler spectra in a positive column discharge.

Our experiment uses the same discharge cell that was used for the first report of the CH_5^+ spectrum. We are attempting to reproduce the plasma conditions as closely as possible, but the CH_5^+ signal is exquisitely sensitive to the exact discharge conditions and we are still in the process of optimizing the system. Nevertheless, we have obtained several comb-calibrated scans of the transition Oka's group reported at 2898.008 cm^{-1}, with a signal-to-noise ratio that is somewhat higher than that of the Oka group. Given our ~10-fold longer effective pathlength (from the cavity enhancement) and the fact that our noise level should be lower than Oka's (because of the frequency modulation), we suspect that further tuning of plasma conditions should lead to significantly stronger signals.

The average of five spectra of this transition is displayed in Figure 9, and represents the first sub-Doppler spectrum of CH_5^+. A fit to the averaged spectrum yields a linecenter of 86 880 178.469(126) MHz; the precision of this fit is more than two orders of magnitude lower than the ~90 MHz uncertainty from the Oka group's measurements. The Schlemmer group has independently measured a CH_5^+ line centered at 86 880 178.22(63) MHz.[38] This transition is only ~240 kHz different from our measurement, which agrees with our transition frequency within 1σ of their uncertainty and 2σ of our uncertainty. This provides independent confirmation of the accuracy of our technique. The weakness of the CH_5^+ Lamb dip, compared to those seen in H_3^+ and HCO^+, is likely the result of the lower transition dipole moment of CH_5^+. Although we are not aware of any predictions for the transition dipole moment, the MULTIMODE calculations of Huang *et al.*[31] show

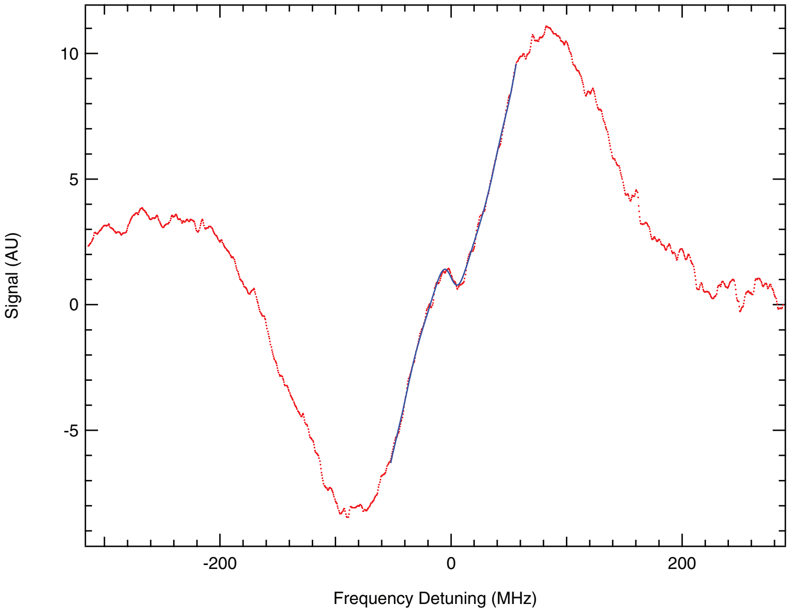

FIG. 9. Comb-calibrated NICE-OHVMS spectrum of Oka's "2898.008 cm^{-1}" transition of CH_5^+. The data are shown as red dots and the fit to the Lamb dip is shown as a blue line.

an integrated band intensity of ∼50 km/mol, which is considerably lower than the calculated value of 227 km/mol[39] for HCO^+.

In the future, we hope to increase the Lamb dip depth by increasing the power injected into our cavity and/or by obtaining mirrors with higher reflectivity. Even if this is not effective, we expect to be able to improve the signal-to-noise ratio on the Lamb dip by further optimization of the plasma conditions and by reducing technical noise sources in our spectrometer.

IV. CONCLUSIONS

We have demonstrated the first instrument capable of routine sub-Doppler spectroscopy of a wide variety of molecular ions, offering both high precision from optical saturation and high accuracy from optical frequency comb calibration. Using this instrument, ten lines of the doubly degenerate ν_2 band of H_3^+ have been measured, eight of which have sub-MHz uncertainties. Two lines from the ν_1 band of HCO^+ have also been measured with similar uncertainties, and their combination difference is in excellent agreement with pure rotational spectroscopy. The first sub-Doppler spectrum of CH_5^+ has also been recorded with sub-MHz precision, a substantial improvement over the ∼90 MHz uncertainty of the initial detection in the Oka group.[3]

Because our measurements of H_3^+ transitions disagree with those reported by Shy's group[22,23] by ∼5 MHz, we have conducted an extensive analysis of potential sources of experimental error in our instrument. The limiting factor in our frequency determinations appears to be scan-to-scan variability that is not yet understood, but results in a standard deviation among individual scans of ∼1 MHz. The standard error of a set of scans can be reduced to ∼250 kHz by performing multiple scans. The scan-to-scan variability may be due to varying asymmetry of the Doppler-broadened lineshape, but our attempts to find correlations between the center frequency deviations and measures of the asymmetry have not been successful. All indications are that our determined standard errors accurately capture the random errors in our measurements. This conclusion is further supported by the excellent combination difference between the HCO^+ transitions we measured. We have also excluded the possibility of systematic errors due to pressure shift, and we have confirmed the accuracy of our frequency comb calibration within tens of kHz using a known transition of methane. Most importantly, the independent measurement of the same CH_5^+ transition by Schlemmer's group[38] is the strongest evidence that our technique does not exhibit errors of order 5 MHz, which provides us with the utmost confidence in the values that we have reported.

The instrument is currently limited in wavelength coverage by the coverage of our OPO module (3.2–3.9 μm), and to some extent by the coatings of our external cavity mirrors (nominally 3.0–3.4 μm, but usable outside this range). However, OPO modules are available that cover 2.3–4.6 μm, and it should be possible to produce moderate reflectivity (∼99.0–99.7%) cavity mirrors across that range. Considering the chemical versatility of the positive column discharge and the general applicability of direct absorption/dispersion spectroscopy, our technique will enable the high-precision, high-accuracy spectroscopy of a wide variety of molecular ions. Possible applications include tests of high accuracy *ab initio* calculations, supporting astronomical observations, and aiding in the assignment of congested spectra.

ACKNOWLEDGMENTS

We would like to acknowledge support from a National Science Foundation Chemistry grant (CHE 12-13811) and a NASA Laboratory Astrophysics grant (NNX13AE62G). J.N.H. is grateful for the support from a Robert & Carolyn Springborn Fellowship and an NSF Graduate Research Fellowship (DGE 11-44245 FLLW). J.N.H. and A.J.P. are grateful to Mr. George S. Kocheril for assisting with the HCO^+ and CH_5^+ data acquisition. We also are especially thankful to Professor Takeshi Oka for providing the liquid nitrogen cooled discharge cell and associated pumps and electronics.

[1] C. Gudeman, M. Begemann, J. Pfaff, and R. Saykally, Phys. Rev. Lett. **50**, 727 (1983).
[2] S. K. Stephenson and R. J. Saykally, Chem. Rev. **105**, 3220 (2005).
[3] E. T. White, J. Tang, and T. Oka, Science **284**, 135 (1999).
[4] T. Amano, J. Chem. Phys. **79**, 3595 (1983).
[5] A. A. Mills, B. M. Siller, and B. J. McCall, Chem. Phys. Lett. **501**, 1 (2010).
[6] B. M. Siller, A. A. Mills, and B. J. McCall, Opt. Lett. **35**, 1266 (2010).
[7] B. M. Siller, M. W. Porambo, A. A. Mills, and B. J. McCall, Opt. Express **19**, 24822 (2011).
[8] L.-S. Ma, J. Ye, P. Dubé, and J. L. Hall, J. Opt. Soc. Am. B **16**, 2255 (1999).
[9] K. N. Crabtree, J. N. Hodges, B. M. Siller, A. J. Perry, J. E. Kelly, P. A. Jenkins, and B. J. McCall, Chem. Phys. Lett. **551**, 1 (2012).
[10] B. M. Siller, J. N. Hodges, A. J. Perry, and B. J. McCall, "Indirect rotational spectroscopy of HCO^+," J. Phys. Chem. A **117**(39), 10034–10040 (2013).
[11] M. Pavanello, L. Adamowicz, A. Alijah, N. F. Zobov, I. I. Mizus, O. L. Polyansky, J. Tennyson, T. Szidarovszky, A. G. Császár, M. Berg, A. Petrignani, and A. Wolf, Phys. Rev. Lett. **108**, 023002 (2012).
[12] J. Komasa, K. Piszczatowski, G. Łach, M. Przybytek, B. Jeziorski, and K. Pachucki, J. Chem. Theory Comput. **7**, 3105 (2011).
[13] P. Pyykkö, K. Dyall, A. Császár, G. Tarczay, O. Polyansky, and J. Tennyson, Phys. Rev. A **63**, 024502 (2001).
[14] T. R. Geballe and T. Oka, Nature **384**, 334 (1996).
[15] N. Indriolo and B. J. McCall, Astrophys. J. **745**, 91 (2012).
[16] P. Drossart, J.-P. Maillard, J. Caldwell, S. J. Kim, J. K. G. Watson, W. A. Majewski, J. Tennyson, S. Miller, S. K. Atreya, J. T. Clarke, J. H. Waite, and R. Wagener, Nature **340**, 539 (1989).
[17] D. Rego, N. Achilleos, T. Stallard, and S. Miller, Nature **399**, 121 (1999).
[18] C. Savage, F. Dong, and D. J. Nesbitt, in *60th International Symposium on Molecular Spectroscopy, Talk MG06* (2005).
[19] K.-Y. Wu, "Precision Measurement of the ν_2-band of triatomic hydrogen molecular ion H_3^+," Ph.D. thesis, National Tsing Hua University, 2008.
[20] A. McKellar and J. Watson, J. Mol. Spectrosc. **191**, 215 (1998).
[21] T. Oka, Philos. Trans. R. Soc. London, Ser. A **303**, 543 (1981).
[22] H.-C. Chen, C.-Y. Hsiao, J.-L. Peng, T. Amano, and J.-T. Shy, Phys. Rev. Lett. **109**, 263002 (2012).
[23] H.-C. Chen, J.-L. Peng, T. Amano, and J.-T. Shy, in *68th International Symposium on Molecular Spectroscopy, Talk MG05* (2013).
[24] K. Takahata, T. Kobayashi, H. Sasada, Y. Nakajima, H. Inaba, and F.-L. Hong, Phys. Rev. A **80**, 032518 (2009).
[25] A. Foltynowicz, W. Ma, and O. Axner, Opt. Express **16**, 14689 (2008).
[26] A. Foltynowicz, I. Silander, and O. Axner, J. Opt. Soc. Am. B **28**, 2797 (2011).
[27] J. Westberg, P. Kluczynski, S. Lundqvist, and O. Axner, J. Quant. Spectrosc. Radiat. Transf. **112**, 1443 (2011).
[28] G. Cazzoli, L. Cludi, G. Buffa, and C. Puzzarini, Astrophys. J., Suppl. Ser. **203**, 11 (2012).
[29] P. R. Bunker, B. Ostojić, and S. Yurchenko, J. Mol. Struct. **695–696**, 253 (2004).
[30] Z. Jin, B. J. Braams, and J. M. Bowman, J. Phys. Chem. A. **110**, 1569 (2006).
[31] X. Huang, A. B. McCoy, J. M. Bowman, L. M. Johnson, C. Savage, F. Dong, and D. J. Nesbitt, Science **311**, 60 (2006).
[32] M. P. Deskevich, A. B. McCoy, J. M. Hutson, and D. J. Nesbitt, J. Chem. Phys. **128**, 094306 (2008).
[33] C. E. Hinkle and A. B. McCoy, J. Phys. Chem. A **112**, 2058 (2008).
[34] X.-G. Wang and T. Carrington, Jr., J. Chem. Phys. **129**, 234102 (2008).
[35] C. E. Hinkle, A. S. Petit, and A. B. McCoy, J. Mol. Spectrosc. **268**, 189 (2011).
[36] O. Asvany, P. Kumar, B. Redlich, I. Hegemann, S. Schlemmer, and D. Marx, Science **309**, 1219 (2005).
[37] O. Asvany, J. Krieg, and S. Schlemmer, Rev. Sci. Instrum. **83**, 093110 (2012).
[38] S. Schlemmer, private communication (2013).
[39] J. M. L. Martin, P. R. Taylor, and T. J. Lee, J. Chem. Phys. **99**, 286 (1993).

Appendix D

Communication: High Precision Sub-Doppler Infrared Spectroscopy of the HeH^+ Ion

This appendix is a complete reprint with permission from Adam J. Perry, James N. Hodges, Charles R. Markus, G. Stephen Kocheril, Benjamin J. McCall. Journal of Chemical Physics, 141 (2014) 101101, Copyright American Physical Society 2014.

THE JOURNAL OF CHEMICAL PHYSICS **141**, 101101 (2014)

Communication: High precision sub-Doppler infrared spectroscopy of the HeH$^+$ ion

Adam J. Perry,[1] James N. Hodges,[1] Charles R. Markus,[1] G. Stephen Kocheril,[1]
and Benjamin J. McCall[1,2,a)]
[1]*Department of Chemistry, University of Illinois, Urbana, Illinois 61801, USA*
[2]*Departments of Astronomy and Physics, University of Illinois, Urbana, Illinois 61801, USA*

(Received 30 July 2014; accepted 28 August 2014; published online 9 September 2014)

The hydrohelium cation, HeH$^+$, serves as an important benchmark for *ab initio* calculations that take into account non-adiabatic, relativistic, and quantum electrodynamic effects. Such calculations are capable of predicting molecular transitions to an accuracy of ∼300 MHz or less. However, in order to continue to push the boundaries on these calculations, new measurements of these transitions are required. Here we measure seven rovibrational transitions in the fundamental vibrational band to a precision of ∼1 MHz using the technique of Noise Immune Cavity Enhanced Optical Heterodyne Velocity Modulation Spectroscopy. These newly measured transitions are included in a fit to the rotation-vibration term values to derive refined spectroscopic constants in the v = 0 and v = 1 vibrational states, as well as to calculate rotation-vibration energy levels with high precision. © *2014 AIP Publishing LLC*. [http://dx.doi.org/10.1063/1.4895505]

I. INTRODUCTION

Composed of the two most abundant elements in the universe, the HeH$^+$ cation is predicted to be among the first molecules ever formed,[1,2] which makes this species of vital significance to chemical models of the early universe. Astronomical observations targeted at HeH$^+$ have yet to yield an unequivocal detection of this molecule. The difficulty in detecting this species is attributed to the many chemical processes that compete with the formation of HeH$^+$, ultimately resulting in a low abundance of this molecule. However, this molecule is easily formed in laboratory plasmas, which has spurred much experimental work on this fundamental species.

First discovered in 1925,[3] the HeH$^+$ ion has been the subject of many spectroscopic studies. In 1979, the first rovibrational spectrum of this molecule was acquired by Tolliver and co-workers, who observed the P(12) and P(13) lines in the fundamental vibrational band as well as the P(9)-P(11) transitions in the $v = 2 \leftarrow 1$ hot band with an accuracy of ~ 0.002 cm^{-1}.[4] In 1982, Bernath and Amano reported the first observation of the low J transitions in the fundamental band, covering the P(4)-R(4) rovibrational transitions.[5] After this work various studies of hot bands were published, including transitions from bound to quasibound states as well as quasibound to quasibound transitions.[6–8] In 1989, Crofton and co-workers measured a few new transitions in the fundamental band along with several lines in the $v = 2 \leftarrow 1$ hot band as well as in the fundamental bands of the ^{3}HeH$^+$, ^{4}HeD$^+$, and ^{3}HeD$^+$ isotopologues.[9] Pure rotational studies were first carried out by Liu *et al.* where the $J = 7 \leftarrow 6$ transition was measured,[10] followed by the measurement of $J = 1 \leftarrow 0$ and $J = 2 \leftarrow 1$ by Matsushima *et al.*[11] as well as some low J rotational transitions of the ^{3}HeH$^+$, ^{4}HeD$^+$, and ^{3}HeD$^+$ isotopologues. Higher J rotational transitions were measured by Liu and Davies[8,12] with J as high as 25.

From a theoretical standpoint the HeH$^+$ ion is a relatively simple species that is isoelectronic to H$_2$. This makes HeH$^+$ an important benchmark molecule for high-level *ab initio* calculations that take into account not only non-adiabatic corrections to the Born Oppenheimer approximation, but also relativistic and quantum electrodynamic (QED) effects. Recent *ab initio* calculations by Pachucki and Kosama,[13] which have treated the non-adiabatic corrections using Non-Adiabatic Perturbation Theory as well as the relativistic (α^2) and leading QED (α^3) corrections to the Born-Oppenheimer approximation, have been able to reproduce many experimentally measured rovibrational transitions with an accuracy on the order of 0.01 cm^{-1}(∼300 MHz). This sort of accuracy is only currently achievable for a select few molecular systems, namely, H_2, H_2^+, H_3^+, and HeH$^+$.[13–17] In order to predict transition frequencies with accuracies on the level of 0.001 cm^{-1}or better for more complicated systems, it is imperative that the theoretical treatment of the aforementioned benchmark systems be well developed. Since theory must be informed by experiment to push the boundaries of these calculations, experimentalists need to provide highly accurate and precise measurements of molecular transitions for these species.

The HeH$^+$ molecule has also proven to be a useful benchmark system for theoretical treatments that go beyond the Born-Oppenheimer approximation.[18] These methods rely on using a set of correlated Gaussian functions that are functions of the separations between the nuclei and electrons, thus eliminating the traditional separation of the nuclear and electronic wavefunctions of the Born-Oppenheimer approximation. Within this framework the authors also developed algorithms for calculating the complete relativistic correction for this molecule.[19,20] To date, these sorts of calculations have

---

[a)] Electronic mail: bjmccall@illinois.edu only been performed on states with no angular momentum (i.e., "rotationless" states).

Another approach has been to develop a global empirical potential that is based on the available spectroscopic data.[21] This work used all available spectroscopic data from all isotopomers in a fit to a modified Lennard-Jones potential that is able to provide the correct behavior at large internuclear separations near the dissociation limit. This approach also allows for experimental determination of the Born-Oppenheimer breakdown functions which showed reasonable agreement with a fitted theoretical potential based on the calculations of Bishop and Cheung.[22]

II. EXPERIMENTAL

The instrument used in this work has been described in detail in Ref. 23 and therefore will be described here only briefly. For this work, we used a technique that has been previously developed in our lab called Noise Immune Cavity Enhanced Optical Heterodyne Velocity Modulation Spectroscopy (NICE-OHVMS)[23–25] which combines the high sensitivity of Noise Immune Cavity Enhanced Optical Heterodyne Molecular Spectroscopy (NICE-OHMS)[26] with the ion/neutral discrimination of velocity modulation spectroscopy.[27]

The spectrometer is based on a commercially available continuous wave optical parametric oscillator (Aculight Argos 2400 SF) that is tunable across the 3.2–3.9 μm range. The pump laser (Koheras Adjustik Y-10) is phase modulated at a frequency of ~80 MHz to produce a pair of RF sidebands that are imprinted onto the idler wave. The idler wave is then coupled into an external optical cavity (finesse of ~150) which surrounds a liquid nitrogen cooled positive column discharge cell, in which ions of interest are produced from precursor gasses (a 2 Torr mixture of H_2 and He in a 1:100 ratio) and where their absorption profiles are velocity modulated. Light transmitted through the cavity is detected by a fast photodiode detector (Boston Electronics Vigo PVM-10.6-1×1), from which the signal is demodulated at the same frequency used to generate the 80 MHz sidebands, using a pair of frequency mixers that are 90° out of phase with one another. Further demodulation of the mixer outputs at twice the velocity modulation frequency (~80 kHz) is accomplished by a pair of lock-in amplifiers, which acts to recover the velocity modulation information.

Frequency calibration of our spectra was accomplished using an optical frequency comb (Menlo Systems FC-1500 with 100 MHz repetition rate) to measure the difference in frequency of the pump and signal beams at each point. Initial measurements of the frequencies of both beams (ten measurements for each) are performed using a near-infrared wavemeter (Burleigh WA-1500) to determine the mode number of the nearest comb tooth. The accuracy of the wavemeter was enhanced by measuring nearby reference lines of CH_4.[28] These reference line frequencies are all determined to within ~5 MHz and any systematic errors introduced by the wavemeter can be corrected to ensure that the proper comb mode numbers are determined.

III. RESULTS

Figure 1 shows a typical NICE-OHVMS spectrum of the P(1) transition of HeH^+ at 85258146.86(35) MHz. The lineshapes have an odd symmetry resulting from the heterodyne detection and velocity modulation schemes. The narrow features near the center of the lines are blends of several individual Lamb dips that are spaced by half-integer multiples of the heterodyne frequency about the center of the transition. To extract the transition line centers, we fit the data from all four of the detection channels simultaneously (Figure 2) with some shared parameters between the data channels such as the line center, full-width of the blended feature, and the heterodyne detection angle. Further information regarding the fitting routines has been given by Hodges *et al.*[23]

Table I shows that our measurements exhibit good agreement with the values measured by Bernath and Amano as all measured transitions lie within or only slightly outside their 30–60 MHz claimed uncertainties. However, in this work we

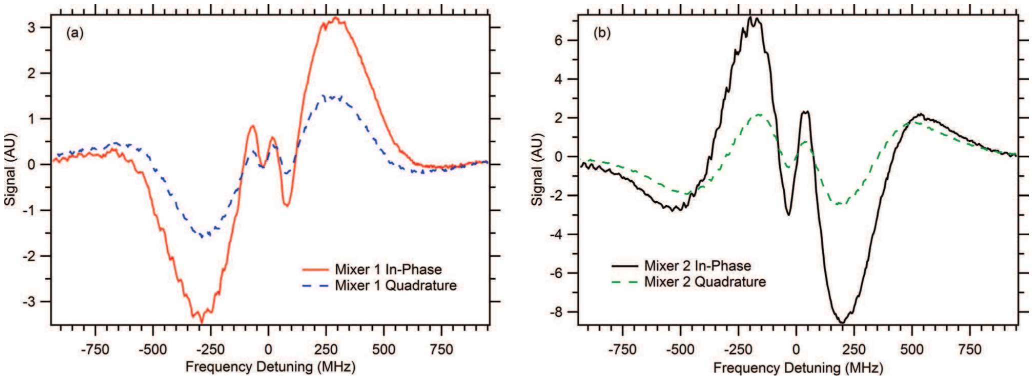

FIG. 1. Typical NICE-OHVMS scan of the P(1) fundamental band transition of HeH^+ showing the central Lamb dip feature sitting on top of the Doppler profile of the line. Signals from each of the four detection channels are shown with the in-phase (red solid trace) and quadrature (blue dashed trace) channels from mixer 1 plotted in panel (a) and the in-phase (black solid trace) and quadrature (green dashed trace) channels of mixer 2 in panel (b).

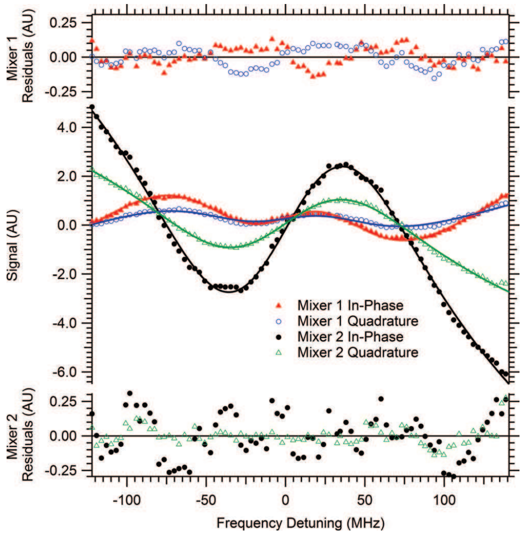

FIG. 2. Frequency comb calibrated scan of the central sub-Doppler Lamb dip feature in the P(1) rovibrational transition of HeH^+, along with a simultaneous fit of all four data acquisition channels. Colored markers represent the experimental data, while the colored solid traces show the fit of the data to the equation outlined in Hodges *et al.*[23] Fit residuals from each detection channel are plotted on the upper (channels from mixer 1) and lower (channels from mixer 2) axes. For clarity, only every third data point is shown.

have improved the precision on these measurements by two orders of magnitude. For all of the measurements we were able to obtain precisions on the order of 1 MHz for the line centers due to both our ability to saturate the transitions which allows us to fit the relatively narrow sub-Doppler features, and the frequency calibration provided by the optical frequency comb which allows us to go far beyond the typical tens of MHz measurement uncertainty provided by mid-infrared wavemeters and Doppler-broadened reference gas lines.

TABLE I. All measured rovibrational transitions in the fundamental vibrational band of HeH^+ and a comparison to those values measured by Bernath and Amano.[5] All units are in MHz.

Transition	Freq.	St. Dev.	Prev. value[5]	Diff.
P(3)	80795499.88	0.99	80795566.39	− 66.51
P(2)	83096617.69	1.34	83096650.39	− 32.69
P(1)	85258146.86	0.35	85258082.06	64.80
R(0)	89115533.66	1.38	89115502.62	31.04
R(1)	90788380.66	0.40	90788398.50	− 17.84
R(2)	92275879.63	0.77	92275875.74	3.89
R(3)	93567523.38	0.92	93567519.55	3.82

TABLE II. Rovibrational parameters from a fit of experimentally measured rotation and rovibration transitions to Eq. (1). All units are in MHz.

Parameter	This work	Liu and Davies[8]
ν_0	87268330.62(54)	87268319(33)
B_0	1006063.39(15)	1006063.3(45)
D_0	486.1762(187)	486.512(96)
H_0	0.1807358(2628)	0.18428(84)
$L_0 \times 10^4$	−1.17975(1418)	−1.331(36)
$M_0 \times 10^7$	0.73228(3114)	1.022(69)
$N_0 \times 10^{10}$	−0.49376(2392)	−0.702(48)
B_1	924550.54(17)	924554.8(45)
D_1	475.1636(138)	475.606(99)
H_1	0.1660888(3241)	0.17049(84)
$L_1 \times 10^4$	−1.31950(2056)	−1.499(33)
$M_1 \times 10^7$	1.05510(4957)	1.385(60)
$N_1 \times 10^{10}$	−1.12488(4121)	−1.352(42)

These new measurements together with all available data for the fundamental band[4,5,7,9] as well as pure rotational data[8,10,11] were included in a fit to a power-series expansion of the vibration-rotation term values for a $^1\Sigma$ linear molecule as shown in Eq. (1) [The measurements of P(9)-P(11) by Purder *et al.* were not included in the fit as no uncertainties were reported],[29]

$$F_v = G_v + B_v J(J+1) - D_v[J(J+1)]^2 + H_v[J(J+1)]^3 + L_v[J(J+1)]^4 + M_v[J(J+1)]^5 + N_v[J(J+1)]^6. \quad (1)$$

The fit was performed using PGOPHER,[30] floating all parameters in both the ground and first excited vibrational states. In addition to our high-precision rovibrational measurements and the remaining fundamental band data, the fit includes the two pure rotational transitions ($J = 1 \leftarrow 0$ and $J = 2 \leftarrow 1$) measured by Matsushima *et al.* with very high precision (∼200 kHz), as well as the pure rotational transitions of Liu and Davies, which includes 11 transitions in both the $v = 0$ and $v = 1$ vibrational states covering a range of J'' from 10 to 20. Parameters from the fit are given in Table II along with a comparison to those values obtained by Liu and Davies.[8] Full details of the fit can be found in the supplementary material.[31] Inclusion of these high precision measurements allows for a more precise determination (by roughly an order of magnitude) of the band origin as well as the B rotational constants and the lower order centrifugal distortion terms up to H.

It is interesting to note that for all the centrifugal distortion terms there are significant differences between our values and those of Liu and Davies. However, the results of the fit showed that the weighted residuals were randomly distributed across the entire range of J'', which suggests that the differences in the fit parameters may be due to a high degree of correlation among the higher order parameters. Indeed, when the correlation matrix is examined it is clear that this is the case as the H, L, M, and N parameters all show correlations of ≥ 0.9 with each other.

Another comparison can be made to the fit produced by Matsushima *et al.*[11] In their fit they only included their $J = 1 \leftarrow 0$ and $J = 2 \leftarrow 1$ transitions along with the available rovibrational data in the fundamental band, while only including terms up to L (the values of L were fixed to the *ab initio* predictions of Bishop and Cheung[22]). By doing so they were able to obtain very precise values for the B, D, and H values, which are nearly an order of magnitude more precise

TABLE III. Experimentally determined rotation-vibration energy levels E(v,J) for $^4HeH^+$. All units are in MHz.

J	E(0,J)	E(1,J)
0	0	87268330.76(41)
1	2010183.86(20)	89115533.7(14)
2	6018916.87(28)	92798564.52(44)
3	12003064.7(11)	98294796.51(83)
4	19928164(60)	105570588.0(14)
5	29749118(30)	114581537(85)
6	41409933(172)	125273098(153)
7	54845432(194)	137580625(228)
8		151431127(245)

than the values reported in Table II. It may be the case, however, that the quality of their fit was somewhat fortuitous, due to the weighting of the highly precise values for the rotational transitions and their influence on the values of the lower order rotational parameters. We conjecture that since these lower order parameters were tightly constrained by only two transitions, their fit may have yielded well-determined parameters because there was so much more relative uncertainty in the rovibrational transition frequencies. The inclusion of our data, which also probe the J = 0, 1, and 2 levels in the ground vibrational state and carry a similar weighting in the fit as Matsushima's rotational transitions, may explain the apparent increase in the uncertainty of our parameters.

To further assess the accuracy of our measurements we performed a test by adding Gaussian noise of varying amounts (as determined by the standard deviation of this added noise) to our transition frequencies and running the fit described above using these modified frequencies. For noise with a standard deviation of 2 MHz we begin to see a noticeable degradation in the quality of the fit in terms of the residuals of our seven measured transitions. With this amount of "noise" we find that the RMS of the residuals for these seven transitions increases by roughly a factor of two. Though this test may not be 100% conclusive due to the random nature of adding in this noise, it does give us confidence that our claimed uncertainties are appropriate in size.

Using these new data along with previous infrared and pure rotational work, a set of experimentally determined rovibrational energy levels can be derived using a combination difference analysis. Evaluating the energy levels in this way is advantageous because they are not based on any model Hamiltonian. The energy levels covering J = 0–7 in the vibrational ground state and J = 0–8 in the v = 1 vibrational excited state can be computed based on the available spectroscopic data. Table III summarizes the results.

The high precision (no larger than 1.4 MHz) of the J = 3 level in the ground vibrational state and the first five rotational levels in the v = 1 vibrational state, will allow these energy levels to serve as excellent benchmark values for new *ab initio* calculations on this molecule.

IV. CONCLUSION

We have performed sub-Doppler mid-infrared spectroscopy on the HeH^+ cation. By using the technique of NICE-OHVMS in conjunction with frequency calibration provided by an optical frequency comb, we have re-measured seven fundamental band transitions of this molecule with a precision on the order of 1 MHz, and were able to achieve sub-MHz precision on most of the measured transitions. Using these new transitions with their improved uncertainties we have improved the values of the band origin as well as the B rotational constants and the lower order centrifugal distortion terms in a fit that includes all available spectroscopic data for the v = 0 and v = 1 states of the $^4HeH^+$ molecule. These new measurements also allowed for very precise determination of the low J rotation-vibration energy levels in the ground and v = 1 states, which will serve as new benchmarks for theorists to test *ab initio* calculations as higher level non-adiabatic, relativistic, and QED corrections are included. These measurements could also be used in a refinement of the empirical potential originally published by Coxon and Hajigergiou.[21]

ACKNOWLEDGMENTS

We would first like to acknowledge financial support from the National Science Foundation (CHE 12-13811). A.J.P., J.N.H., and C.R.M. are grateful to Mr. Paul A. Jenkins II for his assistance with setting up the spectrometer. J.N.H. is thankful for support from an NSF Graduate Research Fellowship (DGE 11-44245 FLLW). G.S.K. is thankful for financial support from a Gieseking scholarship. We would especially like to express gratitude to Professor Takeshi Oka for providing the glass discharge cell (Black Widow) along with the associated pumps and electronics.

[1] S. Lepp, P. C. Stancil, and A. Dalgarno, J. Phys. B **35**, R57 (2002).
[2] S. Lepp, Astrophys. Space Sci. **285**, 737 (2003).
[3] T. R. Hogness and E. G. Lunn, Phys. Rev. **26**, 44 (1925).
[4] D. E. Tolliver, G. A. Kyrala, and W. H. Wing, Phys. Rev. Lett. **43**, 1719 (1979).
[5] P. Bernath and T. Amano, Phys. Rev. Lett. **48**, 20 (1982).
[6] A. Carrington, R. A. Kennedy, T. P. Softley, P. G. Fournier, and E. G. Richard, Chem. Phys. **81**, 251 (1983).
[7] C. E. Blom, K. Möller, and R. R. Filgueira, Chem. Phys. Lett. **140**, 489 (1987).
[8] Z. Liu and P. B. Davies, J. Chem. Phys. **107**, 337 (1997).
[9] M. W. Crofton, R. S. Altman, N. N. Haese, and T. Oka, J. Chem. Phys. **91**, 5882 (1989).
[10] D.-J. Liu, W.-C. Ho, and T. Oka, J. Chem. Phys. **87**, 2442 (1987).
[11] F. Matsushima, T. Oka, and K. Takagi, Phys. Rev. Lett. **78**, 1664 (1997).
[12] Z. Liu and P. B. Davies, Phys. Rev. Lett. **79**, 2779 (1997).
[13] K. Pachucki and J. Komasa, J. Chem. Phys. **137**, 204314 (2012).
[14] J. Komasa, K. Piszczatowski, G. Łach, M. Przybytek, B. Jeziorski, and K. Pachucki, J. Chem. Theory Comput. **7**, 3105 (2011).
[15] R. E. Moss, J. Phys. B **32**, L89 (1999).
[16] L. Lodi, O. L. Polyansky, J. Tennyson, A. Alijah, and N. F. Zobov, Phys. Rev. A **89**, 032505 (2014).
[17] W.-C. Tung, M. Pavanello, and L. Adamowicz, J. Chem. Phys. **137**, 164305 (2012).
[18] M. Stanke, D. Kędziera, M. Molski, S. Bubin, M. Barysz, and L. Adamowicz, Phys. Rev. Lett. **96**, 233002 (2006).
[19] S. Bubin, M. Stanke, D. Kędziera, and L. Adamowicz, Phys. Rev. A **76**, 022512 (2007).
[20] M. Stanke, D. Kędziera, S. Bubin, and L. Adamowicz, Phys. Rev. A **77**, 022506 (2008).
[21] J. A. Coxon and P. G. Hajigeorgiou, J. Mol. Spectrosc. **193**, 306 (1999).

[22] D. M. Bishop and L. M. Cheung, J. Mol. Spectrosc. **75**, 462 (1979).

[23] J. N. Hodges, A. J. Perry, P. A. Jenkins, B. M. Siller, and B. J. McCall, J. Chem. Phys. **139**, 164201 (2013).

[24] B. M. Siller, M. W. Porambo, A. A. Mills, and B. J. McCall, Opt. Exp. **19**, 24822 (2011).

[25] K. N. Crabtree, J. N. Hodges, B. M. Siller, A. J. Perry, J. E. Kelly, P. A. Jenkins, and B. J. McCall, Chem. Phys. Lett. **551**, 1 (2012).

[26] J. Ye, L.-S. Ma, and J. L. Hall, J. Opt. Soc. Am. B **15**, 6 (1998).

[27] C. S. Gudeman, M. H. Begemann, J. Pfaff, and R. J. Saykally, Phys. Rev. Lett. **50**, 727 (1983).

[28] L. S. Rothman, I. E. Gordon, Y. Babikov, A. Barbe, D. Chris Benner, P. F. Bernath, M. Birk, L. Bizzocchi, V. Boudon, L. R. Brown, A. Campargue, K. Chance, E. A. Cohen, L. H. Coudert, V. M. Devi, B. J. Drouin, A. Fayt, J.-M. Flaud, R. R. Gamache, J. J. Harrison, J.-M. Hartmann, C. Hill, J. T. Hodges, D. Jacquemart, A. Jolly, J. Lamouroux, R. J. Le Roy, G. Li, D. A. Long, O. M. Lyulin, C. J. Mackie, S. T. Massie, S. Mikhailenko, H. S. P. Müller, O. V. Naumenko, A. V. Nikitin, J. Orphal, V. Perevalov, A. Perrin, E. R. Polovtseva, C. Richard, M. A. H. Smith, E. Starikova, K. Sung, S. Tashkun, J. Tennyson, G. C. Toon, Vl. G. Tyuterev, and G. Wagner, J. Quant. Spectrosc. Radiat. Transf. **130**, 4 (2013).

[29] J. Purder, S. Civiš, C. E. Blom, and M. C. van Hemert, J. Mol. Spectrosc. **153**, 701 (1992).

[30] C. M. Western, PGOPHER, a Program for Simulating Rotational Structure, University of Bristol, http://pgopher.chm.bris.ac.uk.

[31] See supplementary material at http://dx.doi.org/10.1063/1.4895505 for the fit details of each experimentally measured transition.

Appendix E

High-precision R-branch Transition Frequencies in the ν_2 Fundamental Band of H_3^+

This appendix is a complete reprint with permission from Adam J. Perry, James N. Hodges, Charles R. Markus, G. Stephen Kocheril, Benjamin J. McCall. Journal of Molecular Spectroscopy, 317 (2015) 71-73, Copyright Elsevier 2015.

Journal of Molecular Spectroscopy 317 (2015) 71–73

Contents lists available at ScienceDirect

Journal of Molecular Spectroscopy

journal homepage: www.elsevier.com/locate/jms

Note

High-precision *R*-branch transition frequencies in the ν_2 fundamental band of H_3^+

Adam J. Perry [a], James N. Hodges [a], Charles R. Markus [a], G. Stephen Kocheril [a], Benjamin J. McCall [a,b,*]

[a] Department of Chemistry, University of Illinois, Urbana, IL 61801, USA
[b] Department of Astronomy, University of Illinois, Urbana, IL 61801, USA

ARTICLE INFO

Article history:
Received 10 July 2015
In revised form 4 September 2015
Available online 11 September 2015

Keywords:
Rovibrational spectroscopy
High-precision spectroscopy
Sub-Doppler spectroscopy
Ion spectroscopy
H_3^+

ABSTRACT

The H_3^+ molecular ion has served as a long-standing benchmark for state-of-the-art *ab initio* calculations of molecular potentials and variational calculations of rovibrational energy levels. However, the accuracy of such calculations would not have been confirmed if not for the wealth of spectroscopic data that has been made available for this molecule. Recently, a new high-precision ion spectroscopy technique was demonstrated by Hodges et al., which led to the first highly accurate and precise (~MHz) H_3^+ transition frequencies. As an extension of this work, we present ten additional *R*-branch transitions measured to similar precision as a next step toward the ultimate goal of producing a comprehensive high-precision survey of this molecule, from which rovibrational energy levels can be calculated.

As the simplest polyatomic molecule, H_3^+ serves as an important benchmark system for *ab initio* calculation of molecular potential energy surfaces (PES) and spectra. The degree to which state-of-the-art calculations of the rovibrational transitions agree with experimental measurements is impressive, and is approaching the limit of the experimental uncertainty, typically on the order of 150–300 MHz (for a thorough review on previous laboratory spectroscopy of H_3^+ see Ref. [1]). Recent calculations [2] based on the highly accurate Born–Oppenheimer PES of Pavanello et al. [3], which included diagonal Born–Oppenheimer corrections (*i.e.* the adiabatic correction) and relativistic corrections, reproduce all known rovibrational energy levels for all isotopologues within 0.2 cm^{-1}. Shortly thereafter, Diniz et al. [4] developed a method for approximating the non-adiabatic effects using a "core-mass" approach whereby the nuclei are given coordinate-dependent masses as they undergo vibrational motion. Comparison to twelve high-precision (~10 MHz) transitions arising from low-lying rovibrational energy levels yields an agreement between experiment and theory of ~0.001 cm^{-1} (~30 MHz). Beyond these calculations Lodi and co-workers [5] have developed the first quantum electrodynamic correction surface for H_3^+, which demonstrated the importance of including these effects, as well as the need for a more complete model for taking into account non-adiabatic effects.

Since the accuracy of theoretical calculations is now reaching the level of the experimental uncertainty, improved spectroscopic measurements are needed in order to push the bounds of theoretical calculations. In this note we present ten new high-precision spectroscopic measurements in the ν_2 fundamental band of H_3^+. These new frequencies, combined with those measured by Hodges et al. [6], represent a step towards completing a thorough high-precision spectroscopic survey for this important fundamental species. The spectra were acquired using the technique Noise-Immune Cavity Enhanced Optical Heterodyne Velocity Modulation Spectroscopy (NICE-OHVMS), in which traditional velocity modulation spectroscopy [7] is augmented with cavity enhancement and heterodyne modulation [8]. The instrument (described in detail in [6,9]) utilizes a high-power, continuous wave, optical parametric oscillator whose idler beam is coupled into an external optical cavity which surrounds a water-cooled AC positive column discharge of H_2 gas. Inside the cell, the pressure is maintained at 300–400 mTorr and the discharge is driven at frequencies of 40–50 kHz. Light transmitted through the cavity is detected by a fast photodiode detector whose signal is demodulated first at the heterodyne frequency (~80 MHz) by a pair of electronic mixers and then again at twice the discharge frequency (80–100 kHz) by a pair of lock-in amplifiers. This detection scheme results in four channels of detection, producing signals from each heterodyne mixer that are in-phase and 90° out of phase (in quadrature) with the sinusoidal driving voltage of the discharge. Frequency calibration of the spectra is accomplished by measuring the difference in frequency between the pump and signal waves. Measurements of these beams are obtained with a near-infrared wavelength meter and optical frequency comb.

---

[*] Corresponding author at: Department of Chemistry, University of Illinois, Urbana, IL 61801, USA.

http://dx.doi.org/10.1016/j.jms.2015.09.004
0022-2852/© 2015 Elsevier Inc. All rights reserved.

Due to the bi-directional nature and optical power enhancement of the external optical cavity, it is possible to perform sub-Doppler spectroscopy which enables high-precision line center measurements. Such a spectrum is illustrated in Fig. 1. Line centers are extracted via a simultaneous fit of all four detection channels to the sub-Doppler features. In the fit the line center, heterodyne detection angle, and full-width of the feature are all shared parameters between the four channels. Previous high-precision measurements were limited to transitions from lower-J levels and these new measurements have expanded the range up to $J = 6$. All newly measured transition frequencies are reported in Table 1. Uncertainties in the line centers are assigned as the standard deviation of a data set composed of at least five scans for each transition, and as a result are highly dependent on the signal-to-noise ratio of the sub-Doppler features. The precision to which these lines have been measured represents an improvement over previous measurements of two orders of magnitude for most of the transitions. It is worth noting that the works of Oka [10], and Lindsay et al. [1] appear to be highly accurate, and their claimed uncertainties may be a bit conservative.

The only new measurement that falls outside of the stated uncertainties of the previous work is that of $R(3,3)^u$, for which we record a frequency that is 15 MHz lower than that reported by Wu et al. [11]. Though this discrepancy is not completely unreasonable (1.5σ), we set out to confirm this frequency by performing a second, independent measurement of this transition. Doing so yielded the same value (to within our specified uncertainty). To eliminate any possibility of an unexpected systematic error in our frequency calibration, we immediately remeasured the $R(1,0)$ transition, which was in good agreement with Hodges et al. and Wu et al., and we still obtain the same value for its line center. These tests leave us confident in the accuracy of our $R(3,3)^u$ measurement.

Table 1
Newly measured rovibrational transitions in the ν_2 fundamental band of H_3^+ and a comparison to previous values. All units are in MHz.

Transition[a]	This work	Previous	Diff.
$R(4,3)^l$	86778433.66(76)	86778225(300)[b]	208.66
$R(3,3)^u$	87480191.43(117)	87480207(10)[c]	−15.57
$R(3,2)^u$	87640201.59(254)	87640158(300)[b]	43.59
$R(3,1)^u$	87789812.71(130)	87789754(300)[b]	58.71
$R(3,0)$	87844195.67(122)	87844077(300)[b]	118.67
$R(5,5)^l$	88620962.34(144)	88620809(300)[b]	153.34
$R(6,6)^l$	90368280.18(102)	90368359(150)[d]	−78.82
$R(4,3)^u$	90394720.09(232)	90394651(150)[d]	69.09
$R(4,2)^u$	90673895.29(179)	90673968(300)[d]	−72.71
$R(4,1)^u$	90831978.56(177)	90832078(150)[d]	−99.44

[a] Labels for these transitions refer to (J,G); for more details on H_3^+ notation see [1].
[b] Ref. [10].
[c] Ref. [11].
[d] Ref. [12].

Work is now underway to extend the frequency coverage of the spectrometer which will allow us to measure P and Q branch transitions in this band. Once this is accomplished it will be possible to begin measuring energy level spacings in the ground vibrational state with precision that has never before been achieved. Upon completion of the fundamental band measurements, a survey of transitions in the $2\nu_2^{\ell=2} \leftarrow \nu_2$ hot band along with transitions in the first overtone band ($2\nu_2^{\ell=2} \leftarrow 0$) will allow us to determine relative energy spacings among levels within the *ortho* and *para* species. Finally, a fit of the ground state energy levels to a modified Watson-type Hamiltonian will allow for absolute energy levels to be extracted. Once completed this work will equip theorists with a complete and highly precise list of experimentally determined

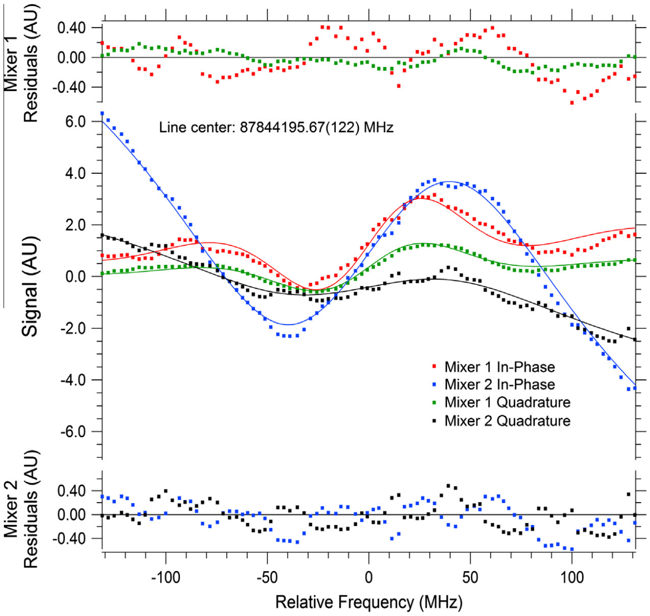

Fig. 1. A NICE-OHVMS scan of sub-Doppler feature of the $R(3,0)$ fundamental band transition of H_3^+ centered at 87844195.67(122) MHz. Signals from each of the four detection channels are shown (dots) and are fitted simultaneously (solid traces) with the line center as a shared parameter. The odd symmetry of the line shapes is a result of the applied modulation scheme.

rovibrational energy levels for this critically important molecular system.

Acknowledgments

This work was funded by the National Science Foundation (PHY 14-04330). J.N.H. is grateful for support from an NSF Graduate Research Fellowship (DGE 11-44245 FLLW). G.S.K. is thankful for financial support from a Gieseking scholarship.

References

[1] C. Lindsay, B.J. McCall, J. Mol. Spectrosc. 210 (2001) 60–83.
[2] O.L. Polyansky, A. Alijah, N.F. Zobov, I.I. Mizus, R.I. Ovsyannikov, J. Tennyson, L. Lodi, T. Szidarovszky, A.G. Császár, Philos. Trans. A Math. Phys. Eng. Sci. 370 (2012) 5014–5027.
[3] M. Pavanello, L. Adamowicz, A. Alijah, N.F. Zobov, I.I. Mizus, O.L. Polyansky, J. Tennyson, T. Szidarovszky, A.G. Császár, J. Chem. Phys. 136 (2012) 184303.
[4] L.G. Diniz, J.R. Mohallem, A. Alijah, M. Pavanello, L. Adamowicz, O.L. Polyansky, J. Tennyson, Phys. Rev. A 88 (2013) 032506.
[5] L. Lodi, O.L. Polyansky, J. Tennyson, A. Alijah, N.F. Zobov, Phys. Rev. A 89 (2014) 032505.
[6] J.N. Hodges, A.J. Perry, P.A. Jenkins II, B.M. Siller, B.J. McCall, J. Chem. Phys. 139 (2013) 164201.
[7] C. Gudeman, M. Begemann, J. Pfaff, R. Saykally, Phys. Rev. Lett. 50 (1983) 727–731.
[8] B.M. Siller, M.W. Porambo, A.A. Mills, B.J. McCall, Opt. Express 19 (2011) 24822–24827.
[9] K.N. Crabtree, J.N. Hodges, B.M. Siller, A.J. Perry, J.E. Kelly, P.A. Jenkins II, B.J. McCall, Chem. Phys. Lett. 551 (2012) 1–6.
[10] T. Oka, Philos. Trans. R. Soc. A 303 (1981) 543–549.
[11] K.-Y. Wu, Y.-H. Lien, C.-C. Liao, Y.-R. Lin, J.-T. Shy, Phys. Rev. A 88 (2013) 032507.
[12] C. Lindsay, R.M. Rade, T. Oka, J. Mol. Spectrosc. 210 (2001) 51–59.

Appendix F

High Precision Rovibrational Spectroscopy of OH^+

This appendix is a complete reprint with permission from Charles R. Markus, James N. Hodges, Adam J. Perry, G. Stephen Kocheril, Holger S. P. Müller, Benjamin J. McCall. The Astrophysical Journal, 817 (2016) 138, Copyright The American Astronomical Society 2016.

The Astrophysical Journal, 817:138 (5pp), 2016 February 1 doi:10.3847/0004-637X/817/2/138

HIGH PRECISION ROVIBRATIONAL SPECTROSCOPY OF OH^+

Charles R. Markus[1], James N. Hodges[1], Adam J. Perry[1], G. Stephen Kocheril[1],
Holger S. P. Müller[2], and Benjamin J. McCall[1,3]
[1] Department of Chemistry, University of Illinois, Urbana, IL 61801, USA; bjmccall@illinois.edu
[2] I. Physikalisches Institut, Universität zu Köln, Zülpicher Str. 77, D-50937 Köln, Germany
[3] Department of Astronomy, University of Illinois, Urbana, IL 61801, USA

Received 2015 November 5; accepted 2015 December 18; published 2016 January 27

ABSTRACT

The molecular ion OH^+ has long been known to be an important component of the interstellar medium. Its relative abundance can be used to indirectly measure cosmic ray ionization rates of hydrogen, and it is the first intermediate in the interstellar formation of water. To date, only a limited number of pure rotational transitions have been observed in the laboratory making it necessary to indirectly calculate rotational levels from high-precision rovibrational spectroscopy. We have remeasured 30 transitions in the fundamental band with MHz-level precision, in order to enable the prediction of a THz spectrum of OH^+. The ions were produced in a water cooled discharge of O_2, H_2, and He, and the rovibrational transitions were measured with the technique Noise Immune Cavity Enhanced Optical Heterodyne Velocity Modulation Spectroscopy. These values have been included in a global fit of field free data to a $^3\Sigma^-$ linear molecule effective Hamiltonian to determine improved spectroscopic parameters which were used to predict the pure rotational transition frequencies.

Key words: astrochemistry – ISM: molecules – methods: laboratory: atomic – submillimeter: ISM

1. INTRODUCTION

Molecular ions play a central role in the chemistry of the interstellar medium. Their reactivity with neutral species overshadows other chemical processes in the cold and diffuse environments of molecular clouds. One important example is OH^+, which is involved in a number of astrochemical processes. Its formation in diffuse clouds is initiated by cosmic ray ionization of atomic hydrogen into H^+, which can undergo an endothermic charge transfer with atomic oxygen to form O^+. Hydrogen abstraction with H_2 then leads to the subsequent formation of OH^+, H_2O^+, and H_3O^+. Dissociative recombination with electrons destroys all three of these species yielding neutral OH and H_2O along with other products. These competing processes allow for the relative abundances of OH^+, H_2O^+, and H_3O^+ to act as a probe of cosmic ray ionization rates and molecular hydrogen fractions in molecular clouds (van Dishoeck & Black 1986; Hollenbach et al. 2012; Indriolo et al. 2015).

Due to interference of telluric water, observatories were only able to detect rotational transitions of H_3O^+ (Wootten et al. 1991) until recently. The Heterodyne Instrument for the Far-Infrared aboard the orbiting telescope *Herschel* and high altitude ground based facilities enabled the first observations of H_2O^+ and OH^+ (Ossenkopf et al. 2010; Wyrowski et al. 2010). Near-ultraviolet absorption from OH^+ was detected shortly thereafter using the Very Large Telescope's Ultraviolet and Visual Echelle Spectrograph (Krełowski et al. 2010). The termination of *Herschel* has limited terahertz observations of OH^+ to high altitude observatories on the Atacama plateau and aboard aircraft such as the Stratospheric Observatory For Infrared Astronomy (SOFIA). Because of the low temperatures in translucent and diffuse molecular clouds, most of these measurements are of the ground state rotational transitions near 1 THz. There have also been observations of OH^+ by emission within our galaxy in photon-dominated regions (van der Tak et al. 2013; Aleman et al. 2014; Etxaluze et al. 2014). Highly rotationally excited transitions of OH^+ were detected with the moderate resolution Photodetector Array Camera and Spectrometer on board *Herschel* in absorption in the nearby galaxies Arp 220 and NGC 4418 by González-Alfonso et al. (2013) and in emission in our galaxy by Aleman et al. (2014).

The rotational structure of OH^+ arises from its $^3\Sigma^-$ ground electronic state. In this configuration, electron spin angular momentum $\boldsymbol{S}$ couples with the rotational angular momentum $\boldsymbol{N}$ as $\boldsymbol{J} = \boldsymbol{S} + \boldsymbol{N}$. A spin of $S = 1$ leads to the rotational levels splitting into fine structure triplets of $J = N + 1$, N, $N - 1$ with the exception of $N = 0$ where the only level is $J = 1$. The nuclear spin of $I = 1/2$ from the hydrogen nucleus splits each of these levels further into $F = J \pm 1/2$, where $\boldsymbol{F}$ is the total angular momentum. The strongest transitions follow the selection rule $\Delta F = \Delta J = \Delta N$. The only field free pure rotational measurements have been of the $N = 1 \leftarrow 0$ (Bekooy et al. 1985) and $N = 13 \leftarrow 12$ transitions (Liu et al. 1987). There have also been investigations with laser magnetic resonance (LMR) going as far as $N = 3 \leftarrow 2$ (Gruebele et al. 1986); though there have been cases, such as H_2O^+ and CH_2, where the field-free transition frequencies extrapolated from LMR data had errors much larger than the claimed uncertainties (Brünken et al. 2005; Ossenkopf et al. 2010). Rovibrational spectroscopy can help to improve the predictions of rotational transitions. Müller et al. (2005) combined the field free rotational data (Bekooy et al. 1985; Liu et al. 1987) with extensive infrared data by Rehfuss et al. (1992) with reported uncertainties of 0.003 cm^{-1} (90 MHz) to determine an accurate set of Dunham-type spectroscopic parameters and to predict the rotational spectrum of OH^+ well into the terahertz region. Even at high frequencies, these predictions were accurate enough for studies with moderate resolution instruments (González-Alfonso et al. 2013; Aleman et al. 2014), but they may not be accurate enough for high resolution instruments, such as the German REceiver At Terahertz frequencies (GREAT, Heyminck et al. 2012) on board SOFIA. In the present work, we have therefore revisited the $v = 1 \leftarrow 0$ band of OH^+ with megahertz-level accuracy and determined improved molecular parameters from a least squares fit to a $^3\Sigma^-$ linear molecule effective Hamiltonian. The pure rotational spectrum was predicted in turn to assist future astronomical observations with high resolution instruments at terahertz frequencies.

2. METHODS

The spectra were acquired with the technique Noise Immune Cavity Enhanced Optical Heterodyne Velocity Modulation Spectroscopy (NICE-OHVMS) (Siller et al. 2011). A detailed description of the instrument can be found in Hodges et al. (2013). In brief, a commercially available optical parametric oscillator (Aculight Argos 2400 SF) generates a continuous wave mid-infrared idler beam tunable from 3.2–3.9 μm with approximately 1 W of power. An electro-optic modulator applies an ~80 MHz phase modulation to the pump laser, imprinting RF sidebands onto the idler. The idler is coupled into an external cavity (finesse $\approx$ 150) which surrounds a water-cooled positive column discharge cell. The OH^+ ions were generated by flowing a 2:3:100 H_2:O_2:He mixture at 1.0 Torr through the cell and applying a 50 kHz sinusoidal discharge. Light transmitted through the cavity is focused onto a fast photodiode detector (Boston Electronics Vigo PVM-10.6-1x1). Two mixers referenced 90° out of phase with one another demodulate the signal from the detector at the frequency used to generate the sidebands. The velocity modulation signal is recovered by demodulating the output of each mixer at twice the driving frequency of the discharge (100 kHz) with a set of lock-in amplifiers. This improves our sensitivity by reducing residual amplitude modulation (RAM) from our electro-optic modulator and filtering out the strong signals from neutral species. The in-phase and quadrature outputs of each lock-in amplifier produce two channels for each mixer, resulting in four total channels of detection.

Frequency calibration of the idler is accomplished by taking the difference of the pump and signal frequencies which are calibrated with an optical frequency comb (Menlo Systems FC-1500; 100 MHz repetition rate). Initially, an infrared wavemeter (Bristol 621:IR-A) was used to measure the pump and signal beams and determine the integer number of comb modes between them. The difference in frequency measured by the wavemeter must be accurate to within half the repetition rate (50 MHz), otherwise a 100 MHz systematic error would occur. To ensure proper determination of the difference in comb modes, systematic offsets of the wavemeter measurements are corrected by measuring methane reference transitions in the HITRAN database (Rothman et al. 2013).

3. RESULTS AND ANALYSIS

Thirty lines were measured in the fundamental band with an average uncertainty of ~2.5 MHz, covering transitions $P(5)$ to $R(5)$. These results are displayed in Table 1. The frequencies reported by Rehfuss et al. (1992) are frequently lower than the remeasured values, and only three transitions are at a higher frequency.

A typical NICE-OHVMS scan can be seen in Figure 1(a). The odd lineshape is a result of the heterodyne and velocity modulation detection scheme. The sub-Doppler feature arises from the bidirectional nature of the cavity, and the line center can be extracted from this using a least squares fitting routine. Figure 1(b) is an example of a typical two channel fit with residuals. A technical description of the sub-Doppler fitting procedure can be found in Hodges et al. (2013). The feature is a blend of several Lamb dips, resulting in a sub-Doppler width of ~100 MHz. The width of each individual Lamb dip is larger than what would be expected from pressure broadening alone, and a proposed mechanism for this can be found in Mills et al. (2010). A large fringe, similar to the one seen in Figure 1, appeared in many of the spectra. The sub-Doppler fit does not appear to have been appreciably affected by the fringe since it is well reproduced within the residuals. Any random offset was further mitigated by collecting five measurements of each transition and averaging the line center frequencies. The uncertainty of each transition is reported as the standard deviation and shows an order of magnitude improvement over previous values. However, the precision of this study is not at the sub-MHz level as was achieved in other NICE-OHVMS studies (Hodges et al. 2013; Perry et al. 2014). This can be attributed to the lower signal-to-noise which is known to decrease the precision of the line centers (Hodges et al. 2013). The weak signals are likely a result of competing chemical processes such as the formation of H_2O^+. Gas mixtures with dilute quantities of H_2 can minimize this effect but still result in relatively weak signals.

Table 1
Present Transition Frequencies (cm^{-1}) of the $v = 1 \leftarrow 0$ Band of OH^+ with Quantum Numbers, Uncertainties Unc. (10^{-6} cm^{-1}), and Residuals O−C (10^{-6} cm^{-1})

N'	J'	N''	J''	$F' - F''$ [a]	Frequency	Unc.	O−C
4	4	5	5	⋯	2778.543347	43	−29.2
4	5	5	6	⋯	2778.752326	100	−101.5
3	2	4	3	1.5–2.5, 2.5–3.5	2816.464225	55	151.0
3	3	4	4	⋯	2816.730510	100	−28.3
3	4	4	5	3.5–4.5, 4.5–5.5	2816.948108	61	142.9
2	1	3	2	0.5–1.5, 1.5–2.5	2853.236859	25	−36.6
2	2	3	3	⋯	2853.653079	80	21.6
2	3	3	4	2.5–3.5, 3.5–4.5	2853.889147	91	−92.4
1	0	2	1	0.5–1.5	2887.654424	230	−33.0
1	1	2	2	⋯	2889.261936	110	26.0
1	2	2	3	1.5–2.5, 2.5–3.5	2889.544385	46	−22.1
1	1	2	1	0.5–1.5, 1.5–1.5	2891.773633	105	−157.3
0	1	1	2	0.5–1.5, 1.5–2.5	2923.940929	63	−9.9
1	2	0	1	2.5–1.5, 1.5–0.5	2987.324274	96	9.9
1	1	0	1	0.5–1.5, 1.5–1.5	2989.353127	63	111.2
2	3	1	2	3.5–2.5, 2.5–1.5	3017.368784	61	−24.3
2	2	1	1	⋯	3017.612933	52	59.8
2	1	1	0	1.5–0.5	3019.241547	93	87.0
3	4	2	3	4.5–3.5, 3.5–2.5	3045.765058	65	25.1
3	3	2	2	⋯	3045.952199	69	63.0
3	2	2	1	2.5–1.5, 1.5–0.5	3046.372950	47	−59.5
4	5	3	4	5.5–4.5, 4.5–3.5	3072.547147	25	8.2
4	4	3	3	⋯	3072.705383	39	−45.4
4	3	3	2	3.5–2.5, 2.5–1.5	3072.964615	74	63.5
5	6	4	5	⋯	3097.691735	88	15.3
5	5	4	4	⋯	3097.831772	110	−126.9
5	4	4	3	⋯	3098.033887	230	13.1
6	7	5	6	⋯	3121.165108	130	−65.4
6	6	5	5	⋯	3121.292151	220	−76.2
6	5	5	4	⋯	3121.465385	70	84.3

Note.
[a] Overlapping hyperfine structure (HFS) components (with two sets of F quantum numbers) treated as intensity weighted averages. No HFS was resolved for entries without data, and transitions were treated as such.

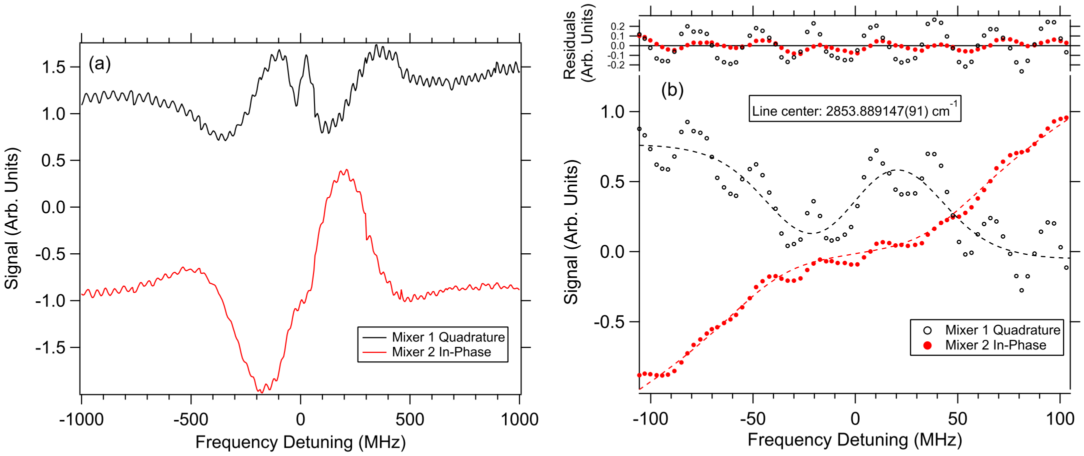

Figure 1. (a) A NICE-OHVMS scan of $P(3)$ $J = 3 \leftarrow 4$ centered at 2853.889147 cm^{-1}. The top trace is the quadrature component of the velocity modulation of the first mixer and the bottom trace is the in-phase component of the second mixer. For clarity the traces are offset from one another. (b) An enlarged comb calibrated scan of the sub-Doppler feature of $P(3)$ $J = 3 \leftarrow 4$. The colored markers represent the experimental data and the dashed lines represent the fit to the equations derived by Hodges et al. (2013). The residuals from the fit are shown above, which reproduce the fringing seen in the experimental trace.

Parameters for the $v = 0$ and $v = 1$ states were determined initially with a two-state fit of the newly measured frequencies and all data in CDMS (Müller et al. 2005) up to $v = 1$ in order to compare the compatibility of the previously reported transition frequencies and the derived spectroscopic parameters with our data. Overlapping hyperfine structure (HFS) components were treated in the fits as intensity-weighted averages, as is commonly done in fits employing the spfit/spcat program suite (Pickett 1991).

Comparing the new experimental transition frequencies with a prediction of the $v = 1 \leftarrow 0$ spectrum with ^{1}H HFS revealed that a total of four of our lines should show partially resolved HFS splitting of ~0.004 cm^{-1} or ~120 MHz, slightly larger than the sub-Doppler feature's width. Ultimately, trial fits and comparisons with Doppler-limited spectra established that in all four cases the frequencies determined by the Lamb dips corresponded to the stronger of the two lines with similar intensities. In all four cases the weaker line was on the side of the stronger line's Doppler profile, making precise frequency determination impossible. Hyperfine splitting turned out to be non-negligible for lower-N transitions with $J = N \pm 1$ because the weak $\Delta F \neq \Delta J$ HFS components were separated from the two much stronger $\Delta F = \Delta J$ components by ~120 MHz. Because of the small uncertainties of some of our lines, these differences were important for lower-N transitions. The relative intensities of these HFS components diminish rapidly with N, so the effects were negligible at higher N.

The quality of the fit was measured using the root mean square (rms) of the errors between the observed and calculated frequencies normalized to their uncertainties, which ideally should be close to 1.0. Starting with the spectroscopic parameters used by Rehfuss et al. (1992) and the HFS constants b_F and c, it was found that the spin–spin distortion constant λ_D was needed to achieve an rms error of 1.006. The results are shown in Table 2 with comparisons to Rehfuss et al. (1992) and Gruebele et al. (1986). The uncertainties of the rotational constant B, centrifugal distortion constant D, and the spin–spin coupling constant λ for both $v = 0$ and $v = 1$ states were significantly improved. The constants determined by Gruebele et al. (1986) from LMR data are in strong agreement, with every parameter falling within their reported uncertainty. Nearly every parameter from Rehfuss et al. (1992) agrees with the results with the exception of the band origin ν_0 which is 343 MHz higher. We have not been able to determine the cause of this discrepancy.

Table 2
Spectroscopic Parameters from a Two-state Fit (MHz) of OH$^+$ in Comparison to Previous Studies

Parameter	This Work	Prev. IR[a]	Prev. LMR[b]
B_0	492346.278(146)	492345(2)	492346.21(69)
D_0	57.6166(52)	57.614(24)	57.544(75)
H_0	0.0040488(259)	0.004062(87)	0.0037
λ_0	64246.00(55)	64258(18)	64242.9(28)
λ_{D0}	−0.54(12)	…	…
γ_0	−4533.85(34)	−4529.3(53)	−4534.76(124)
γ_{D0}	0.7847(153)	0.79(15)	…
$b_F(^1\mathrm{H})$	−75.14(50)	…	−71.9(125)
$c(^1\mathrm{H})$	126.01(87)	…	130.8(202)
ν_0	88629394.08(91)	88629737(30)	…
B_1	470532.242(135)	470532(2)	…
D_1	56.1557(44)	56.16(2)	…
H_1	0.0039501(243)	0.003969(81)	…
λ_1	63947.4(13)	63949(15)	…
λ_{D1}	−0.86(12)	…	…
γ_1	−4393.34(38)	−4394.1(45)	…
γ_{D1}	0.7473(130)	0.812(48)	…

Notes.
[a] Rehfuss et al. (1992).
[b] Gruebele et al. (1986).

Subsequently, our data were combined with the complete set of previously available field-free data to determine an improved set of Dunham-type spectroscopic parameters. The parameter set used by Müller et al. (2005) for the analysis of OH$^+$ was not sufficient to reproduce the present data adequately. Trial fits

Table 3
Present and Previous Spectroscopic Parameters[a] of OH^+ in Comparison to Those of SH^+

Parameter	This Work	Previous[b]	SH^+[c]
Y_{10}[d]	3119.2892 (56)	3119.3173 (27)	2547.4948 (104)
Y_{20}[d]	−83.1273 (57)	−83.1606 (19)	−49.4293 (90)
Y_{30}[d]	1.01953 (241)	1.03525 (55)	0.2097 (30)
$Y_{40} \times 10^3$ [d]	2.435 (453)	−0.795 (54)	−16.01 (34)
$Y_{50} \times 10^3$ [d]	−0.241 (31)	⋯	⋯
Y_{01}	503486.90 (26)	503486.86 (70)	278094.99 (36)
Y_{11}	−22435.77 (62)	−22435.87 (151)	−8577.33 (85)
Y_{21}	308.47 (39)	308.28 (55)	16.15 (32)
Y_{31}	−1.410 (51)	−1.434 (61)	⋯
Y_{02}	−58.3436 (59)	−58.3607 (128)	−14.7380 (76)
Y_{12}	1.4523 (37)	1.4649 (105)	0.1229 (27)
$Y_{22} \times 10^3$	7.51 (137)	7.03 (192)	⋯
$Y_{03} \times 10^3$	4.115 (31)	4.184 (57)	0.46[e]
$Y_{13} \times 10^3$	−0.1326 (187)	−0.1733 (288)	⋯
λ_{00}	64379.5 (26)	64413.2 (38)	171488.3 (58)
λ_{10}	−254.3 (66)	−340.2 (79)	−471.8 (146)
λ_{20}	−24.1 (33)	⋯	−79.1 (67)
λ_{01}	−0.68 (11)	0.75 (59)	−1.13 (24)
γ_{00}	−4605.16 (42)	−4604.23 (108)	−5036.29 (91)
γ_{10}	143.47 (67)	142.58 (220)	116.4 (20)
γ_{20}	−1.45 (35)	−2.14 (52)	3.52 (64)
γ_{01}	0.796 (17)	0.789 (36)	0.432 (35)
γ_{11}	−0.0354 (88)	⋯	⋯
$b_{F,00}(^1H)$	−75.11 (49)	−74.78 (54)	−55.15 (40)[f]
$b_{F,10}(^1H)$	⋯	⋯	−3.46 (79)
$c_{00}(^1H)$	125.95 (87)	125.48 (94)	33.60 (67)

Notes. All values are in units of MHz unless otherwise stated.

[a] Numbers in parentheses are one standard deviation in units of the least significant digits.

[b] Müller et al. (2005).

[c] Müller et al. (2014).

[d] In units of cm^{-1}.

[e] Held fixed in Müller et al. (2014).

[f] Derived from the ground state b_F and $b_{F,10}$ from Müller et al. (2014).

Table 4
Predicted Rotational Transitions of OH^+ (MHz)

N'–N''	J'–J''	F'–F''	This Work	CDMS[a]
1–0	0–1	1/2–1/2	909045.0(8)	909045.2(10)[b]
1–0	0–1	1/2–3/2	909159.4(8)	909158.8(10)[b]
1–0	2–1	5/2–3/2	971804.2(5)	971803.8(15)[b]
1–0	2–1	3/2–1/2	971805.3(5)	971805.3(15)[b]
1–0	2–1	3/2–3/2	971919.7(7)	971919.2(10)[b]
1–0	1–1	1/2–1/2	1032998.5(7)	1032997.9(8)
1–0	1–1	3/2–1/2	1033005.1(7)	1033004.4(10)[b]
1–0	1–1	1/2–3/2	1033112.9(7)	1033111.8(9)
1–0	1–1	3/2–3/2	1033119.5(7)	1033118.6(10)[b]
2–1	1–1	1/2–3/2	1892111.1(9)	1892106.5(20)
2–1	1–1	1/2–1/2	1892117.7(9)	1892113.2(19)
2–1	1–1	3/2–3/2	1892232.1(8)	1892227.1(19)
2–1	1–1	3/2–1/2	1892238.7(8)	1892233.7(19)
2–1	3–2	7/2–5/2	1959561.6(6)	1959560.0(13)
2–1	3–2	5/2–3/2	1959562.0(6)	1959560.4(13)
2–1	2–1	3/2–3/2	1967533.1(6)	1967535.9(19)
2–1	2–1	5/2–3/2	1967536.7(6)	1967539.6(19)
2–1	2–1	3/2–1/2	1967539.7(6)	1967542.6(19)
2–1	1–0	1/2–1/2	2016071.1(8)	2016066.1(20)
2–1	1–0	3/2–1/2	2016192.2(7)	2016186.6(19)
2–1	2–2	3/2–3/2	2028732.9(10)	2028735.2(20)
2–1	2–2	5/2–5/2	2028852.0(11)	2028853.9(20)
3–2	2–2	3/2–3/2	2885078.7(13)	2885065.0(51)
3–2	2–2	5/2–5/2	2885194.2(13)	2885179.9(51)
3–2	4–3	9/2–7/2	2941432.3(6)	2941428.8(21)
3–2	4–3	7/2–5/2	2941432.5(6)	2941429.0(21)
3–2	4–3	7/2–7/2	2941548.4(8)	2941544.5(20)
3–2	3–2	5/2–5/2	2947851.2(6)	2947854.9(28)
3–2	3–2	7/2–5/2	2947853.8(6)	2947857.5(28)
3–2	3–2	5/2–3/2	2947854.9(6)	2947858.6(28)
3–2	2–1	3/2–3/2	2960379.6(10)	2960373.8(25)
3–2	2–1	5/2–3/2	2960498.8(6)	2960492.5(23)
3–2	2–1	3/2–1/2	2960500.7(6)	2960494.4(23)
3–2	3–3	5/2–5/2	3017025.7(15)	3017033.4(48)
3–2	3–3	7/2–7/2	3017144.2(16)	3017151.3(48)
4–3	3–3	7/2–7/2	3869337.1(22)	3869310.2(97)
4–3	5–4	11/2–9/2	3918330.7(8)	3918324.8(33)
4–3	5–4	9/2–7/2	3918330.8(8)	3918324.9(33)
4–3	4–3	9/2–7/2	3924036.3(7)	3924040.2(41)
4–3	4–3	7/2–5/2	3924036.8(7)	3924040.8(41)
4–3	3–2	7/2–5/2	3931996.7(9)	3931987.8(35)
4–3	3–2	5/2–3/2	3931997.4(9)	3931988.4(35)
4–3	4–4	9/2–9/2	3999748.2(22)	3999762.7(90)
5–4	6–5	13/2–11/2	4889412.3(13)	4889403.4(52)
5–4	6–5	11/2–9/2	4889412.4(13)	4889403.5(52)
5–4	5–4	11/2–9/2	4894719.8(9)	4894723.3(57)
5–4	5–4	9/2–7/2	4894720.2(9)	4894723.7(57)
5–4	4–3	9/2–7/2	4901121.3(15)	4901108.8(53)
5–4	4–3	7/2–5/2	4901121.7(15)	4901109.2(53)

Notes.

[a] Müller et al. (2005).

[b] Frequencies and uncertainties are the experimental values from Bekooy et al. (1985).

were performed to search among all plausible parameters for the one which reduced the rms error of the fit the most. The parameter λ_{20}, the second vibrational correction to the spin–spin coupling parameter λ_{00}, was added first. The vibrational correction γ_{11} to the spin-rotation distortion term had a moderate effect in the overall fit, but improved the reproduction of our transition frequencies by ~16 %. Finally, we noted that the $v = 5 \leftarrow 4$ transition frequencies from Rehfuss et al. (1992) showed very similar deviations somewhat larger than the increased uncertainties of 0.010 cm^{-1}. Inclusion of Y_{50} in the fit not only reproduced these data much better, but also reduced the rms error of the fit considerably. Consequently, the uncertainties of this vibrational band were set to the initial 0.003 cm^{-1}, and the fit was rerun. The resulting spectroscopic parameters are in Table 3 together with previous values for OH^+ (Müller et al. 2005) as well as recent values for its heavier homolog SH^+ (Müller et al. 2014).

The rms error of the present fit is 0.908, hence on average the experimental transition frequencies have been reproduced within their uncertainties. The values for our data and the $v = 1 \leftarrow 0$ data of Rehfuss et al. (1992) are 1.062 and 1.107, respectively. The latter data are on average lower than the calculated frequencies by 0.0013 cm^{-1} or 40 MHz, which may indicate a calibration error of approximately that magnitude. The deviations are, however, within the reported uncertainties of 0.003 cm^{-1} or 90 MHz (Rehfuss et al. 1992). An *a posteriori* correction of these data will likely improve the reproduction of these data and may even be beneficial for reproducing our data.

Most of the present spectroscopic parameters of OH^+ are close to the previous ones. Larger changes occur for parameters which have relatively large uncertainties, e.g., λ_{01}, or by inclusion of additional higher order parameters if their values appear rather small in magnitude compared to the parameters of lower and higher order (Y_{40} and λ_{10}). The Y_{ij} of different isotopic species scale with $\mu^{-j-i/2}$, where μ is the reduced mass. The ratios of several spectroscopic parameters of OH^+ and SH^+ are surprisingly close to these ratios, but the magnitude of Y_{40} of SH^+ is actually much larger than that of OH^+.

The ratio of λ_{00} of related molecules such as SH^+ and OH^+ scale with the ratios of A_{SO}, ~2.64, which holds quite well in the present case. The slight change in b_F and the larger change in c are usually seen for light hydrides compared to their heavier homologs. Predictions from $N = 1 - 0$ to $N = 5 - 4$ are presented in Table 4 with comparison to predictions from the current version of the CDMS. The predicted THz transitions from this work show strong agreement with the predictions from CDMS and improve the precision by a factor of 2–5. More extended predictions will be available in the catalog section of the CDMS.

These predictions can guide new searches in regions where it is feasible that OH^+ is rotationally excited. The only spectrograph currently capable of observing transitions of OH^+ above $N = 1 - 0$ is the recently upgraded GREAT instrument aboard the airborne SOFIA which covers all of the $N = 2 - 1$ rotational transitions. Rotational emission of OH^+ has been observed in the Orion Bar. Calculations performed by van der Tak et al. (2013) suggest that the reason for the excitation of OH^+ in the Orion Bar is likely a combination of collisional excitation, radiative pumping, and formation pumping. It would be interesting to search this region for $N = 2 - 1$ emission, which would enable deeper understanding of this environment. Rotationally excited transitions of OH^+ were already detected at moderate resolution in nearby galaxies (González-Alfonso et al. 2013) and in our galaxy (Aleman et al. 2014).

4. CONCLUSIONS

We have revisited the infrared spectrum of the molecular ion OH^+ using the spectroscopic technique NICE-OHVMS. Each transition was measured with MHz-level uncertainty by taking advantage of the narrow sub-Doppler features provided by the NICE-OHVMS technique. These values improve a number of molecular constants by at least an order of magnitude. With these improved values, ground state rotational transitions have been predicted with lower uncertainties than previously possible. This work can be used to inform future THz observations of OH^+.

Financial support for this work was provided by the National Aeronautics and Space Administration through project NNX13AE62G and the National Science Foundation (PHY 14-04330). J.N.H. is grateful for support from an NSF Graduate Research Fellowship (DGE 11-44245 FLLW). G.S.K. is thankful for financial support from a Gieseking Scholarship. We would also like to thank Dr. Nick Indriolo for helpful discussions.

REFERENCES

Aleman, I., Ueta, T., Ladjal, D., et al. 2014, A&A, 566, A79
Bekooy, J. P., Verhoeve, P., Meerts, W. L., & Dymanus, A. 1985, JChPh, 82, 3868
Brünken, S., Müller, H. S. P., Lewen, F., & Giesen, T. F. 2005, JChPh, 123, 164315
Etxaluze, M., Cernicharo, J., Goicoechea, J. R., et al. 2014, A&A, 566, A78
González-Alfonso, E., Fischer, J., Bruderer, S., et al. 2013, A&A, 550, A25
Gruebele, M. H. W., Müller, R. P., & Saykally, R. J. 1986, JChPh, 84, 2489
Heyminck, S., Graf, U. U., Güsten, R., et al. 2012, A&A, 542, L1
Hodges, J. N., Perry, A. J., Jenkins, P. A., II, Siller, B. M., & McCall, B. J. 2013, JChPh, 139, 164201
Hollenbach, D., Kaufman, M. J., Neufeld, D., Wolfire, M., & Goicoechea, J. R. 2012, ApJ, 754, 105
Indriolo, N., Neufeld, D. A., Gerin, M., et al. 2015, ApJ, 800, 40
Krełowski, J., Beletsky, Y., & Galazutdinov, G. A. 2010, ApJL, 719, L20
Liu, D.-J., Ho, W.-C., & Oka, T. 1987, JChPh, 87, 2442
Mills, A. A., Siller, B. M., & McCall, B. J. 2010, CPL, 501, 1
Müller, H. S. P., Goicoechea, J. R., Cernicharo, J., et al. 2014, A&A, 569, L5
Müller, H. S. P., Schlöder, F., Stutzki, J., & Winnewisser, G. 2005, JMoSt, 742, 215
Ossenkopf, V., Müller, H. S. P., Lis, D. C., et al. 2010, A&A, 518, L111
Perry, A. J., Hodges, J. N., Markus, C. R., Kocheril, G. S., & McCall, B. J. 2014, JChPh, 141, 101101
Pickett, H. M. 1991, JMoSp, 148, 371
Rehfuss, B. D., Jagod, M.-F., Xu, L.-W., & Oka, T. 1992, JMoSp, 151, 59
Rothman, L. S., Gordon, I. E., Babikov, Y., et al. 2013, JQSRT, 130, 4
Siller, B. M., Porambo, M. W., Mills, A. A., & McCall, B. J. 2011, OExpr, 19, 24822
van der Tak, F. F. S., Nagy, Z., Ossenkopf, V., et al. 2013, A&A, 560, A95
van Dishoeck, E. F., & Black, J. H. 1986, ApJS, 62, 109
Wootten, A., Mangum, J. G., Turner, B. E., et al. 1991, ApJL, 380, L79
Wyrowski, F., Menten, K. M., Güsten, R., & Belloche, A. 2010, A&A, 518, A26

Appendix G

Quantitative Velocity Modulation Spectroscopy

This appendix is a complete reprint with permission from James N. Hodges, Benjamin J. McCall. The Journal of Chemical Physics, 144 (2016) 184201, Copyright American Physical Society 2016.

THE JOURNAL OF CHEMICAL PHYSICS **144**, 184201 (2016)

Quantitative velocity modulation spectroscopy

James N. Hodges[1] and Benjamin J. McCall[1,2,a)]
[1]*Department of Chemistry, University of Illinois, Urbana, Illinois 61801, USA*
[2]*Departments of Physics and Astronomy, University of Illinois, Urbana, Illinois 61801, USA*

(Received 3 March 2016; accepted 22 April 2016; published online 13 May 2016)

Velocity Modulation Spectroscopy (VMS) is arguably the most important development in the 20th century for spectroscopic study of molecular ions. For decades, interpretation of VMS lineshapes has presented challenges due to the intrinsic covariance of fit parameters including velocity modulation amplitude, linewidth, and intensity. This limitation has stifled the growth of this technique into the quantitative realm. In this work, we show that subtle changes in the lineshape can be used to help address this complexity. This allows for determination of the linewidth, intensity relative to other transitions, velocity modulation amplitude, and electric field strength in the positive column of a glow discharge. Additionally, we explain the large homogeneous component of the linewidth that has been previously described. Using this component, the ion mobility can be determined. *Published by AIP Publishing.* [http://dx.doi.org/10.1063/1.4948740]

I. INTRODUCTION

The study of molecular ions poses several challenges to traditional direct absorption spectroscopy, such as low number density in glow discharges and large numbers of interfering neutrals. For 35 years, the gold standard for addressing these obstacles has been velocity modulation spectroscopy (VMS), which is a sensitive, ion-selective technique. Since its inception,[1] VMS has been used to study ~50 individual molecules[2] and has been enhanced by combination with heterodyne modulation, cavity enhancement, and direct frequency comb spectroscopy.[3–9] Despite the fact that VMS was developed in the infrared spectral region, it has seen extensive deployment in the millimeter/submillimeter wavelengths in support of rotational spectroscopy of molecular ions.[10–12]

The key to understanding ion selectivity in VMS is that the source responsible for generating the ions, the positive column of a glow discharge, is driven by an alternating electric field. As the polarity of the positive column changes, the ions experience a force that is proportional to the magnitude of the electric field and is along the axis of the discharge in the direction of the cathode. This ionic motion results in an oscillatory Doppler shift that can be detected by demodulation of the photo-signal with a phase sensitive detector, such as a lock-in amplifier. Under most conditions, the signals of neutrals are largely not affected by the electric field (the notable exception being processes involving excitation from charge transfer), so neutral signals can be filtered out at the demodulated frequency.[2] The demodulation scheme results in a derivative-like lineshape which makes it difficult to accurately determine linewidths, line strengths, and modulation depths (the ratio of the Doppler shift to the linewidth), as all these parameters are strongly correlated.

The theory of VMS lineshapes has been well established by John Farley in 1991.[13] The drift velocity (v) of ions in a positive column is directly proportional to the electric field magnitude (E), the proportionality constant being the ion mobility (K). The drift velocity of an ion in a static electric field is well known[14] and described in Equation (1)

$$v = KE. \tag{1}$$

The ion mobility depends on the temperature and pressure of the neutral collision partner, and it is often reported as a reduced ion mobility, K_0, adjusted to standard temperature and pressure. Because molecular collisions occur on the nanosecond time scale, whereas the period of the discharge is on the order of tens or hundreds of microseconds, we can assume that ions will rapidly achieve drift velocity,[13] because there are on the order of 10^3 to 10^4 collisions per half-cycle of the discharge. For experiments with a sinusoidal variation in electric field, there is, therefore, a sinusoidal variation in velocity such that

$$v(t) = KE\cos(2\pi t). \tag{2}$$

In this work we define the time (t) in fractional periods, a dimensionless quantity. This is a convenient choice as it avoids consideration of the driving frequency and any prefactors in the equations as a result of integration. The Doppler shift formula can be used to rewrite Equation (2) in frequency space,

$$\nu_{mod}(t) = v(t)\frac{\nu_0}{c} = \nu_{ma}\cos(2\pi t), \tag{3}$$

where $\nu_{mod}(t)$ is the time dependent transition frequency modulation in terms of ν_{ma}, the velocity modulation amplitude (VMA). The term, ν_0, is the center frequency of the transition. Over the course of the discharge cycle the line center changes as a function of time so the following transform must be applied to the spectroscopic lineshape (χ, a function of frequency detuning, ν) in order to model the

---

[a)]Electronic mail: bjmccall@illinois.edu. URL: http://bjm.scs.illinois.edu.

experiment

$$\chi(\nu) \rightarrow \chi(\nu + \nu_{mod}(t)). \tag{4}$$

Incidentally, this same transformation is used to model wavelength modulation lineshapes.[15] Velocity modulation and wavelength modulation are mathematically equivalent but differ in experimental realization. The former modulates the transition linecenter and the latter modulates the laser frequency. Wavelength modulation is sensitive to both ions and neutrals and lacks the ability to discriminate between the two, which is why VMS is preferentially used for molecular ion spectroscopy.

In most VMS experiments, there are two ion-related modulation processes that occur in tandem, and velocity modulation is not the only process that must be considered. Concentration modulation, the creation and destruction of ions during every half-cycle of the discharge, occurs at twice the frequency of the discharge. This is a challenging process to model *a priori*, but typically it has been assumed to follow the magnitude of the current sourced to the plasma. Generally, ion concentration increases with increased electron concentration,[13,16] so we assume a functional form for the ion concentration (ρ)

$$\rho(t) = \rho_0 |\cos(2\pi t)|, \tag{5}$$

where ρ_0 is the maximum ion concentration. This form is the same one previously used in other VMS works.[13,16]

The detected signal, the product of Equation (5) and the lineshape $\chi(\nu,t)$ as transformed by Equation (4), is demodulated by a lock-in amplifier, which may be considered a Fourier filter that selects only a single frequency component of the incoming signal. This is a multiplication of the signal by a reference signal and integration of the result over a period of the reference signal

$$\chi_{vms}(\nu) = \int_{-1/2}^{1/2} \rho(t)\chi(\nu,t)\cos(2\pi t + \phi)\,\mathrm{d}t. \tag{6}$$

Equation (6) describes the recorded lineshape, with an arbitrary phase, ϕ, which results in a maximum signal when velocity modulation is in-phase with the reference signal.

A proper fit of the VMS lineshape, though challenging due to the correlation of the width, intensity, and modulation depth, would allow for simultaneous determination of the electric field strength, the ion mobility, and the kinetic temperature of the spectral carrier. In cases where the carrier is unidentified, determination of the linewidth with sufficient precision could determine the mass of the carrier relative to the other species in the discharge, which has seen limited success in practice due to the problematic simultaneous determination of linewidth and VMA. Only large differences in mass were found to be reliable, such as the difference between one and two carbon atoms. As positive columns are rich chemical environments, mass identification by VMS is an untapped resource with many applications.

Presumably due to the difficulty of reliably determining covariant fit parameters, only two attempts to extract information from fits to VMS data have been made. The first was a study on $\mathrm{ArH^+}$ and $\mathrm{ArD^+}$ in 1994, wherein the lineshapes were integrated and fit to two overlapping Voigt profiles.[17] Although the results of that work are interesting, integration is not physically meaningful as VMS lineshapes are not the derivative of the underlying lineshape; rather, they are the time average of a function that oscillates in frequency and amplitude. In the second lineshape study by Gao *et al.*,[16] $\mathrm{N_2^+}$ rovibronic transitions were fit with a Voigt profile as the fundamental lineshape, and they attributed the substantial homogeneous linewidth to pressure broadening. The primary limitation in that work is that the velocity modulation amplitude was held fixed to a theoretical value.

In this work, we present a computationally rapid method of separating the velocity modulation depth and the linewidth. The application of a pseudo-Voigt profile[18] is used as a reasonably accurate (~1%) and computationally trivial replacement to the full Voigt profile. Translational temperature assuming a known ionic mass, ion mobility, peak electric field strength, and line intensity is determined with low uncertainty. As VMS continues to be utilized in more complex techniques with additional layers of modulation,[4–6] a quantitative understanding of the fundamental VMS lineshape is crucial to successful fitting and analysis of more complicated data.

II. EXPERIMENT AND METHODOLOGY

A. Experiment

VMS experiments, though varied with specific light sources and detection scheme complexity, all are fundamentally the same type of experiment. Effectively, a laser passes through an AC modulated discharge cell and irradiates a detector. The output of that detector is read by a lock-in amplifier which is referenced to the discharge voltage. The output of the lock-in amplifier is then recorded as the frequency of the laser is tuned. A basic experiment is depicted in Fig. 1.

The molecule that is experimentally examined in this work is $\mathrm{H_3^+}$. In this case, a continuous wave laser is single passed through a discharge cell and demodulated with a lock-in amplifier. For this work, a mid-IR optical parametric oscillator is used to scan the R(1,0) transition of the ν_2 fundamental band. Ions are generated in a liquid nitrogen cooled discharge of $\mathrm{H_2}$ at a pressure of 500 mTorr. The cell has a central bore diameter of 18 mm.[19] The discharge is driven at 40 kHz by a ~4 kV peak-to-peak sinusoid. Frequency calibration

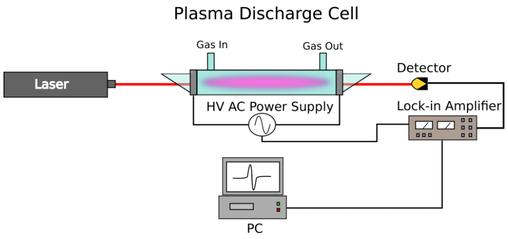

FIG. 1. A typical layout of a VMS spectrometer. It comprises a laser that spectroscopically probes a velocity modulated plasma. A detector converts the light into a voltage that is read by a lock-in amplifier, which is referenced to the voltage that drives the discharge.

is accomplished with a wavemeter (Bristol 621 IR-A) with a nominal uncertainty of 0.2 ppm. However, sub-optimal alignment results in less accurate readings. In the present work, the sole purpose of frequency calibration is to ensure a linear frequency axis as precision is more important to the contour of the lineshape than absolute frequency calibration. The light source, detector, and lock-in amplifiers used in the present work are described in detail in Crabtree *et al.*[20]

B. Method

As alluded to in Section I, the Voigt profile is required to adequately model the lineshape. Due to the fact that a nonlinear least squares routine makes multiple calls, and recognizing that numerical integration is part of the lineshape model, it is advantageous to have a computationally inexpensive form of the Voigt profile with which to work. Hence, we chose to use the pseudo-Voigt profile described in Thompson *et al.*[18]

The pseudo-Voigt profile (χ_{pV}) approximates the Voigt profile as a linear combination of Lorentzian and Gaussian transition profiles, given by Equation (7)[18]

$$\chi_{pV}(\nu;\nu_0,\Delta_V,\eta) = \eta L(\nu;\nu_0,\Delta_V) + (1-\eta)G(\nu;\nu_0,\Delta_V) \tag{7}$$

where

$$L(\nu;\nu_0,\Delta_V) = \frac{2\Delta_V}{\pi(4(\nu-\nu_0)^2+\Delta_V^2)} \tag{8}$$

and

$$G(\nu;\nu_0,\Delta_V) = \frac{2\sqrt{\ln 2}}{\Delta_V\sqrt{\pi}}e^{\frac{-(\nu-\nu_0)^2 4\ln 2}{\Delta_V^2}}. \tag{9}$$

The relevant parameters are the linear combination coefficient (η), the Voigt full-width at half-maximum (Δ_V), and the linecenter (ν_0). The η coefficient can be described in terms of the Lorentzian (Δ_L) and Voigt full-widths (Δ_V), and the Voigt full-width can be written in terms of the individual contributions to the full-width from the underlying Gaussian (Δ_G) and Lorentzian (Δ_L) profiles, which are the spectroscopically relevant parameters[18]

$$\Delta_V(\Delta_L,\Delta_G) = (\Delta_G^5 + 2.692\,69\Delta_G^4\Delta_L + 2.428\,43\Delta_G^3\Delta_L^2 + 4.471\,63\Delta_G^2\Delta_L^3 + 0.078\,42\Delta_G\Delta_L^4 + \Delta_L^5)^{\frac{1}{5}}, \tag{10}$$

$$\eta(\Delta_L,\Delta_V) = 1.366\,03\left(\frac{\Delta_L}{\Delta_V}\right) - 0.477\,19\left(\frac{\Delta_L}{\Delta_V}\right)^2 + 0.111\,16\left(\frac{\Delta_L}{\Delta_V}\right)^3. \tag{11}$$

This approximation has a maximum deviation of 1.2% at the center of the profile,[21] which contributes to the minimum relative uncertainty for any contour-based parameters extracted from the fit, i.e., terms that affect the actual lineshape such as width and velocity modulation amplitude. With a suitable expression for the fundamental lineshape (Equation (7)), the transform from Equation (4) is applied to cause the linecenter to oscillate in time with an amplitude of ν_{ma}, resulting in

$$\begin{aligned}\chi_{pV}&(\nu,t;\nu_0,\Delta_V,\eta,\nu_{ma})\\ &= \eta L(\nu+\nu_{ma}\cos 2\pi t;\nu_0,\Delta_V)\\ &\quad + (1-\eta)G(\nu+\nu_{ma}\cos 2\pi t;\nu_0,\Delta_V).\end{aligned} \tag{12}$$

In order to arrive at a final functional form for integration, Equation (12) is multiplied by $\cos 2\pi t$ (selecting the frequency component equal to the driving frequency), multiplied by a transition intensity (A), and a y-offset (y_0) is added to account for a non-zero baseline. By integrating over a full discharge period, the final lineshape, χ_{vms}, is

$$\begin{aligned}\chi_{vms}&(\nu;A,\nu_0,\Delta_L,\Delta_G,\nu_{ma},y_0)\\ &= A\int_{-\frac{1}{2}}^{\frac{1}{2}}\chi_{pV}(\nu,t;\nu_0,\Delta_V(\Delta_L,\Delta_G),\eta(\Delta_L,\Delta_V),\nu_{ma})\\ &\quad\times\cos 2\pi t\,\mathrm{d}t + y_0.\end{aligned} \tag{13}$$

To summarize, the parameters from Equation (13) that are to be determined by the fit of Equation (13) to the experimental spectrum are the line intensity (A), linecenter (ν_0), homogeneous and inhomogeneous full-widths (Δ_L,Δ_V), velocity modulation amplitude (ν_{ma}), and y-offset (y_0).

In order to fit VMS lineshapes, a custom fitting program was written in `python3`, using the extensive `numpy` and `scipy` modules. The core functionality of the program is derived from the Levenberg-Marquardt nonlinear least squares routine from the `scipy.optimize` module. Integration is performed by the `numpy` module's `trapz` function, which is a trapezoidal rule numerical integration. The first step for integration is to define a two-dimensional array with frequency along one axis and time along the other. The size of the array is determined by a combination of the experimentally measured frequency data and the time step size that gives a sufficiently converged lineshape. Moreover, the number of time points is equal to the period divided by the step size, and the step size is chosen as a compromise between accuracy and integration time. Once the array is populated, the `trapz` function integrates along the time axis, which results in a one-dimensional array equivalent to the observed lineshape.

In order to determine a good step size, the integration was performed repeatedly with incrementally decreasing step size for a variety of different lineshape parameters. The integration time and the peak-to-peak intensity were recorded. Additionally, the standard deviation of the difference between the resultant lineshape with a given time step size and the lineshape of the previous step size are determined. In other words, after a new, smaller time step size is used for the integration, the new lineshape is differenced with the lineshape determined by a larger step size, and the standard deviation of the differences is recorded. This metric is useful as a measure of how much the line's contour changes from one time step size to the next smaller one.

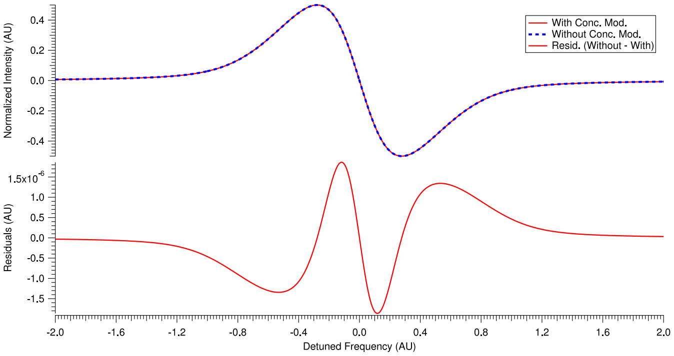

FIG. 2. Here, the effect of including concentration modulation versus ignoring it is highlighted. The overall peak-to-peak signal with concentration modulation is smaller than without it, so the signal for each was normalized to unity to illustrate errors in the contour. The residuals show some clear structure, though it is insignificant (∼2 ppm) relative to other sources of error (∼2%).

As a result of this convergence testing, a step size of 0.004 was chosen due to its reasonably quick integration time. The chosen step size exhibits less than 1% error as compared to the smallest time step (taken as the converged lineshape), 0.000 25 fractional periods. The 1% is the discrepancy between the peak-to-peak values of the chosen time step and the converged time step, and it is considered a contributing source of error to the contour of the lineshape.

Farley and Gao *et al.* include in their VMS models a term that accounts for concentration modulation, as described in Equation (5).[13,16] In tests we found that inclusion of Equation (5) does affect the absolute intensity; however, the overall effect on the contour is less than 2 ppm. As 2 ppm is far less than the error introduced by the pseudo-Voigt approximation and the numerical integration (∼2% total), we have omitted concentration modulation from fits and simulations. Figure 2 illustrates the effect of including concentration modulation. The intensities were normalized to examine contour-based errors.

Fits of experimental data to Equation (13) with all parameters floating initially did not converge due to the large covariance between the velocity modulation amplitude (VMA) and full-width parameters. To circumvent this problem, the fit was performed first by holding the VMA constant at a value that corresponds to a rough estimate informed by the magnitude of the electric field and the ion mobility. The ion mobility can be approximated by the equation for the reduced ion mobility in Mason and McDaniel[14]

$$K_0 = \frac{13.876}{\sqrt{\alpha\mu}}. \tag{14}$$

The only necessary information is the polarizability of the neutral species (α in Å^3) and the reduced mass of the ion and its collision partner (μ in amu). The electric field strength can be approximated by dividing the applied voltage to the electrodes by the distance between the electrodes and reducing the result by an order of magnitude to account for the fact that most of the voltage drop in a glow discharge occurs in the space before the negative glow.[22] After the first fit converges, the residuals are examined for structure that indicates that the velocity modulation depth or VMD (ν_{ma}/Δ_V) is incorrect. The fixed VMA fit is performed several times to refine the VMA estimate, each time examining the residuals. When a good value for the VMA is determined, the fit is performed again floating all the parameters, and convergence is achieved. This approach works because the VMD has subtle effects on the central slope and extrema of the two lobes of VMS-type lines as summarized in Figures 3 and 4. As the VMD is increased, the interior of the extrema becomes more curved and the interior slope becomes less steep. The reason for these differences is that as the VMD is increased, the individual Doppler-shifted components become more resolved. For VMD < 10% it becomes more difficult to distinguish one value of VMD from another. Fits to data with low VMD are therefore likely prone to substantial error. The VMD determined from the fits to the data presented in this work is ∼30%, which gives

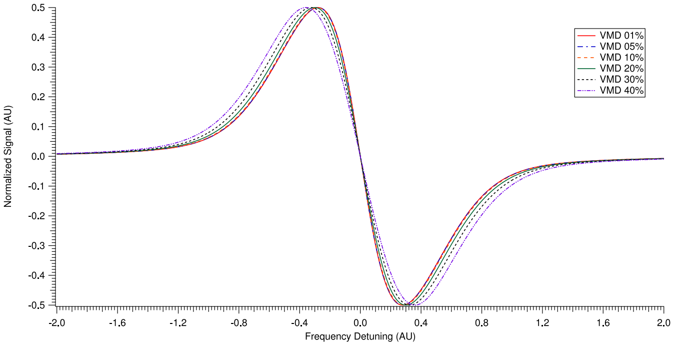

FIG. 3. The velocity modulation depth (VMD) has a subtle effect on the contour of VMS lineshapes. The peak-to-peak intensities of each lineshape are normalized to unity.

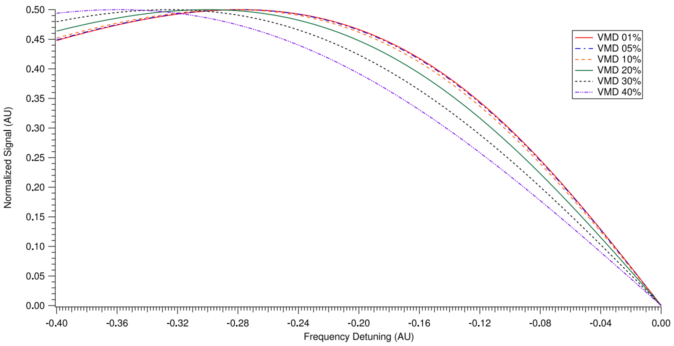

FIG. 4. Closer inspection of Figure 3 makes plain the effect of velocity modulation depth (VMD) on the lineshape.

confidence in the fitting approach. After the fit was converged, the value of the VMA can be substantially changed and the fit with the floating VMA will converge on the correct result.

III. RESULTS AND DISCUSSION

A single scan of the R(1,0) transition was recorded as described in Section II A. Using the method described in Section II B, a good fit was determined. The data, fit, and residuals can be seen in Figure 5, and a summary of the fitted parameters is presented in Table I.

The fitted parameters all exhibit extremely small uncertainties as reported by the least squares regression. In the case of the linecenter and y-offset these values can be taken as is, since they are not determined by the contour of the line and are not subject to the convergence error or the pseudo-Voigt approximation, which combined present the need for an additional 2% relative error to be added to the overall uncertainty of the remaining parameters (1% from the pseudo-Voigt approximation and 1% from the convergence error).

The intensity of the transition is sufficiently well determined as to present the opportunity for determining the relative populations of rovibrational levels. The absolute populations cannot be determined because concentration modulation has been excluded from the model. Under the assumption that the same concentration modulation uniformly affects each quantum state, relative determinations of populations are possible. Testing this hypothesis may provide for an interesting avenue of future investigation. Regardless of this limitation, more precise intensity will lead to more accurate rotational/vibrational temperature determination.

Another exciting prospect is that the relative uncertainty of the linecenter is sub-MHz. Though this work was performed with a wavemeter which has an appreciable accuracy error (~200 MHz), proper calibration with a frequency comb and careful control of the experimental conditions may allow this approach to rival the uncertainties determined by sub-Doppler techniques[5,6] without the added experimental difficulty. This would rely on the lines being very symmetric and highly reproducible, which may not always be the case. This problem could be mitigated with balanced detection of counter-propagating beams but would still be susceptible to any average drift velocity caused by asymmetries in the electrodes. This has been confirmed with these discharge electronics in the case of HCO$^+$, which exhibited between a 13 and 14 m/s average drift velocity.[23]

Both the inhomogeneous and homogeneous components of the linewidth were well determined. The two dominant broadening mechanisms for VMS spectroscopy are Doppler and collisional broadening. Plasmas are used for ion generation and result in large thermal energies. Typical VMS targets are low mass ions[2] which when combined with high temperatures result in mid-IR Doppler widths on the order of ~0.5 to ~1.0 GHz. The importance of collisional broadening is less obvious, considering a typical value for the

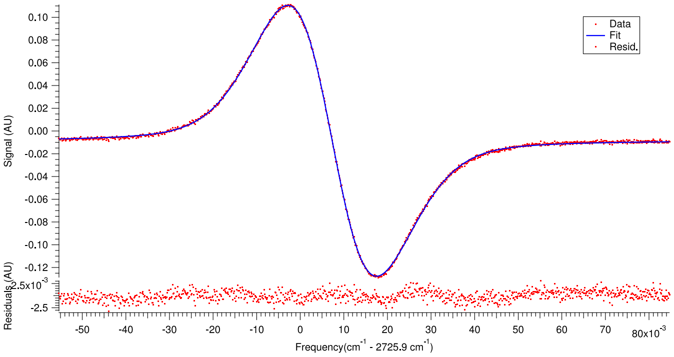

FIG. 5. Experimental spectrum and fit to the R(1,0) rovibrational transition in the ν_2 fundamental band of H$_3^+$. The standard deviation of the residuals is less than 1% of the peak-to-peak signal. The signal-to-noise ratio is ~240 which is very useful in determining the values accurately. There is some structure remaining in the residuals, but it is attributed to the negative lobe being slightly wider than the positive lobe, possibly as a result of an asymmetric drift velocity during half the discharge cycle.

TABLE I. Fit parameters from the R(1,0) transition of H_3^+.

Parameter	Symbol	Value	Error
Intensity	A	0.0220 V	0.0003 V
Linecenter	ν_0	2725.907 331 cm^{-1}	0.000 006 cm^{-1}[a]
Homogeneous linewidth	Δ_L	0.0140 cm^{-1}	0.0001 cm^{-1}
Inhomogeneous linewidth	Δ_G	0.0163 cm^{-1}	0.0001 cm^{-1}
Modulation amplitude	ν_{ma}	0.0079 cm^{-1}	0.0002 cm^{-1}
y-offset	y_0	−0.008 59 V	0.000 03 V

[a] This is not to suggest this is the total uncertainty of the transition frequency; rather, it is the uncertainty of the fit. This work is calibrated via a wavemeter, limiting the accuracy. For an accurate linecenter determination, see Hodges *et al.*[5]

pressure broadening coefficient is ~1-10 MHz/Torr, and VMS spectroscopy is generally performed at pressures between 0.5 and 10 Torr. Nevertheless, Gao *et al.* showed that treating the lineshapes as completely inhomogeneously broadened is insufficient to describe the lineshape.[16] The magnitude of both these broadening mechanisms requires the use of a Voigt profile.

The Doppler width (Gaussian, Δ_G) is determined by the formula

$$\Delta_G = \sqrt{\frac{8kT\ln 2}{mc^2}} \tag{15}$$

and depends on the translational temperature (T) and mass (m) of the ion. The collisionally broadened full-width (Lorentzian, Δ_L) is inversely proportional to the mean time between phase-changing collisions (τ),

$$\Delta_L = \frac{1}{\pi\tau}. \tag{16}$$

To characterize the collisional process, we must consider the predominant collision partner for ions in a plasma. A typical fractional ionization is 10^{-4}, indicating that there are 10 000 more neutral molecules than ions or electrons in a plasma. Conventionally, the ion-ion and ion-electron collisions are neglected because the positive column is assumed to have zero net charge.[14] Higher order corrections for the non-uniform distribution of charge are generally neglected.[2] Therefore, the relevant collision partner is the more abundant neutral, and ion-neutral collisions are the principal type assumed in all VMS experiments.[2,13] Collisions of this type are typically described by Langevin capture theory, a simple model that has been successfully utilized to predict pressure broadening.[24]

The Langevin rate coefficient (k) is expressed in Equation (17) in terms of the polarizability of the neutral (α), the charge of the ion (q), and the reduced mass (μ) of the ion and its collision partner

$$k = 2\pi q\sqrt{\frac{\alpha}{\mu}}. \tag{17}$$

The relationship between the Langevin rate coefficient and the pressure broadening coefficient (γ), pressure (P), and mean time between collisions (τ) is given in Equation (18),[24]

$$\frac{1}{\tau} = nk = 2\pi\gamma P, \tag{18}$$

which can be combined with the ideal gas law and solved for the pressure broadening coefficient

$$\gamma = \frac{q\sqrt{\frac{\alpha}{\mu}}}{kT}. \tag{19}$$

This linewidth is a half-width value, so one would expect $\Delta_L = 2\gamma P$, resulting in a Δ_L on the order of tens of MHz, but Gao and coworkers required much larger values[16] as did the fits in the present work, indicating that Equation (19) is insufficient. Using the Langevin model, the expected homogeneous linewidth in Gao's experiment (N_2^+ at a pressure of 10 Torr) would be 26 MHz; however, Gao's reported homogeneous linewidth is much larger, on the order of the Gaussian linewidth. The collisional process must not be well described by the Langevin model, and there must be a different source for the homogeneous contribution to the linewidth.

In order to better understand the collisional environment that an ion in a positive column experiences, we must start from basic principles. Let us begin by considering the equation of motion for ions in an electric field, as described by Chen[25] and summarized by Civiš[17]

$$\mu\frac{\partial v}{\partial t} = qE - \frac{\mu}{\tau_D}v, \tag{20}$$

where the reduced mass of the ion and its collision partner is μ, v is the drift velocity, t is time, τ_D is the mean time between momentum transfer or diffusion related collisions, q is charge, and E is electric field strength. The first term on the right hand side is the force of the electric field on a charged particle, and the second term is analogous to a drag force linearly proportional to the speed of the charged particle. Solving this equation of motion by assuming a constant electric field gives

$$v(t) = \frac{q\tau_D}{\mu}E(1 - e^{-t/\tau_D}) + v_0 e^{-t/\tau_D}, \tag{21}$$

where $v_0 e^{-t/\tau_D}$ is a collisional deceleration term indicating that as time increases, the initial velocity is less significant. Likewise, as time increases the velocity approaches $\frac{q\tau_D}{\mu}E$.

Equation (21) is a complete description of an ion's speed, but it can be greatly simplified. Recall that the relationship between drift velocity (v), ion mobility (K), and electric field strength (E) is given by Equation (1). As the time scale of the discharge is many orders larger than the time scale of molecular collisions, the relevant time, t, is much greater than τ_D, and Equation (21) can be simplified to

$$v(t) \cong \frac{q\tau_D}{\mu}E. \tag{22}$$

Comparison of Equation (22) to Equation (1) reveals that the ion mobility is

$$K \cong \frac{q\tau_D}{\mu}, \tag{23}$$

which indicates that an estimate of the ion mobility can be made provided information about the mean time between momentum transfer collisions can be determined.

However, τ from Equation (16) and τ_D from Equation (22) are not equivalent. The value τ is related to an ion's collisional cross section ($\sigma(\bar{v})$) at a mean speed ($\bar{v}$) by $\tau = (n\bar{v}\sigma(\bar{v}))^{-1}$; whereas, τ_D is related to the momentum transfer/diffusional cross section (Q_D) by $\tau_D = (n\bar{v}Q_D)^{-1}$. Here n is the number density and $\bar{v}$ is the mean velocity. Both values of τ can be related through n and $\bar{v}$:

$$\tau_D = \frac{\sigma}{Q_D}\tau. \tag{24}$$

The definition of Q_D, as described by Mason and McDaniel,[14] is

$$Q_D \equiv 2\pi \int_0^\pi (1-\cos\theta)\sigma(\theta,\bar{v})\sin\theta \,\mathrm{d}\theta, \tag{25}$$

where $\sigma(\theta,\bar{v})$ is the collisional cross section as a function of scattering angle, θ and mean relative speed of the ion, $\bar{v}$. Without detailed knowledge of the potential energy surface of a scattering event for a particular ion-neutral pair, it is impossible to determine $\sigma(\theta,\bar{v})$. For simplicity, we make the assumption that the cross section is only weakly dependent on the scattering angle such that $\sigma(\bar{v}) \approx \sigma(\theta,\bar{v})$. Using this assumption, Equation (25) becomes

$$Q_D \approx 2\pi\sigma \int_0^\pi (1-\cos\theta)\sin\theta \,\mathrm{d}\theta = 4\pi\sigma. \tag{26}$$

Combining Equations (24) and (26), an approximate relation for τ and τ_D can be formulated

$$\tau_D \cong \frac{\tau}{4\pi}. \tag{27}$$

This simple equation relates the spectroscopically observed linewidth from τ and Equation (16) to the ion mobility through τ_D and Equation (23). Simultaneously it provides an explanation of the large values of the homogeneous linewidth with a simple model derived from the equation of motion presented in Equation (20). The source of the homogeneous linewidth is the collisional enhancement due to the macroscopic motion of the ions in the plasma. As the electric field drives the ions, collisions with neutrals create a drag force balancing the electromagnetic force resulting in a fixed single velocity. The rate of these collisions is determined by the diffusional cross section, which ultimately determines an ion's mobility. This relationship allows us to express the homogeneous full-width in terms of the ion mobility by

$$\Delta_L = \frac{q}{4\pi^2 \,\mu\, K(T,p)}. \tag{28}$$

With a clear understanding of the homogeneous and inhomogeneous linewidths, the fitted values can be used to infer information about the physical conditions and molecule being spectroscopically interrogated. Application of Equation (15) results in a translational temperature of 209 ± 10 K. This is a reasonable temperature and is in accord with previous estimates (200-400 K) of the temperature of liquid nitrogen cooled discharges of molecular hydrogen.[19,26] As the inhomogeneous linewidth is also mass dependent, an analysis of many spectral lines could, in principle, be used to properly distinguish the relative masses of carriers, assuming a Maxwellian velocity distribution. In this case, the mass resolution is 0.03 amu, which is determined by propagating the linewidth error in Equation (15) using a fixed value for temperature. With such a small mass resolution, VMS could be a very powerful tool for distinguishing spectral carriers in chemically rich positive columns, which would be invaluable for assigning unknown spectra.

Using the homogeneous linewidth we can determine the ion mobility. The Langevin model linewidth is estimated using the temperature and the polarizability of molecular hydrogen (0.787 Å^3 ± 5%).[27] This results in a Langevin pressure broadened component equal to 14 ± 2 MHz. Just as in Gao's measurements of N_2^+, this is a dramatic underestimate. With Equation (16), τ is determined to be $7.8 \pm 0.3 \times 10^{-10}$ s. With Equation (27), the value of τ_D is calculated to be $6.0 \pm 0.2 \times 10^{-11}$ s. This can be used with Equation (23) to infer the ion mobility. The determination of reduced ion mobility assumes that the reading of the pressure capacitance monometer is accurate to 5%, and it is calculated to be 12.5 ± 1.5 cm^2 V^{-1} s^{-1} which agrees with the most recent literature value of 11.1 cm^2 V^{-1} s^{-1} within 13% error.[28]

In this case it is fortunate that there is a large signal-to-noise ratio and the VMD (~30%) is in a range that allows for reasonable determination of the VMA (refer to Figure 4). This may not be the case in all VMS experiments. Since the VMD is the ratio of the VMA to the linewidth there are only a limited number of experimental parameters that can be adjusted to ensure a large VMD. The temperature can be reduced and the pressure decreased to minimize the linewidth, and the applied voltage to the electrodes can be increased in order to increase the VMA. Nevertheless, the VMD may still prove too small for some systems. Moving forward, caution is required to properly determine the fitted parameters. Determination of fit parameters below a VMD of ~20% becomes more challenging and ultimately becomes an exercise in futility. This is a direct consequence of how insensitive the contour of the lineshape becomes to changes in VMD (refer to Figure 4).

The RMS value of the drift velocity (determined as 614 ± 16 m/s from Equation (4) and the VMA from the fit) can be used to determine the RMS field strength using Equation (1), provided the ion mobility is accurately known. Using the literature value, the RMS field strength is determined to be 4.8 ± 0.6 V/cm. If one were to take the applied voltage and divide it by the distance between the electrodes, the resultant RMS field strength would be 24 V/cm. Typically, the values in the positive column are an order of magnitude lower,[22] and our inferred field strength of 4.8 V/cm is in accord with that rough estimate. The calculated value of the ion mobility can be used in cases where the reduced ion mobility is not known. With this method, the RMS field strength is determined to be 4.2 ± 0.2 V/cm, which is in reasonable agreement with the other measurement.

IV. CONCLUSIONS

In this work, we present a method for quantitatively fitting VMS lineshapes. This method relies on a detailed examination of the slope of the center portion of the profile and the curvature near the edges of the lobes. Additionally, we confirm that there is a large homogeneous component to the linewidth of VMS greater than what can be explained by Langevin capture theory. This is attributed to the macroscopic movement of ions at the drift speed and the resulting collisional enhancement. From the fit, the translational temperature, transition intensity, ion mobility, and electric field strength are handily determined to reasonable uncertainty.

Together, these values are critical for the quantitative understanding of both the plasma environment and the species being interrogated spectroscopically. This may help lead to better quantification of relative ion populations, rotational and vibrational temperatures, mass identification of spectral carriers, and a better understanding of the lineshapes of more complicated VMS experiments with additional layers of modulation. As a final note, although this method is completely general to any VMS experiment, it does require high data quality and that the VMD be appreciably sized. As the VMD value becomes smaller the task becomes more challenging and requires higher signal-to-noise data.

So long as there is highly reproducible data with high signal-to-noise, it is expected that statistical errors, determined by scanning the same transition multiple times, will be on the same order as the estimated error of fitted parameters. This might be an interesting endeavor for future experiments. Additionally, this same analysis should be performed on different molecules to confirm the generality of this approach.

ACKNOWLEDGMENTS

We would like to acknowledge support from the National Science Foundation (Grant No. CHE 12-13811) and the NASA Laboratory Astrophysics program (Grant No. NNX13AE62G). J.N.H. is appreciative for the support from a Robert and Carolyn Springborn Fellowship and an NSF Graduate Research Fellowship (Grant No. DGE 11-44245 FLLW). J.N.H. is grateful to Adam J. Perry for his assistance in collecting data for the paper. J.N.H. is also appreciative to Thomas C. Allen for useful discussions regarding approaches to fast and accurate numerical integration, Charles R. Markus for useful discussions regarding the homogeneous broadening model, and Daniel N. Gresh for sharing his experimental data that was useful in demonstrating the necessity of high signal-to-noise ratios for the success of this approach. J.N.H. is also especially appreciative of Yahsin Chen for her hard work in translation of H. Gao's paper.

[1] C. Gudeman, M. Begemann, J. Pfaff, and R. Saykally, Phys. Rev. Lett. **50**, 727 (1983).
[2] S. K. Stephenson and R. J. Saykally, Chem. Rev. **105**, 3220 (2005).
[3] B. M. Siller, A. A. Mills, and B. J. McCall, Opt. Lett. **35**, 1266 (2010).
[4] B. M. Siller, M. W. Porambo, A. A. Mills, and B. J. McCall, Opt. Express **19**, 24822 (2011).
[5] J. N. Hodges, A. J. Perry, P. A. Jenkins II, B. M. Siller, and B. J. McCall, J. Chem. Phys. **139**, 164201 (2013).
[6] A. J. Perry, J. N. Hodges, C. R. Markus, G. S. Kocheril, and B. J. McCall, J. Chem. Phys. **141**, 101101 (2014).
[7] A. J. Perry, J. N. Hodges, C. R. Markus, G. S. Kocheril, and B. J. McCall, J. Mol. Spectrosc. **317**, 71 (2015).
[8] C. R. Markus, J. N. Hodges, A. J. Perry, G. S. Kocheril, H. S. P. Müller, and B. J. McCall, Astrophys. J. **817**, 138 (2016).
[9] D. N. Gresh, K. C. Cossel, Y. Zhou, J. Ye, and E. A. Cornell, J. Mol. Spectrosc. **319**, 1 (2016).
[10] C. Savage, A. J. Apponi, and L. M. Ziurys, Astrophys. J. **608**, L73 (2004).
[11] D. T. Halfen and L. M. Ziurys, J. Mol. Spectrosc. **234**, 34 (2005).
[12] D. T. Halfen and L. M. Ziurys, Chem. Phys. Lett. **496**, 8 (2010).
[13] J. W. Farley, J. Chem. Phys. **95**, 5590 (1991).
[14] E. A. Mason and E. W. McDaniel, *Transport Properties of Ions in Gases* (John Wiley & Sons, New York, 1988).
[15] P. Kluczynski, J. Gustafsson, Å. M. Lindberg, and O. Axner, Spectrochim. Acta B **56**, 1277 (2001).
[16] H. Gao, Y.-Y. Liu, J.-L. Lin, J. Shi, G.-G. Xiong, Z.-H. Zhang, and D.-C. Tian, Acta Phys. Sin. **50**, 1463 (2001).
[17] S. Civiš, Chem. Phys. **186**, 63 (1994).
[18] P. Thompson, D. E. Cox, and J. B. Hastings, J. Appl. Crystallogr. **20**, 79 (1987).
[19] B. J. McCall, "Spectroscopy of H_3^+ in Laboratory and Astrophysical Plasmas," Ph.D. thesis, University of Chicago, 2001.
[20] K. N. Crabtree, J. N. Hodges, B. M. Siller, A. J. Perry, J. E. Kelly, P. A. Jenkins II, and B. J. McCall, Chem. Phys. Lett. **551**, 1 (2012).
[21] T. Ida, M. Ando, and H. Toraya, J. Appl. Crystallogr. **33**, 1311 (2000).
[22] A. von Engel, *Ionized Gases* (AIP Press, New York, 1965).
[23] B. M. Siller, J. N. Hodges, A. J. Perry, and B. J. McCall, J. Phys. Chem. A **117**, 10034 (2013).
[24] J. C. Pearson, L. C. Oesterling, E. Herbst, and F. C. De Lucia, Phys. Rev. Lett. **75**, 2940 (1995).
[25] F. F. Chen, *Introduction to Plasma Physics* (Plenum Press, New York, 1974).
[26] T. Oka, Phys. Rev. Lett. **45**, 531 (1980).
[27] T. N. Olney, N. Cann, G. Cooper, and C. Brion, Chem. Phys. **223**, 59 (1997).
[28] P. Neves, J. Escada, F. Borges, L. Tavora, and C. Conde, *IEEE Nuclear Science Symposium Conference Record* (IEEE, 2011), pp. 1793–1794.

Appendix H

Understanding the Origin of the NICE-OHVMS Etalon

H.1 Background

Since the first realization of the mid-IR NICE-OHVMS instrument with the OPO there has been a dramatic fringe that is part of the background. This fringe limits the detection limit and confounds the ability to extract useful information out of all but the largest signals, such as the strong fundamental band transitions of H_3^+. Despite the impressive feats that have been accomplished up to this point, without some form of mitigation of this fringe there are limited prospects for NICE-OHVMS.

The fringe is interesting in that there appear to be many frequency components, creating a large envelope. Somehow this fringe is not removed by the Fourier filtering of the lock-in amplifiers. This suggests that the fringe must change at twice the frequency at which the plasma is being discharged. We also know that it must be caused by the plasma, because it only occurs when the plasma is discharging. If the laser is locked to the cavity, and there is no discharge, then there is no fringe. This correlation led us to believe for a very long time that there was something going on that could not be related to something mundane, *e.g.* an optical etalon.

Etalons do very clearly make it through ordinary NICE-OHMS experiments in the form of residual amplitude modulation (RAM).[91] As the fm-triplet scans over a fringe, each component experiences a variable attenuation and optical phase shift. When the detection phase is set to absorption, only the attenuation of the sidebands matter. However, the case is more complicated when the detection phase is set to dispersion. In that case the phase shift of all three components must be accounted for.

H.2 Origin

After careful consideration of as many of the factors that can be taken into account, the fringe must be caused by an optical etalon that is intensity modulated by the cavity. If the cavity does not remain perfectly on resonance then the maximum intensity of light that is transmitted by the cavity is reduced. If that intensity were modulated at the detection frequency, then that signal would not be filtered out by the lock-in detection scheme.

Intensity modulation is not a particularly exotic source of noise in a lock-in detection scheme. However, the method that causes the cavity to come off-resonance, reducing the intensity, is unique to NICE-OHVMS. Within the optical cavity, there is an AC modulated plasma driven at around 40 kHz. The lock-in detectors are set to detect at twice that frequency. The plasma voltage is driven by a sinusoid, and the number density of all the species generated by the discharge tend to increase with increasing voltage. This change of material within the optical cavity may slightly change the index of refraction. The free spectral range of the cavity is given by $\frac{c}{2nL}$, which implies that the resonance condition of the cavity must change with a change in the index of refraction. Additionally, the bandwidth of the laser lock to cavity is at most 10 kHz, indicating that the lock cannot possibly respond quickly enough to maintain resonance.

Using the equation governing the transmittance of an etalon, we can determine the relationship between the change in index and the change in transmitted intensity,

$$T = \frac{1}{1 + F\sin^2(\delta/2)}. \tag{H.1}$$

The parameter F is the finesse of the resonator (taken as 300 for the NICE-OHVMS system) and δ is the round trip phase shift defined as

$$\delta = \left(\frac{2\pi}{\lambda}\right) 2nl\cos(\theta). \tag{H.2}$$

The wavelength (λ) is taken as 3.67 μm which is typical for this work and the angle of incidence (θ) is zero radians. The length of the etalon (l) is chosen to be 180 cm, also selected to correspond to the NICE-OHVMS experiment. The starting value for the index is 1. Figure H.1 shows how small changes in the index result in large changes in the transmitted light, while holding the wavelength fixed. As can be seen, a small change of only 0.1 ppm in the index results in a reduction of ∼97% of the intensity. If we assume that electron resonances in the plasma are responsible for the change in index, we can estimate relative change as 10^{-12}.[92] This corresponds to an intensity reduction of 10^{-7}. It is clear this has the potential to cause intensity modulation that can be detected, especially considering how lock-ins are specifically designed to measure a very small change in signal. We can model the change in intensity as a time varying sinusoid that follows the voltage of the discharge. The assumption is that as the voltage becomes large there is greater current in the discharge. Larger current means there must be more electrons flowing through. The plasma has a net zero charge, so increased current must mean more ions.[73] This same logic can hold true for charge transfer reactions, and Rydberg states for neutrals. It follows that electronic excitations would happen in

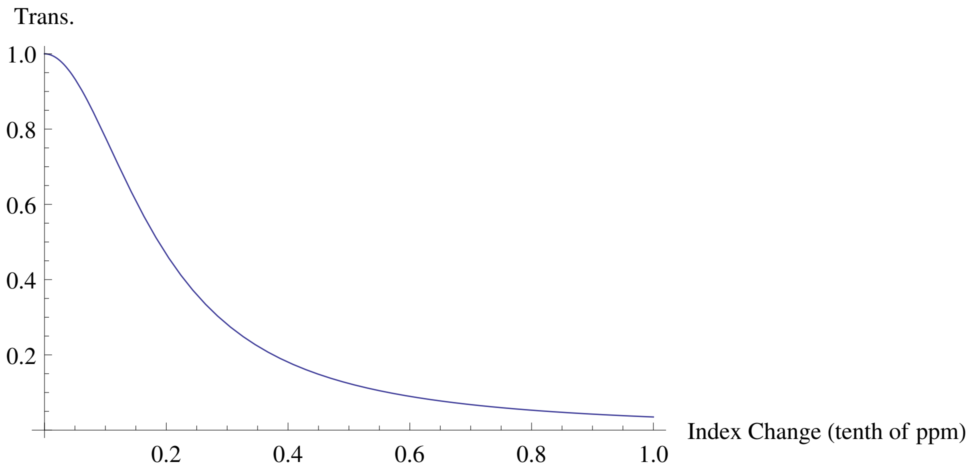

Figure H.1: The effect of changing the index of refraction on the transmittance through an etalon, assuming all other experimental parameters are held constant. Even a small change in the index results in a very large change in intensity transmitted through a cavity.

the same fashion, and it is possible that the varying intensity of visible and near-infrared transitions from species in the discharge could contribute to a varying change in the index in the mid-infrared.

To avoid all of the complex physics that were just described, we will assume that there is an intensity of light transmitted through the cavity, and it varies in time.

$$A(t) = (1 - \alpha_e) + \alpha_e |\cos(2\pi t)| \tag{H.3}$$

The optical extinction amplitude (α_e) is the fraction of the light that is attenuated during a half cycle of the plasma. It is proportional to the change in index of refraction. This amplitude, $A(t)$, is then multiplied by any functional form of the baseline, $F_B(\nu)$ and demodulated at twice the frequency of the discharge.

$$\int_{-0.5}^{0.5} A(t) F_B(\nu) \cos(4\pi t)\ \mathrm{d}t \tag{H.4}$$

The baseline is a function of frequency (ν) and not time so it does not affect the results of the integral. Figures H.2, H.3 and H.4 show the trend solving Equation H.4 for varying sizes of α_e assuming $F_B(\nu)$ is a Lorentzian with the peak intensity at 1.

Using this simple model, it is readily shown that any changes in the baseline that occur at the demodulation frequency can be detected, and also it is clear that a change in index of refraction is a likely culprit for modulating the intensity of the transition.

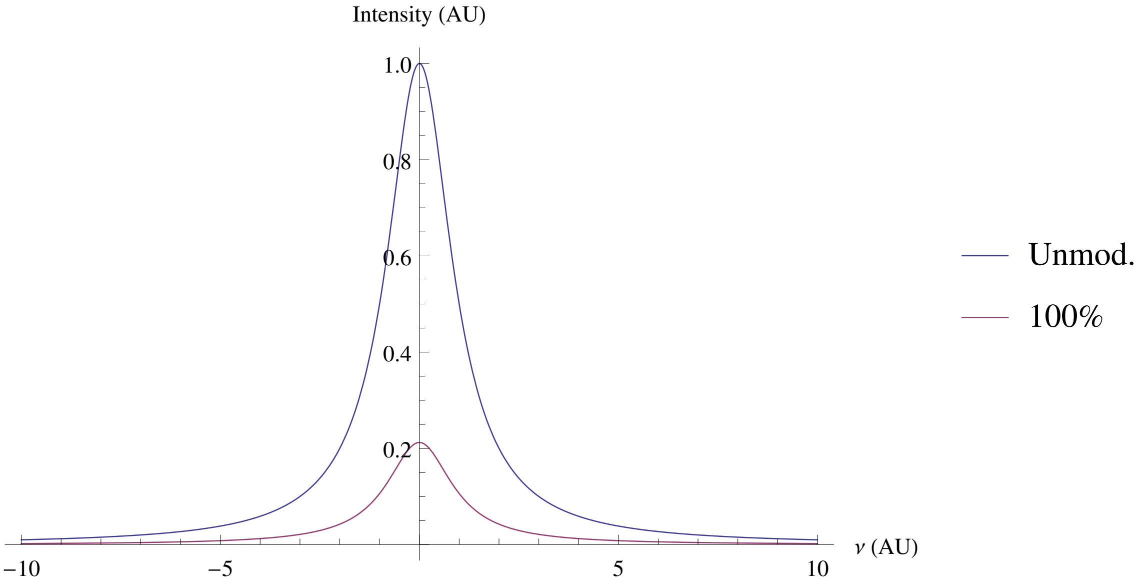

Figure H.2: The effect of turning intensity modulation on for a Lorentzian lineshape. With the optical extinction amplitude equal to 1, *i.e.* the cavity completely comes off resonance every half cycle of the discharge, the demodulated amplitude is reduced to about 0.2.

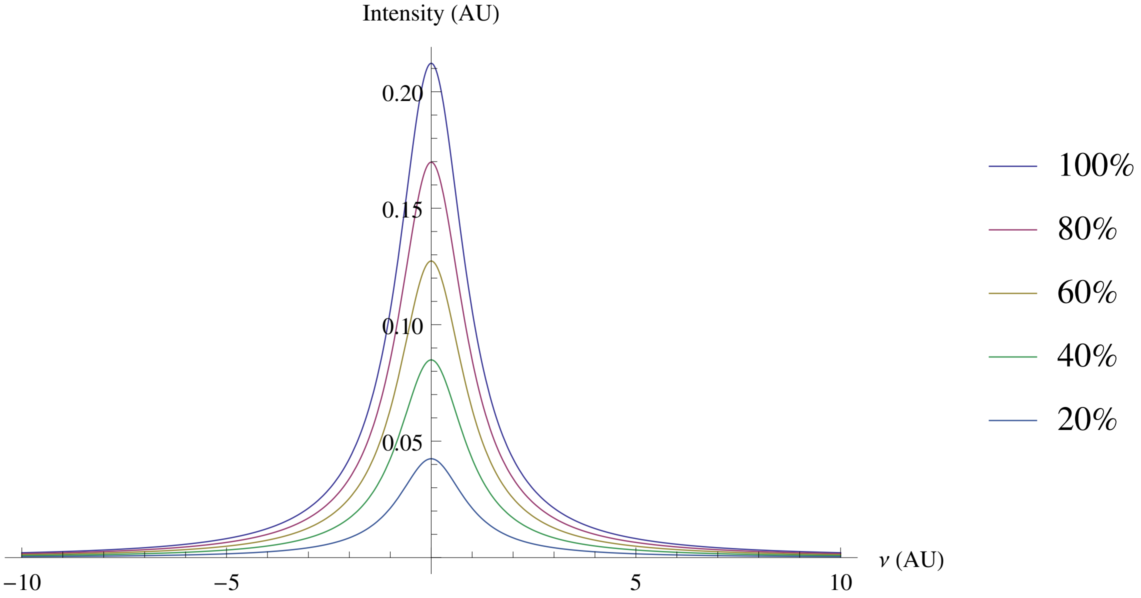

Figure H.3: The effect of decreasing the optical extinction amplitude. As α_e is further decreased there is a linear reduction in the signal. Signal reduction roughly follows the trend $0.25(\alpha_e)$.

H.3 Solution

Since it is clear that the problem is an etalon, there are simple approaches to dealing with it that have been explored and described. The first, is to place all the optics that contribute to etalons at etalon immune

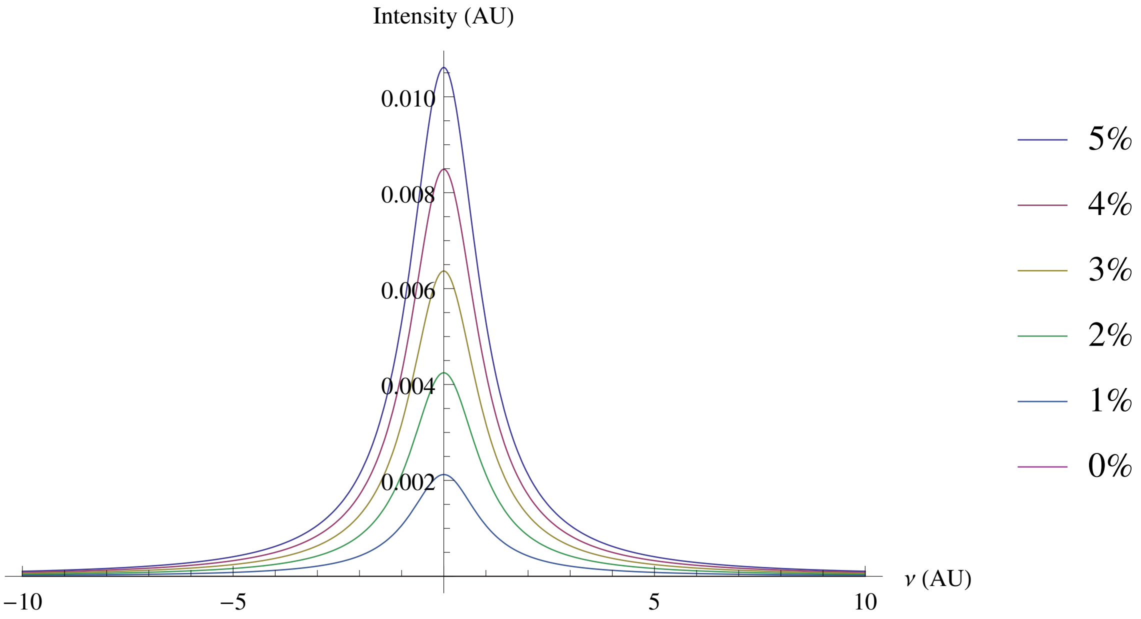

Figure H.4: As the value for the optical extinction amplitude decreases to 0, so too does the intensity of the Lorentzian. The linear relation appears to hold true for the entire dynamic range of α_e.

distances.[91] This is effectively picking a spacing such that the modulation of the sidebands in a frequency modulation scheme are attenuated/phase-shifted the same amount as the laser frequency is scanned over an etalon. For absorption, this means that the frequency of the etalon must be equal to half-integer multiples of the free spectral range, and for dispersion the frequency of the etalon must be equal to integer multiples of the free spectral range. This is very tricky to do for systems such as the NICE-OHVMS system. Both modes of detection are useful which limits selection of etalon immune distances to whole integer multiples. Because we have such a long external optical cavity (180 cm), the etalon immune distances would be equal to 180, 360, 540 etc. cm. This is just not practical. Many optics must be placed at shorter distances.

Another approach is to add a small wavelength jitter which has an amplitude equal to an integer number of fringes.[93] This jitter must be slower than the integration time and effectively averages out a fringe. This would be attractive except it requires an additional layer of modulation. The NICE-OHVMS light source has an insufficient number of control handles to add an additional layer of modulation. This is especially true considering the frequency comb locking servo. Moreover, wavelength modulation would limit the resolution which could negatively impact the Lamb dip measurements. It may be possible to use a mid-IR AOM on the idler beam to add a fast control handle, but the power losses would be significant as it would need to be used in a retroreflector configuration doubling the diffraction efficiency losses. Additionally, the fast corrections have been measured to cause a ∼500 kHz broadening, which is on the order of the Lamb dips and would also negatively affect the resolution of those measurements in the same manner as the wavelength modulation.

The approach that we have opted to use is to insert Brewster plate spoilers in the beam path.[94] The pathlength is slowly changed by tilting the angle of a Brewster plate; this is a type of phase modulation and a small change in angle can sweep over many fringes. In principle, because it is near Brewster's Angle, there are limited power losses which would weaken the ability to perform saturation spectroscopy. The only limitation is that integration must be performed more slowly than the rate at which the Brewster plate shakes. We have observed marked improvements with the introduction of Brewster plates and expect their continued use will serve to push back the limitations of NICE-OHVMS.

Appendix I

Error Analysis of Frequency Determination with a Frequency Comb

In the course of deciding how to appropriately determine the idler frequency with a comb, there were many discussions about whether it was inherently better to determine the frequency of the pump and signal first and subtract them to determine the idler or whether it was better to determine the idler by determining the number of comb modes spanned by the pump and signal. The situation was a problem because the repetition rate of our frequency comb is small enough that errors in the wavemeter must be carefully considered. These discussions became confusing and it made sense to apply mathematical formalism to the wavemeter error.

I.1 For a Single Laser

First let us examine the equation that governs frequency determination via beating a cw laser against a comb, where f is the frequency of the laser, f_{rep} is the repetition rate of the laser, f_{ceo} is the carrier envelope offset, and f_{beat} is the beat note.

$$f = nf_{rep} \pm f_{ceo} \pm f_{beat} \tag{I.1}$$

In order to determine the mode number n, a rough measurement is made with a wavemeter, f_{wm}, to estimate n. The estimate is denoted n_{raw}.

$$f_{wm} = n_{raw}f_{rep} \pm f_{ceo} \pm f_{beat} \tag{I.2}$$

The error in the wavemeter is the difference between the measured frequency f_{wm} and the actual frequency f.

$$f - f_{wm} = nf_{rep} \pm f_{ceo} \pm f_{beat} - (n_{raw}f_{rep} \pm f_{ceo} \pm f_{beat}) \tag{I.3}$$

$$f - f_{wm} = (n - n_{raw})f_{rep} \tag{I.4}$$

Let

$$\delta = n - n_{raw} \tag{I.5}$$

and

$$\xi = f - f_{wm} \tag{I.6}$$

such that

$$\xi = \epsilon_{syst} + \epsilon_{rand} \tag{I.7}$$

$$\delta f_{rep} = \epsilon_{syst} + \epsilon_{rand} \tag{I.8}$$

where ϵ_{syst} and ϵ_{rand} represent the systematic and random errors associated with the wavemeter measurement. With adequate frequency standards these values are experimentally quantifiable.

In order to correctly determine n, $\delta \in [-0.5, 0.5]$. Ultimately, this leads to the simple conclusion that $|\xi|$ must be $< \frac{1}{2} f_{rep}$.

I.2 For the Difference of Two Lasers

What about for the more complex case of measuring the frequency difference (f_i) of two lasers denoted f_p and f_s? Starting with equation I.1:

$$f_i = f_p - f_s = n_p f_{rep} - n_s f_{rep} \pm f_{p-beat} \mp f_{s-beat} \tag{I.9}$$

$$f_{i-wm} = f_{p-wm} - f_{s-wm} = n_{p-raw} f_{rep} - n_{s-raw} f_{rep} \pm f_{p-beat} \mp f_{s-beat} \tag{I.10}$$

$$f_i - f_{i-wm} = n_p f_{rep} - n_s f_{rep} - (n_{p-raw} f_{rep} - n_{s-raw} f_{rep}) \tag{I.11}$$

$$f_i - f_{i-wm} = ((n_p - n_s) - (n_{p-raw} - n_{s-raw})) f_{rep} \tag{I.12}$$

$$f_i - f_{i-wm} = (\Delta n - \Delta n_{raw}) f_{rep} \tag{I.13}$$

We can define an analogous term describing the difference between the estimated Δn_{raw} and Δn.

$$\delta = \Delta n - \Delta n_{raw} \tag{I.14}$$

Similarly, we can define the errors associated with the two lasers ξ_p and ξ_s and determine the total error in the difference, ξ, and it associated random and systematic errors, which means

$$\xi_p = \epsilon_{p-syst} + \epsilon_{p-rand} \tag{I.15}$$

$$\xi_s = \epsilon_{s-syst} + \epsilon_{s-rand} \tag{I.16}$$

$$\xi = \xi_p - \xi_s = f_i - f_{i-wm} \tag{I.17}$$

and

$$\xi = \delta f_{rep} \tag{I.18}$$

$$\xi = \delta f_{rep} = (\epsilon_{p-syst} + \epsilon_{p-rand}) - (\epsilon_{s-syst} + \epsilon_{s-rand}) \tag{I.19}$$

$$\xi = \delta f_{rep} = (\epsilon_{p-syst} - \epsilon_{s-syst}) + (\epsilon_{p-rand} - \epsilon_{s-rand}) \tag{I.20}$$

so that

$$\delta f_{rep} = (\epsilon_{p-syst} - \epsilon_{s-syst}) + (\epsilon_{p-rand} - \epsilon_{s-rand}) \tag{I.21}$$

$$\delta f_{rep} = \epsilon_{syst} + \epsilon_{rand} \tag{I.22}$$

Again, this is in terms of experimental observables as above. Likewise $\delta \in [-0.5, 0.5]$ so that $|\xi|$ must be $< \frac{1}{2} f_{rep}$.

In the case of our system, we know f_{rep} is 100 MHz. We also know that ϵ_{rand} can be either sign and is ~ 5 MHz, which constrains $|\epsilon_{syst}| < 50\text{MHz} \mp \sim 5\text{MHz}$. This model seems to be supported by the experimental data.

There are two especially important results from this analysis. One, we can explicitly see that the difference approach only allows systematic errors that are frequency dependent, such as errors in index of refraction measurement by the wavemeter, like relative humidity, temperature, and atmospheric pressure. Two, we now see the value in using the difference in mode number measurement instead of determining individual frequencies and differencing them. The latter relies on two subsequent measurements that have maximum allowed uncertainties less than 50 MHz, whereas the former only requires a single one. Performing the measurement twice increases the probability that an error in mode number determination affects the final frequency measurement of the idler.

Appendix J

NICE-OHVMS Lineshape Atlas

J.1 Overview

In the course of my NICE-OHVMS lineshape work, I found that it was necessary to develop a sense of how various parameters affected the overall lineshape. This skill is crucial for properly adjusting initial guesses for parameters. By creating this atlas, I hope to qualitatively demonstrate some of the effects of adjusting parameters in the model. Referring to this atlas may provide some useful information to a NICE-OHVMS lineshape fitting novice before he/she attempts a fit.

The relevant parameters for lineshape fitting are the linecenter (ν_0), the transition intensity (A), the concentration modulation depth (α), the concentration modulation phase (ϕ), the inhomogeneous linewidth (Δ_G), the homogeneous linewidth (Δ_L), the heterodyne modulation frequency (ν_{het}), the velocity modulation amplitude (ν_{ma}), and the velocity modulation phase (θ). For the purposes of describing trends it is more useful to use the reduced parameters, velocity modulation depth ($VMD = \nu_{ma}/\Delta_V$) and heterodyne modulation depth ($HMD = \nu_{het}/\Delta_V$) in place of their respective amplitude type parameters. Δ_V is the full-width at half-maximum of a Voigt profile estimated by $\Delta_V \approx 0.5346\Delta_L + \sqrt{0.2166\Delta_L^2 + \Delta_G^2}$.

The caption of each figure labels the illustrated trend, and each figure has an accompanying table listing the parameters used in simulation. All units are arbitrary except angular parameters which are in degrees.

J.2 Concentration Modulation Depth

J.2.1 Absorption

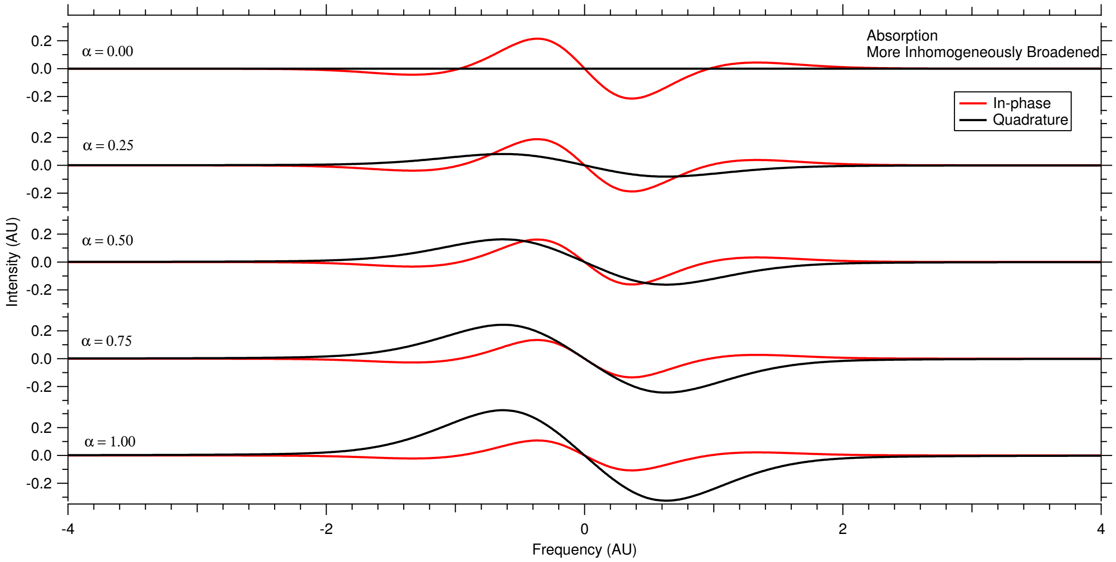

Figure J.1: Concentration modulation series on a more inhomogeneously broadened absorption line.

Table J.1: Simulation parameters for Figure J.1.

Symbol	**Value**
ν_0	0
A	10
α	-
ϕ	45°
Δ_G	1.0
Δ_L	0.5
ν_{het}	0.25
VMD	0.3
θ	0°

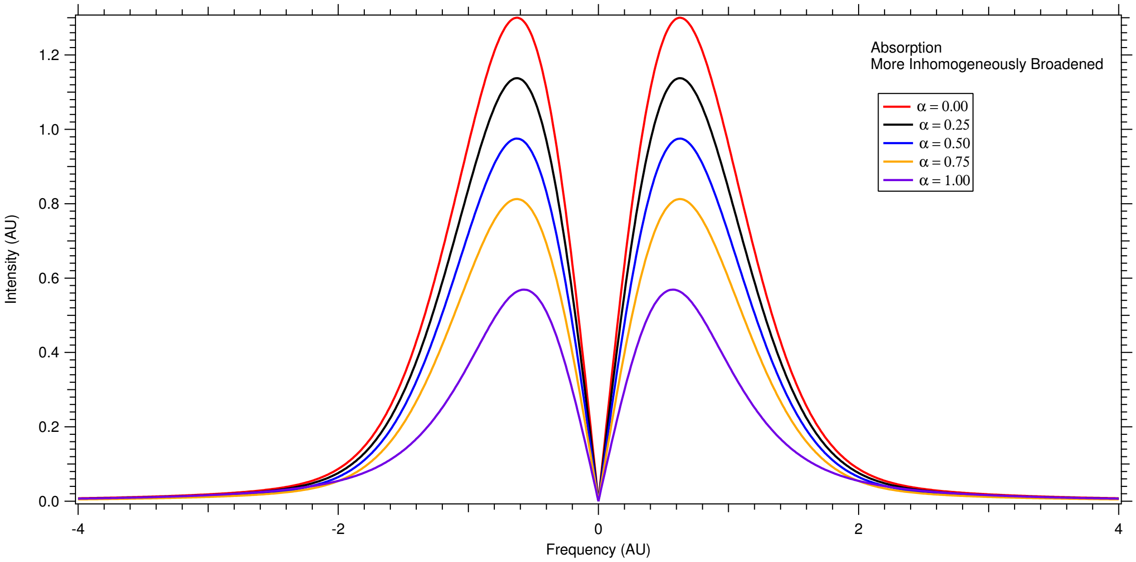

Figure J.2: Concentration modulation series on a more inhomogeneously broadened absorption line magnitude.

Table J.2: Simulation parameters for Figure J.2.

Symbol	**Value**
ν_0	0
A	10
α	-
ϕ	45°
Δ_G	1.0
Δ_L	0.5
ν_{het}	0.25
VMD	0.3
θ	0°

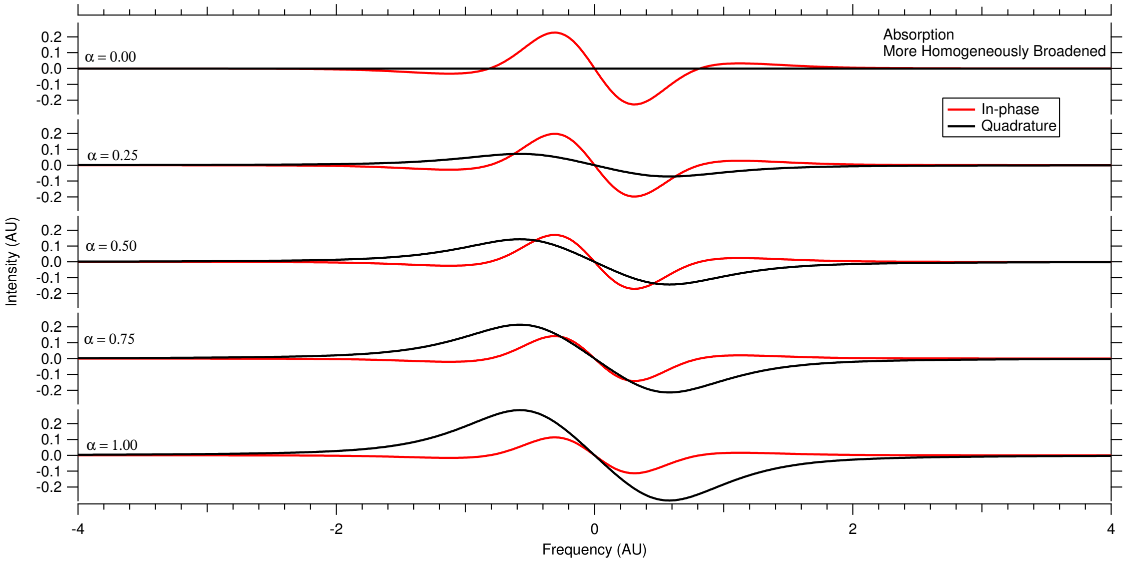

Figure J.3: Concentration modulation series on a more homogeneously broadened absorption line.

Table J.3: Simulation parameters for Figure J.3.

Symbol	**Value**
ν_0	0
A	10
α	-
ϕ	45°
Δ_G	0.5
Δ_L	1.0
ν_{het}	0.25
VMD	0.3
θ	0°

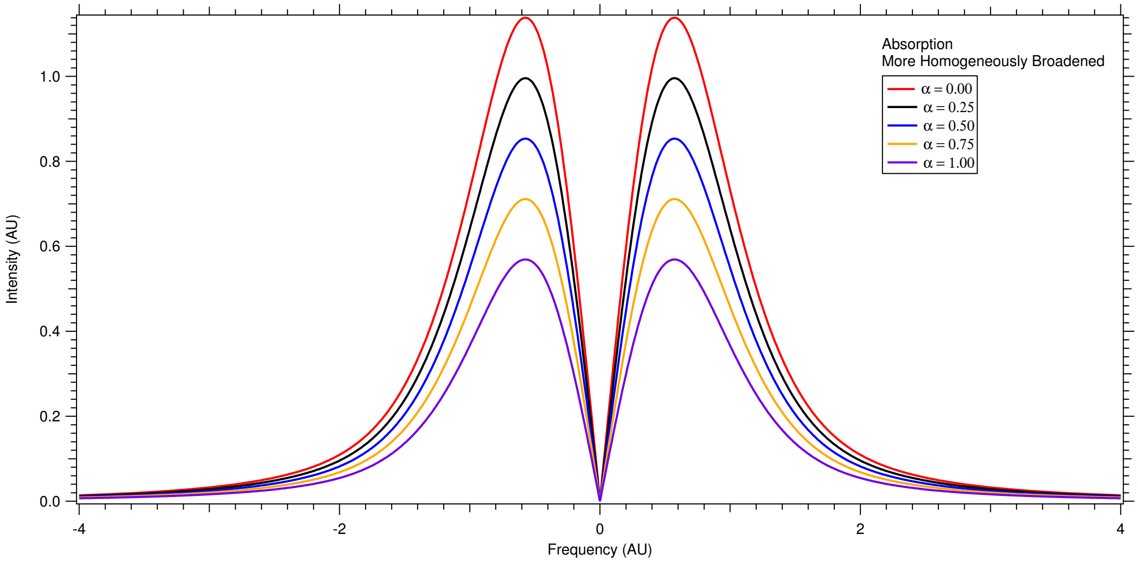

Figure J.4: Concentration modulation series on a more homogeneously broadened absorption line magnitude.

Table J.4: Simulation parameters for Figure J.4.

Symbol	**Value**
ν_0	0
A	10
α	-
ϕ	45°
Δ_G	0.5
Δ_L	1.0
ν_{het}	0.25
VMD	0.3
θ	0°

J.2.2 Dispersion

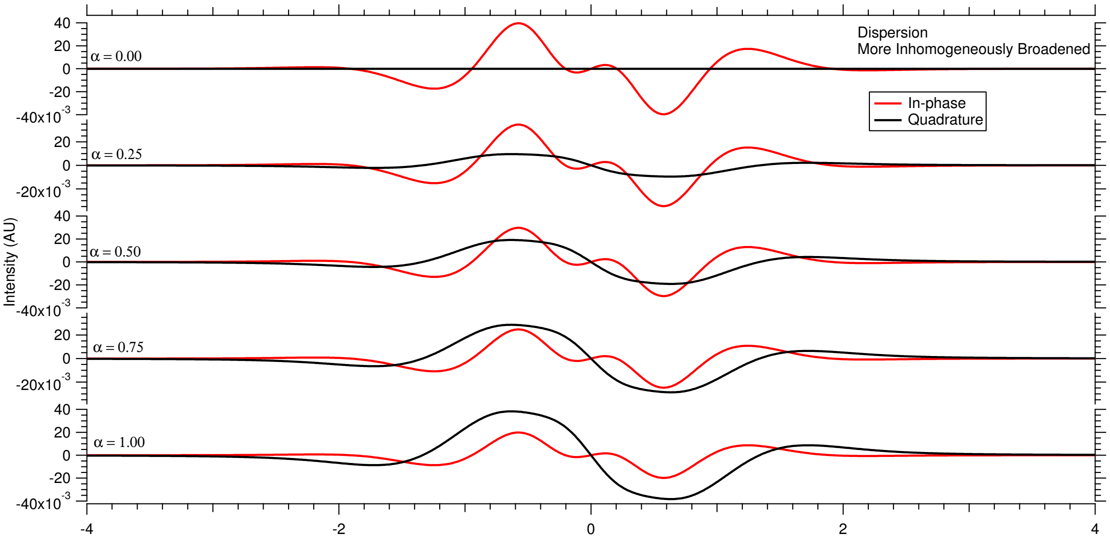

Figure J.5: Concentration modulation series on a more inhomogeneously broadened dispersion line.

Table J.5: Simulation parameters for Figure J.5.

Symbol	**Value**
ν_0	0
A	10
α	-
ϕ	45°
Δ_G	1.0
Δ_L	0.5
ν_{het}	0.25
VMD	0.3
θ	0°

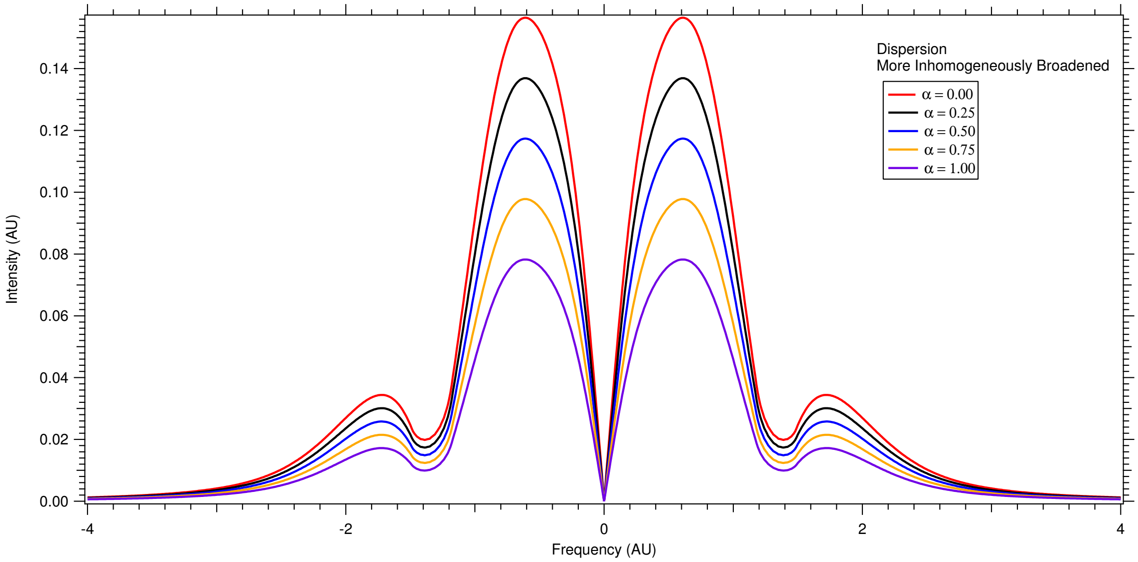

Figure J.6: Concentration modulation series on a more inhomogeneously broadened dispersion line magnitude.

Table J.6: Simulation parameters for Figure J.6.

Symbol	**Value**
ν_0	0
A	10
α	-
ϕ	45°
Δ_G	1.0
Δ_L	0.5
ν_{het}	0.25
VMD	0.3
θ	0°

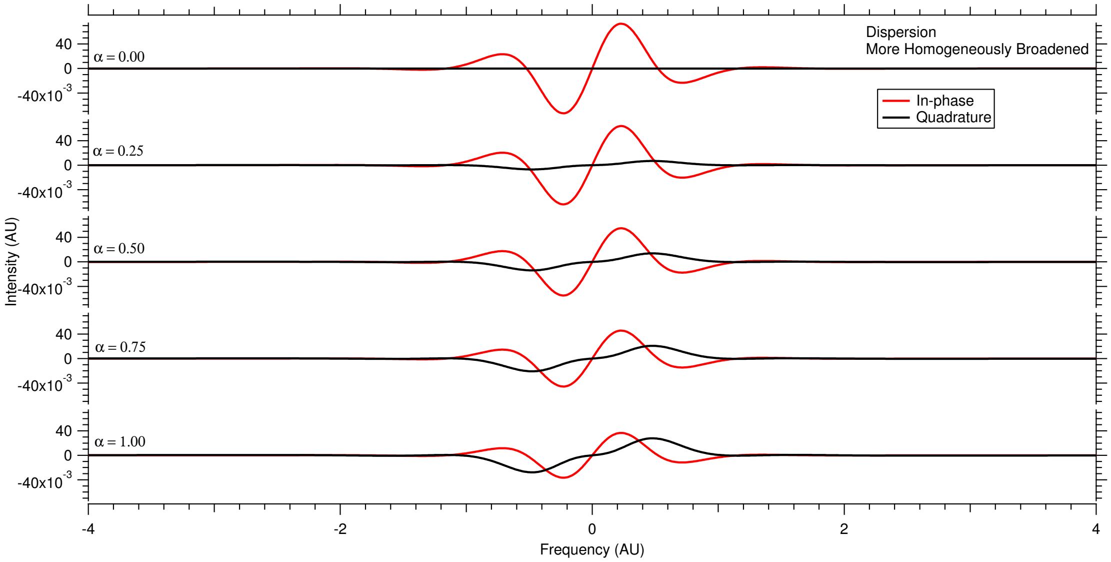

Figure J.7: Concentration modulation series on a more homogeneously broadened dispersion line.

Table J.7: Simulation parameters for Figure J.7.

Symbol	**Value**
ν_0	0
A	10
α	-
ϕ	45°
Δ_G	0.5
Δ_L	1.0
ν_{het}	0.25
VMD	0.3
θ	0°

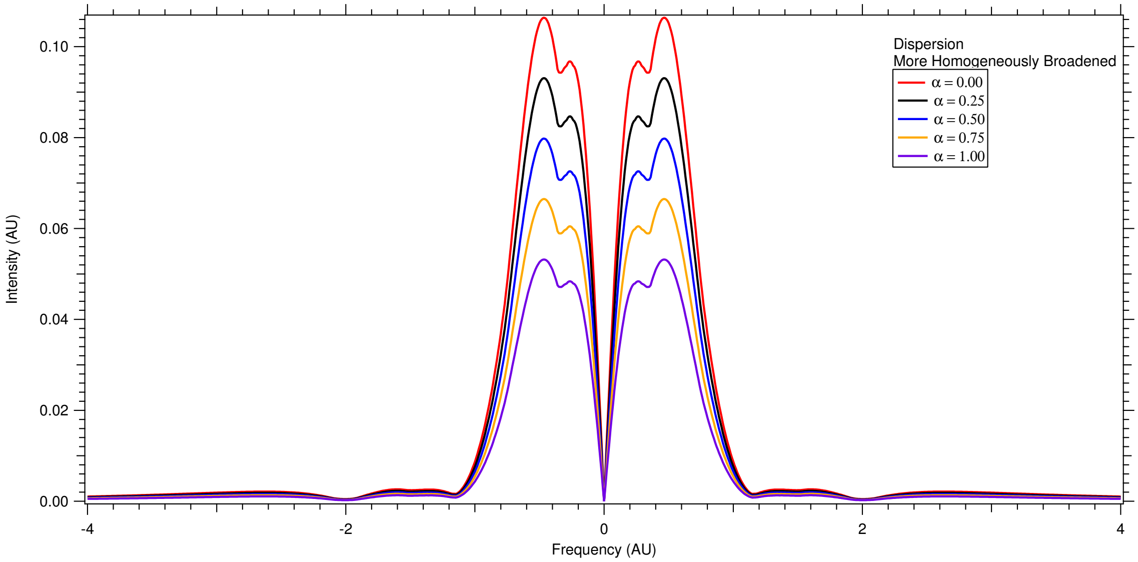

Figure J.8: Concentration modulation series on a more homogeneously broadened dispersion line magnitude.

Table J.8: Simulation parameters for Figure J.8.

Symbol	**Value**
ν_0	0
A	10
α	-
ϕ	45°
Δ_G	0.5
Δ_L	1.0
ν_{het}	0.25
VMD	0.3
θ	0°

J.3 Concentration Modulation Phase

J.3.1 Absorption

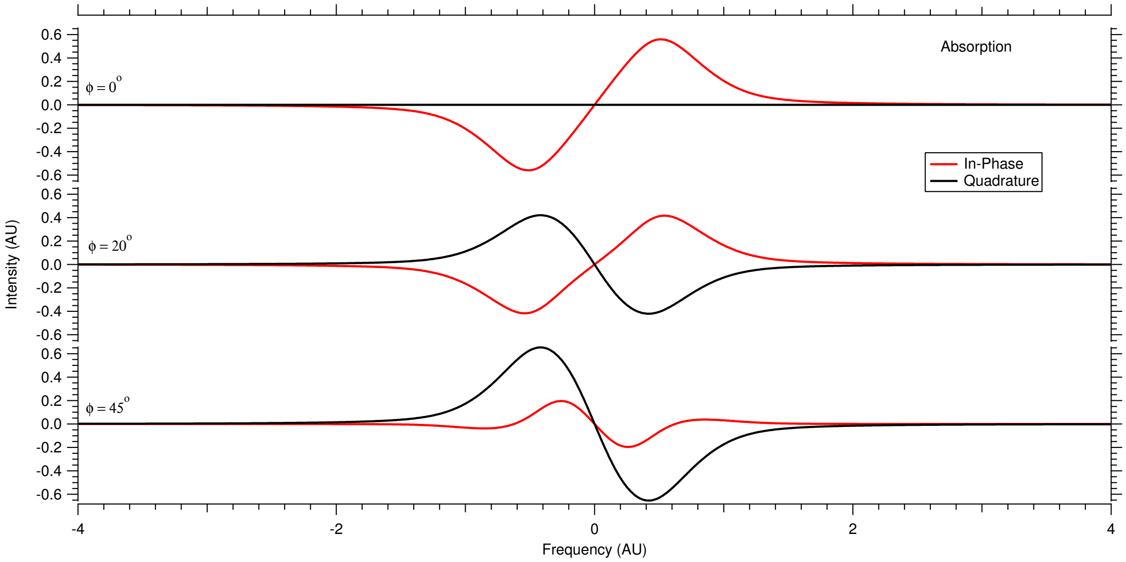

Figure J.9: Concentration modulation phase series on an absorption line.

Table J.9: Simulation parameters for Figure J.9.

Symbol	**Value**
ν_0	0
A	10
α	1.0
ϕ	-
Δ_G	0.5
Δ_L	0.5
ν_{het}	0.25
VMD	0.3
θ	0°

J.3.2 Dispersion

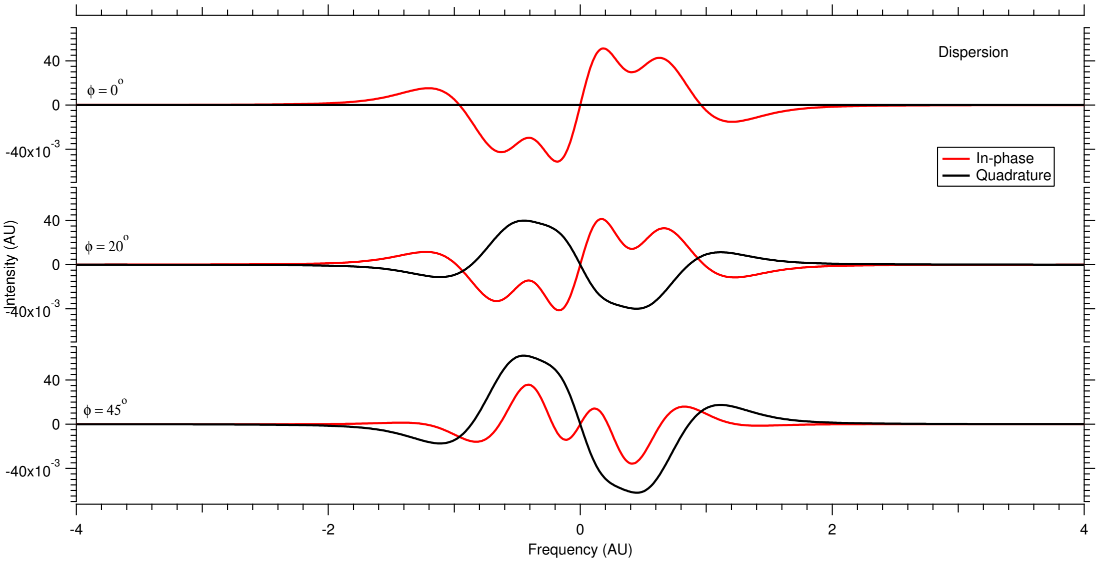

Figure J.10: Concentration modulation phase series on a dispersion line.

Table J.10: Simulation parameters for Figure J.10.

Symbol	Value
ν_0	0
A	10
α	1.0
ϕ	-
Δ_G	0.5
Δ_L	0.5
ν_{het}	0.25
VMD	0.3
θ	0°

J.4 Velocity Modulation Depth

J.4.1 Absorption

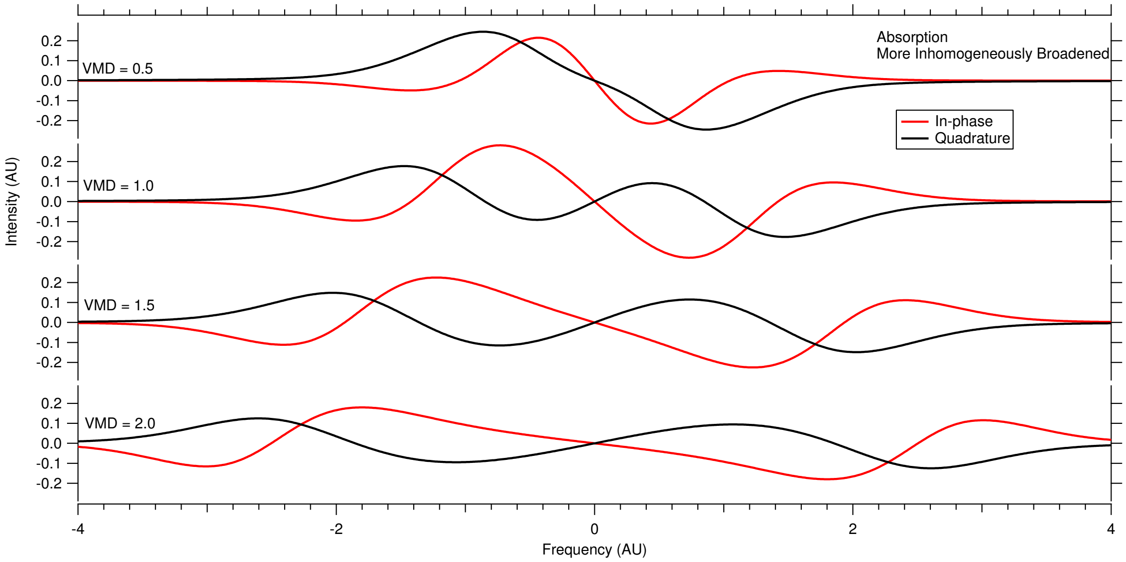

Figure J.11: Velocity modulation series on a more inhomogeneously broadened absorption line.

Table J.11: Simulation parameters for Figure J.11.

Symbol	**Value**
ν_0	0
A	10
α	1.0
ϕ	45°
Δ_G	1.0
Δ_L	0.5
ν_{het}	0.25
VMD	-
θ	0°

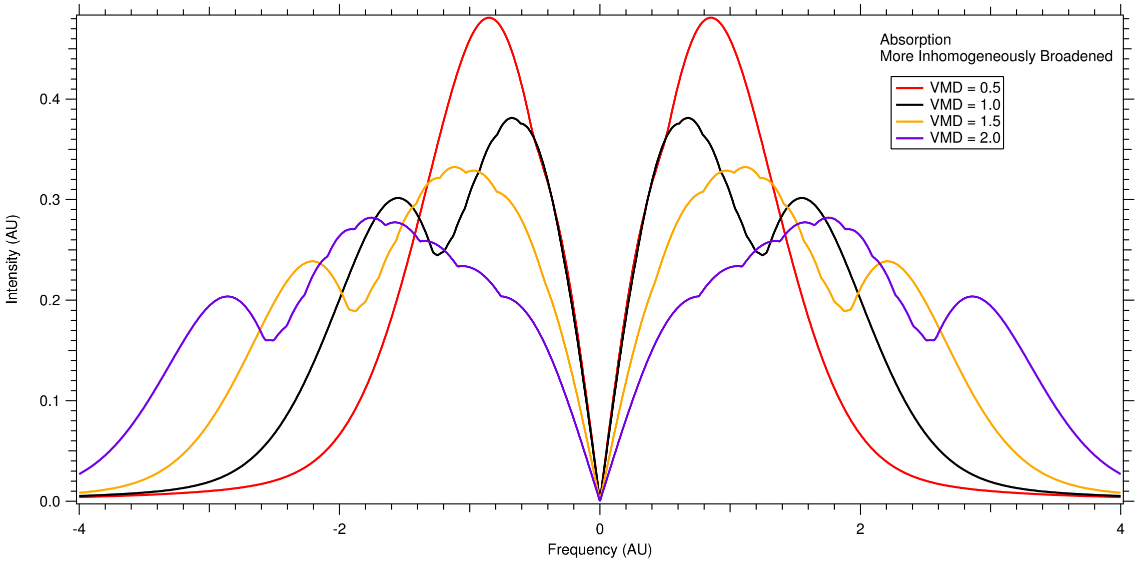

Figure J.12: Velocity modulation series on a more inhomogeneously broadened absorption line magnitude.

Table J.12: Simulation parameters for Figure J.12.

Symbol	**Value**
ν_0	0
A	10
α	1.0
ϕ	45°
Δ_G	1.0
Δ_L	0.5
ν_{het}	0.25
VMD	-
θ	0°

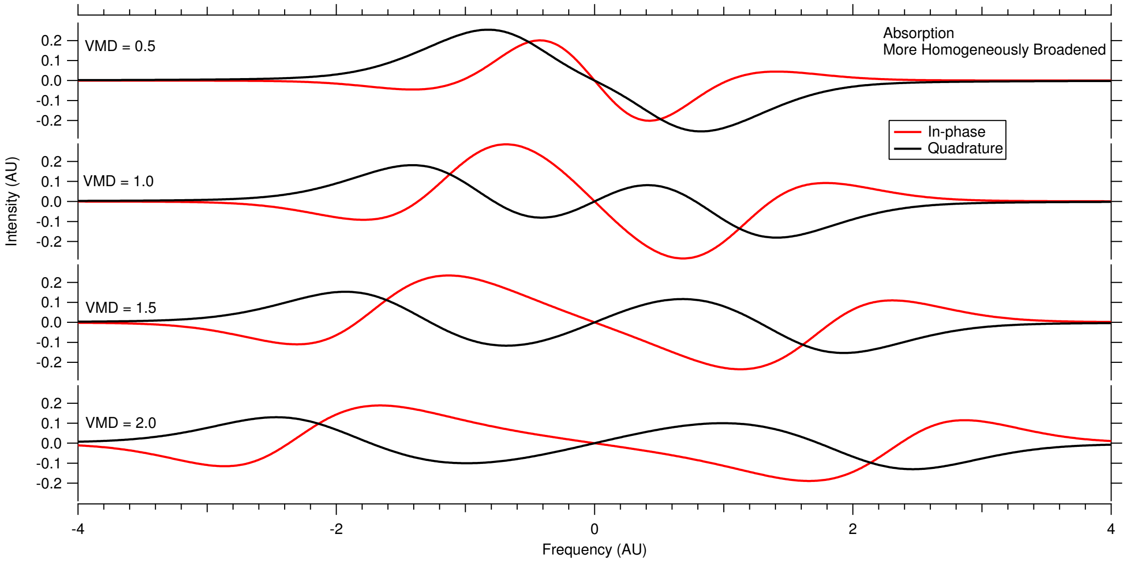

Figure J.13: Velocity modulation series on a more homogeneously broadened absorption line.

Table J.13: Simulation parameters for Figure J.13.

Symbol	**Value**
ν_0	0
A	10
α	1.0
ϕ	45°
Δ_G	0.5
Δ_L	1.0
ν_{het}	0.25
VMD	-
θ	0°

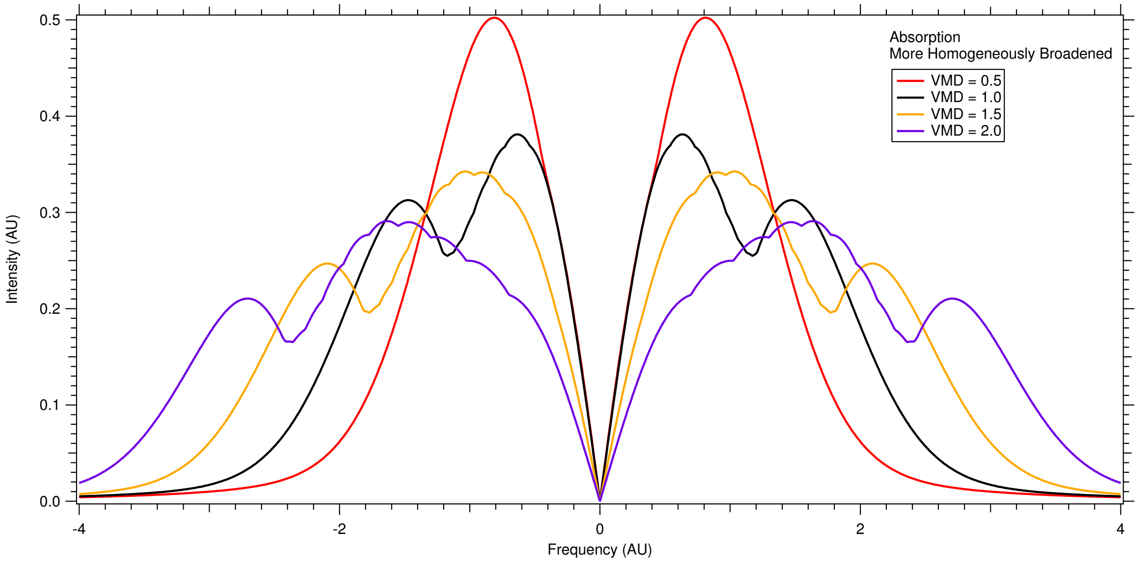

Figure J.14: Velocity modulation series on a more homogeneously broadened absorption line magnitude.

Table J.14: Simulation parameters for Figure J.14.

Symbol	**Value**
ν_0	0
A	10
α	1.0
ϕ	45°
Δ_G	0.5
Δ_L	1.0
ν_{het}	0.25
VMD	-
θ	0°

J.4.2 Dispersion

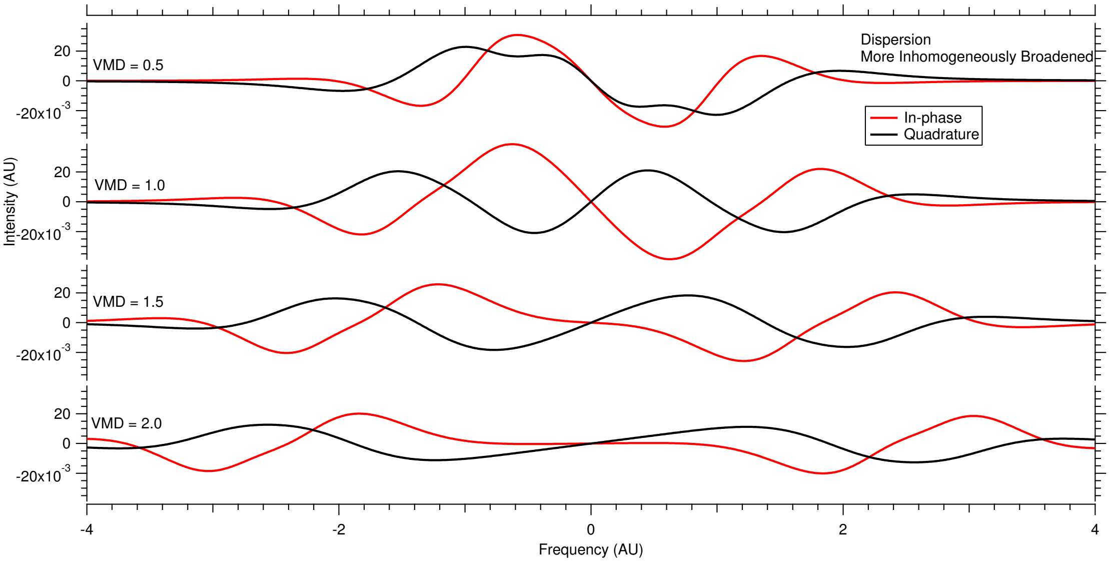

Figure J.15: Velocity modulation series on a more inhomogeneously broadened dispersion line.

Table J.15: Simulation parameters for Figure J.15.

Symbol	**Value**
ν_0	0
A	10
α	1.0
ϕ	45°
Δ_G	1.0
Δ_L	0.5
ν_{het}	0.25
VMD	-
θ	0°

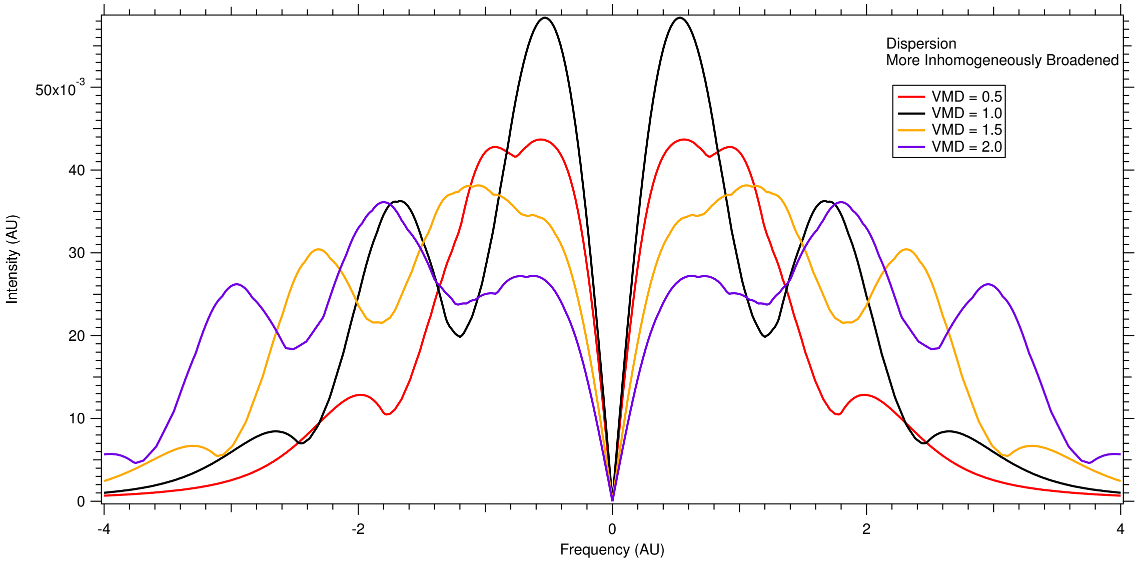

Figure J.16: Velocity modulation series on a more inhomogeneously broadened dispersion line magnitude.

Table J.16: Simulation parameters for Figure J.16.

Symbol	**Value**
ν_0	0
A	10
α	1.0
ϕ	45°
Δ_G	1.0
Δ_L	0.5
ν_{het}	0.25
VMD	-
θ	0°

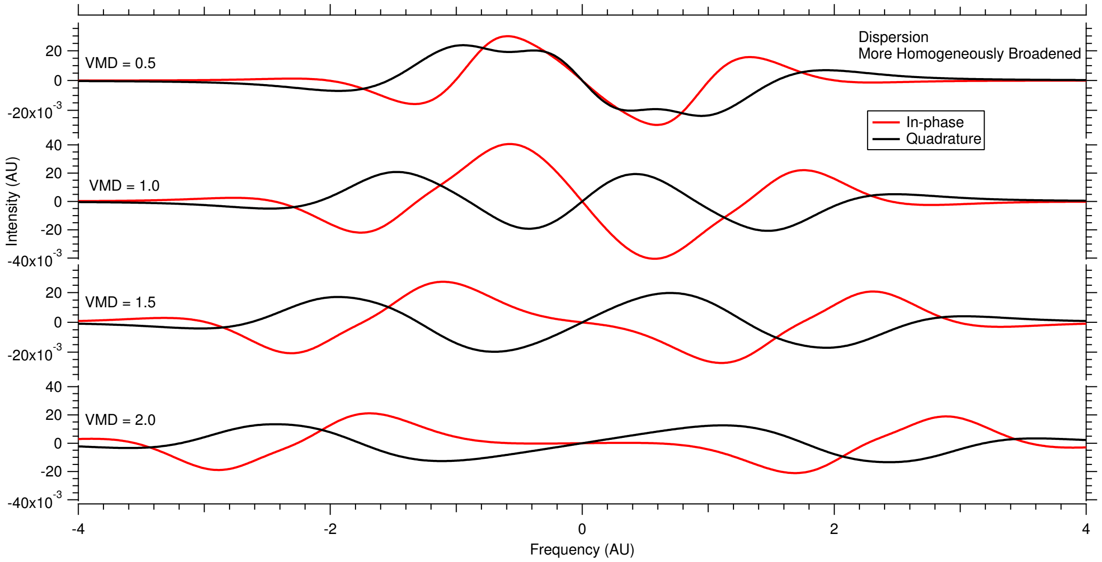

Figure J.17: Velocity modulation series on a more homogeneously broadened dispersion line.

Table J.17: Simulation parameters for Figure J.17.

Symbol	**Value**
ν_0	0
A	10
α	1.0
ϕ	45°
Δ_G	0.5
Δ_L	1.0
ν_{het}	0.25
VMD	-
θ	0°

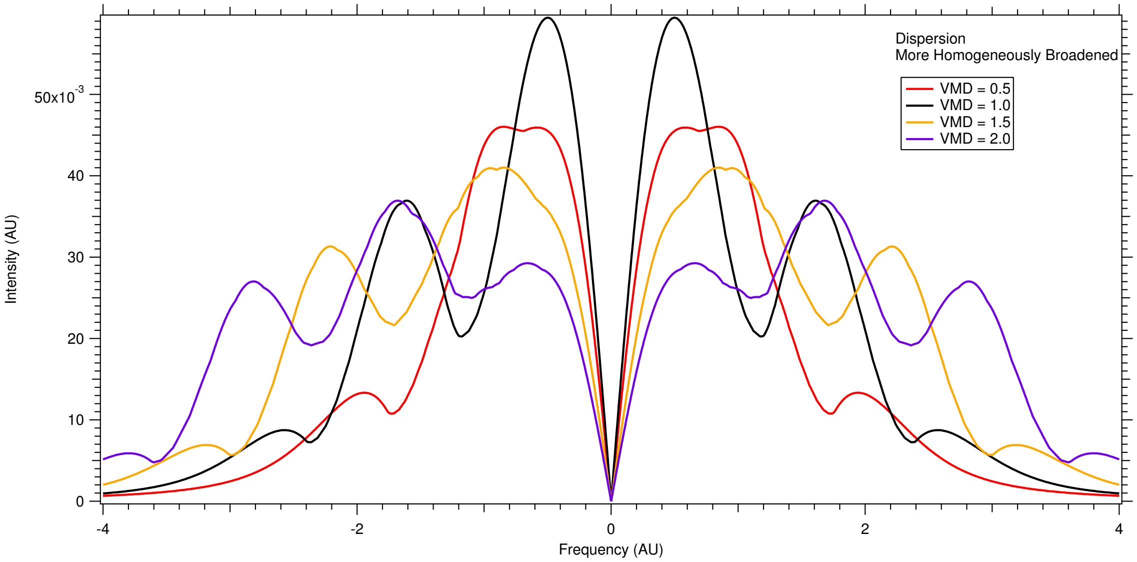

Figure J.18: Velocity modulation series on a more homogeneously broadened dispersion line magnitude.

Table J.18: Simulation parameters for Figure J.18.

Symbol	**Value**
ν_0	0
A	10
α	1.0
ϕ	45°
Δ_G	0.5
Δ_L	1.0
ν_{het}	0.25
VMD	-
θ	0°

J.5 Heterodyne Modulation Depth

J.5.1 Absorption

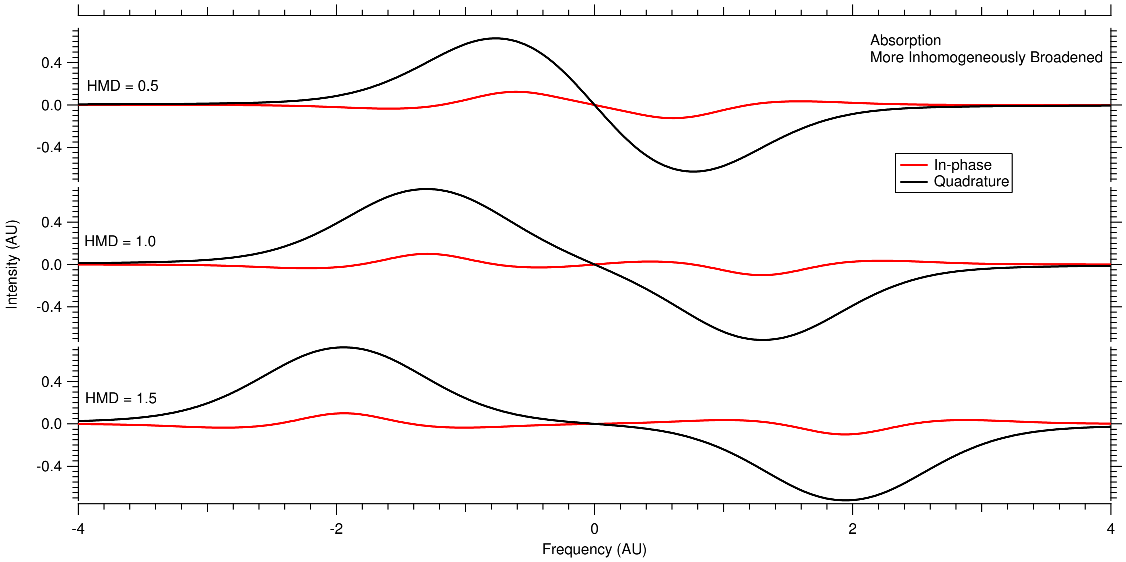

Figure J.19: Heterodyne modulation series on a more inhomogeneously broadened absorption line.

Table J.19: Simulation parameters for Figure J.19.

Symbol	**Value**
ν_0	0
A	10
α	1.0
ϕ	45°
Δ_G	1.0
Δ_L	0.5
HMD	-
VMD	0.3
θ	0°

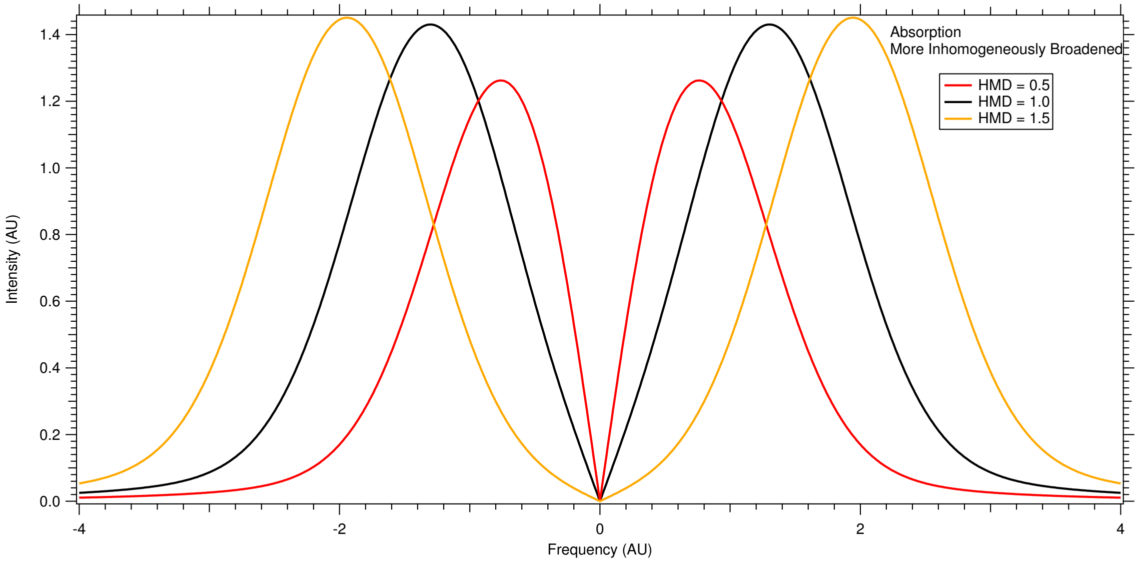

Figure J.20: Heterodyne modulation series on a more inhomogeneously broadened absorption line magnitude.

Table J.20: Simulation parameters for Figure J.20.

Symbol	**Value**
ν_0	0
A	10
α	1.0
ϕ	45°
Δ_G	1.0
Δ_L	0.5
HMD	-
VMD	0.3
θ	0°

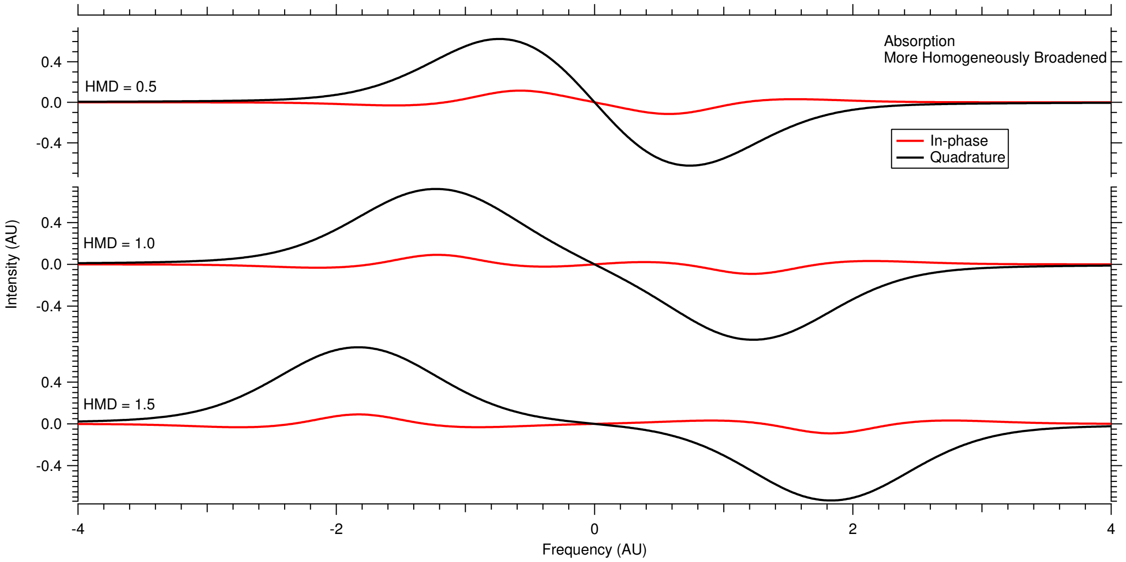

Figure J.21: Heterodyne modulation series on a more homogeneously broadened absorption line.

Table J.21: Simulation parameters for Figure J.21.

Symbol	**Value**
ν_0	0
A	10
α	1.0
ϕ	45°
Δ_G	0.5
Δ_L	1.0
HMD	-
VMD	0.3
θ	0°

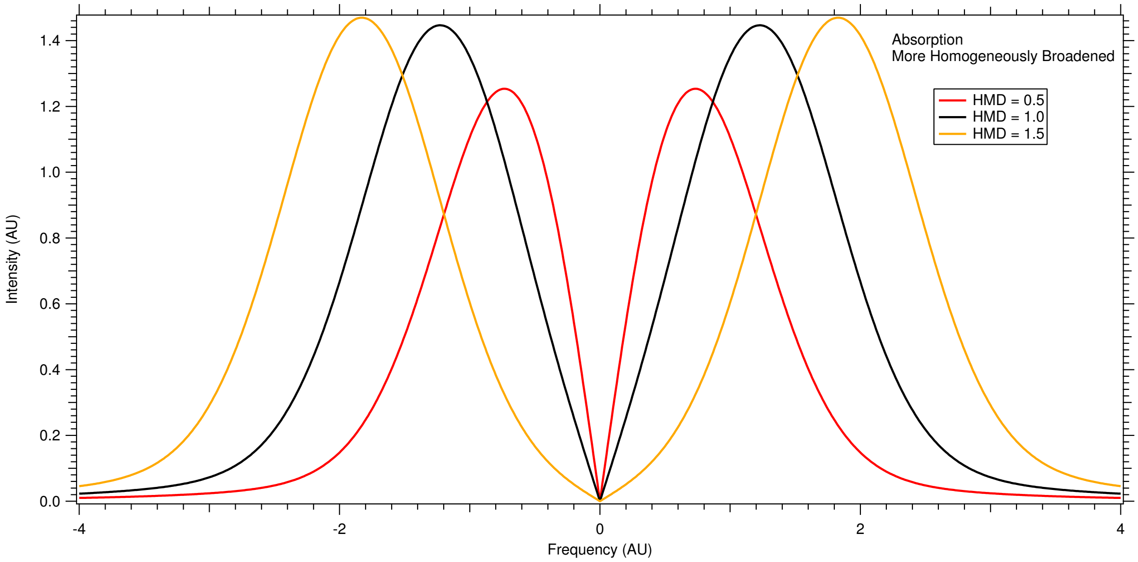

Figure J.22: Heterodyne modulation series on a more homogeneously broadened absorption line magnitude.

Table J.22: Simulation parameters for Figure J.22.

Symbol	**Value**
ν_0	0
A	10
α	1.0
ϕ	45°
Δ_G	0.5
Δ_L	1.0
HMD	-
VMD	0.3
θ	0°

J.5.2 Dispersion

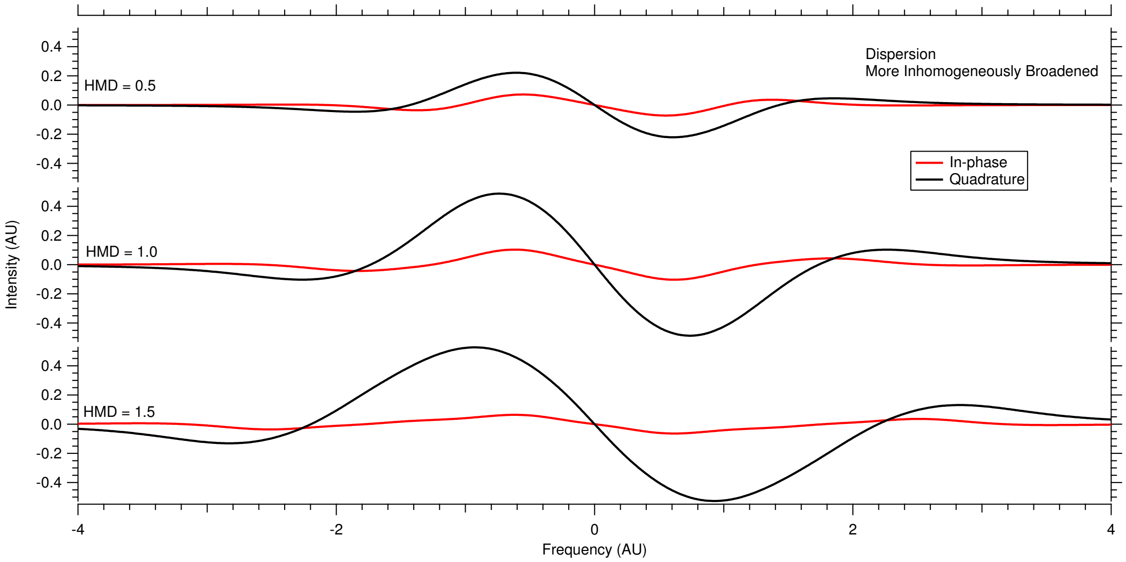

Figure J.23: Heterodyne modulation series on a more inhomogeneously broadened dispersion line.

Table J.23: Simulation parameters for Figure J.23.

Symbol	**Value**
ν_0	0
A	10
α	1.0
ϕ	45°
Δ_G	1.0
Δ_L	0.5
HMD	-
VMD	0.3
θ	0°

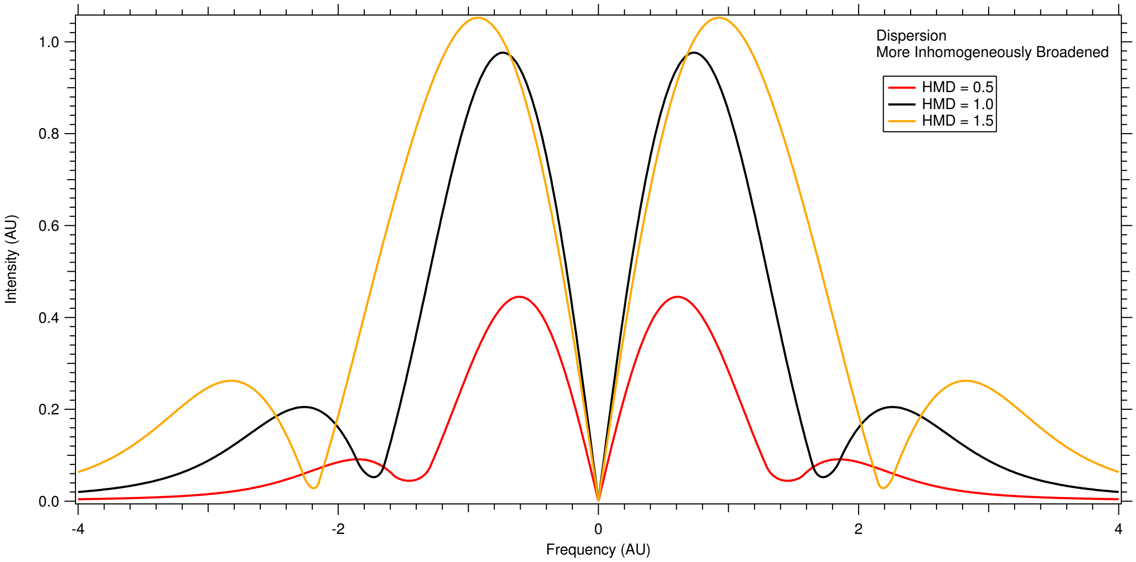

Figure J.24: Heterodyne modulation series on a more inhomogeneously broadened dispersion line magnitude.

Table J.24: Simulation parameters for Figure J.24.

Symbol	**Value**
ν_0	0
A	10
α	1.0
ϕ	45°
Δ_G	1.0
Δ_L	0.5
HMD	-
VMD	0.3
θ	0°

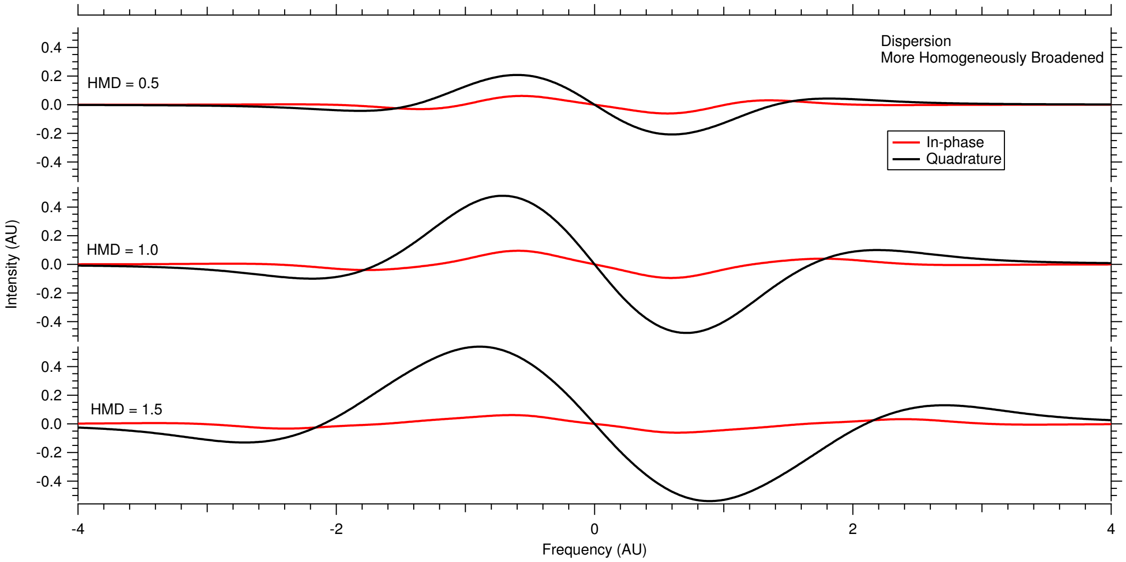

Figure J.25: Heterodyne modulation series on a more homogeneously broadened dispersion line.

Table J.25: Simulation parameters for Figure J.25.

Symbol	**Value**
ν_0	0
A	10
α	1.0
ϕ	45°
Δ_G	0.5
Δ_L	1.0
HMD	-
VMD	0.3
θ	0°

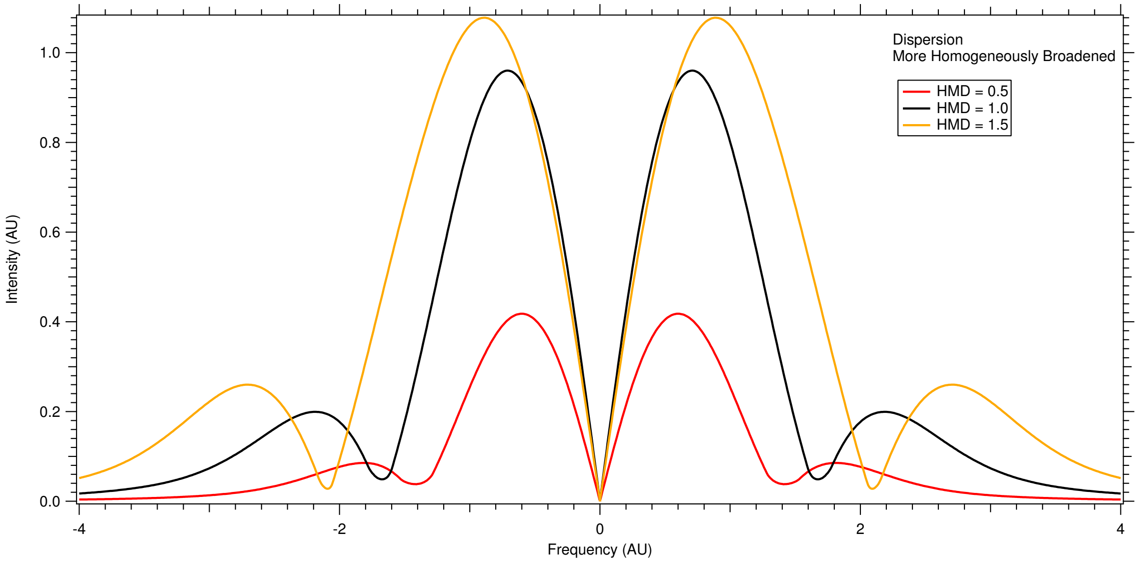

Figure J.26: Heterodyne modulation series on a more homogeneously broadened dispersion line magnitude.

Table J.26: Simulation parameters for Figure J.26.

Symbol	**Value**
ν_0	0
A	10
α	1.0
ϕ	45°
Δ_G	0.5
Δ_L	1.0
HMD	-
VMD	0.3
θ	0°

J.6 Velocity Modulation Phase

J.6.1 Absorption

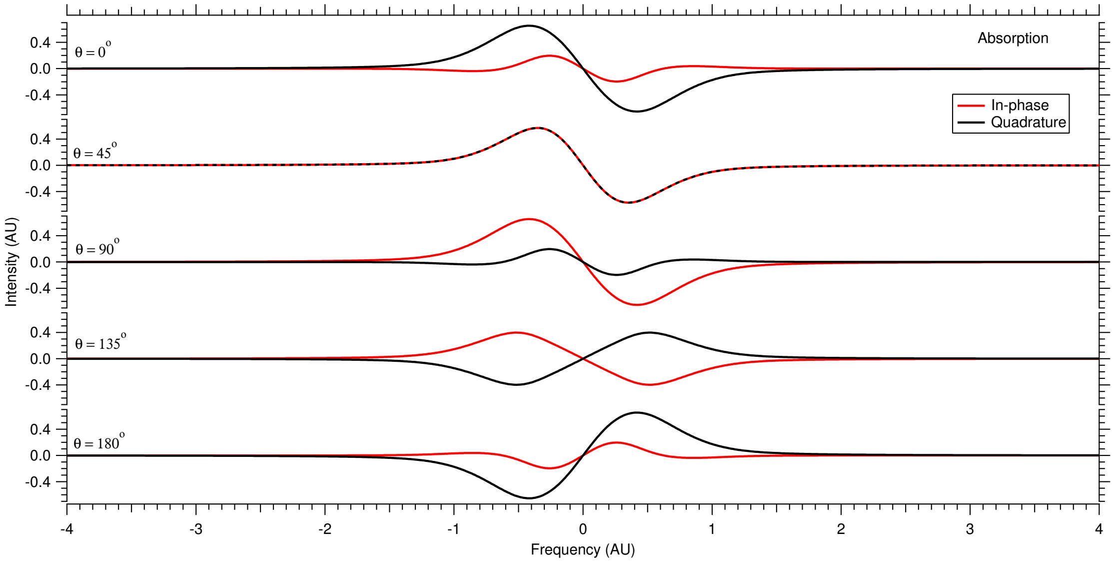

Figure J.27: Velocity modulation phase series on an absorption line.

Table J.27: Simulation parameters for Figure J.27.

Symbol	**Value**
ν_0	0
A	10
α	1.0
ϕ	45°
Δ_G	0.5
Δ_L	0.5
ν_{het}	0.25
VMD	0.3
θ	-

J.6.2 Dispersion

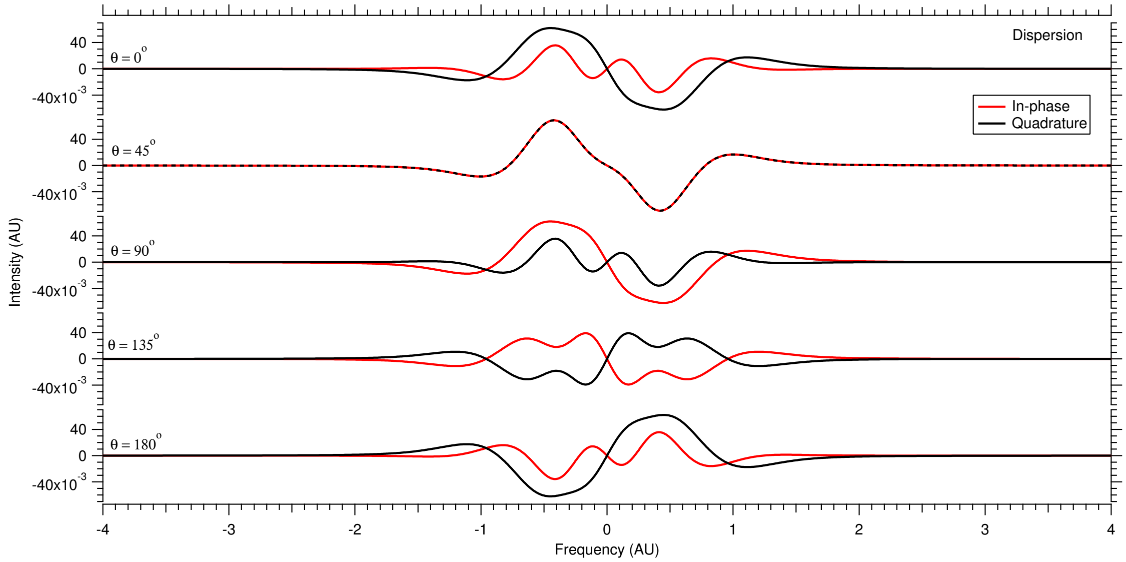

Figure J.28: Velocity modulation phase series on a dispersion line.

Table J.28: Simulation parameters for Figure J.28.

Symbol	**Value**
ν_0	0
A	10
α	1.0
ϕ	45°
Δ_G	0.5
Δ_L	0.5
ν_{het}	0.25
VMD	0.3
θ	-

Appendix K

JFit Software and Documentation

JFit 4.0 is a velocity modulation and NICE-OHVMS simulation/fitting suite. It was developed in `python 3.3.0` with `numpy 1.6.2` and `scipy 0.12.0`. It is run as a python script from the linux command line with arguments. The main sections describe the individual modules that make up the total functionality. Within each section, functions and classes are described.

K.1 JFit.py

Imports useful system and os python modules and also imports the `DataFitter` and `DataSimulator` modules from JFit. Calls `main`.

K.1.1 Functions

main

Calls `getFileName` and stores the filename if any is returned in the variable `filename`. The remainder of the code in `main` is never executed as the system exit call is always executed in `getFileName`.

getFileName

Uses the `sys` module to return a list of options and arguments. It uses the argument of the "-f" option to store a filename as the string `filename`. `getFileName` loops through the options again and determines the mode of operation: simulation or fitting and what type of each. It also has an import option that creates the directory structure so data can be used. For a full list of options, in the JFit directory, run `./JFit.py -h`. Once the mode of operation has been determined, a nested call to the function `fileformatchk` is executed with the filename as the argument, and the output is used as an argument in the mode function that was chosen via the option passed to JFit from the command line.

fileformatchk

Creates a token in the working directory for easy reference using the `filename`, and ensures that data folders for `filename` exist and are directories. If they do not exist, they are created. Appends the proper path to `filename` and returns it.

simAbsShort

Is a mode function for simulating absorption lines. Takes string `filename` as an argument. Opens the file `LineParams.txt` and stores parameters in variables. Creates a `NiceOhvmsAbsData` object named `newdata`. Calls the object's `dataGen` function to generate data. Calls the object's `dataWriter` function to store the data in a file. The ultimate location of that file is `./JFitData/<filename>/`.

fitAbsShort

Is a mode function for fitting the phase information of absorption lines. Takes string `filename` as an argument. Opens the file `LineParams.txt` and stores parameters in variables. Creates a `NiceOhvmsAbsDataSet` object named `newfit`. Calls the object's `loadFromText` function to get the data. Calls the object's `fitR` function to fit data. Calls the object's `writeToFile` function to store the fit data in a file. The ultimate location of that file is `./JFitData/<filename>/`.

simAbsMagShort

Is a mode function for simulating absorption magnitude lines. Takes string `filename` as an argument. Opens the file `LineParams.txt` and stores parameters in variables. Creates a `NiceOhvmsAbsMagData` data object named `newdata`. Calls the object's `dataGen` function to generate data. Calls the object's `dataWriter` function to store the data in a file. The ultimate location of that file is `./JFitData/<filename>/`.

fitAbsMagShort

Is a mode function for fitting the magnitude information of absorption lines. Takes string `filename` as an argument. Opens the file `LineParams.txt` and stores parameters in variables. Creates a `NiceOhvmsAbsMagDataSet` object named `newfit`. Calls the object's `loadFromText` function to get the data. Calls the object's `fitR` function to fit data. Calls the object's `writeToFile` function to store the fit data in a file. The ultimate location of that file is `./JFitData/<filename>/`.

simDispShort

Is a mode function for simulating dispersion lines. Takes string `filename` as an argument. Opens the file `LineParams.txt` and stores parameters in variables. Creates a `NiceOhvmsDispData` object named `newdata`. Calls the object's `dataGen` function to generate data. Calls the object's `dataWriter` function to store the data in a file. The ultimate location of that file is `./JFitData/<filename>/`.

fitDispShort

Is a mode function for fitting the phase information of dispersion lines. Takes string `filename` as an argument. Opens the file `LineParams.txt` and stores parameters in variables. Creates a `NiceOhvmsDispDataSet` object named `newfit`. Calls the object's `loadFromText` function to get the data. Calls the object's `fitR` function to fit data. Calls the object's `writeToFile` function to store the fit data in a file. The ultimate location of that file is `./JFitData/<filename>/`.

simDispMagShort

Is a mode function for simulating dispersion magnitude lines. Takes string `filename` as an argument. Opens the file `LineParams.txt` and stores parameters in variables. Creates a `NiceOhvmsDispMagData` data object named `newdata`. Calls the object's `dataGen` function to generate data. Calls the object's `dataWriter` function to store the data in a file. The ultimate location of that file is `./JFitData/<filename>/`.

fitDispMagShort

Is a mode function for fitting the magnitude information of dispersion lines. Takes string `filename` as an argument. Opens the file `LineParams.txt` and stores parameters in variables. Creates a `NiceOhvmsDispMagDataSet` object named `newfit`. Calls the object's `loadFromText` function to get the data. Calls the object's `fitR` function to fit data. Calls the object's `writeToFile` function to store the fit data in a file. The ultimate location of that file is `./JFitData/<filename>/`.

simVMSShort

Is a mode function for simulating velocity modulation lines. Takes string `filename` as an argument. Opens the file `LineParams.txt` and stores parameters in variables. Creates a `VMSData` object named `newdata`. Calls the object's `dataGen` function to generate data. Calls the object's `dataWriter` function to store the data in a file. The ultimate location of that file is `./JFitData/<filename>/`.

fitVMSShort

Is a mode function for fitting velocity modulation lines. Takes string `filename` as an argument. Opens the file `LineParams.txt` and stores parameters in variables. Creates a `VMSDataSet` object named `newfit`. Calls the object's `loadFromText` function to get the data. Calls the object's `fitR` function to fit data. Calls the object's `writeToFile` function to store the fit data in a file. The ultimate location of that file is `./JFitData/<filename>/`.

K.1.2 Code

The following pages are code for the JFit 4.0 software. The lines are numbered for ease of reading. Some lines roll onto the next line in the print form but they are still the same line. Recall that `python` is sensitive to white space.

```
#! /usr/bin/python3

# JFit by James Hodges
# A Program for Simulating and Fitting Data v4.0

import sys, getopt, os, os.path
import DataFitter as df
import DataSimulator as ds
import numpy as np

def getFileName(argv):
   """This function is called to get the file name. It is used to retrieve options and arguments"""
   inputfile = ''
   outputfile = ''
   try:
      opts, args = getopt.getopt(argv,"abmndeopvwhif:",["file="])
   except getopt.GetoptError:
      print('./JFit.py -f <filename>')
      sys.exit(2)
   for opt, arg in opts:
      if opt == '-h':
         print("\n\n\nAll calls must include the file name flag and an additional flag instructing JFit on the expected action.")
         print("\n\nFor example\n./JFit.py -f <filename> -X & ./JFit.py -X -f <filename>\nare acceptable input formats.\n\n")
         print("The available input flags are:\n -a \t Simulate NICE-OHVMS Abs\n -b \t Fit NICE-OHVMS Abs Phases\n -m \t Simulate NICE-OHVMS Abs Mag")
         print(" -n \t Fit NICE-OHVMS Abs Mag\n -d \t Simulate NICE-OHVMS Disp\n -e \t Fit NICE-OHVMS Disp Phases\n -o \t Simulate NICE-OHVMS Disp Mag")
         print(" -p \t Fitting NICE-OHVMS Disp Mag\n -v \t Simulate VMS \n -w \t Fit VMS \n -i \t Import using specified file name")
         sys.exit()
      elif opt in ("-f", "--file"):
         filename = arg
   for opt, arg in opts:
      if opt == '-a':
         print("Simming Abs using params from file.")
         print("Working file is ", filename)
         simAbsShort(fileformatchk(filename))
         sys.exit()
      elif opt == '-b':
         print("Fitting Abs Phases using params from file.")
         print("Working file is ", filename)
         fitAbsShort(fileformatchk(filename))
         sys.exit()
      elif opt == '-m':
         print("Simming Abs Mag using params from file.")
         print("Working file is ", filename)
         simAbsMagShort(fileformatchk(filename))
         sys.exit()
      elif opt == '-n':
         print("Fitting Abs Mag using params from file.")
         print("Working file is ", filename)
         fitAbsMagShort(fileformatchk(filename))
         sys.exit()
      elif opt == '-d':
```

```
         print("Simming Disp using params from file.")
         print("Working file is ", filename)
         simDispShort(fileformatchk(filename))
         sys.exit()
      elif opt == '-e':
         print("Fitting Disp Phases using params from file.")
         print("Working file is ", filename)
         fitDispShort(fileformatchk(filename))
         sys.exit()
      elif opt == '-o':
         print("Simming Disp Mag using params from file.")
         print("Working file is ", filename)
         simDispMagShort(fileformatchk(filename))
         sys.exit()
      elif opt == '-p':
         print("Fitting Disp Mag using params from file.")
         print("Working file is ", filename)
         fitDispMagShort(fileformatchk(filename))
         sys.exit()
      elif opt == '-v':
         print("Simming VMS using params from file.")
         print("Working file is ", filename)
         simVMSShort(fileformatchk(filename))
         sys.exit()
      elif opt == '-w':
         print("Fitting VMS using params from file.")
         print("Working file is ", filename)
         fitVMSShort(fileformatchk(filename))
         sys.exit()
      elif opt == '-i':
         print("Importing", filename)
         fileformatchk(filename)
         print("Please Place Data File in ./JFitData/"+filename+"/\nEnsure file is named "+filename+".txt and that the file is properly formated with # denoting comments.")
         print("There should be three columns seperated by tabs. The first is the frequency axis, the second is the in-phase channel, and the third is the quadrature channel.")
         sys.exit()
      else:
         print("Bad Argument. Try -h for more info.")
         sys.exit()

   print ('Working file is ', filename)
   return filename

def fileformatchk(filename):
   token = open(filename, "w")
   token.close()
   if not os.path.exists("./JFitData"):
      os.mkdir("JFitData")
   if not os.path.exists("./JFitData/"+filename):
      os.mkdir("./JFitData/"+filename)
   if os.path.exists("./JFitData/"+filename) and os.path.isdir("./JFitData/"+filename):
      filename = "./JFitData/"+filename+"/"+filename
      return filename
   else:
      print("Data Directory Error")
```

```
      sys.exit()

def simAbsShort(filename):
   print("Loading from LineParams.txt")
   paramsfile = open("LineParams.txt","r")
   line = paramsfile.readline()
   while line is not "":
      if line[0] is not "#":
         v0, A, delta, kappa, alpha, phi, va, garb1, garb2, theta, noise, low,
         high, interval  = line.split()
         v0 = float(v0)
         A = float(A)
         delta = float(delta)
         kappa = float(kappa)
         alpha = float(alpha)
         phi = float(phi)*(np.pi/180)
         va = float(va)
         theta = float(theta)*(np.pi/180)
         noise = float(noise)
         low = float(low)
         high = float(high)
         interval = float(interval)

      line = paramsfile.readline()
   paramsfile.close()

   newdata = ds.NiceOhvmsAbsData(low, high, interval, filename)
   newdata.dataGen(alpha, phi, A, v0, delta, kappa, va, theta, noise)
   newdata.dataWriter()

def fitAbsShort(filename):
   print("Loading from LineParams.txt")
   paramsfile = open("LineParams.txt","r")
   line = paramsfile.readline()
   while line is not "":
      if line[0] is not "#":
         v0, A, delta, kappa, alpha, phi, va, y01, y02, theta, garb1, garb2,
         garb3, garb4 = line.split()
         v0 = float(v0)
         A = float(A)
         delta = float(delta)
         kappa = float(kappa)
         alpha = float(alpha)
         phi = float(phi)*(np.pi/180)
         va = float(va)
         y01 = float(y01)
         y02 = float(y02)
         theta = float(theta)

      line = paramsfile.readline()
   paramsfile.close()

   newfit = df.NiceOhvmsAbsDataSet(filename, filename+"_fit")
   newfit.loadFromText()
   newfit.fitR(alpha,phi,A,v0,delta,kappa,va,y01,y02,theta)
   newfit.writeToFile()

def simAbsMagShort(filename):
   print("Loading from LineParams.txt")
```

```
   paramsfile = open("LineParams.txt","r")
   line = paramsfile.readline()
   while line is not "":
      if line[0] is not "#":
         v0, A, delta, kappa, alpha, phi, va, garb1, garb2, theta, noise, low, high, interval  = line.split()
         v0 = float(v0)
         A = float(A)
         delta = float(delta)
         kappa = float(kappa)
         alpha = float(alpha)
         phi = float(phi)*(np.pi/180)
         va = float(va)
         noise = float(noise)
         low = float(low)
         high = float(high)
         interval = float(interval)

      line = paramsfile.readline()
   paramsfile.close()

   newdata = ds.NiceOhvmsAbsMagData(low, high, interval, filename)
   newdata.dataGen(alpha, phi, A, v0, delta, kappa, va, noise)
   newdata.dataWriter()

def fitAbsMagShort(filename):
   print("Loading from LineParams.txt")
   paramsfile = open("LineParams.txt","r")
   line = paramsfile.readline()
   while line is not "":
      if line[0] is not "#":
         v0, A, delta, kappa, alpha, phi, va, y0, garb1, garb2, noise, low, high, interval  = line.split()
         v0 = float(v0)
         A = float(A)
         delta = float(delta)
         kappa = float(kappa)
         alpha = float(alpha)
         phi = float(phi)*(np.pi/180)
         va = float(va)
         y0 = float(y0)
         noise = float(noise)
         low = float(low)
         high = float(high)
         interval = float(interval)

      line = paramsfile.readline()
   paramsfile.close()

   newfit = df.NiceOhvmsAbsMagDataSet(filename, filename+"_fit")
   newfit.loadFromText()
   newfit.fitR(alpha,phi,A,v0,delta,kappa,va,y0)
   newfit.writeToFile()

def simDispShort(filename):
   print("Loading from LineParams.txt")
   paramsfile = open("LineParams.txt","r")
   line = paramsfile.readline()
   while line is not "":
```

```python
      if line[0] is not "#":
         v0, A, delta, kappa, alpha, phi, va, garb1, garb2, theta, noise, low, high, interval  = line.split()
         v0 = float(v0)
         A = float(A)
         delta = float(delta)
         kappa = float(kappa)
         alpha = float(alpha)
         phi = float(phi)*(np.pi/180)
         va = float(va)
         theta = float(theta)*(np.pi/180)
         noise = float(noise)
         low = float(low)
         high = float(high)
         interval = float(interval)

      line = paramsfile.readline()
   paramsfile.close()

   newdata = ds.NiceOhvmsDispData(low, high, interval, filename)
   newdata.dataGen(alpha, phi, A, v0, delta, kappa, va, theta, noise)
   newdata.dataWriter()

def fitDispShort(filename):
   print("Loading from LineParams.txt")
   paramsfile = open("LineParams.txt","r")
   line = paramsfile.readline()
   while line is not "":
      if line[0] is not "#":
         v0, A, delta, kappa, alpha, phi, va, y01, y02, theta, garb1, garb2, garb3, garb4 = line.split()
         v0 = float(v0)
         A = float(A)
         delta = float(delta)
         kappa = float(kappa)
         alpha = float(alpha)
         phi = float(phi)*(np.pi/180)
         va = float(va)
         y01 = float(y01)
         y02 = float(y02)
         theta = float(theta)

      line = paramsfile.readline()
   paramsfile.close()

   newfit = df.NiceOhvmsDispDataSet(filename, filename+"_fit")
   newfit.loadFromText()
   newfit.fitR(alpha,phi,A,v0,delta,kappa,va,y01,y02,theta)
   newfit.writeToFile()
def simDispMagShort(filename):
   print("Loading from LineParams.txt")
   paramsfile = open("LineParams.txt","r")
   line = paramsfile.readline()
   while line is not "":
      if line[0] is not "#":
         v0, A, delta, kappa, alpha, phi, va, garb1, garb2, theta, noise, low, high, interval  = line.split()
         v0 = float(v0)
         A = float(A)
```

```
         delta = float(delta)
         kappa = float(kappa)
         alpha = float(alpha)
         phi = float(phi)*(np.pi/180)
         va = float(va)
         noise = float(noise)
         low = float(low)
         high = float(high)
         interval = float(interval)

      line = paramsfile.readline()
   paramsfile.close()

   newdata = ds.NiceOhvmsDispMagData(low, high, interval, filename)
   newdata.dataGen(alpha, phi, A, v0, delta, kappa, va, noise)
   newdata.dataWriter()

def fitDispMagShort(filename):
   print("Loading from LineParams.txt")
   paramsfile = open("LineParams.txt","r")
   line = paramsfile.readline()
   while line is not "":
      if line[0] is not "#":
         v0, A, delta, kappa, alpha, phi, va, y0, garb1, garb2, noise, low, high, interval  = line.split()
         v0 = float(v0)
         A = float(A)
         delta = float(delta)
         kappa = float(kappa)
         alpha = float(alpha)
         phi = float(phi)*(np.pi/180)
         va = float(va)
         y0 = float(y0)
         noise = float(noise)
         low = float(low)
         high = float(high)
         interval = float(interval)

      line = paramsfile.readline()
   paramsfile.close()

   newfit = df.NiceOhvmsDispMagDataSet(filename, filename+"_fit")
   newfit.loadFromText()
   newfit.fitR(alpha,phi,A,v0,delta,kappa,va,y0)
   newfit.writeToFile()
def simVMSShort(filename):
   print("Loading from LineParams.txt")
   paramsfile = open("LineParams.txt","r")
   line = paramsfile.readline()
   while line is not "":
      if line[0] is not "#":
         v0, A, delta, kappa, alpha, phi, va, y0, garb1, garb2, noise, low, high, interval  = line.split()
         v0 = float(v0)
         A = float(A)
         delta = float(delta)
         kappa = float(kappa)
         alpha = float(alpha)
         phi = float(phi)*(np.pi/180)
```

```
         va = float(va)
         y0 = float(y0)
         noise = float(noise)
         low = float(low)
         high = float(high)
         interval = float(interval)

   line = paramsfile.readline()
   paramsfile.close()

   newdata = ds.VMSData(low, high, interval, filename)
   newdata.dataGen(A, v0, delta, kappa, va, noise)
   newdata.dataWriter()

def fitVMSShort(filename):
   print("Loading from LineParams.txt")
   paramsfile = open("LineParams.txt","r")
   line = paramsfile.readline()
   while line is not "":
      if line[0] is not "#":
         v0, A, delta, kappa, alpha, phi, va, y0, garb1, garb2, garb3, garb4, garb5, garb6 = line.split()
         v0 = float(v0)
         A = float(A)
         delta = float(delta)
         kappa = float(kappa)
         alpha = float(alpha)
         phi = float(phi)*(np.pi/180)
         va = float(va)
         y0 = float(y0)

      line = paramsfile.readline()
   paramsfile.close()

   newfit = df.VMSDataSet(filename, filename+"_fit")
   newfit.loadFromText()
   newfit.fitR(A,v0,delta,kappa,va,y0)
   newfit.writeToFile()

def main():
   """Main Function"""
   filename = getFileName(sys.argv[1:])

   token = open(filename, "w")
   token.close()

   if not os.path.exists("./JFitData"):
      os.mkdir("JFitData")
   if not os.path.exists("./JFitData/"+filename):
      os.mkdir("./JFitData/"+filename)
   if os.path.exists("./JFitData/"+filename) and os.path.isdir("./JFitData/"+filename):
      filename = "./JFitData/"+filename+"/"+filename
   else:
      print("Data Directory Error")
      sys.exit()

   print ('Working file is ', filename)

```

```
if __name__ == "__main__":
    main()

```

K.2 DataSimulator.py

Imports `numpy` and `datetime` and the entire `FunctionLibrary` module. Defines `P` as a bookkeeping constant for Gaussian prefactors.

K.2.1 Classes

SimData

__init__:

The constructor for the class. Creates a frequency array from the supplied range. Creates a string for the name of the output file, `self.outputfile`. Creates in-phase and quadrature channel arrays of the same length as the frequency array and initializes them to zero.

dataWriter:

Opens `self.outputfile`. Writes a header with the date and time. Writes column labels. Loops through the frequency, in-phase, and quadrature arrays writing the values to the file. Closes the file.

NiceOhvmsAbsData

This is a sub-class of `SimData` for absorption data.

dataGen:

Creates an array for the time dimension. Loops through the time array using the functions `niceohvmsAbsEven` and `niceohvmsAbsOdd` to populate an array `toInt`. Using a trapezoidal rule integration, `trapz`, `toInt` is integrated along the time dimension to determine the final lineshape. This process is performed twice, once for the in-phase and once for the quadrature channel. `dataGen` can also optionally add noise to the simulated lineshape.

NiceOhvmsDispData

This is a sub-class of `SimData` for dispersion data.

dataGen:

Creates an array for the time dimension. Loops through the time array using the functions `niceohvmsDispEven` and `niceohvmsDispOdd` to populate an array `toInt`. Using a trapezoidal rule integration, `trapz`, `toInt` is integrated along the time dimension to determine the final lineshape. This process is performed twice, once for the in-phase and once for the quadrature channel. `dataGen` can also optionally add noise to the simulated lineshape.

NiceOhvmsAbsMagData

This is a sub-class of `SimData` for absorption magnitude data.

dataGen:

Creates an array for the time dimension. Loops through the time array using the functions `niceohvmsAbsMag` to populate an array `toInt`. Using a trapezoidal rule integration, `trapz`, `toInt` is integrated along the time dimension to determine the final lineshape. `dataGen` can also optionally add noise to the simulated lineshape.

NiceOhvmsDispMagData

This is a sub-class of `SimData` for dispersion magnitude data.

dataGen:

Creates an array for the time dimension. Loops through the time array using the functions `niceohvmsDispMag` to populate an array `toInt`. Using a trapezoidal rule integration, `trapz`, `toInt` is integrated along the time dimension to determine the final lineshape. `dataGen` can also optionally add noise to the simulated lineshape.

VMSData

This is a sub-class of `SimData`.

dataGen:

Creates an array for the time dimension. Loops through the time array using the functions `vms` to populate an array `toInt`. Using a trapezoidal rule integration, `trapz`, `toInt` is integrated along the time dimension to determine the final lineshape. `dataGen` can also optionally add noise to the simulated lineshape.

K.2.2 Code

The following pages are code for the data simulator module used by the JFit 4.0 software. The lines are numbered for ease of reading. Some lines roll onto the next line in the print form but they are still the same line. Recall that `python` is sensitive to white space.

```
# Data Simulator Module
# By James Hodges v4.0

import numpy as np
import datetime
from FunctionLibrary import *


P = 2*np.sqrt(2*np.log(2))

class SimData(object):
    """Data Simulator: calls to dataGen followed by dataWriter creates data, then writes it to file"""
    FUNC_FORMS = ["gauss"]

    def __init__(self, low=-10.0, high=10.0, interval=0.1, outputfile="output.txt"):
        """Constructor"""
        self.domain = np.arange(low, high+interval, interval)
        self.outputfile = outputfile
        self.rangeI = np.zeros(len(self.domain))
        self.rangeQ = np.zeros(len(self.domain))

    def dataWriter(self):
        """Writes data to specified file"""
        text_file = open(self.outputfile+".txt", "w")
        text_file.write("#Simulated by JFit\t"+str(datetime.datetime.today())+"\n")
        text_file.write("#Domain\tRangeI\tRangeQ\n")

        for i in range(len(self.domain)):
            text_file.write(str(self.domain[i])+"\t"+str(self.rangeI[i])+"\t"+str(self.rangeQ[i])+"\n")

        text_file.close()

class NiceOhvmsAbsData(SimData):
    """Sub-Class of SimData specific to Absorption in NICE-OHVMS Data"""
    def dataGen(self,alpha,phi,A,v0,delta,kappa,va,theta,noise):
        domlength = len(self.domain)
        timearray = np.arange(-0.5,0.5+0.04,0.04)

        isFirst = True

        for timept in timearray:
            row = np.cos(theta)*niceohvmsAbsEven(self.domain,alpha,phi,A,v0,delta,kappa,va,0,timept)\
                  +np.sin(theta)*niceohvmsAbsOdd(self.domain,alpha,phi,A,v0,delta,kappa,va,0,timept)
            row = np.resize(row,(1,len(row)))

            if isFirst:
                toIntEven = row[:]
                isFirst = False
            else:
                toIntEven = np.append(toIntEven,row,axis=0)

        if noise == 0.0:
```

```
            self.rangeI = np.trapz(toIntEven, x=timearray, axis=0)
        else:
            self.rangeI = np.trapz(toIntEven, x=timearray, axis=0) + np.random.normal(0,noise,size=domlength)
            print("SNR: ",self.rangeI.ptp()/noise)

        isFirst = True

        for timept in timearray:
            row = np.sin(theta)*niceohvmsAbsEven(self.domain,alpha,phi,A,v0,delta,kappa,va,0,timept)\
                  +np.cos(theta)*niceohvmsAbsOdd(self.domain,alpha,phi,A,v0,delta,kappa,va,0,timept)
            row = np.resize(row,(1,len(row)))

            if isFirst:
                toIntOdd = row[:]
                isFirst = False
            else:
                toIntOdd = np.append(toIntOdd,row,axis=0)

        if noise == 0.0:
            self.rangeQ = np.trapz(toIntOdd, x=timearray, axis=0)
        else:
            self.rangeQ = np.trapz(toIntOdd, x=timearray, axis=0) + np.random.normal(0,noise,size=domlength)
            print("SNR: ",self.rangeQ.ptp()/noise)

class NiceOhvmsDispData(SimData):
    """Sub-Class of SimData specific to Absorption in NICE-OHVMS Data"""
    def dataGen(self,alpha,phi,A,v0,delta,kappa,va,theta,noise):
        domlength = len(self.domain)
        timearray = np.arange(-0.5,0.5+0.04,0.04)

        isFirst = True

        for timept in timearray:
            row = np.cos(theta)*niceohvmsDispEven(self.domain,alpha,phi,A,v0,delta,kappa,va,0,timept)\
                  +np.sin(theta)*niceohvmsDispOdd(self.domain,alpha,phi,A,v0,delta,kappa,va,0,timept)
            row = np.resize(row,(1,len(row)))

            if isFirst:
                toIntEven = row[:]
                isFirst = False
            else:
                toIntEven = np.append(toIntEven,row,axis=0)

        if noise == 0.0:
            self.rangeI = np.trapz(toIntEven, x=timearray, axis=0)
        else:
            self.rangeI = np.trapz(toIntEven, x=timearray, axis=0) + np.random.normal(0,noise,size=domlength)
            print("SNR: ",self.rangeI.ptp()/noise)

        isFirst = True
```

```

        for timept in timearray:
            row = np.sin(theta)*niceohvmsDispEven(self.domain,alpha,phi,A,v0,delta,kappa,va,0,timept)\
                  +np.cos(theta)*niceohvmsDispOdd(self.domain,alpha,phi,A,v0,delta,kappa,va,0,timept)
            row = np.resize(row,(1,len(row)))

            if isFirst:
                toIntOdd = row[:]
                isFirst = False
            else:
                toIntOdd = np.append(toIntOdd,row,axis=0)

        if noise == 0.0:
            self.rangeQ = np.trapz(toIntOdd, x=timearray, axis=0)
        else:
            self.rangeQ = np.trapz(toIntOdd, x=timearray, axis=0) + np.random.normal(0,noise,size=domlength)
            print("SNR: ",self.rangeQ.ptp()/noise)

class NiceOhvmsAbsMagData(SimData):
    def dataGen(self,alpha,phi,A,v0,delta,kappa,va,noise):
        domlength = len(self.domain)
        timearray = np.arange(-0.5,0.5+0.04,0.04)

        isFirst = True

        for timept in timearray:
            row = niceohvmsAbsMag(self.domain,alpha,phi,A,v0,delta,kappa,va,0,timept)
            row = np.resize(row,(1,len(row)))

            if isFirst:
                toIntEven = row[:]
                isFirst = False
            else:
                toIntEven = np.append(toIntEven,row,axis=0)

        if noise == 0.0:
            self.rangeI = np.trapz(toIntEven, x=timearray, axis=0)+lambMag(self.domain)
        else:
            self.rangeI = np.trapz(toIntEven, x=timearray, axis=0)+lambMag(self.domain) + np.random.normal(0,noise,size=domlength)
            print("SNR: ",self.rangeI.ptp()/noise)

class NiceOhvmsDispMagData(SimData):
    def dataGen(self,alpha,phi,A,v0,delta,kappa,va,noise):
        domlength = len(self.domain)
        timearray = np.arange(-0.5,0.5+0.04,0.04)

        isFirst = True

        for timept in timearray:
            row =
```

```
            niceohvmsDispMag(self.domain,alpha,phi,A,v0,delta,kappa,va,0,timept)
            row = np.resize(row,(1,len(row)))

            if isFirst:
                toIntEven = row[:]
                isFirst = False
            else:
                toIntEven = np.append(toIntEven,row,axis=0)

        if noise == 0.0:
            self.rangeI = np.trapz(toIntEven, x=timearray, axis=0)+lambMag(self.domain)
        else:
            self.rangeI = np.trapz(toIntEven, x=timearray, axis=0)+lambMag(self.domain) + np.random.normal(0,noise,size=domlength)
            print("SNR: ",self.rangeI.ptp()/noise)

class VMSData(SimData):
    def dataGen(self,A,v0,delta,kappa,va,noise):
        domlength = len(self.domain)
        timearray = np.arange(-0.5,0.5+0.004,0.004)

        isFirst = True

        for timept in timearray:
            row = vms(self.domain,A,v0,delta,kappa,va,0,timept)
            row = np.resize(row,(1,len(row)))

            if isFirst:
                toIntEven = row[:]
                isFirst = False
            else:
                toIntEven = np.append(toIntEven,row,axis=0)

        if noise == 0.0:
            self.rangeI = np.trapz(toIntEven, x=timearray, axis=0)
        else:
            self.rangeI = np.trapz(toIntEven, x=timearray, axis=0) + np.random.normal(0,noise,size=domlength)
            print("SNR: ",self.rangeI.ptp()/noise)

if __name__ == "__main__":
    print("This module meant for import only.")

```

K.3 DataFitter.py

Imports `numpy`, `leastsq` from `scipy.optimize`, `datetime`, and the entire `FunctionLibrary` module. Defines `P` as a bookkeeping constant for Gaussian prefactors.

K.3.1 Classes

DataSet

__init__:

Creates a pair of strings to hold the input filename and the output filename. Creates and initializes a frequency array, an in-phase array, and a quadrature array. Also creates arrays for the fits and residuals for the in-phase and quadrature arrays.

loadFromText:

Opens a file containing data. The file must have three columns separated by tabs. All comments and headers must be commented with a "#". Column 1 must be the frequency column, Column 2 must be the in-phase column, and column 3 must be the quadrature column. It loops through the file reading the values and appending them to an arrays of `float64` type. It matches the size of the fit and residuals arrays to the size of the arrays from the file.

writeToFile:

Opens the output file. Writes a header with the date and time. Loops through arrays defined in the constructor writing them to the file.

NiceOhvmsDataSet

A sub-class of `DataSet`.

__init__:

Invokes the parent constructor and defines the variables relevant for storing the values of the fitted parameters and the uncertainties from the fit.

writeToFile:

Invokes the parent `writeToFile` and then opens a second file to write the parameters and their uncertainties that are generated by the fitting routine.

NiceOhvmsAbsDataSet

A sub-class of `NiceOhvmsDataSet` for absorption phase information fitting.

fitR:

Makes a copy of the frequency and intensity arrays. Populates a list with the initial guesses for the concentration modulation phase, velocity modulation phase, and y-offsets. Calls the `leastsq` routine, thereby minimizing the function `absResiduals`. The fitted parameters are stored in the appropriate variables, and the diagonal of the covariance matrix is used to calculate the uncertainties of the parameters. The uncertainties are stored. The fit arrays are populated using the functions `lineNAI` and `lineNAQ`.

NiceOhvmsAbsMagDataSet

A sub-class of `NiceOhvmsDataSet` for absorption magnitude information fitting.

fitR:

Makes a copy of the frequency and intensity arrays. Populates a list with the initial guesses for the concentration modulation depth, line intensity, linecenter, linewidths, velocity modulation amplitude, and y-offset. Calls the `leastsq` routine, thereby minimizing the function `absMagResiduals`. The fitted parameters are stored in the appropriate variables, and the diagonal of the covariance matrix is used to calculate the uncertainties of the parameters. The uncertainties are stored. The fit arrays are populated using the function `lineNA`.

NiceOhvmsDispDataSet

A sub-class of `NiceOhvmsDataSet` for dispersion phase information fitting.

fitR:

Makes a copy of the frequency and intensity arrays. Populates a list with the initial guesses for the concentration modulation phase, velocity modulation phase, and y-offsets. Calls the `leastsq` routine, thereby minimizing the function `dispResiduals`. The fitted parameters are stored in the appropriate variables, and the diagonal of the covariance matrix is used to calculate the uncertainties of the parameters. The uncertainties are stored. The fit arrays are populated using the functions `lineNDI` and `lineNDQ`.

NiceOhvmsAbsMagDataSet

A sub-class of `NiceOhvmsDataSet` for dispersion magnitude information fitting.

fitR:

Makes a copy of the frequency and intensity arrays. Populates a list with the initial guesses for the concentration modulation depth, line intensity, linecenter, linewidths, velocity modulation amplitude, and y-offset. Calls the `leastsq` routine, thereby minimizing the function `dispMagResiduals`. The fitted parameters are stored in the appropriate variables, and the diagonal of the covariance matrix is used to calculate the uncertainties of the parameters. The uncertainties are stored. The fit arrays are populated using the function `lineND`.

VMSDataSet

A sub-class of `DataSet` for velocity modulation spectroscopy fitting.

__init__:

Invokes the parent constructor and defines the variables relevant for storing the values of the fitted parameters and the uncertainties from the fit.

writeToFile:

Invokes the parent `writeToFile` and then opens a second file to write the parameters and their uncertainties that are generated by the fitting routine.

fitR:

Performs one of three types of fits depending on a parameter (`FIXRHO`) that is loaded by the `FunctionLibrary`. The first type of fit is done with all parameters floating. The second type is performed with a fixed velocity modulation amplitude. The final type that can be performed is with all parameters fixed except velocity modulation amplitude and transition intensity. In all cases the `leastsq` routine is called. The functions that are minimized are either `vmsResiduals`, `vmsResidualsFRho`, or `vmsResidualsFreeRho`. These are listed in the same order as the type of fit to be performed. After the fit is performed, regardless of the type, the parameters and uncertainties are stored in the appropriate variables.

K.3.2 Code

The following pages are code for the data fitter module used by the JFit 4.0 software. The lines are numbered for ease of reading. Some lines roll onto the next line in the print form but they are still the same line. Recall that `python` is sensitive to white space.

```
# Data Fitter Module
# By James Hodges v4.0

import datetime
import numpy as np
from scipy.optimize import curve_fit
from scipy.optimize import leastsq
from FunctionLibrary import *

P = 2*np.sqrt(2*np.log(2))

class DataSet(object):
    """A Class for loading, fitting, and writing fits and residuals."""
    FUNC_FORMS = ["gauss"]
    def __init__(self, infile, outfile):
        """Constructor for initialization"""
        self.infile = infile
        self.outfile = outfile
        self.domain = np.empty([1],dtype="float64")
        self.rangeI = np.empty([1],dtype="float64")
        self.rangeQ = np.empty([1],dtype="float64")
        self.fitI = np.empty([1],dtype="float64")
        self.residI = np.empty([1],dtype="float64")
        self.fitQ = np.empty([1],dtype="float64")
        self.residQ = np.empty([1],dtype="float64")

    def loadFromText(self, file="default"):
        """Reads data from a specified text file"""
        if file == "default":
            file = self.infile+".txt"

        textfile = open(file,"r")

        line = textfile.readline()
        while line is not "":

            isComment = False

            if line[0] == "#":
                isComment = True
            else:
                d,ri,rq = line.split()


            if not isComment:
                self.domain = np.append(self.domain, float(d))
                self.rangeI = np.append(self.rangeI, float(ri))
                self.rangeQ = np.append(self.rangeQ, float(rq))
            line = textfile.readline()

        textfile.close()
        self.domain = self.domain[1:]
        self.rangeI = self.rangeI[1:]
        self.rangeQ = self.rangeQ[1:]
        self.fitI = np.zeros(len(self.domain),dtype="float64")
        self.residI = np.zeros(len(self.domain),dtype="float64")
        self.fitQ = np.zeros(len(self.domain),dtype="float64")
        self.residQ = np.zeros(len(self.domain),dtype="float64")

```

```
    def writeToFile(self):
        """Writes data from a specified text file"""
        textfile = open(self.outfile+".txt", "w")
        textfile.write("#Fit by JFit\t"+str(datetime.datetime.today())+"\n")
        textfile.write("#Domain\tRangeI\tFitI\tResidI\tRangeQ\tFitQ\tResidQ\n")

        for i in range(len(self.domain)):
            textfile.write(str(self.domain[i])+"\t"+\
                           str(self.rangeI[i])+"\t"+\
                           str(self.fitI[i])+"\t"+\
                           str(self.residI[i])+"\t"+\
                           str(self.rangeQ[i])+"\t"+\
                           str(self.fitQ[i])+"\t"+\
                           str(self.residQ[i])+"\n")

        textfile.close()


class NiceOhvmsDataSet(DataSet):
    """Subclass for NICE-OHVMS Data"""
    def __init__(self, infile, outfile):
        super(NiceOhvmsDataSet, self).__init__(infile, outfile)
        self.alpha = 0.0
        self.phi = 0.0
        self.A = 0.0
        self.v0 = 0.0
        self.delta = 0.0
        self.kappa = 0.0
        self.va = 0.0
        self.y01 = 0.0
        self.y02 = 0.0
        self.theta = 0.0

        self.alpha_stdev = 0.0
        self.phi_stdev = 0.0
        self.A_stdev = 0.0
        self.v0_stdev = 0.0
        self.delta_stdev = 0.0
        self.kappa_stdev = 0.0
        self.va_stdev = 0.0
        self.y0_stdev = 0.0
        self.y01_stdev = 0.0
        self.y02_stdev = 0.0
        self.theta_stdev = 0.0

    def writeToFile(self):
        """Calls the parent class's writeToFile()Function and creates a parameter file"""
        super(NiceOhvmsDataSet,self).writeToFile()
        outparamsfile = open(self.outfile+"_params.txt","w")
        outparamsfile.write("#Fit by JFit\t"+str(datetime.datetime.today())+"\n")
        outparamsfile.write("#Param\t\tValue\t\tSt. Dev\n")
        outparamsfile.write("Alpha\t\t"+str(self.alpha)+"\t\t"+str(self.alpha_stdev)+"\n")
        outparamsfile.write("Phi\t\t"+str(self.phi)+"\t\t"+str(self.phi_stdev)+"\n")
        outparamsfile.write("Amplitude\t\t"+str(self.A)+"\t\t"+str(self.A_stde
```

```
        v)+"\n")
        outparamsfile.write("Center\t\t"+str(self.v0)+"\t\t"+str(self.v0_stdev)+"\n")
        outparamsfile.write("Inhomogeneous FWHM\t\t"+str(self.delta)+"\t\t"+str(self.delta_stdev)+"\n")
        outparamsfile.write("Homogeneous FWHM\t\t"+str(self.kappa)+"\t\t"+str(self.kappa_stdev)+"\n")
        outparamsfile.write("Vel Mod Amp\t\t"+str(self.va)+"\t\t"+str(self.va_stdev)+"\n")
        outparamsfile.write("y01\t\t"+str(self.y01)+"\t\t"+str(self.y01_stdev)+"\n")
        outparamsfile.write("y02\t\t"+str(self.y02)+"\t\t"+str(self.y02_stdev)+"\n")
        outparamsfile.write("Theta\t\t"+str(self.theta)+"\t\t"+str(self.theta_stdev)+"\n")
        outparamsfile.close()

class NiceOhvmsAbsDataSet(NiceOhvmsDataSet):

    def fitR(self,alpha,phi,A,v0,delta,kappa,va,y01,y02,theta):
        x = self.domain[:]
        yI = self.rangeI[:]
        yQ = self.rangeQ[:]


        p0 = [phi,y01,y02,theta]

        popt, pcovf, infodict, mesg, ier  = leastsq(absResiduals,p0,args=(x,yI,yQ,alpha,A,v0,delta,kappa,va),full_output=True)



        if ier not in (1,2,3,4):
            print(mesg)
        else:
            print("Return Int: ",ier)
            print("Number of Calls: ",infodict["nfev"])
            ssq = (absResiduals(popt,x,yI,yQ,alpha,A,v0,delta,kappa,va)**2).sum()/(len(yI)-len(popt))
            try:
                pcov = pcovf*ssq
            except TypeError:
                print("Singular Matrix Error: Co-variance Matrix is Zeros")
                pcov = np.zeros([4,4])

            self.alpha = alpha
            self.phi = popt[0]
            self.A = A
            self.v0 = v0
            self.delta = delta
            self.kappa = kappa
            self.va = va
            self.y01 = popt[1]
            self.y02 = popt[2]
            self.theta = popt[3]

            self.alpha_stdev = 0.0
```

```
            self.phi_stdev = 180/np.pi*np.sqrt(pcov[0,0])
            self.A_stdev = 0.0
            self.v0_stdev = 0.0
            self.delta_stdev = 0.0
            self.kappa_stdev = 0.0
            self.va_stdev = 0.0
            self.y01_stdev = np.sqrt(pcov[1,1])
            self.y02_stdev = np.sqrt(pcov[2,2])
            self.theta_stdev = 180/np.pi*np.sqrt(pcov[3,3])

            self.fitI = lineNAI(self.domain, self.alpha, self.phi, self.A, self.v0, self.delta, self.kappa, self.va, self.y01, self.theta)
            self.residI = self.rangeI-self.fitI

            self.fitQ = lineNAQ(self.domain, self.alpha, self.phi, self.A, self.v0, self.delta, self.kappa, self.va, self.y02, self.theta)
            self.residQ = self.rangeQ-self.fitQ

            print("Params:")
            print(popt)
            print("Co-var Matrix:")
            print(pcov)

            self.phi *= 180/np.pi
            self.theta *= 180/np.pi


class NiceOhvmsAbsMagDataSet(NiceOhvmsDataSet):

    def fitR(self,alpha,phi,A,v0,delta,kappa,va,y0):
        x = self.domain[:]
        yI = self.rangeI[:]


        p0 = [alpha,A,v0,delta,kappa,va]

        popt, pcovf, infodict, mesg, ier  = leastsq(absMagResiduals,p0,args=(x,yI,phi,y0),full_output=True)

        if ier not in (1,2,3,4):
            print(mesg)
        else:
            print("Return Int: ",ier)
            print("Number of Calls: ",infodict["nfev"])
            ssq = (absMagResiduals(popt,x,yI,phi,y0)**2).sum()/(len(yI)-len(popt))
            try:
                pcov = pcovf*ssq
            except TypeError:
                print("Singular Matrix Error: Co-variance Matrix is Zeros")
                pcov = np.zeros([6,6])

            self.alpha = popt[0]
            self.phi = phi
            self.A = popt[1]
            self.v0 = popt[2]
            self.delta = popt[3]
            self.kappa = popt[4]
            self.va = popt[5]
```

```


            self.alpha_stdev = np.sqrt(pcov[0,0])
            self.A_stdev = np.sqrt(pcov[1,1])
            self.v0_stdev = np.sqrt(pcov[2,2])
            self.delta_stdev = np.sqrt(pcov[3,3])
            self.kappa_stdev = np.sqrt(pcov[4,4])
            self.va_stdev = np.sqrt(pcov[5,5])


            print(pcov[0,0],pcov[1,1],pcov[2,2],pcov[3,3],pcov[4,4],pcov[5,5])

            self.fitI = lineNA(self.domain, self.alpha, self.phi, self.A, self.v0, self.delta, self.kappa, self.va, self.y0)+lambMag(self.domain)
            self.residI = self.rangeI-self.fitI

            print("Params:")
            print(popt)
            print("Co-var Matrix:")
            print(pcov)

            self.phi *= 180/np.pi

class NiceOhvmsDispDataSet(NiceOhvmsDataSet):

    def fitR(self,alpha,phi,A,v0,delta,kappa,va,y01,y02,theta):
        x = self.domain[:]
        yI = self.rangeI[:]
        yQ = self.rangeQ[:]


        p0 = [phi,y01,y02,theta]

        popt, pcovf, infodict, mesg, ier  = leastsq(dispResiduals,p0,args=(x,yI,yQ,alpha,A,v0,delta,kappa,va),full_output=True)



        if ier not in (1,2,3,4):
            print(mesg)
        else:
            print("Return Int: ",ier)
            print("Number of Calls: ",infodict["nfev"])
            ssq = (dispResiduals(popt,x,yI,yQ,alpha,A,v0,delta,kappa,va)**2).sum()/(len(yI)-len(popt))
            try:
                pcov = pcovf*ssq
            except TypeError:
                print("Singular Matrix Error: Co-variance Matrix is Zeros")
                pcov = np.zeros([4,4])

            self.alpha = alpha
            self.phi = popt[0]
            self.A = A
            self.v0 = v0
            self.delta = delta
```

```
            self.kappa = kappa
            self.va = va
            self.y01 = popt[1]
            self.y02 = popt[2]
            self.theta = popt[3]

            self.alpha_stdev = 0.0
            self.phi_stdev = 180/np.pi*np.sqrt(pcov[0,0])
            self.A_stdev = 0.0
            self.v0_stdev = 0.0
            self.delta_stdev = 0.0
            self.kappa_stdev = 0.0
            self.va_stdev = 0.0
            self.y01_stdev = np.sqrt(pcov[1,1])
            self.y02_stdev = np.sqrt(pcov[2,2])
            self.theta_stdev = 180/np.pi*np.sqrt(pcov[3,3])

            self.fitI = lineNDI(self.domain, self.alpha, self.phi, self.A, self.v0, self.delta, self.kappa, self.va, self.y01, self.theta)
            self.residI = self.rangeI-self.fitI

            self.fitQ = lineNDQ(self.domain, self.alpha, self.phi, self.A, self.v0, self.delta, self.kappa, self.va, self.y02, self.theta)
            self.residQ = self.rangeQ-self.fitQ

            print("Params:")
            print(popt)
            print("Co-var Matrix:")
            print(pcov)

            self.phi *= 180/np.pi
            self.theta *= 180/np.pi

class NiceOhvmsDispMagDataSet(NiceOhvmsDataSet):

    def fitR(self,alpha,phi,A,v0,delta,kappa,va,y0):
        x = self.domain[:]
        yI = self.rangeI[:]


        p0 = [alpha,A,v0,delta,kappa,va]

        popt, pcovf, infodict, mesg, ier  = leastsq(dispMagResiduals,p0,args=(x,yI,phi,y0),full_output=True)

        if ier not in (1,2,3,4):
            print(mesg)
        else:
            print("Return Int: ",ier)
            print("Number of Calls: ",infodict["nfev"])
            ssq = (dispMagResiduals(popt,x,yI,phi,y0)**2).sum()/(len(yI)-len(popt))

            try:
                pcov = pcovf*ssq
            except TypeError:
                print("Singular Matrix Error: Co-variance Matrix is Zeros")
                pcov = np.zeros([6,6])

```

```
            self.alpha = popt[0]
            self.phi = phi
            self.A = popt[1]
            self.v0 = popt[2]
            self.delta = popt[3]
            self.kappa = popt[4]
            self.va = popt[5]


            self.alpha_stdev = np.sqrt(pcov[0,0])
            self.A_stdev = np.sqrt(pcov[1,1])
            self.v0_stdev = np.sqrt(pcov[2,2])
            self.delta_stdev = np.sqrt(pcov[3,3])
            self.kappa_stdev = np.sqrt(pcov[4,4])
            self.va_stdev = np.sqrt(pcov[5,5])


            print(pcov[0,0],pcov[1,1],pcov[2,2],pcov[3,3],pcov[4,4],pcov[5,5])

            self.fitI = lineND(self.domain, self.alpha, self.phi, self.A, self.v0, self.delta, self.kappa, self.va, self.y0)+lambMag(self.domain)
            self.residI = self.rangeI-self.fitI

            print("Params:")
            print(popt)
            print("Co-var Matrix:")
            print(pcov)

            self.phi *= 180/np.pi

class VMSDataSet(DataSet):
    """Subclass for VMS Data"""
    def __init__(self, infile, outfile):
        super(VMSDataSet, self).__init__(infile, outfile)
        self.A = 0.0
        self.v0 = 0.0
        self.delta = 0.0
        self.kappa = 0.0
        self.va = 0.0
        self.y0 = 0.0

        self.A_stdev = 0.0
        self.v0_stdev = 0.0
        self.delta_stdev = 0.0
        self.kappa_stdev = 0.0
        self.va_stdev = 0.0
        self.y0_stdev = 0.0

    def writeToFile(self):
        """Calls the parent class's writeToFile()Function and creates a parameter file"""
        super(VMSDataSet,self).writeToFile()
        outparamsfile = open(self.outfile+"_params_"+str(datetime.datetime.today())+".txt","w")
        outparamsfile.write("#Fit by JFit\t"+str(datetime.datetime.today())+"\n")
        outparamsfile.write("#Param\t\tValue\t\tSt. Dev\n")
```

```
        outparamsfile.write("Amplitude\t\t"+str(self.A)+"\t\t"+str(self.A_stdev)+"\n")
        outparamsfile.write("Center\t\t"+str(self.v0)+"\t\t"+str(self.v0_stdev)+"\n")
        outparamsfile.write("Inhomog. FWHM\t\t"+str(self.delta)+"\t\t"+str(self.delta_stdev)+"\n")
        outparamsfile.write("Homog. FWHM\t\t"+str(self.kappa)+"\t\t"+str(self.kappa_stdev)+"\n")
        outparamsfile.write("Vel Mod Amp\t\t"+str(self.va)+"\t\t"+str(self.va_stdev)+"\n")
        outparamsfile.write("y0\t\t"+str(self.y0)+"\t\t"+str(self.y0_stdev)+"\n")
        outparamsfile.close()

    def fitR(self,A,v0,delta,kappa,va,y0):
        x = self.domain[:]
        yI = self.rangeI[:]


        if FIXRHO is 0:
            p0 = [A,v0,delta,kappa,va,y0]
            print(p0)

            popt, pcovf, infodict, mesg, ier  = leastsq(vmsResiduals,p0,args=(x,yI),full_output=True)

            if ier not in (1,2,3,4):
                print(mesg)
            else:
                print("Return Int: ",ier)
                print(mesg)
                print("Number of Calls: ",infodict["nfev"])

                ssq = (vmsResiduals(popt,x,yI)**2).sum()/(len(yI)-len(popt))
                try:
                    pcov = pcovf*ssq
                except TypeError:
                    print("Singular Matrix Error: Co-variance Matrix is Zeros")
                    pcov = np.zeros([6,6])

                self.A = popt[0]
                self.v0 = popt[1]
                self.delta = popt[2]
                self.kappa = popt[3]
                self.va = popt[4]
                self.y0 = popt[5]

                self.A_stdev = np.sqrt(pcov[0,0])
                self.v0_stdev = np.sqrt(pcov[1,1])
                self.delta_stdev = np.sqrt(pcov[2,2])
                self.kappa_stdev = np.sqrt(pcov[3,3])
                self.va_stdev = np.sqrt(pcov[4,4])
                self.y0_stdev = np.sqrt(pcov[5,5])

                self.fitI = lineVMS(self.domain, self.A, self.v0, self.delta, self.kappa, self.va, self.y0)
                self.residI = self.rangeI-self.fitI

```

```
                print("Params:")
                print(popt)
                print("Co-var Matrix:")
                print(pcov)
        elif FIXRHO is 1:
            p0 = [A,v0,delta,kappa,y0]
            print(p0)

            popt, pcovf, infodict, mesg, ier  = leastsq(vmsResidualsFRho,p0,args=(x,yI,va),full_output=True)

            if ier not in (1,2,3,4):
                print(mesg)
            else:
                print("Return Int: ",ier)
                print(mesg)
                print("Number of Calls: ",infodict["nfev"])

                ssq = (vmsResidualsFRho(popt,x,yI,va)**2).sum()/(len(yI)-len(popt))
                try:
                    pcov = pcovf*ssq
                except TypeError:
                    print("Singular Matrix Error: Co-variance Matrix is Zeros")
                    pcov = np.zeros([5,5])

                self.A = popt[0]
                self.v0 = popt[1]
                self.delta = popt[2]
                self.kappa = popt[3]
                self.va = va
                self.y0 = popt[4]

                self.A_stdev = np.sqrt(pcov[0,0])
                self.v0_stdev = np.sqrt(pcov[1,1])
                self.delta_stdev = np.sqrt(pcov[2,2])
                self.kappa_stdev = np.sqrt(pcov[3,3])
                self.y0_stdev = np.sqrt(pcov[4,4])

                self.fitI = lineVMS(self.domain, self.A, self.v0, self.delta, self.kappa, self.va, self.y0)
                self.residI = self.rangeI-self.fitI

                print("Params:")
                print(popt)
                print("Co-var Matrix:")
                print(pcov)
        elif FIXRHO is 2:
            p0 = [A,va]
            print(p0)

            popt, pcovf, infodict, mesg, ier  = leastsq(vmsResidualsFreeRho,p0,args=(x,yI,v0,delta,kappa,y0),full_output=True)

            if ier not in (1,2,3,4):
                print(mesg)
            else:
```

```
                print("Return Int: ",ier)
                print(mesg)
                print("Number of Calls: ",infodict["nfev"])

                ssq = (vmsResidualsFreeRho(popt,x,yI,v0,delta,kappa,y0)**2).sum()/(len(yI)-len(popt))
                try:
                    pcov = pcovf*ssq
                except TypeError:
                    print("Singular Matrix Error: Co-variance Matrix is Zeros")
                    pcov = np.zeros([2,2])

                self.A = popt[0]
                self.va = popt[1]
                self.v0 = v0
                self.delta = delta
                self.kappa = kappa
                self.y0 = y0

                self.A_stdev = np.sqrt(pcov[0,0])
                self.va_stdev = np.sqrt(pcov[1,1])

                self.fitI = lineVMS(self.domain, self.A, self.v0, self.delta, self.kappa, self.va, self.y0)
                self.residI = self.rangeI-self.fitI

                print("Params:")
                print(popt)
                print("Co-var Matrix:")
                print(pcov)

if __name__ == "__main__":
    print("This module meant for import only.")

```

K.4 Function Library

Imports `numpy`, `scipy.special`, and `scipy.signal`. Opens `FuncParams.txt` and reads parameters that are primarily instrument based and sets them to constants. The include modulation beta, heterodyne frequency, Fourier coefficient and several others. Also, from that file the necessary parameters required to create model the Lamb dip in the spectrum are loaded.

K.4.1 Functions

lambDip

This function simulates a Lamb dip via a psuedo-Voigt profile exactly as reported by Crabtree and Hodges.[2, 26]

lambMag

Calculates the magnitude of the Lamb dip across the in-phase and quadrature channels.

lGauss

Calculates a Gaussian for Lamb dip.

lDaws

Calculates a Dawson function for Lamb dip.

lLorentzA

Calculates a Lorentzian for Lamb dip.

lLorentzD

Calculates the Kramers-Kronig transform of the Lorentzian for Lamb dip.

niceohvmsAbsEven

Calculates the nth even Fourier coefficient for NICE-OHVMS absorption. This is done with a pseudo-Voigt profile using “f” as the full-width of the Gaussian and Lorentzian components and “eta” as the linear combination coefficient. Refer to Chapters 3 and 4 for more information regarding the calculation. The function also has built-in constraints for the parameters. By setting the parameters that need to be constrained to 10^{50} + the absolute value of the parameter when they exceed the constraint, artificial walls are built into the function to enforce parameter ranges.

niceohvmsAbsOdd

Calculates the nth odd Fourier coefficient for NICE-OHVMS absorption. This is done with a pseudo-Voigt profile using "f" as the full-width of the Gaussian and Lorentzian components and "eta" as the linear combination coefficient. Refer to Chapters 3 and 4 for more information regarding the calculation. The function also has built-in constraints for the parameters. By setting the parameters that need to be constrained to 10^{50} + the absolute value of the parameter when they exceed the constraint, artificial walls are built into the function to enforce parameter ranges.

niceohvmsAbsMag

Calculates the absorption magnitude by taking the square root of the sum of the squares of `niceohvmsAbsEven` and `niceohvmsAbsOdd`. This has some additional built-in constraints.

niceohvmsDispEven

Calculates the nth even Fourier coefficient for NICE-OHVMS dispersion. This is done with the Kramers-Kronig transform of a pseudo-Voigt profile using "f" as the full-width of the Gaussian and Lorentzian components and "eta" as the linear combination coefficient. Refer to Chapters 3 and 4 for more information regarding the calculation. The function also has built-in constraints for the parameters. By setting the parameters that need to be constrained to 10^{50} + the absolute value of the parameter when they exceed the constraint, artificial walls are built into the function to enforce parameter ranges.

niceohvmsDispOdd

Calculates the nth odd Fourier coefficient for NICE-OHVMS dispersion. This is done with the Kramers-Kronig transform of a pseudo-Voigt profile using "f" as the full-width of the Gaussian and Lorentzian components and "eta" as the linear combination coefficient. Refer to Chapters 3 and 4 for more information regarding the calculation. The function also has built-in constraints for the parameters. By setting the parameters that need to be constrained to 10^{50} + the absolute value of the parameter when they exceed the constraint, artificial walls are built into the function to enforce parameter ranges.

niceohvmsDispMag

Calculates the absorption magnitude by taking the square root of the sum of the squares of `niceohvmsDispEven` and `niceohvmsDispOdd`. This has some additional built-in constraints.

concModFunc

Takes the constants `FORM` and `FORMARG` as written in the `FuncParams.txt` file to select the functional form of the concentration modulation. These can be of any form including but not limited to $\cos^2$, square, sawtooth, or a combination of the others. This section of the code can be easily expanded.

lineNAI

Populates a two-dimensional array of frequency and time with the functions `niceohvmsAbsEven` and `niceohvmsAbsOdd`. This is where the velocity modulation angle is introduced, and the constraints of that phase angle are incorporated into this function. The `trapz` function integrates along the time axis of the two-dimensional array, which results in the final in-phase absorption lineshape.

lineNAQ

Populates a two-dimensional array of frequency and time with the functions `niceohvmsAbsEven` and `niceohvmsAbsOdd`. This is where the velocity modulation angle is introduced, and the constraints of that phase angle are incorporated into this function. The `trapz` function integrates along the time axis of the two-dimensional array, which results in the final quadrature absorption lineshape. It is 90°out of phase with `lineNAI`.

lineNDI

Populates a two-dimensional array of frequency and time with the functions `niceohvmsDispEven` and `niceohvmsDispOdd`. This is where the velocity modulation angle is introduced, and the constraints of that phase angle are incorporated into this function. The `trapz` function integrates along the time axis of the two-dimensional array, which results in the final in-phase dispersion lineshape.

lineNDQ

Populates a two-dimensional array of frequency and time with the functions `niceohvmsDispEven` and `niceohvmsDispOdd`. This is where the velocity modulation angle is introduced, and the constraints of that phase angle are incorporated into this function. The `trapz` function integrates along the time axis of the two-dimensional array, which results in the final quadrature dispersion lineshape. It is 90°out of phase with `lineNDI`.

lineNA

Populates a two-dimensional array of frequency and time with the function `niceohvmsAbsMag`. The `trapz` function integrates along the time axis of the two-dimensional array, which results in the final absorption magnitude lineshape.

lineND

Populates a two-dimensional array of frequency and time with the function `niceohvmsDispMag`. The `trapz` function integrates along the time axis of the two-dimensional array, which results in the final dispersion magnitude lineshape. It is 90°out of phase with `lineNA`.

absResiduals

This is the function that `leastsq` minimizes to determine phase related parameters for absorption. It returns the square root of the sum of the square differences between the data and the fit models. The fit models are `lineNAI` an `lineNAQ`.

absMagResiduals

This is the function that `leastsq` minimizes to determine magnitude related parameters for absorption. It returns the differences between the data and the fit models. The fit model is `lineNA`.

dispResiduals

This is the function that `leastsq` minimizes to determine phase related parameters for dispersion. It returns the square root of the sum of the square differences between the data and the fit models. The fit models are `lineNDI` an `lineNDQ`.

absMagResiduals

This is the function that `leastsq` minimizes to determine magnitude related parameters for dispersion. It returns the differences between the data and the fit models. The fit model is `lineND`.

vms

Calculates the nth odd Fourier coefficient for velocity modulation spectroscopy absorption. This is done with a pseudo-Voigt profile using "f" as the full-width of the Gaussian and Lorentzian components and "eta" as the linear combination coefficient. Refer to Chapters 3 and 4 for more information regarding the calculation. The function also has built-in constraints for the parameters. By setting the parameters that need to be constrained to 10^{50} + the absolute value of the parameter when they exceed the constraint, artificial walls are built into the function to enforce parameter ranges.

lineVMS

Populates a two-dimensional array of frequency and time with the function `vms`. The `trapz` function integrates along the time axis of the two-dimensional array, which results in the final in-phase velocity modulation lineshape.

vmsResiduals

This is the function that `leastsq` minimizes to determine parameters for velocity modulation. It returns the differences between the data and the fit models. The fit model is `lineVMS`.

vmsFRho

Calculates the nth odd Fourier coefficient for velocity modulation spectroscopy absorption with fixed velocity modulation amplitude. This is done with a pseudo-Voigt profile using "f" as the full-width of the Gaussian and Lorentzian components and "eta" as the linear combination coefficient. Refer to Chapters 3 and 4 for more information regarding the calculation. The function also has built-in constraints for the parameters. By setting the parameters that need to be constrained to 10^{50} + the absolute value of the parameter when they exceed the constraint, artificial walls are built into the function to enforce parameter ranges.

lineVMSFRho

Populates a two-dimensional array of frequency and time with the function `vmsFRho`. The `trapz` function integrates along the time axis of the two-dimensional array, which results in the final velocity modulation lineshape.

vmsResidualsFRho

This is the function that `leastsq` minimizes to determine parameters for velocity modulation with fixed velocity modulation amplitude. It returns the differences between the data and the fit models. The fit model is `lineVMSFRho`.

vmsResidualsFreeRho

This is the function that `leastsq` minimizes to determine parameters for velocity modulation with all parameters fixed but velocity modulation amplitude and transitions intensity. It returns the differences between the data and the fit models. The fit model is `lineVMS`.

K.4.2 Code

The following pages are code for the function library module used by the JFit 4.0 software. The lines are numbered for ease of reading. Some lines roll onto the next line in the print form but they are still the same line. Recall that `python` is sensitive to white space.

```python
# Function Library v4.0

import numpy as np
from scipy import special as s
from scipy import signal as ss

P = 2*np.sqrt(2*np.log(2))

# Loading Constants: BETA is Bessel Beta, VH is het freq, N is Fourier Coeff, QNV is quad invert y/n, D is Directionality of the cavity 1:bi 0:uni

paramsfile = open("FuncParams.txt","r")
line = paramsfile.readline()
LambBool = False
while line is not "":
    if line[0] is not "#" and LambBool is False:
        BETA, VH, N, QNV, D, FORM, FORMARG, FIXRHO = line.split()
        LambBool = True
    elif line[0] is not "#" and LambBool is True:
        AL1, AL1FRAC1, AL1FRAC2, AL1FRAC3, AL2, AL2FRAC1, AL2FRAC2, AL2FRAC3, FWHM, MU, THETA, GAUSSCHAR = line.split()

    line = paramsfile.readline()
paramsfile.close()

BETA = float(BETA)
VH = float(VH)
N = int(N)
QNV = int(QNV)
D = int(D)
FORM = int(FORM)
FORMARG = float(FORMARG)
FIXRHO = int(FIXRHO)

print("Consts",BETA, VH, N, QNV, D, FORM, FORMARG, FIXRHO)

B = s.jv(0,BETA)*s.jv(1,BETA)
BT = s.jv(1,BETA)*s.jv(2,BETA)

print("Bessel Prod:",B,BT)

AL1 = float(AL1)
AL1FRAC1 = float(AL1FRAC1)
AL1FRAC2 = float(AL1FRAC2)
AL1FRAC3 = float(AL1FRAC3)
AL2 = float(AL2)
AL2FRAC1 = float(AL2FRAC1)
AL2FRAC2 = float(AL2FRAC2)
AL2FRAC3 = float(AL2FRAC3)
FWHM = float(FWHM)
MU = float(MU)
THETA = float(THETA)
GAUSSCHAR = float(GAUSSCHAR)

print("Lamb Consts:",AL1, AL1FRAC1, AL1FRAC2, AL1FRAC3, AL2, AL2FRAC1, AL2FRAC2, AL2FRAC3, FWHM, MU, THETA, GAUSSCHAR)
THETA *= np.pi/180

def lambDip(x,al,alfrac1,alfrac2,alfrac3):
```

```
    AL1 = alfrac1*al
    AL2 = alfrac2*al
    AL3 = alfrac3*al

    GAhalf = AL1*(lGauss(x,FWHM,MU+VH/2)-lGauss(x,FWHM,MU-VH/2))
    GAone = AL2*(lGauss(x,FWHM,MU+VH)-lGauss(x,FWHM,MU-VH))
    GAonehalf = AL3*(lGauss(x,FWHM,MU+3*VH/2)-lGauss(x,FWHM,MU-3*VH/2))
    GTA = GAhalf + GAone + GAonehalf

    GDcenter = -al*lDaws(x,FWHM,MU)
    GDhalf = AL1*(lDaws(x,FWHM,MU+VH/2)+lDaws(x,FWHM,MU-VH/2))
    GDone = AL2*(lDaws(x,FWHM,MU+VH)+lDaws(x,FWHM,MU-VH))
    GDonehalf = AL3*(lDaws(x,FWHM,MU+3*VH/2)+lDaws(x,FWHM,MU-3*VH/2))
    GTD = GDcenter + GDhalf + GDone + GDonehalf

    GTS = GTA*np.sin(THETA) + GTD*np.cos(THETA)

    LAhalf = AL1*(lLorentzA(x,FWHM,MU+VH/2)-lLorentzA(x,FWHM,MU-VH/2))
    LAone = AL2*(lLorentzA(x,FWHM,MU+VH)-lLorentzA(x,FWHM,MU-VH))
    LAonehalf = AL3*(lLorentzA(x,FWHM,MU+3*VH/2)-lLorentzA(x,FWHM,MU-3*VH/2))
    LTA = LAhalf + LAone + LAonehalf

    LDcenter = -al*lLorentzD(x,FWHM,MU)
    LDhalf = AL1*(lLorentzD(x,FWHM,MU+VH/2)+lLorentzD(x,FWHM,MU-VH/2))
    LDone = AL2*(lLorentzD(x,FWHM,MU+VH)+lLorentzD(x,FWHM,MU-VH))
    LDonehalf = AL3*(lLorentzD(x,FWHM,MU+3*VH/2)+lLorentzD(x,FWHM,MU-3*VH/2))
    LTD = LDcenter + LDhalf + LDone + LDonehalf

    LTS = LTA*np.sin(THETA) + LTD*np.cos(THETA)

    return GAUSSCHAR*GTS + (1-GAUSSCHAR)*LTS

def lambMag(x):
    return np.sqrt(lambDip(x,AL1,AL1FRAC1,AL1FRAC2,AL1FRAC3)**2+lambDip(x,AL2,AL2FRAC1,AL2FRAC2,AL2FRAC3)**2)

def lGauss(x,fwhm,x0):
    return np.exp(-(4*np.log(2))*((x-x0)**2)/(fwhm**2))

def lDaws(x,fwhm,x0):
    gam = 2*np.sqrt(np.log(2))*(x-x0)/fwhm
    return (2/np.sqrt(np.pi))*s.dawsn(gam)

def lLorentzA(x,fwhm,x0):
    hwhm = fwhm/2
    return 1/(1+(x-x0)**2/hwhm**2)

def lLorentzD(x,fwhm,x0):
    hwhm = fwhm/2
    return -(x-x0)/hwhm/(1+(x-x0)**2/hwhm**2)

def niceohvmsAbsEven(x,alpha,phi,A,v0,delta,kappa,va,y0,time):
    f = (delta**5+2.69269*(delta**4)*kappa+2.42843*(delta**3)*(kappa**2)\
         +4.47163*(delta**2)*(kappa**3)+0.07842*delta*(kappa**4)+kappa**5)**0.2
    eta = 1.36603*(kappa/f)-0.47719*(kappa/f)**2+0.11116*(kappa/f)**3
    Lpp = B*((2*f)/(np.pi*(4*(x-v0+VH+va*np.cos(2*np.pi*time))**2+f**2)))
    Gpp = B*(P/(f*np.sqrt(2*np.pi))*np.exp(-((x-
```

```
    v0+VH+va*np.cos(2*np.pi*time))*P)**2/(2*f**2)))
    Lpn = B*((2*f)/(np.pi*(4*(x-v0+VH-va*np.cos(2*np.pi*time))**2+f**2)))
    Gpn = B*(P/(f*np.sqrt(2*np.pi))*np.exp(-((x-v0+VH-va*np.cos(2*np.pi*time))*P)**2/(2*f**2)))
    Lnp = B*((2*f)/(np.pi*(4*(x-v0-VH+va*np.cos(2*np.pi*time))**2+f**2)))
    Gnp = B*(P/(f*np.sqrt(2*np.pi))*np.exp(-((x-v0-VH+va*np.cos(2*np.pi*time))*P)**2/(2*f**2)))
    Lnn = B*((2*f)/(np.pi*(4*(x-v0-VH-va*np.cos(2*np.pi*time))**2+f**2)))
    Gnn = B*(P/(f*np.sqrt(2*np.pi))*np.exp(-((x-v0-VH-va*np.cos(2*np.pi*time))*P)**2/(2*f**2)))

    fae = A*concModFunc(alpha,time, phi, FORM, FORMARG)*(eta*(Lnp-Lpp+D*Lnn-D*Lpn)+(1-eta)*(Gnp-Gpp+D*Gnn-D*Gpn))*np.cos(2*N*np.pi*time)+y0

    if alpha < 0 or alpha > 1:
            boundError = np.empty(len(x))
            boundError.fill(1e50)
            boundError *= 1+abs(alpha)
            return boundError
    if phi < 0 or phi > np.pi/2:
            boundError = np.empty(len(x))
            boundError.fill(1e50)
            boundError *= 1+abs(phi)
            return boundError
    if va < 0:
            boundError = np.empty(len(x))
            boundError.fill(1e50)
            boundError *= 1+abs(va)
            return boundError
    return fae

def niceohvmsAbsOdd(x,alpha,phi,A,v0,delta,kappa,va,y0,time):
    f = (delta**5+2.69269*(delta**4)*kappa+2.42843*(delta**3)*(kappa**2)\
         +4.47163*(delta**2)*(kappa**3)+0.07842*delta*(kappa**4)+kappa**5)**0.2
    eta = 1.36603*(kappa/f)-0.47719*(kappa/f)**2+0.11116*(kappa/f)**3
    Lpp = B*((2*f)/(np.pi*(4*(x-v0+VH+va*np.cos(2*np.pi*time))**2+f**2)))
    Gpp = B*(P/(f*np.sqrt(2*np.pi))*np.exp(-((x-v0+VH+va*np.cos(2*np.pi*time))*P)**2/(2*f**2)))
    Lpn = B*((2*f)/(np.pi*(4*(x-v0+VH-va*np.cos(2*np.pi*time))**2+f**2)))
    Gpn = B*(P/(f*np.sqrt(2*np.pi))*np.exp(-((x-v0+VH-va*np.cos(2*np.pi*time))*P)**2/(2*f**2)))
    Lnp = B*((2*f)/(np.pi*(4*(x-v0-VH+va*np.cos(2*np.pi*time))**2+f**2)))
    Gnp = B*(P/(f*np.sqrt(2*np.pi))*np.exp(-((x-v0-VH+va*np.cos(2*np.pi*time))*P)**2/(2*f**2)))
    Lnn = B*((2*f)/(np.pi*(4*(x-v0-VH-va*np.cos(2*np.pi*time))**2+f**2)))
    Gnn = B*(P/(f*np.sqrt(2*np.pi))*np.exp(-((x-v0-VH-va*np.cos(2*np.pi*time))*P)**2/(2*f**2)))

    fao = QNV*A*concModFunc(alpha,time, phi, FORM, FORMARG)*(eta*(Lnp-Lpp+D*Lnn-D*Lpn)+(1-eta)*(Gnp-Gpp+D*Gnn-D*Gpn))*np.sin(2*N*np.pi*time)+y0

    if alpha < 0 or alpha > 1:
            boundError = np.empty(len(x))
            boundError.fill(1e50)
            boundError *= 1+abs(alpha)
            return boundError
    if phi < 0 or phi > np.pi/2:
            boundError = np.empty(len(x))
```

```
            boundError.fill(1e50)
            boundError *= 1+abs(phi)
            return boundError
    if va < 0:
            boundError = np.empty(len(x))
            boundError.fill(1e50)
            boundError *= 1+abs(va)
            return boundError
    return fao

def niceohvmsAbsMag(x,alpha,phi,A,v0,delta,kappa,va,y0,time):
    fa = np.sqrt(niceohvmsAbsEven(x,alpha,phi,A,v0,delta,kappa,va,0,time)**2\
                +niceohvmsAbsOdd(x,alpha,phi,A,v0,delta,kappa,va,0,time)**2)+y0
    if alpha < 0 or alpha > 1:
            boundError = np.empty(len(x))
            boundError.fill(1e50)
            boundError *= 1+abs(alpha)
            return boundError
    if phi < 0 or phi > np.pi/2:
            boundError = np.empty(len(x))
            boundError.fill(1e50)
            boundError *= 1+abs(phi)
            return boundError
    if va < 0:
            boundError = np.empty(len(x))
            boundError.fill(1e50)
            boundError *= 1+abs(va)
            return boundError
    if delta < 0:
            boundError = np.empty(len(x))
            boundError.fill(1e50)
            boundError *= 1+abs(delta)
            return boundError
    if kappa < 0:
            boundError = np.empty(len(x))
            boundError.fill(1e50)
            boundError *= 1+abs(kappa)
            return boundError
    if y0 < 0:
            boundError = np.empty(len(x))
            boundError.fill(1e50)
            boundError *= 1+abs(y0)
            return boundError
    return fa

def niceohvmsDispEven(x,alpha,phi,A,v0,delta,kappa,va,y0,time):
    f = (delta**5+2.69269*(delta**4)*kappa+2.42843*(delta**3)*(kappa**2)\
         +4.47163*(delta**2)*(kappa**3)+0.07842*delta*(kappa**4)+kappa**5)**0.2
    eta = 1.36603*(kappa/f)-0.47719*(kappa/f)**2+0.11116*(kappa/f)**3

    Lnp = B*((2*f*(x-v0-VH+va*np.cos(2*np.pi*time)))/(np.pi*(4*(x-v0-VH+va*np.cos(2*np.pi*time))**2+f**2)))
    Lpp = B*((2*f*(x-v0+VH+va*np.cos(2*np.pi*time)))/(np.pi*(4*(x-v0+VH+va*np.cos(2*np.pi*time))**2+f**2)))
    Lp = B*((2*f*(x-v0+va*np.cos(2*np.pi*time)))/(np.pi*(4*(x-v0+va*np.cos(2*np.pi*time))**2+f**2)))
    Lnn = B*((2*f*(x-v0-VH-va*np.cos(2*np.pi*time)))/(np.pi*(4*(x-v0-VH-
```

```
    va*np.cos(2*np.pi*time))**2+f**2)))
    Lpn = B*((2*f*(x-v0+VH-va*np.cos(2*np.pi*time)))/(np.pi*(4*(x-v0+VH-va*np.cos(2*np.pi*time))**2+f**2)))
    Ln = B*((2*f*(x-v0-va*np.cos(2*np.pi*time)))/(np.pi*(4*(x-v0-va*np.cos(2*np.pi*time))**2+f**2)))
    Gnp = -2*B*P/(np.sqrt(2)*np.pi*f)*s.dawsn(P/(np.sqrt(2)*f)*(x-v0-VH+va*np.cos(2*np.pi*time)))
    Gpp = -2*B*P/(np.sqrt(2)*np.pi*f)*s.dawsn(P/(np.sqrt(2)*f)*(x-v0+VH+va*np.cos(2*np.pi*time)))
    Gp = -2*B*P/(np.sqrt(2)*np.pi*f)*s.dawsn(P/(np.sqrt(2)*f)*(x-v0+va*np.cos(2*np.pi*time)))
    Gnn = -2*B*P/(np.sqrt(2)*np.pi*f)*s.dawsn(P/(np.sqrt(2)*f)*(x-v0-VH-va*np.cos(2*np.pi*time)))
    Gpn = -2*B*P/(np.sqrt(2)*np.pi*f)*s.dawsn(P/(np.sqrt(2)*f)*(x-v0+VH-va*np.cos(2*np.pi*time)))
    Gn = -2*B*P/(np.sqrt(2)*np.pi*f)*s.dawsn(P/(np.sqrt(2)*f)*(x-v0-va*np.cos(2*np.pi*time)))

    fde = QNV*A*concModFunc(alpha,time, phi, FORM, FORMARG)*(eta*(Lnp+Lpp-2*Lp+D*Lnn+D*Lpn-D*2*Ln)+(1-eta)*(Gnp+Gpp-2*Gp+D*Gnn+D*Gpn-D*2*Gn))*np.cos(2*N*np.pi*time)+y0

    if alpha < 0 or alpha > 1:
            boundError = np.empty(len(x))
            boundError.fill(1e50)
            boundError *= 1+abs(alpha)
            return boundError
    if phi < 0 or phi > np.pi/2:
           boundError = np.empty(len(x))
           boundError.fill(1e50)
           boundError *= 1+abs(phi)
           return boundError
    if va < 0:
            boundError = np.empty(len(x))
            boundError.fill(1e50)
            boundError *= 1+abs(va)
            return boundError
    return fde

def niceohvmsDispOdd(x,alpha,phi,A,v0,delta,kappa,va,y0,time):
    f = (delta**5+2.69269*(delta**4)*kappa+2.42843*(delta**3)*(kappa**2)\
         +4.47163*(delta**2)*(kappa**3)+0.07842*delta*(kappa**4)+kappa**5)**0.2
    eta = 1.36603*(kappa/f)-0.47719*(kappa/f)**2+0.11116*(kappa/f)**3

    Lnp = B*((2*f*(x-v0-VH+va*np.cos(2*np.pi*time)))/(np.pi*(4*(x-v0-VH+va*np.cos(2*np.pi*time))**2+f**2)))
    Lpp = B*((2*f*(x-v0+VH+va*np.cos(2*np.pi*time)))/(np.pi*(4*(x-v0+VH+va*np.cos(2*np.pi*time))**2+f**2)))
    Lp = B*((2*f*(x-v0+va*np.cos(2*np.pi*time)))/(np.pi*(4*(x-v0+va*np.cos(2*np.pi*time))**2+f**2)))
    Lnn = B*((2*f*(x-v0-VH-va*np.cos(2*np.pi*time)))/(np.pi*(4*(x-v0-VH-va*np.cos(2*np.pi*time))**2+f**2)))
    Lpn = B*((2*f*(x-v0+VH-va*np.cos(2*np.pi*time)))/(np.pi*(4*(x-v0+VH-va*np.cos(2*np.pi*time))**2+f**2)))
    Ln = B*((2*f*(x-v0-va*np.cos(2*np.pi*time)))/(np.pi*(4*(x-v0-va*np.cos(2*np.pi*time))**2+f**2)))
    Gnp = -2*B*P/(np.sqrt(2)*np.pi*f)*s.dawsn(P/(np.sqrt(2)*f)*(x-v0-VH+va*np.cos(2*np.pi*time)))
```

```
    Gpp = -2*B*P/(np.sqrt(2)*np.pi*f)*s.dawsn(P/(np.sqrt(2)*f)*(x-v0+VH+va*np.cos(2*np.pi*time)))
    Gp = -2*B*P/(np.sqrt(2)*np.pi*f)*s.dawsn(P/(np.sqrt(2)*f)*(x-v0+va*np.cos(2*np.pi*time)))
    Gnn = -2*B*P/(np.sqrt(2)*np.pi*f)*s.dawsn(P/(np.sqrt(2)*f)*(x-v0-VH-va*np.cos(2*np.pi*time)))
    Gpn = -2*B*P/(np.sqrt(2)*np.pi*f)*s.dawsn(P/(np.sqrt(2)*f)*(x-v0+VH-va*np.cos(2*np.pi*time)))
    Gn = -2*B*P/(np.sqrt(2)*np.pi*f)*s.dawsn(P/(np.sqrt(2)*f)*(x-v0-va*np.cos(2*np.pi*time)))

    fdo = QNV*A*concModFunc(alpha,time, phi, FORM, FORMARG)*(eta*(Lnp+Lpp-2*Lp+D*Lnn+D*Lpn-D*2*Ln)+(1-eta)*(Gnp+Gpp-2*Gp+D*Gnn+D*Gpn-D*2*Gn))*np.sin(2*N*np.pi*time)+y0

    if alpha < 0 or alpha > 1:
            boundError = np.empty(len(x))
            boundError.fill(1e50)
            boundError *= 1+abs(alpha)
            return boundError
    if phi < 0 or phi > np.pi/2:
           boundError = np.empty(len(x))
           boundError.fill(1e50)
           boundError *= 1+abs(phi)
           return boundError
    if va < 0:
            boundError = np.empty(len(x))
            boundError.fill(1e50)
            boundError *= 1+abs(va)
            return boundError
    return fdo

def niceohvmsDispMag(x,alpha,phi,A,v0,delta,kappa,va,y0,time):
    fd = np.sqrt(niceohvmsDispEven(x,alpha,phi,A,v0,delta,kappa,va,0,time)**2\
                +niceohvmsDispOdd(x,alpha,phi,A,v0,delta,kappa,va,0,time)**2)+y0
    if alpha < 0 or alpha > 1:
            boundError = np.empty(len(x))
            boundError.fill(1e50)
            boundError *= 1+abs(alpha)
            return boundError
    if phi < 0 or phi > np.pi/2:
            boundError = np.empty(len(x))
            boundError.fill(1e50)
            boundError *= 1+abs(phi)
            return boundError
    if va < 0:
            boundError = np.empty(len(x))
            boundError.fill(1e50)
            boundError *= 1+abs(va)
            return boundError
    if delta < 0:
            boundError = np.empty(len(x))
            boundError.fill(1e50)
            boundError *= 1+abs(delta)
            return boundError
    if kappa < 0:
            boundError = np.empty(len(x))
            boundError.fill(1e50)
```

```
            boundError *= 1+abs(kappa)
            return boundError
    if y0 < 0:
            boundError = np.empty(len(x))
            boundError.fill(1e50)
            boundError *= 1+abs(y0)
            return boundError
    return fd

def concModFunc(alpha,time,phi,form, formarg):
    if form == 0:
      concModFValue = (1-alpha)+alpha*np.square(np.cos(2*np.pi*time+phi))
    elif form == 1:
      concModFValue = (1-alpha)+alpha*np.sqrt(np.square(np.cos(2*np.pi*time+phi)))
    elif form == 2:
      concModFValue = (1-alpha)+alpha*np.square(ss.square(2*np.pi*time+phi))
    elif form == 3:
      concModFValue = (1-alpha)+alpha*np.square(ss.sawtooth(2*np.pi*time+phi))
    elif form == 4:
      concModFValue = (1-alpha)+alpha*np.square((1-abs(formarg))*(np.cos(2*np.pi*time))+formarg*(ss.sawtooth(2*np.pi*time))+phi)
    elif form == 5:
      concModFValue = (1-alpha)+alpha*np.square((1-abs(formarg))*(np.cos(2*np.pi*time))+formarg*(4*np.pi*time)+phi)
    else:
      concModFValue = 1

    return concModFValue

def lineNAI(x,alpha,phi,A,v0,delta,kappa,va,y0,theta):
    timearray = np.arange(-0.5,0.5+0.04,0.04)

    isFirst = True

    for timept in timearray:
        row = np.cos(theta)*niceohvmsAbsEven(x,alpha,phi,A,v0,delta,kappa,va,y0,timept)\
              +np.sin(theta)*niceohvmsAbsOdd(x,alpha,phi,A,v0,delta,kappa,va,y0,timept)
        row = np.resize(row,(1,len(row)))

        if isFirst:
            toInt = row[:]
            isFirst = False
        else:
            toInt = np.append(toInt,row,axis=0)
    if theta < 0.0 or theta > np.pi:
        boundError = np.empty(len(x))
        boundError.fill(1e50)
        boundError *= 1+abs(theta)
        return boundError
    else:
        return np.trapz(toInt,x=timearray,axis=0)

def lineNAQ(x,alpha,phi,A,v0,delta,kappa,va,y0,theta):
    timearray = np.arange(-0.5,0.5+0.04,0.04)
```

```

    isFirst = True

    for timept in timearray:
        row = np.sin(theta)*niceohvmsAbsEven(x,alpha,phi,A,v0,delta,kappa,va,y0,timept)\
              +np.cos(theta)*niceohvmsAbsOdd(x,alpha,phi,A,v0,delta,kappa,va,y0,timept)
        row = np.resize(row,(1,len(row)))

        if isFirst:
            toInt = row[:]
            isFirst = False
        else:
            toInt = np.append(toInt,row,axis=0)
    if theta < 0.0 or theta > np.pi:
        boundError = np.empty(len(x))
        boundError.fill(1e50)
        boundError *= 1+abs(theta)
        return boundError
    else:
        return np.trapz(toInt,x=timearray,axis=0)

def lineNDI(x,alpha,phi,A,v0,delta,kappa,va,y0,theta):
    timearray = np.arange(-0.5,0.5+0.04,0.04)

    isFirst = True

    for timept in timearray:
        row = np.cos(theta)*niceohvmsDispEven(x,alpha,phi,A,v0,delta,kappa,va,y0,timept)\
              +np.sin(theta)*niceohvmsDispOdd(x,alpha,phi,A,v0,delta,kappa,va,y0,timept)
        row = np.resize(row,(1,len(row)))

        if isFirst:
            toInt = row[:]
            isFirst = False
        else:
            toInt = np.append(toInt,row,axis=0)
    if theta < 0.0 or theta > np.pi:
        boundError = np.empty(len(x))
        boundError.fill(1e50)
        boundError *= 1+abs(theta)
        return boundError
    else:
        return np.trapz(toInt,x=timearray,axis=0)

def lineNDQ(x,alpha,phi,A,v0,delta,kappa,va,y0,theta):
    timearray = np.arange(-0.5,0.5+0.04,0.04)

    isFirst = True

    for timept in timearray:
        row = np.sin(theta)*niceohvmsDispEven(x,alpha,phi,A,v0,delta,kappa,va,y0,timept)\
```

```
              +np.cos(theta)*niceohvmsDispOdd(x,alpha,phi,A,v0,delta,kappa,va,y0,timept)
        row = np.resize(row,(1,len(row)))

        if isFirst:
            toInt = row[:]
            isFirst = False
        else:
            toInt = np.append(toInt,row,axis=0)
    if theta < 0.0 or theta > np.pi:
        boundError = np.empty(len(x))
        boundError.fill(1e50)
        boundError *= 1+abs(theta)
        return boundError
    else:
        return np.trapz(toInt,x=timearray,axis=0)

def lineNA(x,alpha,phi,A,v0,delta,kappa,va,y0):
    timearray = np.arange(-0.5,0.5+0.04,0.04)

    isFirst = True

    for timept in timearray:
        row = niceohvmsAbsMag(x,alpha,phi,A,v0,delta,kappa,va,y0,timept)
        row = np.resize(row,(1,len(row)))

        if isFirst:
            toInt = row[:]
            isFirst = False
        else:
            toInt = np.append(toInt,row,axis=0)

    return np.trapz(toInt,x=timearray,axis=0)

def lineND(x,alpha,phi,A,v0,delta,kappa,va,y0):
    timearray = np.arange(-0.5,0.5+0.04,0.04)

    isFirst = True

    for timept in timearray:
        row = niceohvmsDispMag(x,alpha,phi,A,v0,delta,kappa,va,y0,timept)
        row = np.resize(row,(1,len(row)))

        if isFirst:
            toInt = row[:]
            isFirst = False
        else:
            toInt = np.append(toInt,row,axis=0)

    return np.trapz(toInt,x=timearray,axis=0)

def absResiduals(p,x,yI,yQ,alpha,A,v0,delta,kappa,va):
    phi,y01,y02,theta = p
    print(p)
    error = np.sqrt((yI-lineNAI(x,alpha,phi,A,v0,delta,kappa,va,y01,theta))**2+(yQ-lineNAQ(x,alpha,phi,A,v0,delta,kappa,va,y02,theta))**2)
    return error

```

```python
def absMagResiduals(p,x,yI,phi,y0):
    alpha,A,v0,delta,kappa,va = p
    print(p)
    error = (yI-lineNA(x,alpha,phi,A,v0,delta,kappa,va,y0)-lambMag(x))
    return error

def dispResiduals(p,x,yI,yQ,alpha,A,v0,delta,kappa,va):
    phi,y01,y02,theta = p
    print(p)
    error = np.sqrt((yI-lineNDI(x,alpha,phi,A,v0,delta,kappa,va,y01,theta))**2+(yQ-lineNDQ(x,alpha,phi,A,v0,delta,kappa,va,y02,theta))**2)
    return error

def dispMagResiduals(p,x,yI,phi,y0):
    alpha,A,v0,delta,kappa,va = p
    print(p)
    error = (yI-lineND(x,alpha,phi,A,v0,delta,kappa,va,y0)-lambMag(x))
    return error

def vms(x,A,v0,delta,kappa,va,y0,time):
    f = (delta**5+2.69269*(delta**4)*kappa+2.42843*(delta**3)*(kappa**2)\
         +4.47163*(delta**2)*(kappa**3)+0.07842*delta*(kappa**4)+kappa**5)**0.2
    eta = 1.36603*(kappa/f)-0.47719*(kappa/f)**2+0.11116*(kappa/f)**3
    L = (2*f)/(np.pi*(4*(x-v0+va*np.cos(2*np.pi*time))**2+f**2))
    G = P/(f*np.sqrt(2*np.pi))*np.exp(-((x-v0+va*np.cos(2*np.pi*time))*P)**2/(2*f**2))
    fv = A*(eta*L+(1-eta)*G)*np.cos(2*N*np.pi*time)+y0

    if va < 0:
        boundError = np.empty(len(x))
        boundError.fill(1e50)
        boundError *= 1+abs(va)
        return boundError
    if delta < 0:
        boundError = np.empty(len(x))
        boundError.fill(1e50)
        boundError *= 1+abs(delta)
        return boundError
    if kappa < 0:
        boundError = np.empty(len(x))
        boundError.fill(1e50)
        boundError *= 1+abs(kappa)
        return boundError
    return fv

def lineVMS(x,A,v0,delta,kappa,va,y0):
    timearray = np.arange(-0.5,0.5+0.004,0.004)

    isFirst = True

    for timept in timearray:
        row = vms(x,A,v0,delta,kappa,va,y0,timept)
        row = np.resize(row,(1,len(row)))

        if isFirst:
            toInt = row[:]
            isFirst = False
```

```
        else:
            toInt = np.append(toInt,row,axis=0)

    return np.trapz(toInt,x=timearray,axis=0)

def vmsResiduals(p,x,yI):
    A,v0,delta,kappa,va,y0 = p
    error = yI-lineVMS(x,A,v0,delta,kappa,va,y0)
    return error

def vmsFRho(x,A,v0,delta,kappa,va,y0,time):
    R = va/(0.5346*kappa+np.sqrt(0.2166*kappa**2+delta**2))

    f = (delta**5+2.69269*(delta**4)*kappa+2.42843*(delta**3)*(kappa**2)\
         +4.47163*(delta**2)*(kappa**3)+0.07842*delta*(kappa**4)+kappa**5)**(1/5)
    fva = R*f
    eta = 1.36603*(kappa/f)-0.47719*(kappa/f)**2+0.11116*(kappa/f)**3
    L = (2*f)/(np.pi*(4*(x-v0+fva*np.cos(2*np.pi*time))**2+f**2))
    G = P/(f*np.sqrt(2*np.pi))*np.exp(-((x-v0+fva*np.cos(2*np.pi*time))*P)**2/(2*f**2))
    fv = A*(eta*L+(1-eta)*G)*np.cos(2*N*np.pi*time)+y0

    if va < 0:
        boundError = np.empty(len(x))
        boundError.fill(1e50)
        boundError *= 1+abs(va)
        return boundError
    if delta < 0:
        boundError = np.empty(len(x))
        boundError.fill(1e50)
        boundError *= 1+abs(delta)
        return boundError
    if kappa < 0:
        boundError = np.empty(len(x))
        boundError.fill(1e50)
        boundError *= 1+abs(kappa)
        return boundError
    return fv

def lineVMSFRho(x,A,v0,delta,kappa,va,y0):
    timearray = np.arange(-0.5,0.5+0.004,0.004)

    isFirst = True

    for timept in timearray:
        row = vmsFRho(x,A,v0,delta,kappa,va,y0,timept)
        row = np.resize(row,(1,len(row)))

        if isFirst:
            toInt = row[:]
            isFirst = False
        else:
            toInt = np.append(toInt,row,axis=0)

    return np.trapz(toInt,x=timearray,axis=0)

def vmsResidualsFRho(p,x,yI,va):
    A,v0,delta,kappa,y0 = p
```

```
    print(p)
    error = yI-lineVMSFRho(x,A,v0,delta,kappa,va,y0)
    return error

def vmsResidualsFreeRho(p,x,yI,v0,delta,kappa,y0):
    A,va = p
    print(p)
    error = yI-lineVMS(x,A,v0,delta,kappa,va,y0)
    return error
if __name__ == "__main__":
    print("This module is for import only.")

```

K.5 Auxiliary Files

The editable reference files with all the required parameters include `FuncParams.txt` and `LineParams.txt` files. The header explains each parameter. They are tab delineated, and all comments must have a “#” as the first character of the line.

```
# This is a parameter file belonging to JFit by James Hodges
# Do not edit the name of the file or the format
# Comments can be made using a '#' preceding the line
#
# Modulation Beta is the Beta that is used in the Bessel functions
# Heterdonye Frequency is the the Modulation Frequency
# Fourier Coeff determines which fourier component you pick, i.e. 1 for 1f det, 2 for 2f, etc.
# Invert Q Phase should be 1 or -1 which accounts for whether your Q detection phase is +90 or -90
# Directionality refers to whether or not the cavity is unidirectional or bidirectional with regards to the propagation of light 0 is unidirectional and 1 is bidirectional
# Concentration Modulation Functional Form is a integer Ranging from 0 to ?, which uses the functional form of choice for concentration modulation
# Concentration Modulation Form Args is any Args that may be required. See Documentation if any exists.
# Fixed Rho is for fitting with fixed velocity modulation amplitude, 1 for true 0 for false.
#
# Modulation Beta       Heterodyne Frequency    Fourier Coeff   Invert Q Phase  Directionality  Conc Mod Functional Form        Conc Mod Form Args      Fixed Rho
0.63    .25     2       1       1       0       -0.1    1
#
#
# LambDip Parameters
#
#AL1    AL1FRAC1        AL1FRAC2        AL1FRAC3        AL2     AL2FRAC1        AL2FRAC2        AL2FRAC3        FWHM    MU      THETA   GAUSSCHAR
0       0.41    0       0.11    0       0.63    0.06    0       0.0017215       0.0993250       -12     .99
```

```
# This is a parameter file belonging to JFit by James Hodges
# Do not edit the name of the file or the format
# Comments can be made using a '#' preceding the line
#
#
# Linecenter is the center freq of the transition(MHz), A is the absoprtion
depth(AU), FWHM is the full width at half maximum(MHz), CMD is conc. mod.
depth(unitless from 0-1), CMP is conc. mod. phase(degree), VMA is velocity mod.
amp.(MHz), and y0 is the baseline(AU).
# NoiseLevel, LowDom, HighDom, and Step are utilized for simulation purposes.
# Gaussian data only uses the first three parameters and the baseline. You
leave garbarge in the others.
#
#
#Linecenter     A       IFWHM   HFWHM   CMD     CMP     VMA     y01     y02
theta   NoiseLevel      LowDom  HighDom Step
0.0     10      0.5     0.5     1.0     45      0.2456  0.00    0       45
0.0000  -4      4       0.01
```

`JFitGrapher` and `JFitSimGrapher` are useful bash scripts for rapid visualization of fit results in the case of the former and simulation results in the case of the latter. If these tools are used they only take a single argument and it corresponds to the token name of the file of interest in the JFit folder. It uses `gnuplot` to create figures and saves them in the data, and then it uses gwenview to display those images.

```bash
#! /bin/bash

pathname="./JFitData/$1/$1"
end1="_fit.txt"
end2=".png"
end3="_resid.png"

gnuplot << EOF
fileinp='$pathname$end1'
set terminal png size 600,400 enhanced font "Helvetica,10"
set output "$pathname$end2"
plot fileinp u 1:2 title 'In-phase', fileinp u 1:3 title 'fitI' w lines, fileinp u 1:5 title 'Quadrature', fileinp u 1:6 title 'fitQ' w lines
EOF

gnuplot << EOF
fileinp='$pathname$end1'
set terminal png size 600,400 enhanced font "Helvetica,10"
set output "$pathname$end3"
plot fileinp u 1:4 title 'residI', fileinp u 1:7 title 'residQ'
EOF

gwenview $pathname".png" 2> .gwenviewgarbage.txt &

gwenview $pathname"_resid.png" 2> .gwenviewgarbage.txt &

```

```bash
#! /bin/bash

pathname="./JFitData/$1/$1"
end1=".txt"
end2=".png"


gnuplot << EOF
fileinp='$pathname$end1'
set terminal png size 1200,800 enhanced font "Helvetica,10"
set output "$pathname$end2"
plot fileinp u 1:2 title 'In-phase', fileinp u 1:3 title 'quadrature'
EOF

gwenview $pathname".png" 2> .gwenviewgarbage.txt &

```

References

[1] A. R. W. McKellar, J. K. G. Watson, *J. Mol. Spectrosc.* **191**, 215 (1998).

[2] K. N. Crabtree, *et al.*, *Chem. Phys. Lett.* **551**, 1 (2012).

[3] K. Takahata, *et al.*, *Phys. Rev. A* **80**, 032518 (2009).

[4] W. D. Geppert, M. Larsson, *Chem. Rev.* **113**, 8872 (2013).

[5] M. L. Senent, M. Hochlaf, *Astrophys. J.* **768**, 59 (2013).

[6] N. Indriolo, B. J. McCall, *Astrophys. J.* **745**, 91 (2012).

[7] N. Indriolo, T. Oka, T. R. Geballe, B. J. McCall, *Astrophys. J.* **711**, 1338 (2010).

[8] A. Ali, E. C. Sittler Jr., D. Chornay, B. R. Rowe, C. Puzzarini, *Planet. Space Sci.* **87**, 96 (2013).

[9] E. Lellouch, *Philos. Trans. R. Soc. A* **364**, 3139 (2006).

[10] N. S. Shuman, D. E. Hunton, A. A. Viggiano, *Chem. Rev.* **115**, 4542 (2015).

[11] R. S. MacTaylor, A. W. Castleman Jr., *J. Atmos. Chem.* **36**, 23 (2000).

[12] N. M. Semo, W. S. Koski, *J. Phys. Chem.* **88**, 5320 (1984).

[13] R. D. Thomas, *Mass Spectrom. Rev.* **27**, 485 (2008).

[14] E. T. White, J. Tang, T. Oka, *Science* **284**, 135 (1999).

[15] O. Asvany, K. M. T. Yamada, S. Brünken, A. Potapov, S. Schlemmer, *Science* **347**, 1346 (2015).

[16] T. C. Cheng, *et al.*, *J. Phys. Chem. Lett.* **1**, 758 (2010).

[17] C. S. Gudeman, M. Begemann, J. Pfaff, R. J. Saykally, *Phys. Rev. Lett.* **50**, 727 (1983).

[18] S. K. Stephenson, R. J. Saykally, *Chem. Rev.* **105**, 3220 (2005).

[19] A. O'Keefe, D. A. G. Deacon, *Rev. Sci. Instrum.* **59**, 2544 (1988).

[20] G. Berden, R. Peeters, G. Meijer, *Int. Rev. Phys. Chem.* **19**, 565 (2000).

[21] B. M. Siller, A. A. Mills, B. J. McCall, *Opt. Lett.* **35**, 1266 (2010).

[22] G. C. Bjorklund, M. D. Levenson, W. Lenth, C. Ortiz, *Appl. Phys. B* **32**, 145 (1983).

[23] J. L. Gottfried, B. J. McCall, T. Oka, *J. Chem. Phys.* **118**, 10890 (2003).

[24] L.-S. Ma, J. Ye, P. Dubé, J. L. Hall, *J. Opt. Soc. Am. B* **16**, 2255 (1999).

[25] B. M. Siller, M. W. Porambo, A. A. Mills, B. J. McCall, *Opt. Express* **19**, 24822 (2011).

[26] J. N. Hodges, A. J. Perry, P. A. Jenkins II, B. M. Siller, B. J. McCall, *J. Chem. Phys.* **139**, 164201 (2013).

[27] H.-C. Chen, C.-Y. Hsiao, J.-L. Peng, T. Amano, J.-T. Shy, *Phys. Rev. Lett.* **109**, 263002 (2012).

[28] P. Jusko, C. Konietzko, S. Schlemmer, O. Asvany, *J. Mol. Spectrosc.* **319**, 55 (2016).

[29] S. Civiš, *Chem. Phys.* **186**, 63 (1994).

[30] H. Gao, *et al.*, *Acta Phys. Sin.* **50**, 1463 (2001).

[31] J. W. Farley, *J. Chem. Phys.* **95**, 5590 (1991).

[32] J. N. Hodges, B. J. McCall, *J. Chem. Phys.* **144**, 184201 (2016).

[33] T. Amano, *J. Chem. Phys.* **79**, 3595 (1983).

[34] A. A. Mills, B. M. Siller, B. J. McCall, *Chem. Phys. Lett.* **501**, 1 (2010).

[35] B. M. Siller, J. N. Hodges, A. J. Perry, B. J. McCall, *J. Phys. Chem. A* **117**, 10034 (2013).

[36] M. Pavanello, *et al.*, *Phys. Rev. Lett.* **108**, 023002 (2012).

[37] J. Komasa, *et al.*, *J. Chem. Theory Comput.* **7**, 3105 (2011).

[38] P. Pyykkö, *et al.*, *Phys. Rev. A* **63**, 024502 (2001).

[39] T. R. Geballe, T. Oka, *Nature* **384**, 334 (1996).

[40] P. Drossart, *et al.*, *Nature* **340**, 539 (1989).

[41] D. Rego, *et al.*, *Nature* **399**, 121 (1999).

[42] C. Savage, F. Dong, D. J. Nesbitt, *60th International Symposium on Molecular Spectroscopy* (2005).

[43] K.-Y. Wu, Precision Measurement of the ν_2-band of Triatomic Hydrogen Molecular Ion H_3^+, Ph.D. thesis, National Tsing Hua University (2008).

[44] T. Oka, *Philos. Trans. R. Soc. A* **303**, 543 (1981).

[45] H.-C. Chen, J.-L. Peng, T. Amano, J. T. Shy, *68th International Symposium on Molecular Spectroscopy* (2013).

[46] A. Foltynowicz, W. Ma, O. Axner, *Opt. Express* **16**, 14689 (2008).

[47] A. Foltynowicz, I. Silander, O. Axner, *J. Opt. Soc. Am. B* **28**, 2797 (2011).

[48] J. Westberg, P. Kluczynski, S. Lundqvist, O. Axner, *J. Quant. Spectrosc. Radiat. Transf.* **112**, 1443 (2011).

[49] G. Cazzoli, L. Cludi, G. Buffa, C. Puzzarini, *Astrophys. J. Suppl. Ser.* **203**, 11 (2012).

[50] P. R. Bunker, B. Ostojić, S. Yurchenko, *J. Mol. Struct.* **695-696**, 253 (2004).

[51] Z. Jin, B. J. Braams, J. M. Bowman, *J. Phys. Chem. A* **110**, 1569 (2006).

[52] X. Huang, *et al.*, *Science* **311**, 60 (2006).

[53] M. P. Deskevich, A. B. McCoy, J. M. Hutson, D. J. Nesbitt, *J. Chem. Phys.* **128**, 094306 (2008).

[54] C. E. Hinkle, A. B. McCoy, *J. Phys. Chem. A* **112**, 2058 (2008).

[55] X.-G. Wang, T. Carrington Jr., *J. Chem. Phys.* **129**, 234102 (2008).

[56] C. E. Hinkle, A. S. Petit, A. B. McCoy, *J. Mol. Spectrosc.* **268**, 189 (2011).

[57] O. Asvany, *et al.*, *Science* **309**, 1219 (2005).

[58] O. Asvany, J. Krieg, S. Schlemmer, *Rev. Sci. Instrum.* **83**, 093110 (2012).

[59] S. Schlemmer, Private Communication.

[60] J. M. L. Martin, P. R. Taylor, T. J. Lee, *J. Chem. Phys.* **99**, 286 (1993).

[61] A. J. Perry, J. N. Hodges, C. R. Markus, G. S. Kocheril, B. J. McCall, *J. Chem. Phys.* **141**, 101101 (2014).

[62] A. J. Perry, J. N. Hodges, C. R. Markus, G. S. Kocheril, B. J. McCall, *J. Mol. Spectrosc.* **317**, 71 (2015).

[63] C. R. Markus, *et al.*, *Astrophys. J.* **817**, 138 (2016).

[64] D. N. Gresh, K. C. Cossel, Y. Zhou, J. Ye, E. A. Cornell, *J. Mol. Spectrosc.* **319**, 1 (2016).

[65] C. Savage, A. J. Apponi, L. M. Ziurys, *Astrophys. J.* **608**, L73 (2004).

[66] D. T. Halfen, L. M. Ziurys, *J. Mol. Spectrosc.* **234**, 34 (2005).

[67] D. T. Halfen, L. M. Ziurys, *Chem. Phys. Lett.* **496**, 8 (2010).

[68] E. A. Mason, E. W. McDaniel, *Transport Properties of Ions in Gases* (John Wiley & Sons, New York, 1988).

[69] P. Kluczynski, J. Gustafsson, Å. M. Lindberg, O. Axner, *Spectrochim. Acta Part B* **56**, 1277 (2001).

[70] P. Thompson, D. E. Cox, J. B. Hastings, *J. Appl. Crystallogr.* **20**, 79 (1987).

[71] B. J. McCall, Spectroscopy of H_3^+ in Laboratory and Astrophysical Plasmas, Ph.D. thesis, University of Chicago (2001).

[72] T. Ida, M. Ando, H. Toraya, *J. Appl. Crystallogr.* **33**, 1311 (2000).

[73] A. von Engel, *Ionized Gases* (AIP Press, New York, 1965).

[74] J. C. Pearson, L. C. Oesterling, E. Herbst, F. C. De Lucia, *Phys. Rev. Lett.* **75**, 2940 (1995).

[75] F. F. Chen, *Introduction to Plasma Physics* (Plenum Press, New York, 1974).

[76] T. Oka, *Phys. Rev. Lett.* **45**, 531 (1980).

[77] T. N. Olney, N. M. Cann, G. Cooper, C. E. Brion, *Chem. Phys.* **223**, 59 (1997).

[78] P. N. B. Neves, J. Escada, F. I. G. M. Borges, L. M. N. Tavora, C. A. N. Conde, *2011 IEEE Nucl. Sci. Symp. Conf. Rec.* (IEEE, 2011), pp. 1793–1794.

[79] F. M. Schmidt, A. Foltynowicz, W. Ma, O. Axner, *J. Opt. Soc. Am. B* **24**, 1392 (2007).

[80] W. Ma, A. Foltynowicz, O. Axner, *J. Opt. Soc. Am. B* **25**, 1144 (2008).

[81] I. Silander, T. Hausmaninger, W. Ma, F. J. M. Harren, O. Axner, *Opt. Lett.* **40**, 439 (2015).

[82] R. D. L. Kronig, *J. Opt. Soc. Am.* **12**, 547 (1926).

[83] S. W. North, X. S. Zheng, R. Fei, G. E. Hall, *J. Chem. Phys.* **104**, 2129 (1996).

[84] J. Ye, L. S. Ma, J. L. Hall, *Opt. Lett.* **21**, 1000 (1996).

[85] J. Ye, L. S. Ma, J. L. Hall, *J. Opt. Soc. Am. B* **17**, 927 (2000).

[86] W. Demtröder, *Laser Spectroscopy Vol. 1: Basic Princples* (Springer-Verlag, Berlin, 2008).

[87] W. Demtröder, *Laser Spectroscopy Vol. 2: Experimental Techniques* (Springer-Verlag, Berlin, 2008).

[88] J. Ye, Ultrasensitive High Resolution Laser Spectroscopy and Its Applications to Optical Frequency Standards, Ph.D. thesis, University of Colorado (1997).

[89] O. Axner, W. Ma, A. Foltynowicz, *J. Opt. Soc. Am. B* **25**, 1166 (2008).

[90] H_3^+ Resource Center, `http://h3plus.uiuc.edu`. Einstein A coefficients can be used to determine transition dipole moments, and are available as calculated by J.K.G. Watson under the spectroscopic databases tab.

[91] P. Ehlers, A. C. Johansson, I. Silander, A. Foltynowicz, O. Axner, *J. Opt. Soc. Am. B* **31**, 2938 (2014).

[92] V. N. Ochkin, *Spectroscopy of Low Temperature Plasmas* (Wiley-VCH Verlag, Weinheim, 2009).

[93] J. Reid, M. El-Sherbiny, B. K. Garside, E. A. Ballik, *Appl. Opt.* **19**, 3349 (1980).

[94] C. R. Webster, *J. Opt. Soc. Am. B* **2**, 1464 (1985).